UC Berkeley
UC Berkeley Electronic Theses and Dissertations

Title
I. Climate change on ancient Mars. II. Exoplanet geodynamics and climate.

Permalink
https://escholarship.org/uc/item/9tr9s0xx

Author
Kite, Edwin Stephen

Publication Date
2011

Peer reviewed|Thesis/dissertation

eScholarship.org Powered by the California Digital Library
University of California

I. Climate change on ancient Mars.
II. Exoplanet geodynamics and climate.

by

Edwin Stephen Kite

A dissertation submitted in partial satisfaction of the
requirements for the degree of
Doctor of Philosophy

in

Earth and Planetary Science

in the

Graduate Division

of the

University of California, Berkeley

Committee in charge:

Professor Michael Manga, Chair
Professor Eugene Chiang
Professor Geoffrey W. Marcy
Professor William E. Dietrich

Fall 2011

I. Climate change on ancient Mars.
II. Exoplanet geodynamics and climate.

Copyright 2011
by
Edwin Stephen Kite

Abstract

I. Climate change on ancient Mars.
II. Exoplanet geodynamics and climate.

by

Edwin Stephen Kite

Doctor of Philosophy in Earth and Planetary Science

University of California, Berkeley

Professor Michael Manga, Chair

This thesis describes work related to long-term climate stability, on Mars and exoplanets.

Mars is the only planet known to record a major transition in planetary habitability. The evidence for surface temperatures near the melting point of water on Early Mars is difficult to explain, because theory predicts a faint young Sun. Seasonal snowmelt need not require high annual mean temperatures, but surface water ice tends to migrate away from the warmer regions of the planet where melting is energetically possible. In the first part of this thesis I use geological analysis, mesoscale models, and idealized surface energy balance models to examine two possible solutions to this problem.

Impacts into icy targets, groundwater outbursts, and phreatic explosions are all expected to inject water vapor into the Mars atmosphere. I use mesoscale models to track the atmospheric response to these transient, localized vapor sources. Using idealized boundary conditions, I show that storms with updraft speeds >50 m/s and localized precipitation are expected near transient lakes $>10^3$ km^2 in size. Snow deposited in this way is out of equilibrium with orbital forcing, and correspondingly more likely to melt. Canyon paleolakes in the Valles Marineris are frequently associated with streams preserved on the plateaux just downwind of the canyons. Using geologically realistic boundary conditions, I study the atmospheric response to two short-lived paleolakes. In each case, the plateau streams are in the locations expected for localized precipitation.

Liquid water availability favors lithification, so the Martian sedimentary rock record is a wet-pass filter. Orbital variability strongly affects liquid water availability, so considering only averaged orbital conditions is neither sufficient not appropriate. To find the likelihood of snow melting, I consider all possible orbital forcings using an idealized but self-consistent model of snowpack energy balance and the CO_2 greenhouse effect. Seasonal snowmelt on Early Mars is possible under unusual orbital conditions provided that the snow is dust-contaminated. The predicted distribution of snowmelt can explain the distribution of sedimentary rocks on Mars, but only if Mars had a thin atmosphere when the sedimentary

rocks formed. This framework is the first to link upcoming observations by the Mars Science Laboratory Curiosity rover at the lower Gale Crater mound to past global climate on Mars. The model makes predictions about the lower Gale Crater mound that can be tested using Curiosity rover data.

Earth is the only example of long term climate stability that is available for study, so long term climate stability is difficult to understand. Extrasolar planets may ameliorate this problem of uniqueness. It is clear that rates of volcanic activity and of surface weathering are important in regulating long term climate. In the second part of this thesis, I model the rate of volcanism on massive Earth-like planets, and the surface weathering rate on planets in 1:1 spin:orbit resonance. "Super-Earths" in the range 1-10 Earth masses have been detected by radial velocity and transit methods. Using an idealized mantle thermal evolution model to drive mantle-melting models, I show that the rate of volcanism on massive Earth like planets is a weak function of planet mass. Planet mass can, however, affect tectonics by changing the mode of mantle convection. Earth's climate stability depends on a negative feedback involving the temperature-dependent rate of weathering and mean surface temperature. I use an idealized model to show that for intermediate surface pressures and for low-opacity atmospheres, nonlinearities in the surface energy balance can reverse the sign of this dependence on tidally-locked planets. This leads to climate instability.

I conclude by discussing future observations and research aimed at understanding long-term climate stability.

Figure 0.1 The Venus Tablet from the Royal Library at Nineveh. The tablet records astronomical information from ∼3600 years ago (First Dynasty of Babylon). The Assyrian ruler Ashurbanipal, a scholar, caused the information to be copied onto this clay tablet around 700 BCE. His library was uncovered by the explorer Austen Henry Layard and the archeologist Hormuzd Rassam 2500 years later. Through its reference to "the Year of the Golden Throne," this clay tablet now forms the basis for the chronology of the ancient Near East, and of the fall of Babylon. *Wikimedia Commons*.

"It's important that we attempt to extend life beyond Earth now. It is the first time in the four billion-year history of Earth that it's been possible and that window could be open for a long time – hopefully it is – or it could be open for a short time. We should err on the side of caution, and do something now."

– Elon Musk

Contents

List of Figures **viii**

List of Tables **xi**

1 Introduction. **1**
1.1 Motivation and Context 1
1.2 The Early Mars climate problem 4
1.3 Exoplanet observations and models 18

2 Localized precipitation on Mars. **23**
2.1 Introduction 24
2.2 Localized precipitation on Mars: order-of-magnitude reasoning 27
2.3 Model setup 29
2.4 Analysis of reference simulation 31
2.4.1 Time-averaged response 33
2.4.2 Spatially-averaged time dependencies 34
2.4.3 Structure of the buoyant plume 35
2.4.4 Precipitation 36
2.4.5 Precipitation efficiency 36
2.5 Sensitivity tests 39
2.5.1 Vertical resolution 39
2.5.2 Horizontal resolution 40
2.5.3 Size of idealized lake 40
2.5.4 Surface roughness parameterization 43
2.5.5 Line source 43
2.5.6 Season 44
2.5.7 Latitude 44
2.5.8 Faint young sun 44
2.5.9 Paleoatmospheric pressure 45

2.6 A probabilistic model of snowpack melting on ancient Mars . . . 45
2.7 Prospectus and discussion . . . 55
2.7.1 Geomorphic paleobarometer? . . . 56
2.7.2 Applications to the Late Hesperian and Amazonian sedimentary record 56
2.7.3 Can localized precipitation explain Noachian erosion? . . . 58
2.8 Conclusions . . . 59
2.9 Methods . . . 60

3 Chaos terrain, storms, and past climate on Mars. 62
3.1 Introduction . . . 63
3.2 Geologic constraints: Valles Marineris plateau channel networks . . . 64
3.3 Geologic constraints: Boundary conditions at Juventae Chasma . . . 72
3.4 Juventae mesoscale model: precipitation output . . . 77
3.4.1 Analysis of best-fit model . . . 77
3.4.2 Sensitivity to flooding depth . . . 84
3.5 Will snow melt? . . . 86
3.6 Channel and layered deposit formation . . . 89
3.6.1 Implications of constraints for channel-forming mechanisms . . . 92
3.6.2 Alternative interpretations and tests . . . 97
3.7 Echus plateau . . . 99
3.8 Implications for regional and global climate change . . . 101
3.9 Conclusions . . . 102
3.10 Methods . . . 103
3.10.1 Comparison between area of modeled precipitation and area of observed channels . . . 103
3.10.2 Snow melting model . . . 108
3.10.3 HiRISE stereo DTMs . . . 111

4 Snowmelt and sedimentary rock formation on Mars. 113
4.1 Introduction . . . 114
4.2 Snowmelt hypothesis and test . . . 116
4.3 Data . . . 117
4.4 Model . . . 121
4.4.1 Framework . . . 122
4.4.2 Thermal model . . . 123
4.4.3 Snow location prescription . . . 126
4.4.4 Integrating over all orbital states . . . 132
4.4.5 Comparison of model to data at global scale . . . 134

4.5 Results . . . 134
4.6 Discussion . . . 142
4.6.1 Assessment of snowmelt-limited sedimentary rock formation hypothesis against geochemical and textural data at key sites . . . 142
4.6.2 Other data sets: valleys and chlorides . . . 143
4.6.3 Extensions . . . 143
4.7 Predictions for the MSL Curiosity rover at Gale Crater . . . 144
4.8 Conclusions . . . 145

5 Geodynamics and volcanism on Super-Earths. 146
5.1 Introduction . . . 147
5.2 Model description and inputs . . . 149
5.2.1 Radius and mantle depth . . . 149
5.2.2 Thermal model . . . 150
5.2.3 Melting model . . . 153
5.3 Model output . . . 156
5.3.1 Simple scaling laws from thermal equilibrium calculations . . . 156
5.3.2 Plate tectonics . . . 156
5.3.3 Stagnant lid . . . 160
5.3.4 Initial bulk-chemistry and initial radiogenic-power variations . . . 163
5.4 Effect of melting on style of mantle convection . . . 167
5.4.1 Crust thicker than lithosphere . . . 167
5.4.2 Magma-pipe transport energetically trumps conduction . . . 168
5.4.3 Phase transitions within crust . . . 170
5.4.4 A continental throttle? . . . 171
5.4.5 Will trenches jam? . . . 172
5.5 Rate of volcanism and implications for degassing . . . 174
5.5.1 Degassing rate . . . 174
5.5.2 Overburden pressure . . . 179
5.5.3 Melt-residue density inversion: decoupling melting from mantle degassing? . . . 181
5.6 Discussion and conclusions . . . 181
5.6.1 Summary of results . . . 181
5.6.2 Overview of approximations and model limitations . . . 182
5.6.3 Comparison with Solar System data . . . 184

6 Climate instability on tidally locked exoplanets. 187
6.1 Introduction . . . 188
6.2 Idealized energy balance model . . . 190
6.3 Climate destabilization mechanism #1:
Enhanced substellar weathering instability (ESWI) . . . 194

6.3.1 Weathering parameterization 194
6.3.2 ESWI results 196
6.4 Climate destabilization mechanism #2: Substellar dissolution feedback (SDF) 203
6.5 Discussion 207
6.5.1 Solar system climate stability 207
6.5.2 Application to exoplanets 208
6.6 Context and conclusions 211

7 Synthesis and future observations. 214
7.1 Mars 214
7.1.1 Synthesis: Formation of sedimentary rocks by snowmelt-limited induration of atmospherically-transported sediment 214
7.1.2 Future observations and tests 217
7.2 Exoplanets 222
7.3 Climate stability science and technology 223

List of Figures

0.1 The Venus Tablet from the Royal Library at Nineveh. ii

1.1 Evolution of complexity over geological time. 2
1.2 Capsule history of Mars 7
1.3 Map of the Early Mars climate problem: context for the Mars chapters of this thesis 11
1.4 Channels incising both sides of a ridge just NW of Mojave Crater rim 12
1.5 Processes relevant to impact-induced precipitation 14
1.6 HiRISE stereo DTM of part of the Aeolis meanders 16
1.7 Effect of pressure on planetary surface temperature 20
1.8 Effect of solar luminosity on Mars climate stability 22

2.1 Dependence of lake-driven convection on lake temperature and atmospheric pressure 25
2.2 Time averaged response to the idealized lake 32
2.3 Spatially-averaged response to the idealized lake 34
2.4 N-S cross section through lake storm above idealized lake 35
2.5 Precipitation from `ref` simulation. 37
2.6 Fate of vapor released from the lake (precipitation efficiency) 38
2.7 Outcome of vertical resolution sensitivity test 39
2.8 Intensity of moist convection 41
2.9 Dependence of plume convective intensity on lake size 42
2.10 Exceedance probabilities for annual maximum sunlight at Mars' equator . . 48
2.11 Exceedance probabilities for annual peak temperature of snowpack at Mars' equator 50
2.12 Self-normalized cumulative distribution functions for the subset of sampled orbital conditions that produce melt 53
2.13 Contoured probability (%) of melting of rapidly-emplaced equatorial precipitation as a function of albedo and solar luminosity 54
2.14 Seasonal supraglacial lakes on Greenland ice sheet 55
2.15 Two candidate sites of localized precipitation 57

3.1 Location of plateau layered deposits near Valles Marineris, Mars, and location of snowbelts downwind of the Great Lakes, Earth 68
3.2 Topographic context of inverted channels 69
3.3 Sketch of proposed mechanism for plateau layered deposit formation 71
3.4 Site for our hypothesis test – Juventae 73
3.5 Disintegration of Antarctica's Larsen B ice shelf 74
3.6 Temperature and wind field at Juventae in our best-fit lake simulation 76
3.7 Ice and vapor columns at Juventae Chasma 79
3.8 E-W cross section through lake storm 80
3.9 Modeled precipitation contours overlain on observed geology at Juventae . . 81
3.10 Sensitivity test comparing mean precipitation (mm/hr) for 3 different lake levels 83
3.11 Fate of vapor released from the lake (precipitation efficiency) 85
3.12 Equatorial melting probability (in %) for flatlying snowpack 87
3.13 Geological context for measurements of layered deposit thickness, channel drainage density, catchment area, channel slope and channel width 90
3.14 Maximum drainage density at Juventae compared to snowmelt-carved systems in Greenland 91
3.15 Inverted channel systems on the Juventae plateau from which hydraulic parameters were measured 94
3.16 Grain sizes that can be mobilized by the modeled precipitation 96
3.17 Modeled precipitation contours overlain on observed geology at Echus 100
3.18 Comparison of falloff of precipitation with falloff of mapped area of channels and layered deposits 105
3.19 Comparison of azimuth of precipitation with azimuth of mapped channels . . 106

4.1 Latitudinal and elevation dependence of sedimentary rock abundance 119
4.2 Elevation dependence of sedimentary rock abundance 120
4.3 Seasonal cycle of diurnal–peak temperature and diurnal–mean free sublimation rate for 3.5 Gya insolation 128
4.4 Sensitivity of peak snowpack temperature to orbital forcing on an idealized Mars lacking topography 131
4.5 Modeled distribution of snowmelt, and Mars sedimentary rock data 139
4.6 Sensitivity of snowmelt maps to extreme variations in model parameters . . 141

5.1 Sketches of pressure-temperature paths for passively upwelling mantle, and resulting melt fraction 148
5.2 Effect of mass on mantle temperature for a planet in thermal equilibrium . . 152
5.3 Crustal thickness as a function of potential temperature for $M_{Earth} = 1$ . . . 155
5.4 Effect of increasing planet mass on thermal evolution 158
5.5 Evolution of mantle temperature and crustal thickness under plate tectonics 159
5.6 Effect of mode of mantle convection on thermal evolution 162

5.8 Effect of different radiogenic-element complements on thermal evolution . . . 163
5.7 Evolution of crustal thickness, Z_{crust} with time in stagnant lid mode 164
5.9 Abundance of the principal long-lived radionuclides in rocky planet mantles . 165
5.10 Effect of galactic cosmochemical evolution on mantle temperature 166
5.11 Possible limits to plate tectonics 168
5.12 Plate spreading rate (m/yr) as a function of time 170
5.13 Fractional area covered by continents, versus time 172
5.14 Buoyancy stresses as a function of thermal evolution and planet mass 174
5.15 Rate of volcanism per unit mass on massive Earth-like planets experiencing plate tectonics 176
5.16 Rate of volcanism on massive Earth-like planets undergoing stagnant lid convection 178
5.17 Crustal thickness as a function of planet mass and ocean mass for planets with plate tectonics 180
5.18 Effect of changes in activation energy on thermal evolution 185

6.1 Geometry of the idealized energy balance model for an exoplanet in 1:1 spin-orbit resonance 191
6.2 Surface temperature as a function of distance from the substellar point in our energy balance model 195
6.3 Bifurcation diagram to show the enhanced substellar weathering instability for radiative efficiency 197
6.4 Habitable zone (HZ) stability diagrams 200
6.5 Stability phase diagram, showing the effects of the enhanced substellar weathering instability as a function of L_* and Λ 202
6.6 Substellar dissolution feedback, for CO_2/seawater equilibria 205

7.1 Rapid erasure of Mars rover tracks shows high rate of present-day aeolian transport 216

List of Tables

2.1 Idealized simulations: list of runs with parameters 30
2.2 Idealized simulations: fate of released vapor 36

3.1 Valles Marineris simulations: list of runs with parameters 77
3.2 Valles Marineris simulations: evaporation rate and vapor fate 86
3.3 Model skill using method of Pielke and Mahrer (1978) 88
3.4 Measurements relevant to hydrology for 2 adjacent inverted channels 95
3.5 Parameters used in the localized-precipitation melting model 112

4.1 Snowmelt model: parameters, choices, and rationale. 133

5.1 Data for radioisotopes important to mantle convection 156
5.2 Parameters used in interior and thermal models 157

6.1 Solar system climates, showing vulnerability to ESWI and SDF. 207

Acknowledgments

My advisor, Michael Manga, maintained a research environment in which I was always the limiting factor on my own productivity. He made sure that I never lacked for feedback, suggestions, logistic and financial support, or freedom - often on very short notice. To the extent that I have achieved my potential as a grad student, it is in large part because of this support. Bill Dietrich took me under his wing early in my time at Berkeley, and has gently prodded and nudged me to think more thoroughly throughout my time here. Geoff Marcy was a beacon of encouragement. In case you didn't know at the time how valuable this was to me, Geoff - now you do! Eugene Chiang supplied friendly guidance at key moments. His lucid teaching (both at the chalkboard and in writing) is something I will try to emulate. Heather Knutson was not part of my thesis committee, but I learned a lot by working with her. In my career I will try to mimic her relentless rationality.

I am indebted to my collaborators for their tolerance, open-mindedness, and generosity with time and data:– Michael Manga, Eugene Chiang, Bill Dietrich, Heather Knutson, Alyssa Rhoden, Ameeta Patel, James Graham, Paul Kalas, and Leif Karlstrom at Berkeley; Isamu Matsuyama at Arizona; Richard Hindmarsh at the British Antarctic Survey; Itay Halevy at Caltech; Tim Creyts at Columbia; Joe Dufek at Georgia Tech; Sarah Stewart and Jerry Mitrovica at Harvard; Eric Gaidos at Hawaii; Vedran Lekic at Maryland; Taylor Perron at MIT; Susan Conway and Nicolas Mangold at Nantes; Melinda Kahre at NASA Ames; Horton Newsom at New Mexico; Stephanie Werner at Oslo; Scot Rafkin and Timothy Michaels at Southwest Research Institute; Cynthia Phillips and Ross Beyer at SETI; Robin Fergason at USGS Flagstaff; and Maarten Kleinhans at Utrecht. (Ved, I still owe you a paper!) Funding for the first two years of this work was provided by a Berkeley Fellowship, and a NASA Mars Fundamental Research Program grant to M. Manga funded the remainder.

I thank my fellow students for supplying all kinds of diversions; mindful, mindless, adventurous, and tasty. In particular - Alyssa Rhoden, David Shimabukuro, Amanda Thomas, Vedran Lekic, Leif Karlstrom, Ian Rose, Sanne Cottaar, David Mangiante, Percy Link, Jim Watkins, and Pam Kaercher. I thank Micaelee Ellswythe and Dawn Geddes for their tireless assistance.

I am grateful to Niels Hovius, Liz Harper and Nick Butterfield of the University of Cambridge, and Dan Rothman of MIT, for advice and encouragement that shaped my academic choices. Finally, I thank my family for love and support.

Chapter 1

Introduction.

1.1 Motivation and Context

Consciousness and technology are the product of a chain of unique evolutionary innovations. These innovations (steps) are about equally spaced in time (Vermeij, 2006). This is expected if each step requires the preceding step, and each is individually very unlikely in the age of the Earth (Carter, 1983; Watson, 2008; Waltham, 2011) [E. Gaidos,"Seek a minor sun," unpublished manuscript]. Although simple cells cluster, complex multicellularity requires complex cells (Knoll, 2011). These did not flourish until recently (Knoll, 2011). Long wait times for biological innovations indicate that long-term climate stability is necessary for complex life.

It is hard to understand long term climate stability with only one example. Earth's apparent climate stability may be just good luck (Edmond and Huh, 2003). Even if there is a climate regulation mechanism (Walker et al., 1981), its ability to moderate climate may collapse for small shifts in ecological and tectonic boundary conditions. Snowball episodes suggest this (Kopp et al., 2005; Ward, 2009). It is possible that earth scientists will eventually accumulate evidence for climate-regulating mechanisms that are effective for the range of boundary conditions experienced by the Earth over its history (Zeebe and Caldeira, 2008). Even in that case, the Earth's planetary composition, early history, or both, could be fine-tuned to allow climate stability. We cannot be sure if climate stability is common without a second example of long term climate stability.

Mars is the best place to test the generality of climate-moderating processes. It is nearby, and attracts $\sim$1 spacecraft/year. Orbiter data show that fluvial erosion and aqueous chemical weathering was relatively frequent in the first third of Mars history, but much more rare thereafter (Solomon et al., 2005; Murchie et al., 2009b). Surface exploration has confirmed this, and has discovered ancient evaporitic deposits that were reworked by flowing aqueous fluids (McLennan et al., 2005; Grotzinger et al., 2006). The Early Mars climate problem is to explain these observations given the faint light from the young Sun at Mars orbital

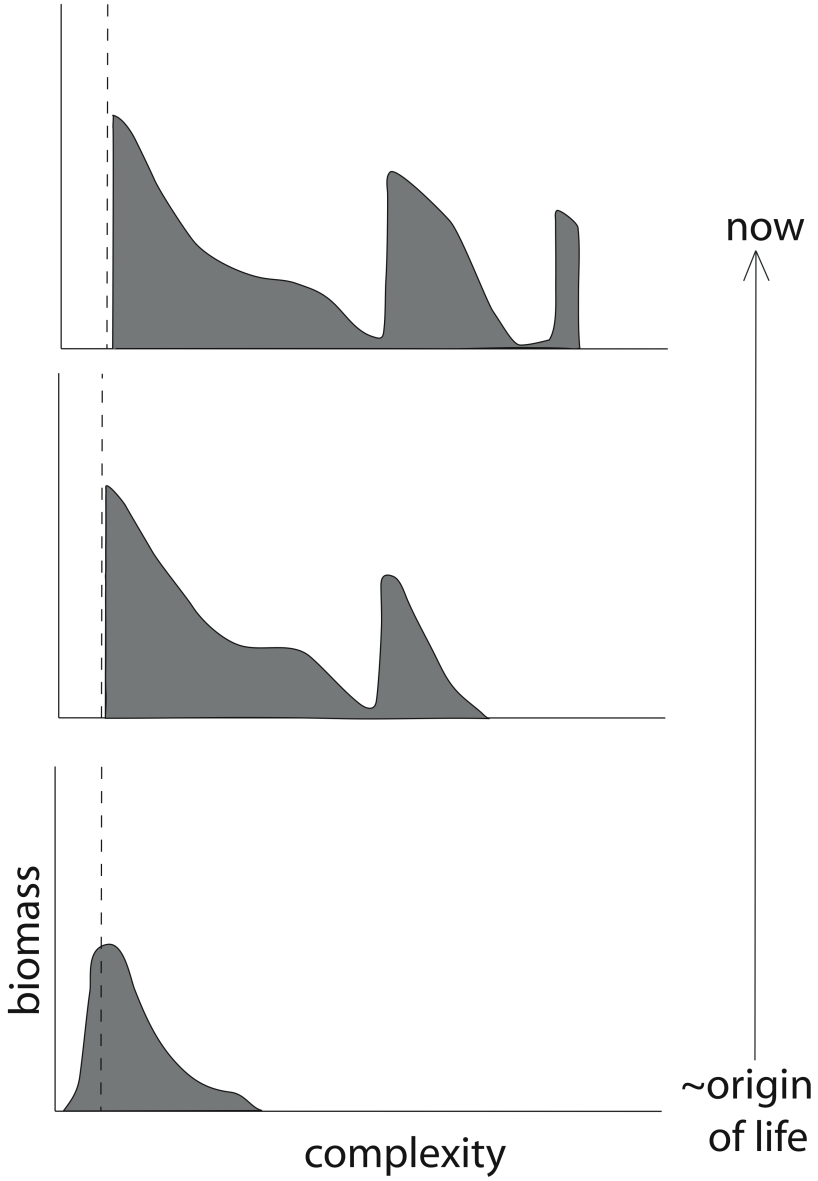

Figure 1.1 Evolution of complexity over geological time. Early evolution consists of relaxation away from a left wall of minimal complexity (Carroll, 2001). Crossing of some thresholds (the human brain; Photosystem II; origin of life) permits explosive biomass growth above that threshold. Threshold crossing leads to major restructuring of the environment, and the biomass of organisms below the threshold is reduced (Pleistocene megafaunal extinctions; Neoproterozoic benthic mats, grazed to destruction by early animals; oxygen toxicity; perhaps protolife). Complexity is hard to define consistently across the tree of life. For example, evolution of mammals from basal eukaryotes involved a gain of regulatory complexity, but a reduced number of protein domains and reduced metabolic capability (Zmasek and Godzik, 2011). Many things are synonymous with biological complexity (Carroll, 2001): energy throughput, efficiency, degree of consciousness, or grace (in the sense of elegance and refinement).

distance (Haberle, 1998). A standard approach is to set up an early high-density greenhouse atmosphere. However, the high-density atmosphere hypothesis has serious weaknesses (Section 1.2). I test alternative, thin-atmosphere hypotheses in Chapters 2–4. Chapters 2–3 are about transient, localized precipitation. Chapter 4 describes a global model in which sedimentary rocks formed in globally cold conditions under a thin atmosphere.

Rocky extrasolar planets were confirmed to exist in 2011 (Batalha et al., 2011; Ferraz-Mello et al., 2011). In principle, rocky exoplanet data are complementary to solar system data in the study of long-term climate stability. Nearby exoplanets approximate a large random sample of planets, but they are spatially unresolved and their sedimentary climate archives are inaccessible (at least for the next few decades). On the other hand, solar system worlds can be studied in high resolution and – at least for worlds with a sedimentary record – studied in deep time. However, there are only a handful of Solar System worlds with surfaces and with atmospheres that significantly alter surface conditions (Venus, Earth, Mars, Titan and Triton). Alongside small-number statistics, another problem is the anthropic shadow of Earth's biosphere (Bostrom, 2010). For example, the solar system's planets have eccentricities that are unusually low, relative to the eccentricities of known exoplanets (Zakamska et al., 2011). Our observation that planets in our own stellar system have low eccentricities is plausibly the result of the existence of Earth's biosphere (if very high eccentricities are unfavorable for life). Exoplanets break these anthropic degeneracies and allow ensemble statistics (Howard et al., 2011).

Walker et al. (1981)'s weathering theory was extended to planets in general by Kasting et al. (1993), who defined the Circumstellar Habitable Zone (CHZ) as a range of stellar fluxes within which weathering feedbacks might moderate climate. Because potentially habitable planets are a high priority, the CHZ is used to scope and prioritize exoplanet detection and characterization missions (e.g. Postman, 2009). If Mars experienced long-term climate stability in the past, then it was probably moderated by an analog of Earth's carbonate-silicate feedback (Halevy et al., 2007).

Requirements for rocky planet climate regulation through a weathering feedback include (1)a supply of greenhouse gases and (2) a positive dependence of weathering rate on atmospheric greenhouse-gas concentration. In Chapters 5 and 6 I study where these minimum requirements break down, narrowing the CHZ. I introduce these chapters in §1.3.

The two parts of this thesis are linked by the goal of reducing the dimensionality of the problem of rocky planet evolution. The long-term dream is a diagram for planets similar to the Hertzsprung-Russell (HR) diagram for stars. When combined with an understanding of nuclear fusion reactions in stellar cores (Burbidge et al., 1957), the HR diagram unifies process and history on a single quantitative plot. Currently, the phase space density, evolution rules, and axes of a planetary equivalent to the HR diagram are all uncertain, though some attempts have been made (Sleep, 2000; Stevenson, 2003, 2004).

1.2 The Early Mars climate problem

In this sub–section I give a short history of Mars climate and state the Early Mars climate problem. I then map out components of the problem, showing the particular processes and rock types targeted by this thesis. Finally, I state my assumptions.

Mars is interesting because it has a climate system like Earth's, and the history of that climate from >4 Gya to the present is recorded by sediments, ice deposits and geomorphology (Forget et al., 2008; Bell, 2008). That history suggests that Mars' surface was (if only briefly) suitable for life early on (MEPAG, 2010). Mars has implications for humans as we move out from Earth: if we choose to establish life beyond Earth, Mars is the obvious place to start.

The purpose of the U.S. Mars Exploration Program is to investigate all these possibilities (MEPAG, 2010). Since 1997, the year of the first Mars rover, the program has achieved enormous success. The Mars Exploration Rovers alone have yielded 27 *Science* research papers and 11 *Nature* papers – and more are expected, because the Opportunity rover has just completed a three-year drive to reach ancient layered materials that contain phyllosilicates (Wray et al., 2009). A measure of this success is that a fifth Mars rover was recommended to NASA as the first priority planetary flagship for the 2013-2022 decade by consensus of the planetary community (National Research Council, 2011).

Mars has several advantages for the student of long term climate change. The evidence is bolted in place, with no evidence for plate tectonics, little faulting, and no evidence for significant (>10°) polar wander (Golombek and Phillips, 2009; Matsuyama and Manga, 2010). Diagenetic alteration of surface deposits has been minimal, so burial metamorphism seems to have been rare (Tosca and Knoll, 2009). Given the relatively small amount of ground truth knowledge from Mars, it is important to iterate between models, landing site selection, and assimilation of lander data. One specific purpose of this thesis was to develop ideas to support the selection of the landing site for the next (fourth) Mars rover, the Mars Science Laboratory's Curiosity (Kite et al., 2010; Kite, 2011; Kite et al., 2011).

Evidence for past climate on Mars divides into 3 epochs (Figure 1.2) (Bibring et al., 2006; Carr and Head, 2010; Fassett and Head, 2011):-

- >4.0 Gya[1] (Pre Noachian - Early/Mid Noachian):
  Deep crustal phyllosilicates, a magnetic field, shallow craters, and planetary-scale impacts.
  Mars differentiated into a core, a largely degassed mantle with multiple geochemical reservoirs, and a crust much faster than Earth (Taylor and McLennan, 2009). Hf-W data indicate that Mars formed so fast (core formation <3 Myr after CAIs) that it is probably a surviving planetesimal, the product of oligarchic growth (Dauphas

[1]There is some overlap between mineralogical epochs that are described here as being separate. Mars absolute dates are based on crater chronologies. These dates are imprecise, because the source craters for the precisely-dated Mars meteorites are not known. Relative dates are also uncertain because erosion variably destroys craters, resetting surface ages.

and Pourmand, 2011). In spite of convective mixing, the mantle retained isotopically distinct magmatic source regions until at least 0.2 Gyr ago, perhaps because dense cumulates from a magma ocean phase formed a persistent dense layer enveloping the core (Debaille et al., 2007; Wenzel et al., 2004). The first few hundred million years of crustal evolution are difficult to reconstruct from orbit (Nimmo and Tanaka, 2005). Radiogenic $^{129}Xe/^{136}Xe$ systematics show that almost all mantle degassing occurred during this period (Marty and Marti, 2002). Deep (presumably very old) crust exposed by faulting in the Nili Fossae is basaltic, with low– to medium-temperature aqueous alteration to clays, carbonate, zeolite, and serpentine (Ehlmann et al., 2009, 2010, 2011). Crater central peaks show pre-impact low-temperature hydrothermal alteration but minimal evidence for amphibolite-grade metamorphism. This relatively low-temperature alterations requires that either early Mars had a lower heat flow than thought, hydrothermal convection reduced the geothermal gradient (Fraeman et al., 2009; Parmentier and Zuber, 2007), or the crater central peaks do not sample as deep in the crust as currently thought. Volcanism had certainly begun by 4.09 Gya, the age of the orthopyroxenite Mars meteorite ALH 84001 (Lapen et al., 2010). Early volcanism may have been predominantly explosive rather than effusive, based on the rarity of the high thermal-inertia bedrock that would be expected to be common in a lava-dominated crust [Joshua L. Bandfield et al., "Pervasive Explosive Volcanism on Early Mars: A Volcaniclastic Planet?" unpublished manuscript]. Mars' early geodynamo apparently shut down around this time, before the Hellas impact (Lillis et al., 2008). Most phyllosilicates date from this time, and probably most shallow, rimless craters also (Bibring et al., 2006; Irwin et al., 2005a; Howard et al., 2005; Forsberg-Taylor et al., 2004; Boyce and Garbeil, 2007). Phyllosilicates formed mainly in the subsurface (Ehlmann et al., 2011). The base of the altered volcaniclastic sequence draping the Columbia Hills (investigated by Spirit) may date from this epoch (Crumpler et al., 2011).

- 4.0 - 3.3 Gya (Late Noachian and Hesperian):
  Valley networks followed by sulfate-rich sediments.
  Regionally integrated, densely dissected valley networks mostly have crater retention ages around the time of the Late Heavy Bombardment (Fassett and Head, 2008a; Hoke and Hynek, 2009). Some have terminal chloride deposits (Osterloo et al., 2010). Sulfate-rich sedimentary rocks (Malin and Edgett, 2000; Malin et al., 2010) formed slightly after the regionally integrated valley networks (with some overlap) (Fassett and Head, 2011). Both the Opportunity mission and the Curiosity mission target sulfate-rich sedimentary rocks. Mineralogical evidence for hydrothermal activity declines (Fairén et al., 2010; Marzo et al., 2010). By the end of this period crater depth:diameter ratios are Moonlike (after correcting for Mars gravity) and fluvial reworking of crater rims is minor relative to the crater volume (Boyce and Garbeil, 2007), although occasionally spectacular (Williams et al., 2011).

- <3.3 Gya ("Terminal Hesperian and Amazonian"):
  Erosion rate falls to ∼1 atom/year (Golombek et al., 2006). Continued volcanism and tectonism, but very limited surface aqueous activity.
  Mars' color is mostly due to anhydrous nanophase ferric oxide, which indicates long dry intervals (Goetz et al., 2005). The Mars surface environment appears to have only marginally permitted snow or ice melting since the Noachian (Chapter 4). Nevertheless, there was some aqueous mineralization and channel formation after Mars' early active period had ended. For example, Spirit's mission ended because of entrapment in sands that had recently become encrusted with sulfates (Arvidson et al., 2010). These sulfates are <10 Mya based on crater statistics [Raymond E. Arvidson, via email]. Veneers, rinds and fracture fills along the Opportunity traverse suggest minor aqueous alteration <3 Gya (Knoll et al., 2008). From orbit, gully morphology suggests top-down seasonal melting of snow on steep slopes within the last 10^6 Myr (Christensen, 2003; Morgan et al., 2010). Repeated warm-season streaks on very steep slopes are consistent with present-day flow of liquid water or brine, although these observations are unconfirmed and the water source is unclear (McEwen et al., 2011). In addition to these apparently insolation-driven flows, volcanically-triggered outburst flooding occurs episodically, most recently at Athabasca Valles (∼ 2 Mya, Vaucher et al. (2009)). Finally, there is clear evidence for impact triggered channel formation (Harrison et al., 2010; Jones et al., 2011; Mangold, 2011) and alluvial fan formation triggered by the <4 Mya Mojave impact [Mojave age from unpublished crater counts by Stephanie C. Werner, via email].

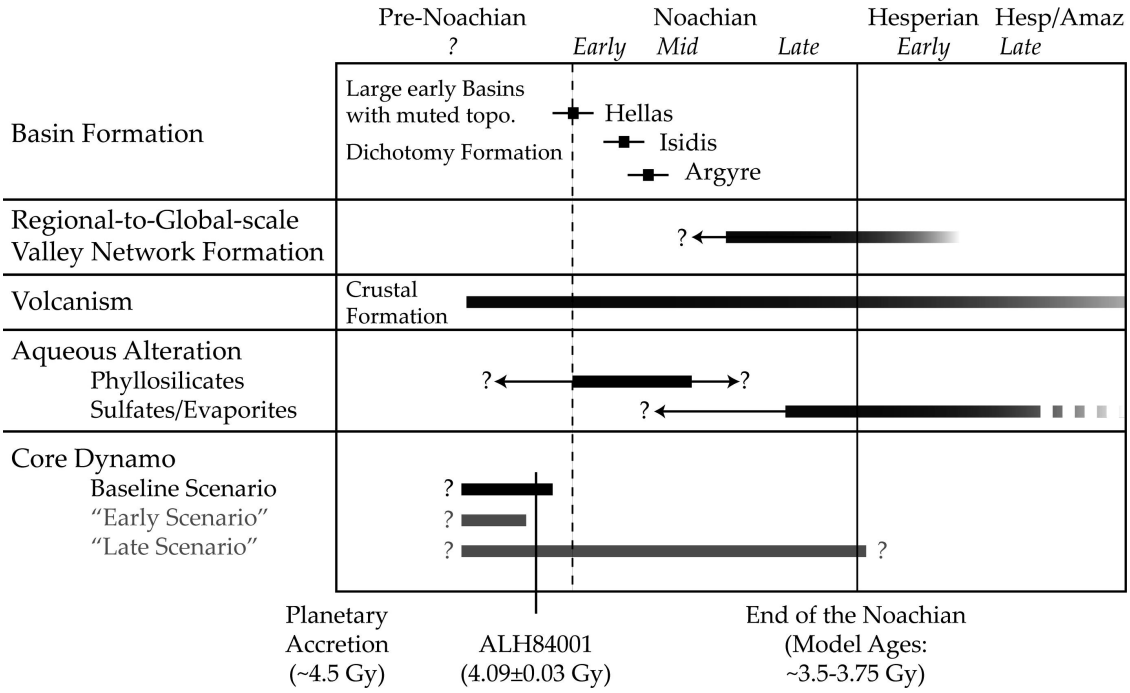

Figure 1.2 Capsule history of Mars. (After (Fassett and Head, 2011), Figure 2.)

This evidence leads to a problem:

The Early Mars climate problem:

1. What allowed widespread dendritic valley networks and sedimentary rocks on a planet in a distant orbit around a faint star?

2. What caused that environment to deteriorate?

Mars currently has a thin (6 mbar) CO_2 atmosphere and an annual average surface temperature of ∼210K. Annual average surface temperature 3.4 Gya, when the Sun was fainter (Bahcall et al., 2001), would have been ∼195K if everything else remained the same. Martian dendritic valley networks and fluvial cross-bedding required stable surface liquid water (Grotzinger et al., 2006; Metz et al., 2009b). Therefore, dendritic valley networks and sedimentary rocks on Mars >3.4 Gya are surprising. Did Mars ever had a feedback-stabilized climate like that of the Earth? If so, how long did it last, and why did it break down?

Past attempts to solve the Early Mars climate problem add 1-10 bars of CO_2 to the Early Mars atmosphere (Pollack et al., 1987; Forget and Pierrehumbert, 1997). The main strength of this approach is that regulation of CO_2 by weathering is thought to have stabilized Earth's

climate against changes in solar luminosity (Walker et al., 1981). Moderation of temperature by [CO_2]-temperature feedback is consistent with the sedimentary record of the last 2.5 x 10^9 yr on Earth (Grotzinger and Kasting, 1993; Grotzinger and James, 2000; Ridgwell and Zeebe, 2005; Kah and Riding, 2007), although the absence of glaciations prior to 2.9 x 10^9 Gyr may require non–[CO_2] greenhouse forcing (Goldblatt and Zahnle, 2011).

This multibar-atmosphere approach has weaknesses:- (1) CO_2 condensation sets an upper limit on CO_2 warming, which may be below the freezing point of water for Early Mars (Squyres and Kasting, 1994). (2) Warming by CO_2 clouds is limited by self-induced local atmospheric warming and associated cloud dispersal (Colaprete and Toon, 2003). (3) Polar collapse of thick CO_2 atmospheres is possible at low obliquity, and largely irreversible (Soto et al., 2011). (4) Cold CO_2 atmospheres are vulnerable to photochemical decomposition into lower-opacity components ($CO_2 \rightarrow CO + O$) (Zahnle et al., 2008). (5) CO_2 has a weaker greenhouse effect in the 100 mbar - 10 bar range than previously thought (Wordsworth et al. (2010), see also Halevy et al. (2009)). (6) During partial melting of Mars' reduced mantle, C tends to remain in the solid phase as graphite (Hirschmann and Withers, 2008; Stanley et al., 2011). Therefore, Mars basaltic eruptions are probably less CO_2 rich than Earth basaltic eruptions, and the total amount of degassed CO_2 may be too small for a greenhouse (Grott et al., 2011). (7) Upper limits on $^{40}Ar^*$ diffusion in ALH 84001 limit the cumulative duration of annual-average temperature ($\bar{T}$) excursions above $\approx$273K since 4.1 Gya to $<10^6$ yr (Shuster and Weiss, 2005). If atmospheric CO_2 maintained $\bar{T}$ >273K, it must have been removed very quickly to match this constraint.[2] (8) Oceans are needed to inject enough water vapor into atmosphere to supplement the CO_2 greenhouse and drive a hydrological cycle. Lakes are insufficient to drive a hydrological cycle (Soto et al., 2010; Wordsworth, 2010). Proposed evidence for a Mars ocean has historically not stood up to further scrutiny (Newcomb, 1907; Hunt, 1909; Lowell, 1910; Parker et al., 1993; Malin and Edgett, 1999; Williams et al., 2000; Carr and Head, 2003b; Matsuyama and Manga, 2010). Currently proposed evidence for a Mars ocean is very ambiguous. There is, however, strong evidence for large paleolakes on Mars. (9) Sinks for a past thick CO_2 atmosphere are lacking. Impact erosion during the Late Heavy Bombardment and an early, intense solar wind could have removed atmosphere more quickly (Brain and Jakosky, 1998). The rate of carbonate formation before the LHB could also have been rapid. However, much of the geological evidence for surface liquid water on Mars postdates the Late Heavy Bombardment. Analyzer of Space Plasma and Energetic Atoms-3 (ASPERA-3) on Mars Express estimated atmospheric erosion rates $\sim$1 mbar CO_2/Gyr (Barabash et al., 2007), far too low to account for significantly increased greenhouse forcing >3.4 Ga. A much more sophisticated inventory of the escaping atmosphere will be made by the Mars Atmosphere and Volatile Evolution Mission (MAVEN). Post-LHB surface sinks are insufficient to remove more than a few tens of mbar CO_2 [E.S. Kite & I. Halevy, "Martian climate under a brightening Sun," unpublished manuscript].

[2]However, Cassata et al. (2010) found less restrictive bounds on radiogenic ^{40}Ar diffusion.

The first and ninth arguments are probably the most important. These weaknesses validate searching for alternative solutions.

Melting-point suppression by high salinity is probably not a viable solution to the Early Mars climate problem, because sulfate brines freeze not far below the melting point of pure water. Chlorides can lower the eutectic point to 218K, which would allow water to persist on Mars' surface under the Faint Young Sun with little change in atmospheric composition. The surface of Don Juan Pond in the Antarctic Dry Valleys does not freeze in the Antarctic winter (<243K) because of hypersalinity. Some Martian valleys do run into chloride deposits, but the majority are either not associated with aqueous mineral deposits or are associated with sulfates. Sulfate brines freeze at ≥263K (Fairén, 2010). Magnesium sulfate salts are the most common sulfate salts on Mars (Murchie et al., 2009a). The $MgSO_4$-water eutectic is 4K below the freezing point of fresh water, not low enough to solve the Early Mars climate problem. Subaqueous ripple morphology does not constrain the salinity of runoff at the Meridiani site (Lamb et al., 2011), so salty Mars rivers have not been ruled out.

A better alternative to a long-lived multibar atmosphere is rainout from ephemeral steam greenhouses triggered by basin-forming impacts into icy crust (Segura et al., 2002, 2008; Toon et al., 2010). Because "one-pass" rainout from each impact is insufficient to account for the total erosion that is observed, the impact greenhouse hypothesis requires that a transient hydrological cycle was triggered by the largest impacts. This is much easier if the cold, pre-impact atmosphere had $>10^2$ mbar CO_2, which adds to radiative forcing from H_2O both directly and by pressure-broadening H_2O lines (Segura et al., 2008). The strongest arguments for the impact hypothesis are:– valley incision appears to have peaked at the same time as the impact flux (Toon et al., 2010); sufficient water is injected into the atmosphere by a large impact to allow for intense rainfall (Segura et al., 2008); and the minor and largely cation-conservative (although pervasive) weathering seen by Mars-orbiting infrared spectrometers is not commensurate with long-distance transport of weathering products away from their source, nor a long-lived global water cycle (Bandfield et al., 2011; Ehlmann et al., 2011). The main arguments in favor of a prolonged water cycle are that not all craters overflowed, as might be expected for a brief post-impact deluge (Barnhart et al., 2009), and the observation of fluvial landforms such as deltas and meandering rivers that on Earth require many decades to form (Malin and Edgett, 2003; Howard, 2009; Burr et al., 2009, 2010). The second argument is stronger. Mars' fluvial landscape does not follow terrestrial scaling laws and the valley bottoms are not graded, suggesting a poorly-integrated, immature fluvial landscape (Aharonson et al., 2002; Som et al., 2009). However this observation is consistent with a long interval of fluvial activity occasionally interrupted by impact-ejecta resetting of the landscape (Howard, 2007), and so does not require short lived impact-triggered flooding events.

Though contradictory, these arguments are individually compelling. Therefore, not all Early Mars landforms can be explained by the same climate. Mars Exploration Program data have resolved the evidence for surface liquid water on Early Mars into about 20 types (Figure 1.3). The existence of stepped deltas is strong evidence that some Martian valleys formed in

$O(10^1)$ years (Kraal et al., 2008b; Kleinhans et al., 2010), because in laboratory experiments this morphology requires rapid water release and the steps correspond to "bank erosion during [valley] widening and incision" (Kraal et al., 2008b). This is consistent with areal runoff driven by transient warming of the watershed surface, or with groundwater release. However, 10^3 km long meandering rivers in the Gale-Aeolis-Zephyria region show multiple periods of activity and inactivity and probably formed slowly [E.S. Kite, R.M.E. Williams, N. Finnegan, L. Karlstrom and M. Manga, "The longest meandering floodplain on Mars: The Aeolis meanders", imaging proposal for potential future Mars landing site]. There is also evidence for stratigraphic alternation of wet and dry conditions along the Opportunity traverse (Metz et al., 2009b). These examples both lie within the time interval of the sedimentary rocks. Quasi-periodic beds and bundles suggest that deposition of sediments that now form the sulfate-rich sedimentary rocks on Mars was orbitally controlled (Lewis et al., 2008), so plausible interpretation of these alternation is wet-dry cycles on orbital timescales. (For Mars, these are precession: 175 Kyr; obliquity: 120 Kyr and 1.3 Myr; eccentricity: 95 Kyr and 1.8-2.3 Myr (Toon et al., 1980). The frequencies vary with the orbital elements (Huybers and Aharonson, 2010). Mars' orbital elements vary chaotically over time (Touma and Wisdom, 1993; Laskar and Robutel, 1993) up to obliquity 65° and eccentricity 0.16 (median of a set of maximum values from an ensemble of Solar System integrations: Laskar (2008).)

There is no *a priori* requirement for paleoclimate constraints from geology to overlap, because Mars' climate may have changed over time. Geomorphological and geochemical classes of observations are spatially and stratigraphically separated, although there is some overlap in time (Figures 1.2-1.3). Determining and quantifying the processes that formed each type, in the context of internally consistent paleoclimate models, is a separate problem. Therefore the Early Mars climate problem can be tackled piece by piece. This thesis relates pre-modern, but still relatively young geomorphic features to local inputs of water and energy. The hope is to provide insight into more ancient features whose geologic context is less clear.

The hypothesis of the first half of this thesis is that the processes that are capable of forming surface liquid water in the present Mars climate – snowmelt (Clow, 1987; Squyres and Kasting, 1994; Gaidos and Marion, 2003), unusual orbital conditions, and transient localized supply of water vapor (Gulick and Baker, 1989) – are also the most important processes for forming surface liquid water in the past. I make minimal changes to the modern Mars climate. This approach is parsimonious, testable, and complementary to warm-wet early Mars models widely used since the 1980s (Pollack et al., 1987).

The motivating image for Chapters 2 and 3 of this thesis is shown in Figure 1.4.

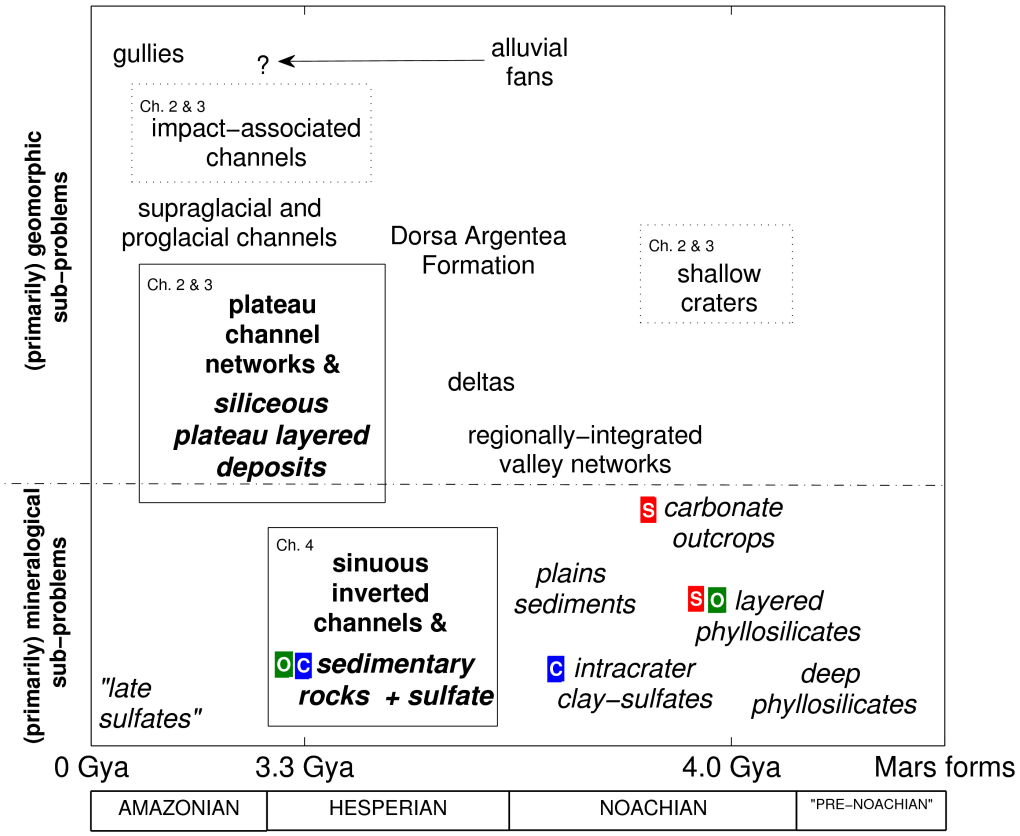

Figure 1.3 Map of the Early Mars climate problem: context for the Mars chapters (2-4) of this thesis. The Early Mars climate problem can be divided into distinct sub-problems. Italicized text corresponds to sub-problems defined by aqueous minerals, upright text corresponds to sub-problems defined by fluvial or fluvioglacial geomorphology. This ignores geomorphology (outflow channels) where inferred paleodischarge is too large to have been sourced from surface runoff. The sub-problems with solid boxes and bold lettering are addressed in this thesis. The work in Chapters 2 and 3 is also relevant to the sub-problems in dotted boxes. All other sub-problems are not directly addressed by this thesis. Colored letters correspond to completed and planned investigations by long range rovers Spirit (red "S"), Opportunity (green "O") and Curiosity (blue "C"). The mineralogy follows Murchie et al. (2009b) and Fassett and Head (2011).

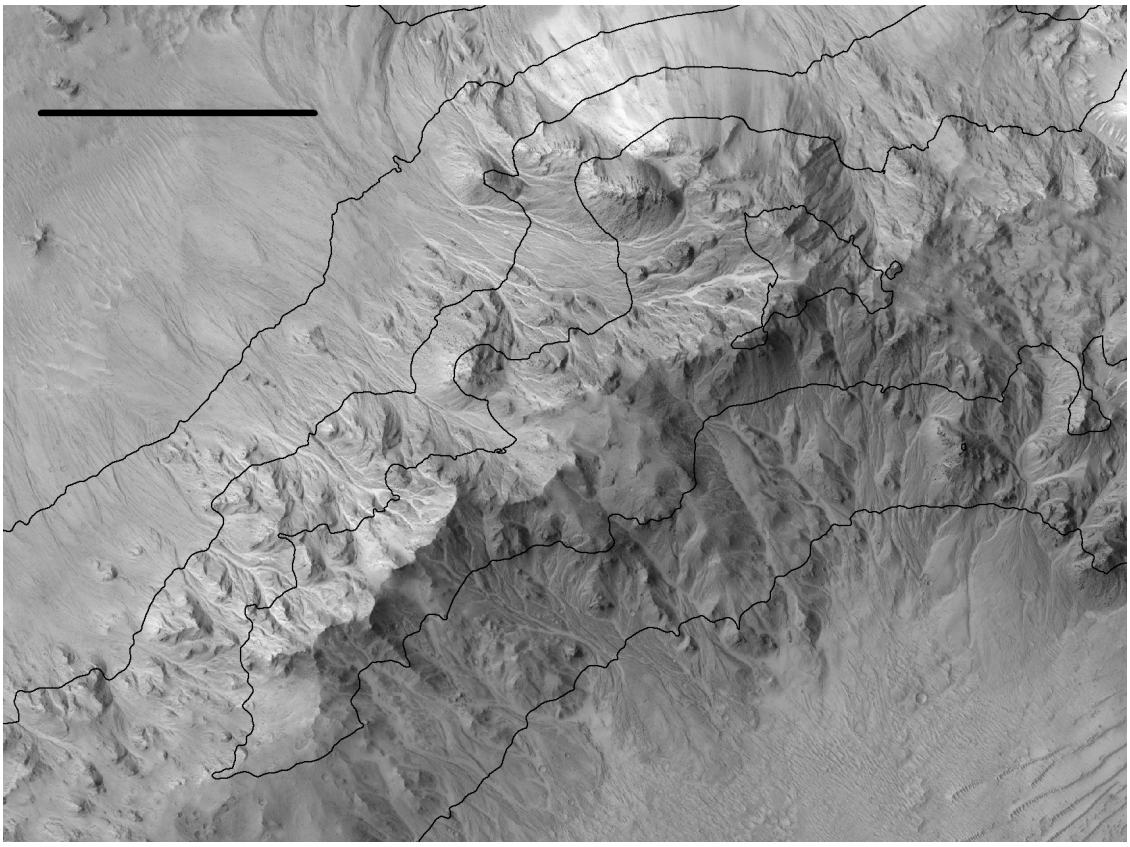

Figure 1.4 Channels incising both sides of a ridge just NW of Mojave Crater rim. Mojave Crater is 60 km diameter, 7.5°N, and has a crater retention age <4 Myr [date from unpublished crater counts by Stephanie C. Werner]. Scale bar is 500m. Channels on both sides incise within 20m of the ridge. HiRISE orthorectified image with 50m contour intervals from a HiRISE stereo DTM. HiRISE images PSP_001481_1875/PSP_002167_1880. N is up. *NASA/JPL/University of Arizona.*

Mojave Crater is ground zero for the study of localized precipitation on Mars. Channels and alluvial fans are found throughout Mojave's inner rim. Mojave–sized impact craters form every ∼40 Myr on Mars, so the young crater retention age of Mojave's proximal ejecta (2-3 Mya) strongly suggests that it is the youngest crater of its size class on Mars (Hartmann isochrons, 2004 iteration; crater retention age courtesy of Stephanie C. Werner, via email). Mojave's young age and the rarity of similar landforms elsewhere show that the Mojave impact caused the channels and alluvial fans. The presence of channels on both sides of a crater ridge that is beyond the rim argue strongly against post impact hydrothermal activity or overflow of ponded ejecta as water sources. Impact-induced precipitation and ejecta dewatering are viable hypotheses. Mojave is not alone: it is the youngest member of a

class of fresh craters whose inner rims are dissected by flows and alluvial fans. For example, degraded alluvial fans are also seen in a fresh crater in SE Isidis. Mojave, and craters like it, suggest that global climate change is not necessary to produce alluvial fans on Mars.

Impact-induced precipitation, which is thought to have produced the Mojave fans (Williams and Malin, 2008), has been proposed as an explanation for planetwide Noachian erosion. The main fluvial-geomorphic observations for the Noachian are regionally-integrated valley networks, fluvially dissected crater rims, and craters with shallow floors that may be the result of erosional infilling. Impact-induced precipitation has been proposed to explain the valley networks and dissected crater rims (Toon et al., 2010). Shallow-floored craters may be caused by ice inflow during the collapse of transient cavities in layered ice-and-rock targets (Senft and Stewart, 2008). The alluvial fans in the young Mojave Crater have a volume too small to affect the crater's overall depth:diameter ratio, which is deep unlike the shallow-floored Noachian craters. D/H ratios show that water has been lost from Mars over time (Greenwood et al., 2008), so early Mars would have more ice. In this view, the absence of young regionally-integrated valley networks on Mars could correspond to a reduction in the volatile content of the target, and not global cooling.

Globally-averaged 1D models show that impacts have enough energy to drive global Mars erosion (Segura et al., 2008). These globally averaged models are difficult to test: impact energy for a 100km crater is 5 orders of magnitude larger than any human-controlled explosion. The coupling constants relating impact energy to vapor release are therefore uncertain (Plesko et al., 2009). Mojave Crater is a relatively small-scale, well-preserved natural experiment in impact-triggered fluvial geomorphology.

Impact-induced precipitation and runoff is not well understood (Plesko et al., 2009). The feedbacks are complex (Figure 1.4). The most poorly understood is the surface vapor injection boundary condition – water vapor release from post-impact mixtures of hot rock and water (ice, liquid and vapor). This could involve diffuse degassing, fumaroles, geysers, intermittent phreatic explosions, or a lake. To start attacking the impact-induced precipitation problem, I take a subset of the problem – atmospheric response to a localized vapor release that does not involve heating of the rock. Localized vapor release must have occurred during outflow channel formation. The surface vapor injection boundary condition here is a liquid water surface with or without ice. This is better understood.

In Chapters 2 and 3 I test the role of localized precipitation in forming opaline layered deposits (Weitz et al., 2008) on plateaux downwind of outflow channel source regions in the Valles Marineris. These layered deposits are interesting because they contain hydrated silica and hydroxylated ferric sulfate, and the highest drainage densities preserved anywhere on Mars – but date from a time when aqueous mineralization had largely shut down elsewhere on Mars. This suggests unusual, localized conditions favored their formation, their preservation, or both. Based on the results from Chapters 2 and 3, I have begun to apply the model to impact induced precipitation more directly (Chapter 8).

The motivating image for Chapter 4 of this thesis is shown in Figure 1.6. This meandering river on Mars requires significant surface liquid water over an extended period of time. How

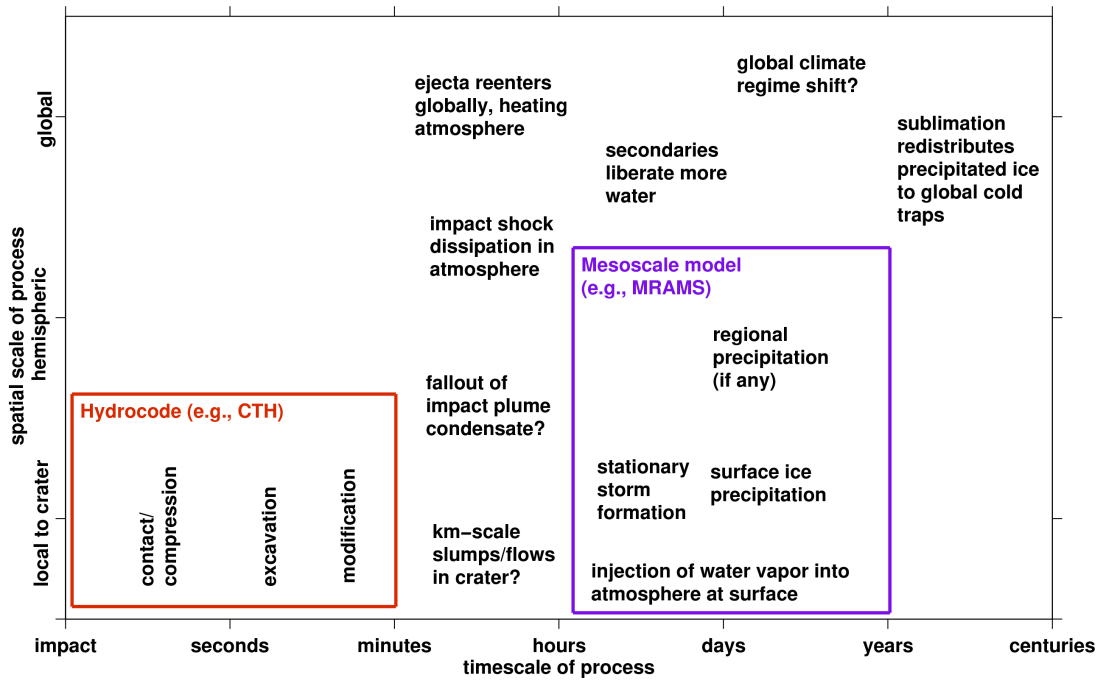

Figure 1.5 Processes relevant to impact-induced precipitation. The figure assumes a 100km-diameter crater forming in a cold climate regime. Chapters 2 and 3 focus on processes in the magenta box (mesoscale meteorological model). Work in progress uses impact shock hydrocode output to set the initial conditions for the mesoscale meteorological model.

does this constrain atmospheric pressure and greenhouse-gas composition at the time that this meandering river formed?

Existing functions for mapping between ancient Mars observations and quantitative paleoclimate may have been adequate for the limited data available from the Viking missions. However, we know enormously more about the surface geology of Mars than a decade ago. For example, Mars Reconnaissance Orbiter has returned more data than all other interplanetary missions combined. We now also have a sophisticated understanding of the relationship between atmospheric composition and greenhouse forcing (Pierrehumbert, 2010). Historically, modelers have used $\bar{T} > 273$K as their goal (Haberle, 1998). Given a model of past atmospheric composition, the transfer function is a radiative-convective model and the goal is to reach $\bar{T} > 273$K. Because it lumps all the data together, this is a weak foundation for reconstructing past climate and climate change - especially given that Early Mars climate change and deterioration is as interesting as the mean state. The most conservative climate scenario that satisfies a given geologic constraint on fluvial discharge will involve seasonal snowmelt. The goal of Chapter 4 is to build and trial a more realistic framework for mapping between Early Mars data and models: a snowmelt framework.

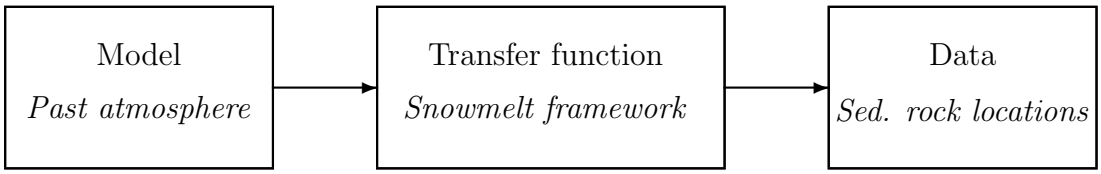

Applied to sedimentary rock location data, the snowmelt model favors a marginally melting system and a relatively thin ($O(10^2)$ mbar) CO_2 paleo-atmosphere (Chapter 4). The snowmelt transfer function is intended to be applied to other data in the future, including downward-mobilized soluble elements at Troy (Arvidson et al., 2010), young channels at Newton-Gorgonum (Howard and Moore, 2011), and perhaps the classic regionally-integrated valley networks.

I make several assumptions about the Early Mars climate problem in the first part of this thesis:

- *Many or most of the sedimentary rocks on Mars formed in the first third of Solar System history.* For the valley networks this is almost certain based on crater chronology calibrated to the absolutely-dated Lunar record and confirmed by measurement of present-day impact rates (Malin et al., 2006; Hoke and Hynek, 2009; Neukum et al., 2010). Sedimentary rock ages are less clear because they are eroded at unknown but relatively high rates by aeolian processes, which obliterate craters (Smith et al., 2008). Despite these uncertainties, it is known that the sulfate sedimentary rocks at both

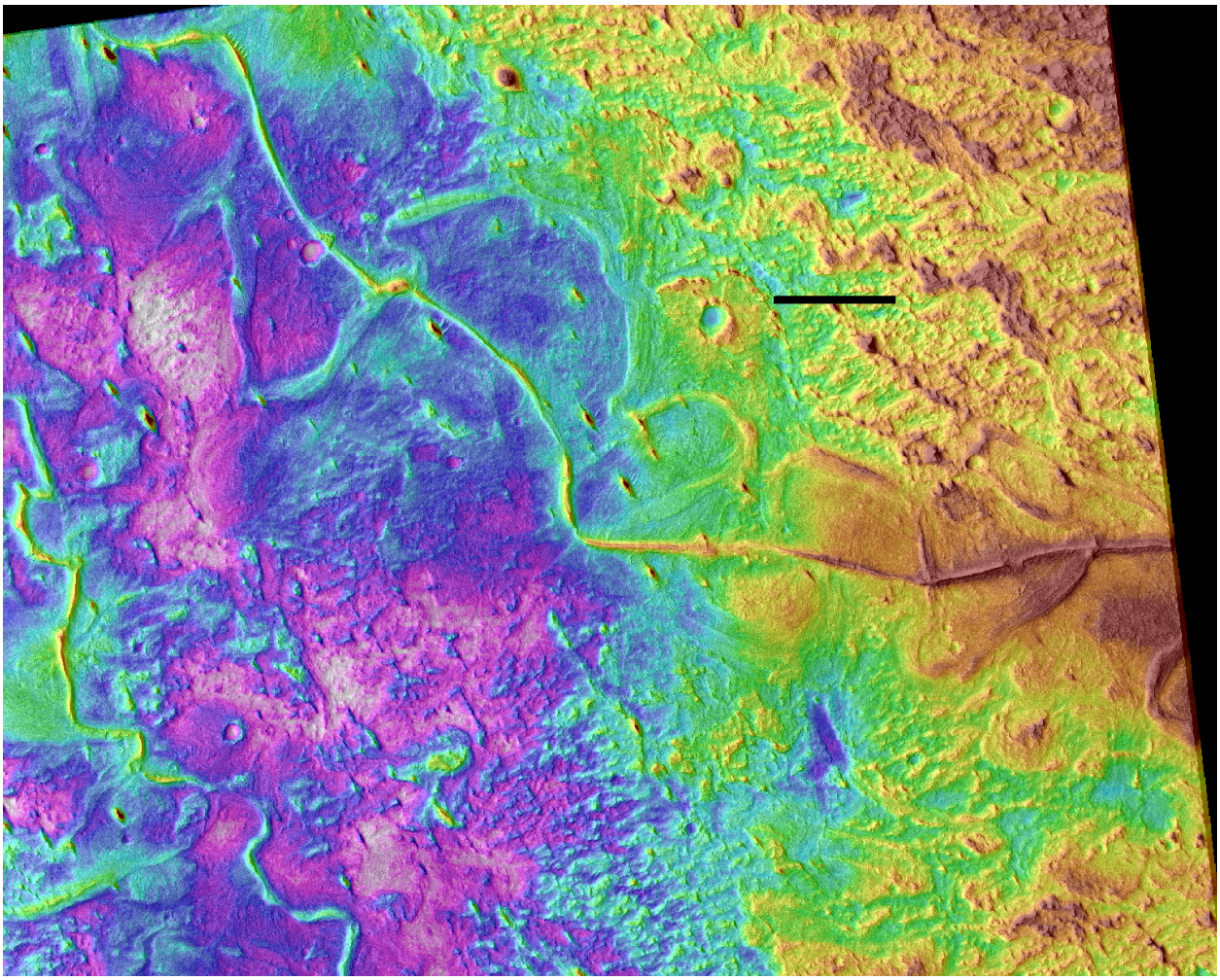

Figure 1.6 HiRISE stereo DTM of part of the Aeolis meanders. HiRISE images PSP_006683_1740/PSP_010322_1740. This is a small part of a >600 km long river network in the Gale-Aeolis-Zephyria region. N is up. Shaded relief with lighting from NW (channels are preserved as ridges). The main (central) channel deposit has a direction of flow from SE to NW based on present-day slope, regional sense of contributory confluences, and upstream truncation of point-bar deposits. Two channel generations are visible in this central deposit: a meandering lower deposit, and an upper deposit that follows the general trend of the lower deposit but is less sinuous, does not meander, and appears to be narrower. At least three chute cutoffs are visible in the lower channel, and there is a candidate crevasse splay deposit emanating from the upper channel at maximum resolution. My DTM gives a slope of 3 x 10^{-3} for the upper channel along this reach, and 1.4 x 10^{-3} for the more sinuous lower channel, following all chute cutoffs. (DTM slopes are not precise for these relatively short distances.) The black scale bar is 500m. Color scale extends from -2250m (red) to -2371m (white). Absolute precision is estimated at ∼20m from comparison with Mars Orbiter Laser Altimeter (MOLA) tracks. All my DTMs (currently there are 12) are available at `www.climatefutures.com/stereo`.

the Opportunity and Curiosity landing sites formed in the first third of solar system history (Carr and Head, 2010; Thomson et al., 2011).

- *Sedimentary rocks and fluvial channels on Mars were in fact formed by liquid water*, rather than lava, wind, granular flow, CO_2 or exotic fluids such as sulfuric acid (e.g., Cutts and Blasius (1981); Hoffman (2000); Leverington (2011)). Aqueous minerals strongly support this assumption on a global scale. However, the liquid water assumption has only been verified at the Opportunity landing site (McLennan and Grotzinger, 2008). It is not certain that liquid water is required for lithification of sedimentary rocks, but this is a reasonable assumption (Lewis et al., 2008). Some of the sedimentary rocks may be accumulations of tephra or ash (Hynek et al., 2003; Squyres et al., 2007). Compaction of evaporites can lead to lithification at low overburden pressures without liquid water (Warren, 2006), but on Earth liquid water is still required to form the evaporites. Mars Exploration Rover observations at both Spirit and Opportunity landing sites show loss of grain definition, indicating cementation (Herkenhoff et al., 2008b; Crumpler et al., 2011). The median unconfined compressive strength of Meridiani sulfate sandstone is 11 MPa, estimated from Microscopic Imager observations of Rock Abrasion Tool grind target porosity (Okubo, 2007), which is inconsistent with an unconsolidated or weakly–indurated accumulation of clasts.

- *Early Mars had a semimajor axis, obliquity pdf and eccentricity pdf similar to the values calculated by Laskar et al. (2004) and Laskar (2008)*, which does not include the reorganization of Solar System architecture around the time of the Late Heavy Bombardment ($\sim$3.8 Gya) proposed by the Nice model (Gomes et al., 2005). Prior to the Late Heavy Bombardment, if the Nice model is correct, Mars' obliquity pdf would have differed from the current chaotic pdf (Brasser and Walsh, 2011). A primordial high Mars eccentricity would favor snowmelt. This has been shown to be possible by Agnor and Lin (2011), but is considered improbable by other dynamicists [A. Morbidelli & R. Brasser, via email]. Even if the Nice model is correct and the reorganization of the giant planets changed Mars' orbit, most of Mars' exposed sedimentary rocks postdate the Late Heavy Bombardment (Carr and Head, 2010).

- *The standard model of the Faint Young Sun is correct.* Neutrinos and helioseismology confirm the stellar structure predicted by the standard solar model, so the standard stellar model seems to be broadly correct (Bahcall et al., 2001). However, the Sun's atmosphere is less metallic than expected from helioseismology (Serenelli, 2010). Adding an early period of mass loss to solar models reduces this discrepancy, and would make the young sun brighter (Guzik and Mussack, 2010; Turck-Chièze et al., 2011). The inferred rates of mass loss are 1-2 orders of magnitude greater than those inferred for nearby Sunlike stars, from astropause Ly-α emission (Minton and Malhotra, 2007), and lack of stellar wind continuum emission in X–band (Gaidos et al., 2000).

- *Greenhouse gases other than CO_2 and H_2O did not significantly warm Early Mars' surface for long enough to explain the "slow-formed" data.* Atmospheric models show that SO_2 is quickly removed from the atmosphere (Tian et al., 2010), undermining a proposed climate–weathering feedback involving SO_2's effect on surface temperature (Halevy et al., 2007). However, photochemical models for Early Mars include neither halogens nor heterogenous chemistry. Therefore, unmodeled exotic persistent greenhouse gases (Gerstell et al., 2001; Marinova et al., 2005) may have been produced by volcanic eruptions on Early Mars and could conceivably have warmed the surface for long periods. This is the weakest assumption, but CO_2/H_2O atmospheres are a simple and conservative starting point.

1.3 Exoplanet observations and models

Earth's atmosphere–ocean–biosphere reservoirs of noncondensible greenhouse gases, which maintain Earth's climate, are small compared to the quantity of CO_2 released into the atmosphere by volcanoes and consumed by weathering over geological time. Therefore, in the absence of a regulatory feedback, Earth's climate would soon be destabilized. Any habitable planet with tectonic activity and surface liquid water (like Earth) probably requires regulatory feedback for long-term climate stability.

It's easy to imagine habitable environments that are buffered against climate change over the age of the Galaxy – but biological activity in these environments would be sluggish and hard to detect. If the chemical reservoirs that maintain climate stability are much larger than the fluxes, then climate destabilization may take longer than the age of the Galaxy. For example, a planet could orbit far from (or unbound from) its parent star with a thick H_2 atmosphere (Pierrehumbert and Gaidos, 2011; Wordsworth, 2011; Abbot and Switzer, 2011). The surface temperature is controlled by radiogenic heat, and decays on Gyr timescales. Subsurface biospheres on Earth (Sleep and Zoback, 2007) and Europa are also buffered against changing insolation. However, all of these systems have extremely low rate of supply of redox disequilibrium (from photons, or hydrothermal reactions) (Soare et al., 2002). Therefore, the rate of biological activity is reduced, and probably hard to detect from interstellar distances. The biosphere of pre-photosynthetic Earth (Sleep and Bird, 2007) may also have been cryptic.

Given the likelihood that regulatory feedback is required for long term stability of observable climates, Chapters 5 and 6 test the sensitivity of the feedback thought to be responsible for Earth's climate stability (carbonate-silicate weathering feedback) to changes in planet parameters away from Earth. In addition, they predict how atmospheric degassing rate and atmospheric thickness changes. Chapter 5 tests sensitivity to planet mass, and Chapter 6 tests sensitivity to spin rate (synchronous versus asynchronous rotation).

Chapter 5 discusses the tectonics of Super-Earths. The Solar System lacks objects between 1 and 14.5 Earth masses, but these are found in large numbers around other stars

(Howard et al., 2010). They are easier to characterize atmospherically (higher S/N) than true Earths (Bean et al., 2010a). They could have rocky or fluid surfaces. It is not clear how common planets with rocky surfaces are. Some planets exist with densities suggestive of rock/metal mixtures, but Kepler's bevy of small-radius planet candidates has an uncertain mean density. The best-fit single density for the ensemble of small-radius planets requires at least some rock component, although this is an extrapolation from objects with radius > 2.0 R_{Earth} (Howard et al., 2011). Jitter measurements by Gaidos et al. (2011) using M2K data suggest a large population of rocky Earths. Smaller-radius planets are more likely to be rocky both because they are less likely to have reached the nucleation mass to accrete significant quantities of nebular gas (Ikoma et al., 2001), and any gas they have accreted is more easily lost by escape to space. At least some Super-Earths do have rocky surfaces (Batalha et al., 2011). Chapter 5 emphasizes super-Earths with rocky surfaces.

The question is how sensitive Earth's rate of volcanism (and Earth's habitability) is to Earth's mass. The rate of volcanism rations the supply of hydrogen to pre-photosynthetic hydrogen-limited ecologies (Sleep and Zoback, 2007). On habitable planets, volcanism offsets weathering losses (and escape to of the atmosphere to space). For a planet that sheds internal energy by conduction through the surface boundary layer at the same rate at which it produces internal energy through radiogenic decay, the rate of convective heat loss is regulated by the viscosity of the mantle (Tozer, 1969). Solid silicate viscosity is exponentially temperature dependent (Karato, 2008), so small changes in mantle temperature lead to large changes in convective heat supply. A bigger Earth must be internally hotter in equilibrium (because of small surface area to volume ratio), but only by order 10^2 K (a few percent). Early Earth is a local analog for Super-Earth tectonics, because of Early Earth's higher rate of radiogenic heat production. Ancient lavas formed at higher temperatures (Herzberg et al., 2010). This suggests that Earth-like plate tectonics and volcanism is possible on Super-Earths. However, there is a major complication: Earth's mantle temperature is only just above the solidus, and only in some regions. Magmatism – and associated volcanic degassing – only just occurs. Because Earth is near the solidus, a small increase in mantle temperature (as expected for super-Earths) could greatly increase the rate of volcanism, perhaps enough to shut down plate tectonics. Chapter 5 explores this possibility.

Chapter 6 discusses climate stability for planets where the principal climate-regulating gas (the "CO_2 equivalent") is also the main component of the atmosphere. For a cloud- and dust- free atmosphere, mean surface temperature always increases with increasing CO_2 pressure. However, the maximum surface temperature can either increase or decrease with increasing pressure. That is because the thickened atmosphere exchanges sensible heat with the surface. Increasing CO_2 buffers the maximum surface temperature by increasing the effective thermal inertia of the surface atmosphere system (reducing noontime temperatures), transporting heat away from the substellar point by advective cooling, or both. The maximum temperature rises when the pressure goes down (Richardson and Mischna, 2005) (Figure 1.6).

To regulate climate, a weathering process must be positively temperature dependent.

However, on a planet where the maximum surface temperature is bigger than the mean surface temperature (atmospheres that are not very thick), the weathering rate can increase as the planet average pressure and temperature goes down. The result is a rapid atmospheric collapse to a much lower pressure level, where weathering rate is limited by the pressure of the greenhouse gas or by the stability of a liquid solvent (e.g., water).

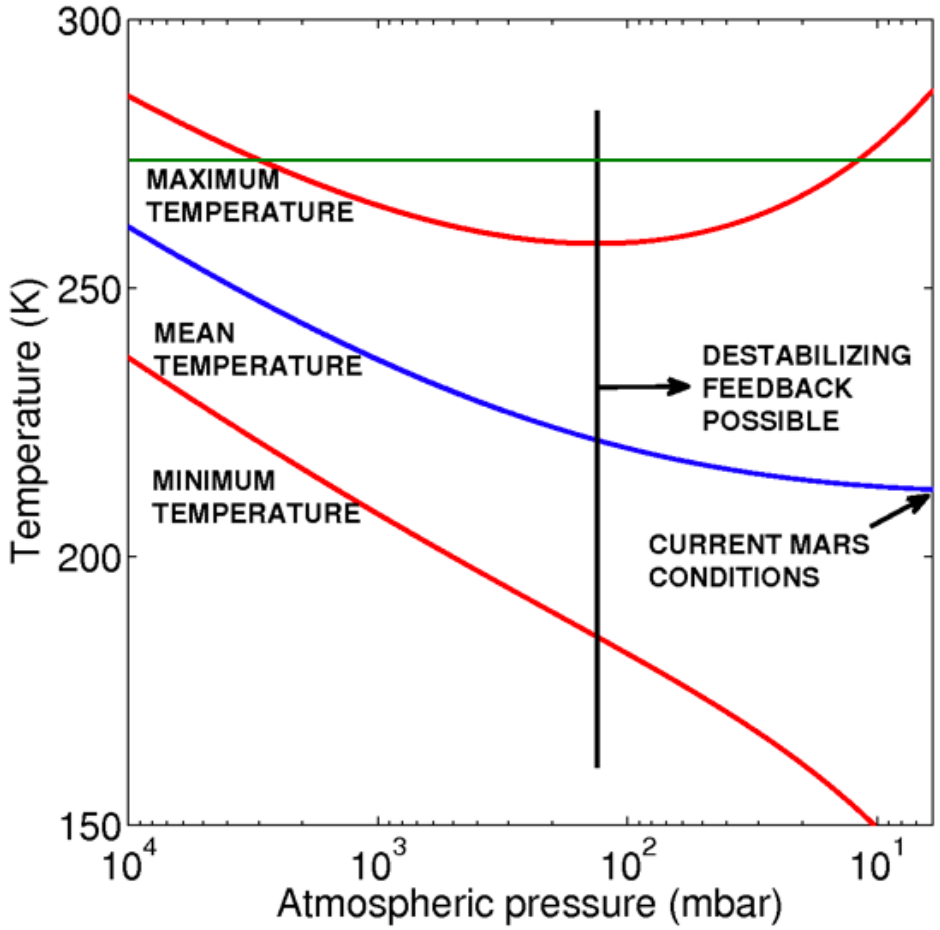

Figure 1.7 Effect of pressure on planetary temperature. Modified after Richardson & Mischna (2005), their Figure 13b. The green line corresponds to the triple point of water. At high pressures, a small decrease in CO_2 concentration lowers maximum temperature so transient liquid water potential, and with it carbonate formation rates, will decrease. This is a negative feedback similar to the carbonate-silicate feedback that is thought to restabilize Earth's climate after temperature excursions. However at the low pressures that are relevant to the past 3 Gyr of climate on Mars, a small decrease in CO_2 concentration will increase maximum temperatures a positive feedback.

Mars may have passed through such an atmospheric collapse (mediated by carbonate formation) in the past. Liquid water stability rectifies weathering rate. For example, microbial activity, which underpins almost all Earth weathering, is much quicker in a fridge than a freezer. As an example, Mars is currently near the triple point of water [E.S. Kite and I. Halevy, "Martian climate under a brightening Sun," unpublished manuscript] (Kahn, 1985; Richardson and Mischna, 2005). Carbonates are present at the percent level in the global soil. The total inventory is up to several tens of mbar. Suppose an initial state after the end of valley network formation, with no liquid water anywhere on the planet ($\sim$ 3.0 Gya). The combined effect of escape of carbon to space, and resupply of carbon by volcanism, is zero. Carbonate cannot form because there is no liquid water. As solar luminosity increases (upwards arrow on Figure 1.8) peak daily temperatures reach the liquid water stability range. Carbon dioxide is drawn down as carbonate, moving the climate system to the right. This reduces the damping effect of the atmosphere on the diurnal temperature range: although mean temperature declines with the decline in greenhouse effect, the diurnal peak temperature increases. The fraction of surface area over which liquid water is stable increases. This causes further CO_2 drawdown, initiating a runaway decline in atmospheric pressure. The speed limit on the runaway is the resupply of fresh minerals to the weathering zone, which will depend on the rates of tectonic uplift and on erosion.

Testing this idea requires accurate measurements of the present-day carbon escape flux from Mars (MAVEN mission), and a histogram of the ages of the carbonates in Mars' soil and dust (which should show a peak at around the atmospheric–collapse age). Until then, we cannot say if this process was important in the history of the real Mars.

This idea is also relevant to planet-averaged weathering rate for planets in 1:1 spin orbit resonance. Planets in the habitable zones around M-dwarfs will be tidally locked. For 1:1 spin-orbit resonance, temperature within the weathering zone (soil/regolith/saprolite) is constant with depth. Therefore, changes in temperature due to weathering-induced pressure changes (which are much slower than the time for propagation of a thermal pulse through the weathering zone) have the same sign with depth. This enormously simplifies the analysis for an Earth–like planet. Rocky planets around nearby M-dwarfs are high priority targets because they are easier to characterize than rocky planets around G-type stars. Chapter 6 discusses weathering-induced destabilization of habitable climates around tidally-locked planets.

The model in Chapter 6 predicts that if the conditions for the instability are met often, then the ensemble of rocky extrasolar planets will have a bimodal histogram of day-night surface temperature contrast. Atmospheric pressures will be either small (large day-night surface temperature contrast) or large (small day-night surface temperature contrast), with intermediate pressures excluded by the instability. The Spitzer Space Telescope has begun to measure day-night temperature contrasts for giant planets (Knutson et al., 2007), and JWST will be able to measure phase curves for close-in rocky extrasolar planets (Deming et al., 2009).

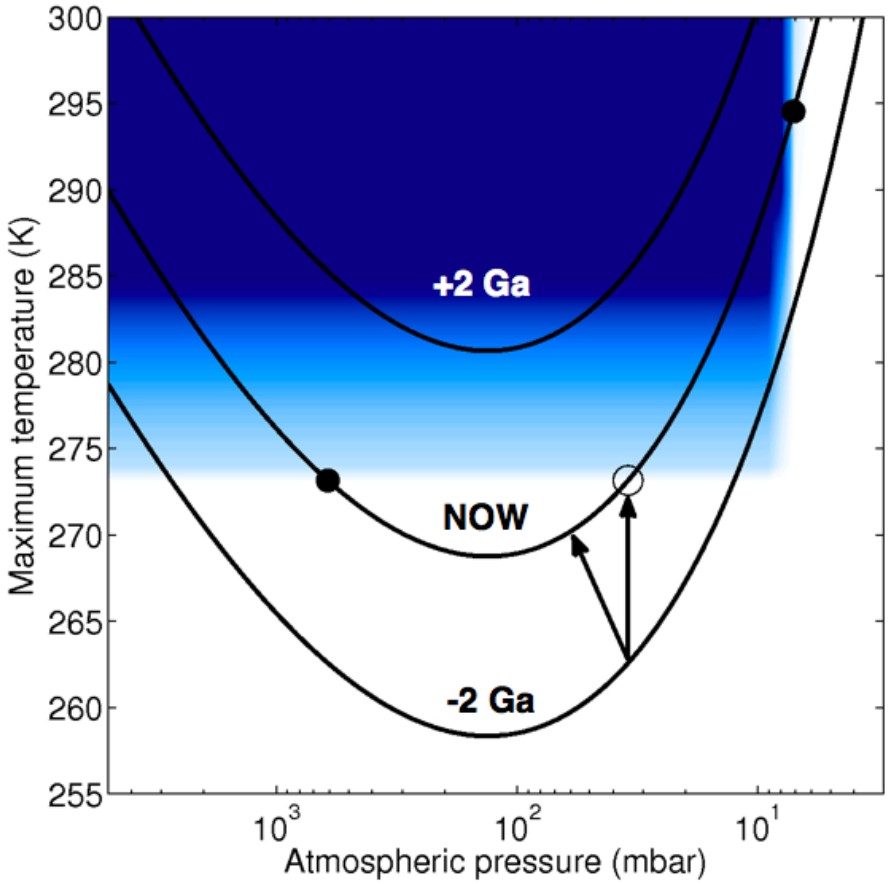

Figure 1.8 Effect of solar luminosity on Mars' maximum temperature. Concave-up curves correspond to the relationship between maximum temperature and pressure for solar luminosity 2 Gyr ago (bottom), now (middle), and 2 Gyr in the future (top). The blue shading corresponds to the extent of transient liquid water potential. For the present solar luminosity, two stable states exist (corresponding to the filled black circles). The high-pressure feedback-stabilized state corresponds to a temperature limit on liquid water formation (e.g. Halevy et al. (2007)), and the low-pressure feedback-stabilized state corresponds to a pressure limit on liquid water formation. The open black circle corresponds to the onset of transient liquid water (without evaporative cooling). Pressure-temperature combinations between the open black circle and the pressure-limited stable state cross the area of transient liquid water potential. Therefore, they are unstable to carbonate formation and will undergo a climate transition to the pressure-limited stable state. Pressure-temperature combinations between the open black circle and the temperature-limited stable state do not cross the area of transient liquid water potential - they are in the dead zone of (Richardson and Mischna, 2005). Therefore, they are neutrally stable. The stabilizing and destabilizing feedbacks in the Martian carbon-climate system evolve under increasing solar luminosity. Pressures that are originally neutrally stable in the dead zone are brought by increasing solar luminosity toward transient liquid water stability (vertical black arrow). However, increasing pressure (for example, through volcanic activity) can delay the climate transition (oblique black arrow). By 2 Gyr in the future (top curve), the "dead zone" no longer exists - transient liquid water occurs for all pressures. At this point, Marslike planets (those that do not degas enough volcanic CO_2 to balance carbonate formation) that until then have resided in the temperature-limited stable state will collapse to the pressure-limited stable state of (Kahn, 1985).

Chapter 2

Localized precipitation on Mars: idealized simulations.

This chapter was published as: Kite, E. S., T. I. Michaels, S. Rafkin, M. Manga, and W. E. Dietrich (2011), "Localized precipitation and runoff on Mars," Journal of Geophysical Research, 116, E07002, doi:10.1029/2010JE003783.

Summary

We use the Mars Regional Atmospheric Modeling System (MRAMS) to simulate lake storms on Mars, finding that intense localized precipitation will occur for lake size $\geq 10^3$ km^2. Mars has a low-density atmosphere, so deep convection can be triggered by small amounts of latent heat release. In our reference simulation, the buoyant plume lifts vapor above condensation level, forming a 20km-high optically-thick cloud. Ice grains grow to 200 μm radius and fall near (or in) the lake at mean rates up to 1.5 mm/hr water equivalent (maximum rates up to 6 mm/hr water equivalent). Because atmospheric temperatures outside the surface layer are always well below 273K, supersaturation and condensation begin at low altitudes above lakes on Mars. In contrast to Earth lake-effect storms, lake storms on Mars involve continuous precipitation, and their vertical velocities and plume heights exceed those of tropical thunderstorms on Earth. For lake sizes $10^{2.5}$ - $10^{3.5}$ km, plume vertical velocity scales linearly with lake area. Convection does not reach above the planetary boundary layer for lakes $\ll 10^3$ km^2 or for atmospheric pressure $> O(10^2)$ mbar. Instead, vapor is advected downwind with little cloud formation. Precipitation occurs as snow, and the daytime radiative forcing at the land surface due to plume vapor and storm clouds is too small to melt snow directly (< 10 W/m^2). However, if orbital conditions are favorable, then the snow may be seasonally unstable to melting and produce runoff to form channels. We calculate the probability of melting by running idealized thermal models for all possible orbital conditions and weighting their outcomes by probabilities given by long-term integrations of the chaotic diffusion of

solar system orbital elements (Laskar et al., 2004). With this approach, we determine that for an equatorial vapor source, sunlight 15% fainter than at present, and snowpack with albedo 0.28 (0.35), melting may occur with 4% (0.1%) probability. This rises to 56% (12%) if the ancient greenhouse effect was modestly (6K) greater than today.

2.1 Introduction

Evidence for runoff on Mars shows it to be patchy in both space and time (Kraal et al., 2008b; Williams, 2007; Weitz et al., 2008; Fassett and Head, 2008b; Hynek et al., 2010; Carr and Malin, 2000), so perhaps past precipitation was also patchy. Because patchy surface vapor sources cannot persist in equilibrium with a dry atmosphere (Richardson and Soto, 2008a,b), vapor would have to be supplied from an environment not in equilibrium with surface conditions. Such environments can be transient, such as an impact lake, or long-lived, such as the base of a wet-based ice-sheet. They can be high-temperature, such as fumaroles (or a lava flow advancing over snowpack), or involve only moderate temperatures, such as groundwater discharge. Liquid water has been present on the surface (though out-of-equilibrium) intermittently over a broad interval of Mars history. For example, groundwater discharges have occurred at least from the Late Noachian through Early Amazonian (Carr and Head, 2010). Impacts into icy targets have probably formed short-lived impact lakes throughout Martian history.

Here we use a mesoscale model to explore the atmospheric response to one example of a non-equilibrium vapor source: an ephemeral lake on a cold desert Mars. We track the fate of vapor supplied by the lake from release, through cloud formation, to precipitation, and consider whether the resulting snow will melt and provide runoff to form channels. Lake size, solar luminosity, lake geometry, and atmospheric pressure all affect the results. Only idealized results are presented in this chapter: Chapter 3 uses the same model for a case study of the Juventae plateau inverted channel networks (Weitz et al., 2008).

Low volumetric heat capacity makes the Mars atmosphere's response to lake vapor release similar to tropical moist convection on Earth, so we borrow ideas from tropical meteorology to understand our results (e.g. Emanuel (1994)). Figure 2.1 shows the low-pressure lake effect: condensation of a small amount of vapor in a thin atmosphere can produce strong convection, which in Earth's thick atmosphere would require condensation of a large amount of vapor and correspondingly high water surface temperatures.

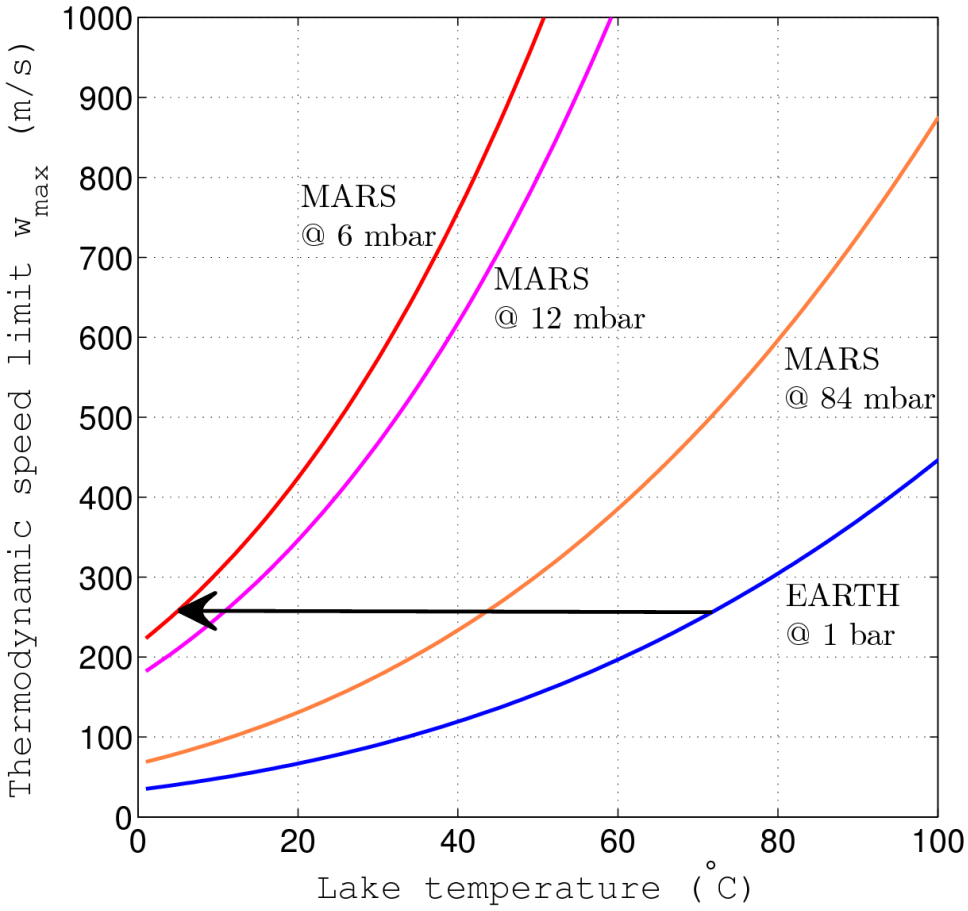

Figure 2.1 To show dependence of lake-driven convection on lake temperature and atmospheric pressure. Moist convection is enhanced on low-pressure Mars relative to 1-bar Earth because more buoyancy is produced for a given sea-surface temperature or lake-surface temperature. One measure of the strength of convection is the maximum vertical velocity of an updraft $w_{\max}$ ($= \sqrt{2CAPE}$, where CAPE is Convective Available Potential Energy), the so-called thermodynamic speed limit (Markowski and Richardson, 2010). Suppose the Level of Free Convection (LFC) to be at the surface and the Equilibrium Level (EL) at 1.5km for both planets. Suppose complete isobaric condensation and precipitation of a parcel at 50% humidity at the surface. In an otherwise dry atmosphere, and neglecting some second-order thermodynamic corrections, $w_{\max}$ is then as shown. The red curve is for today's Mars, the blue curve is for today's Earth, and the magenta curve is the pressure used in our Mars simulations. The black arrow shows that convection above a 5°C lake on Mars may be as vigorous as above a 72°C lake on Earth. The orange curve corresponds to the threshold pressure above which we suspect localized precipitation on Mars does not occur. Values used: $c_{\mathrm{p,Mars}}$ 770 J/kg; $c_{\mathrm{p,Earth}}$ 1003 J/kg; $R_{\mathrm{Earth}} = 287$ J K^{-1} mol $^{-1}$; $R_{\mathrm{Mars}} = 189$ J K^{-1} mol $^{-1}$; Mars gravity $g = 3.7$ m s^{-2}; $g_{\mathrm{Earth}} = 9.8$ m s^{-2}; latent heat of sublimation $L_{\mathrm{s}} \sim$ latent heat of evaporation $L_{\mathrm{e}} \sim 2.5$ x 10^6 J/kg; saturation vapor pressure curve from (Hardy, 1998).

Localized precipitation on a cold desert planet is normally transient precipitation. A warm, wet patch connected to the global atmosphere will lose water to cold traps elsewhere on the planet (Richardson and Soto, 2008a); the water table will withdraw to the subsurface because of evaporative losses (Richardson and Soto, 2008b). In the absence of an external heat source, evaporative and radiative cooling will cause any lake to quickly freeze (Lorenz et al., 2005; Conway et al., 2011)[1]. As the ice thickens, ice surface temperature will fall and the lower saturation vapor pressure will cause the rate of vapor release to greatly decrease. For realistic external heat sources, the lake lifetime is still short. For example, consider an impact-generated lake near the freezing point overlying shocked basalt that is initially at 1000 °C. The lake is assumed to be well-mixed by waves driven by lake-effect and impact-thermal storms, and convection driven by bottom heating. Icing-over is inevitable when the heat flow from the interior of the lake toward the surface is less than the evaporative and radiative losses at the surface. The maximum time before icing over, t, is therefore

$$t \approx \frac{D(T_\mathrm{b} - T)c_\mathrm{b}\rho_\mathrm{b}}{(EL_\mathrm{v} + \sigma T^4)} \tag{2.1}$$

where D is the depth of pervasive fracturing within the rock ejecta, $T_\mathrm{b} = 1273$K is the initial temperature of the basalt, $T = 278.15$K is lake surface temperature, $c_\mathrm{b} = 840$ J/kg/K the specific heat capacity of the basalt, $\rho_\mathrm{b} = 2000$ kg/m^3 the density of the fractured basalt, $L_\mathrm{v} \sim 2.5$ x 10^5 J/kg the latent heat of vaporization, and $\sigma = 5.67$ x 10^{-8} W/m^2/K^4 is the Stefan-Boltzmann constant. From the results in this paper (Table 2), we set the evaporation rate $E = 2$ kg/m^2/hr. We choose $T = 278.15$K because it is just above the temperature of maximum density of pure water at 277.14K. For $D = 100$m we obtain $\sim$4 Earth years: a geological instant. The true timescale will be less. For example, if fractures within the ejecta anneal, the relevant timescale is conductive cooling of a half-space (the ejecta layer) by an isothermal boundary condition (the well-mixed lake) until the heat flow into the bottom of the lake is less than heat loss at the top of the lake (Turcotte and Schubert, 2002):

$$t \approx \left(\frac{k(T_\mathrm{b} - T)}{EL_\mathrm{v} + \sigma T^4}\right)^2 \frac{1}{(\pi\kappa)} \tag{2.2}$$

In this case, the conductive heat flow can only balance evaporative plus radiative losses for $\sim$3 days for thermal diffusivity $\kappa = 10^{-6}$ m^2 s^{-1} and thermal conductivity $k = 2.5$ W/m/K: after this, an ice cover must form.

Therefore, we are interested in spatially restricted (10^0 - 10^3 km) water sources which cease to emit vapor in timescales < 1 year. This is the domain of mesoscale modeling. We use the Mars Regional Atmospheric Modeling System (MRAMS), also used for entry, descent and landing simulations for the Mars Exploration Rovers, Mars Phoenix, and Mars Science

[1]These arguments do not apply to springs, nor proglacial discharge of subglacial meltwater. In these cases, under cold conditions, any given parcel of water will freeze over, but a sustained vapor source can nevertheless exist at the discharge site.

Laboratory (Appendix A; Rafkin et al. (2001); Michaels and Rafkin (2008)). MRAMS explicitly resolves the size spectrum of dust and water ice aerosol for both cloud microphysics and radiative transfer, so it is well-suited for our cloud-forming numerical experiments (Michaels and Rafkin, 2008).

2.2 Localized precipitation on Mars: order-of-magnitude reasoning

Consider liquid water at the surface of Mars: the atmospheric temperature is similar to today. The surface is not entirely frozen because drainage or filling stirs the lake and mechanically disrupts the ice cover, convection mines heat from an underlying hot layer to balance evaporative cooling, subsurface discharge outpaces evaporation, or fumaroles and gas-charged fountains inject vapor and small droplets directly to the atmosphere. The injection rate is approximately (Emanuel, 1994)

$$Q_h \sim C_D |V_a| (r_s^* - r_b) \tag{2.3}$$

where $C_D \sim 10^{-3}$ is a surface exchange coefficient (Emanuel (1994), p.484), $V_a \sim 10$ ms^{-1} is anemometer-level wind speed, $r_s^* \sim 0.5$ is the near-surface vapor mixing ratio, and $r_b \simeq 0$ is the background water vapor mixing ratio. To convert this to the vapor mixing ratio in air that enters the buoyant plume we require a length scale (a vertical distance over which the vapor is mixed) and a timescale (during which the vapor is injected). A reasonable length scale is the thickness of the subcloud layer $\Delta Z_{\rm sc} \sim 2$ km. A reasonable time scale is the fetch timescale $t_{\rm f} = D_{\rm lake}/|V_a| \sim 2$ hours for a 65km lake (where $D_{\rm lake}$ is lake diameter). This gives a vapor mixing ratio in air that enters the buoyant plume, $r \sim 0.01 \equiv 6$ Pa.

Convection initiation is made more likely by Mars' low atmospheric temperatures. Air containing 6 Pa vapor will be supersaturated with respect to ice when $T < 227$K (Hardy, 1998). Mars today has an atmospheric surface layer 20K on average colder than its ground surface temperature (European Mars Climate Database v4.3, described by Lewis et al. (1999); Millour et al. (2008); henceforth European Mars Climate Database). For example, at $L_s = 255^\circ$ (near perihelion) the latitudinal maximum in zonally-averaged diurnal maximum surface temperature is 304K, but the zonal mean daily maximum atmospheric surface layer temperature at this latitude is only 265K. This offset is due to the low atmospheric column density, because (for fixed atmospheric compositional mixing ratios and assuming the atmosphere to be optically thin in the thermal IR) this reduces radiative and mechanical coupling between the atmosphere and surface (Pierrehumbert, 2010). In the current climate, diurnal mean equatorial atmospheric temperature is below 227K at all altitudes and all times of the year (European Mars Climate Database). Because of these low temperatures, supersaturation of the vapor (and nucleation and growth via deposition) occurs close to the ground. On Earth, the strongest lake storms are associated with rare cold-air outbreaks and large

air-lake temperature contrasts (Markowski and Richardson, 2010). For Mars (assuming the atmosphere is similar to the present Mars atmosphere), a large air-lake temperature contrast will occur for ephemeral lakes that form at any season and any latitude.

Mars' low atmospheric pressure promotes deep convection (Figure 2.1). Because of the low volumetric heat capacity, we assume that the plume will accelerate upward until 90% of the vapor has crystallized. Assuming that no precipitation occurs, with an empirical lapse rate of $\Gamma \sim 1.5$ K/km (from the European Mars Climate Database) and the Clapeyron slope for ice at 230K, this occurs 12 km above cloudbase.

During this ascent, the plume will have gained Convectively Available Potential Energy (CAPE):

$$CAPE \approx \rho_{\mathrm{a}} g \int_{\mathrm{CB}}^{\mathrm{MC}} \frac{T}{T'} - (1+\mu)\,\mathrm{d}z \tag{2.4}$$

where ρ_{a} is atmospheric density, $g = 3.7$ m/s^2 is Mars gravity, MC is the elevation of almost-complete condensation, CB is cloud base, T is temperature within the plume, T' the environmental temperature, and μ the ice mixing ratio (Rogers and Yau, 1989). This assumes that there is no precipitation of ice out of the parcel. Approximating the ice crystallization as linear from 0 at CB to complete at MC, we obtain $T - T' = rL_v/c_{\mathrm{CO2}} \sim 30$ K so $T/T' \sim 1.15$ upon complete crystallization (here, c_{CO2} is specific heat capacity for CO_2). $\mu \sim 0.01$ can then be set aside as negligible. Thus $CAPE$ gained during ascent ~ 3000 J/kg and peak vertical velocity $W_{\mathrm{max}} = \sqrt{2CAPE/\rho_{\mathrm{a}}} \sim 80$ m/s. We have ignored differential pressure gradient acceleration and compensating downward motions (Rogers and Yau, 1989) in obtaining this result. The plume will continue to ascend well above MC, but will decelerate as it entrains more ambient air and spreads to form an anvil cloud. The ascent timescale t_{ascend} is 12 km / $0.5W_{\mathrm{max}} = 300$s. Attention now shifts to the growing ice crystals.

We assume heterogenous nucleation of ice occurs on dust. Equatorial dust opacity τ_{d} is typically 0.01-0.05 during northern summer and 0.1-0.8 during southern summer in the thermal infrared (Liu et al., 2003). The present day typical low-latitude effective radius of dust is $\sim 1.6\mu$m (Wolff and Clancy, 2003). A uniform dust density in the lower 30 km implies a number density of 4 x 10^4 m^{-3} ice nuclei (considering geometric cross-section only and neglecting self-shadowing) for $\tau = 0.01$ (or 4 x 10^6 m^{-3} for $\tau = 1$). At 20 km elevation (3 g/m^3 air; 0.03 g/m^3 H_2O), this yields an 'seeder' crystal radius r of 58 μm (or 13 μm for $\tau = 1$) – a minimum, in that it assumes all ice nuclei are consumed. Since crystallization is implicit in the updraft-velocity calculation, we do not assign a separate timescale to nucleation and early growth.

How fast will crystals grow to precipitable size? Assuming that the 'seeder' crystals sink relative to the updraft and anvil cloud while scavenging both vapor and smaller droplets, the growth rate is just (Rogers and Yau, 1989)

$$\frac{\mathrm{d}R}{\mathrm{d}t} \approx \frac{\bar{E}M}{4\rho_{\mathrm{i}}}\Delta W \tag{2.5}$$

where $\bar{E} \approx 1$ is collection efficiency, $M \sim 0.03$ g/m^3 H_2O is cloud total water content at 20 km, $\rho_{\rm i} = 910$ kg/m^3 is ice density, and $\Delta W = 10$ ms^{-1} is a characteristic sink rate relative to the surrounding vapor-laden air. This gives a growth time $t_{\rm growth} \sim 2000$ s to precipitable size (assumed 200 μm). In Earth thunderstorms this also requires tens of minutes.

The crystals now begin to fall. At the low temperatures encountered at high altitudes on Mars, we expect the water to form hexagonal cylinders (Wallace and Hobbs, 2006). The drag coefficient C_D for cylinders is ∼1 over a wide range of Reynolds number Re, 10^2 - 10^5 (Tritton, 1988). Therefore we obtain a terminal velocity of (Tritton, 1988)

$$u_\infty = \sqrt{\frac{2g\rho_i \pi r}{0.5\rho_a}} \tag{2.6}$$

which with $r = 200$ μm gives 40 ms^{-1}. Using the dynamic viscosity of CO_2 at 233K, $\mu_{\rm a}$ = 1.2 x 10^{-7} Pa s, we obtain $Re = \rho_a u_\infty r/\mu_{\rm a} \sim 200$, sustaining the assumption of $10^2 < Re < 10^5$. Fall time from anvil cloud height is then $t_{\rm fall} = H_{\rm plume}/u_\infty \sim 500$ seconds.

The total lifetime of the vapor from release to precipitation as snow is $t = t_{\rm ascend} + t_{\rm grow} + t_{\rm fall} \sim 3000$ s. During the entire process of ascent through the plume, crystal growth, and snow fall, the parcel has been blown sideways by the regional winds. Taking 20 m/s as a representative shear velocity at cloud-forming altitudes of ∼ 20 km (European Mars Climate Database), we find that snowfall will be roughly ∼ 60 km downwind of source. This is small compared to the sizes of many Martian geographic features (craters, canyons, volcanoes). Therefore, provided latent heating powers a strong buoyant plume immediately downwind of the lake that lofts the released vapor to a height at which it will condense, we hypothesize that localized precipitation can occur on Mars.

In order to test this hypothesis, we carry out a set of numerical experiments.

2.3 Model setup

Our numerical experiments used four nested grids with 160 km resolution on the outermost (hemispheric) grid, increasing to 5.9 km on the innermost grid. Model vertical layer thicknesses varied from 2.3 km at altitude to 30 m near the ground. The lake is centered at 6.5S, 299E (the location of Juventae Chasma; paper 2).

For these simulations we prescribed flat land at 0m on all grids, with uniform albedo = 0.16, uniform thermal inertia = 290 kieffers (Mellon et al., 2000), and uniform roughness z = 0.03m (the value determined for the Mars Pathfinder landing site; Sullivan et al. (2000)). We introduced an isothermal lake with albedo = 0.05, and constant roughness z = 0.01m, which is close to the time-averaged roughness value obtained with the sea surface roughness parameterization of Eq. 7.21 of Pielke (2002). Lake surface temperature is pinned to 278.15K, with saturation vapor pressure according to Hardy (1998). Constant lake surface temperature is a reasonable approximation if either (1) the lake is deep and well-mixed (e.g. for the 4km-deep lake at Juventae Chasma, cooling rate ∼0.01 K day^{-1} for an evaporation

rate of 2 mm/hr if the lake is well-mixed), or (2) the lake surface is constantly refreshed by discharge of warm, perhaps gas-charged water from an aquifer (Harrison and Grimm, 2008; Bargery and Wilson, 2010). In either case, the lake temperature will change more slowly than the (strongly diurnal) atmospheric response. The focus of this first study is to identify the steady-state response of the atmosphere to the lake perturbation, so a time-dependent treatment of coupled lake thermodynamics is not appropriate. We use the NASA Ames MGCM (Haberle et al., 1993) to provide atmospheric boundary conditions. To prevent extremely high water substance mixing ratios and to allow metastable surface liquid water at +2 km above datum (the elevation of the Juventae plateau streams in Chapter 3), we double atmospheric pressure relative to today in our simulation by doubling initial and boundary pressures supplied by the GCM. Runs are at $L_s \approx 270°$ (southern summer solstice). Runs were for 7 days, except for the `ref` simulation which was extended to 12 days to test for precipitation variability. Many of these parameters were varied in sensitivity tests: see Table 1 for a list of runs and parameters varied. More details on the model setup are provided in the Appendix.

We carried out a dry run forced by these boundary conditions using flat topography but no lake. In the dry run, surface pressure is 1190-1270 Pa, 40% more than the saturation vapor pressure at 278.15K. Surface temperatures range from 209-281K. Surface winds are from the NNE, backing to the N during the passage of each afternoon's thermal tide. Wind direction rotates anticlockwise with increasing height until, near cloudtop elevation ($\sim$ 30 km in the reference run), wind direction stabilizes at E to ESE (the subtropical jet of Mars' single Hadley cell). There are no significant day-to-day variations in the wind field. The mean 0-6km shear is 22 m s^{-1}.

Table 2.1 Idealized simulations: list of runs with parameters

Run	Full Name	Lake Size (pixels)	Description	Deep Moist Convection?
DRY	lake_0.005_Mar_7_2010	-	Control case without lake	-
REF	lake_0.000_Jan_10_2010	11 × 11	Reference simulation (13 days)	yes
LINE	lake_0.001_Jan_10_2010	5 × 149	Line source in valley	no
S	lake_0.018_Mar_30_2010	1 × 1	Size sensitivity	no
M	lake_0.019_Mar_30_2010	3 × 3	Size sensitivity	no
L	lake_0.030_May_10_2010	7 × 7	Size sensitivity	yes
XXL	lake_0.020_Mar_30_2010	29 × 29	Size sensitivity	yes
ROUGH	lake_0.006_Mar_12_2010	11 × 11	*Garrett* [1992] lake surface roughness	yes
LO_SUN	lake_0.023_Apr_16_2010	11 × 11	0.75 × present solar luminosity	yes
HIRES	lake_0.004_Feb_10_2010	'11 × 11'	Horizontal resolution check	yes
WINTER	lake_0.000_May_1_2010	11 × 11	Seasonal sensitivity (L_s = 90°)	yes
MIDLAT	lake_0.000_Jun_25_2010	11 × 11	Latitude sensitivity (latitude ~45°)	yes
HIPRESS	lake_0.033_Jul_22_2010	11 × 11	60 mbar atmospheric pressure	no
dz_30m	afternoon_dz_test_30m_Jan_11_2010	11 × 11	Vertical resolution check	
dz_10m	afternoon_dz_test_10m_Jan_11_2010	11 × 11	Vertical resolution check	
dz_3m	afternoon_dz_test_3m_Jan_11_2010	11 × 11	Vertical resolution check	
dz_1m	afternoon_dz_test_1m_Jan_11_2010	11 × 11	Vertical resolution check	

2.4 Analysis of reference simulation

For our reference simulation, referred to here as `ref`, we introduce a square lake with sides $\approx$ 65km. This is similar to the diameter of Mojave Crater, a young crater with a fluvially-modified rim (McEwen et al., 2007; Williams and Malin, 2008)). We begin the analysis by describing the time-averaged response.

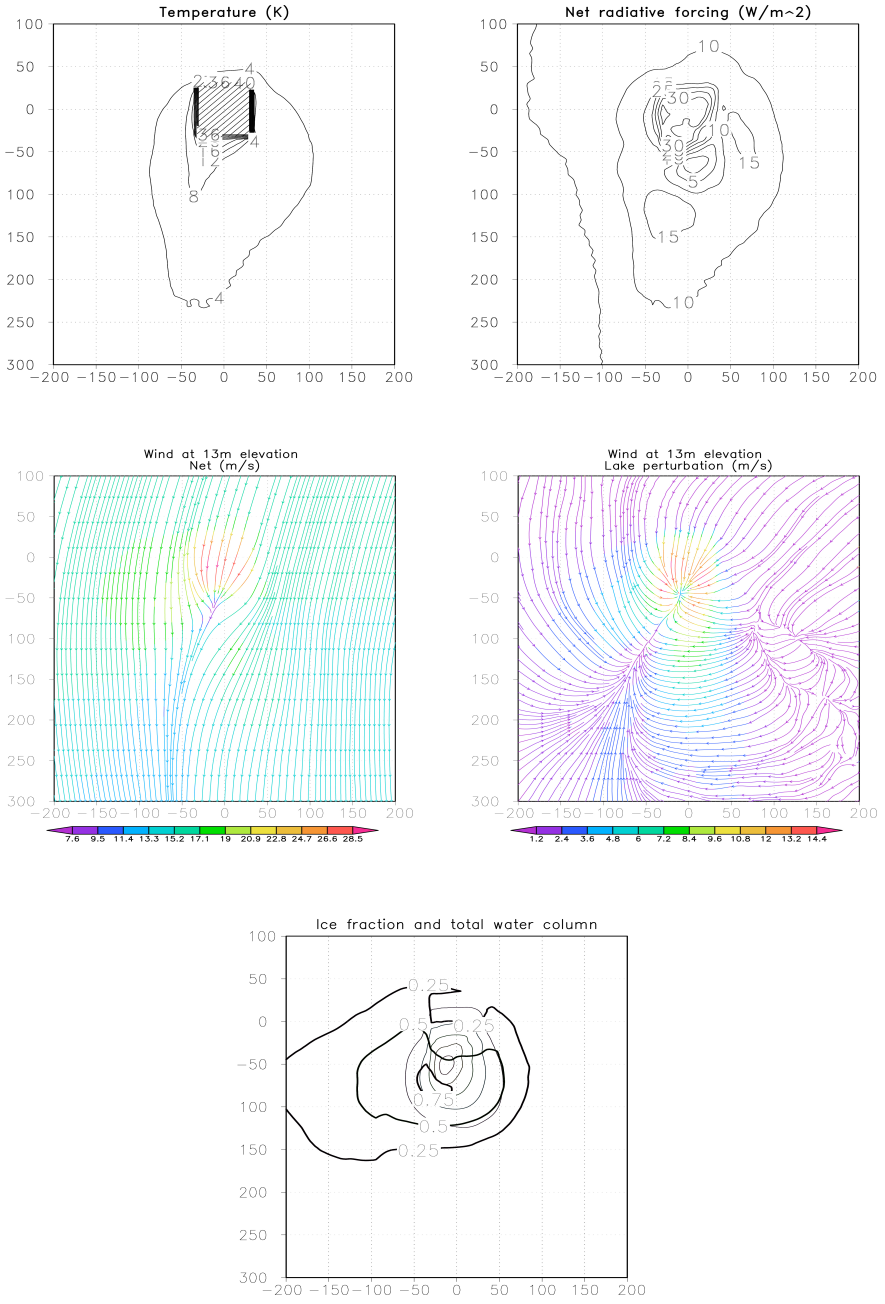

Figure 2.2 Time averaged response to the idealized lake. The area shown is a subset of the inmost grid, and distances are in km from lake center. The shaded area in the first panel shows the extent of the lake. Top left panel: Temperature perturbation due to lake; top right panel: radiative forcing at the surface; center left panel: overall surface-layer wind field with lake added; center right panel: perturbation to surface-layer wind field due to lake; bottom panel: total water column abundance (thin lines at spacing of 0.25 precipitable cm) and fractional ice abundance (thick lines).

2.4.1 Time-averaged response

Because the Mars daily average temperature is below freezing, the lake transfers sensible heat to the atmosphere on average. It also injects radiatively-active water vapor into the atmosphere, whose condensation at altitude releases latent heat and produces strongly-scattering water ice aerosols. Time-averaged surface temperatures up to 100 km downwind of the lake are raised by 8K as a result of these effects (Figure 2.2, top left panel).

This number is small because the time averaged longwave heating (vapor greenhouse and cloud reradiation) and shortwave cooling (ice scattering) due to the lake nearly cancel. Time-averaged longwave forcing peaks at +106 W/m^2 immediately downwind of the lake, which is where vapor column abundance is greatest. Time-averaged shortwave forcing peaks at -83 W/m^2 about 20km further SSE, which is where ice column abundance is greatest. Net radiative forcing is $\sim$ +30 W/m^2 over the lake, but typically between -3 and +15 W/m^2 in the area of greatest ice precipitation (Figure 2.2, top right panel). Because of the near-uniform northerly wind, we can understand the spatial structure of the net radiative forcing in terms of the timescales needed for vapor to ascend and precipitate out:- net forcing is positive just downwind of the lake, where vapor is still ascending to condensation level; it is modestly positive or slightly negative while vapor is being converted into scatterers; and it becomes positive again when those scatterers have had time (equivalently, distance South) to precipitate out.

A vertical slice through the atmosphere shows three components to the time-averaged atmospheric temperature response to the presence of the lake. Atmospheric temperatures in a thin boundary layer above the lake are warmed by 30K. The planetary boundary layer is thickened downwind of the lake because of the increased turbulence associated with the lake. The surface is warmer than the atmosphere, so that part of the atmosphere that is turbulently coupled to the surface (the planetary boundary layer) is warmer than the overlying atmosphere. As a result, temperatures are higher by 4K in that part of the atmosphere that is included in the boundary layer in the lake simulation, but which is not part of the planetary boundary layer in the dry run. Most importantly, a narrow plume of 5-10K increased temperatures extends 10-15 km above the lake. This thermal plume corresponds to the latent heat released by the lake-induced storm. Atmospheric temperatures never exceed 273K, so liquid water droplets are never stable. Supercooled water droplets are not included in our simulations, and could only form very close to the lake surface.

Strong low-level convergence results from the release of latent heat (Figure 2.2, center panels).

The total water column abundance (thin lines in Figure 2.2, bottom panel) shows the narrow extent of the weather system induced by the lake: its core is similar in horizontal extent to a terrestrial thunderstorm. The contours of (ice/total water) fraction (thick lines in Figure 2.2, bottom panel) are extended to the west of the lake because the ice-rich uppermost levels of the cloud are affected by the Easterly subtropical jet. Resublimation within this jet lowers the ice fraction with increasing distance to the west.

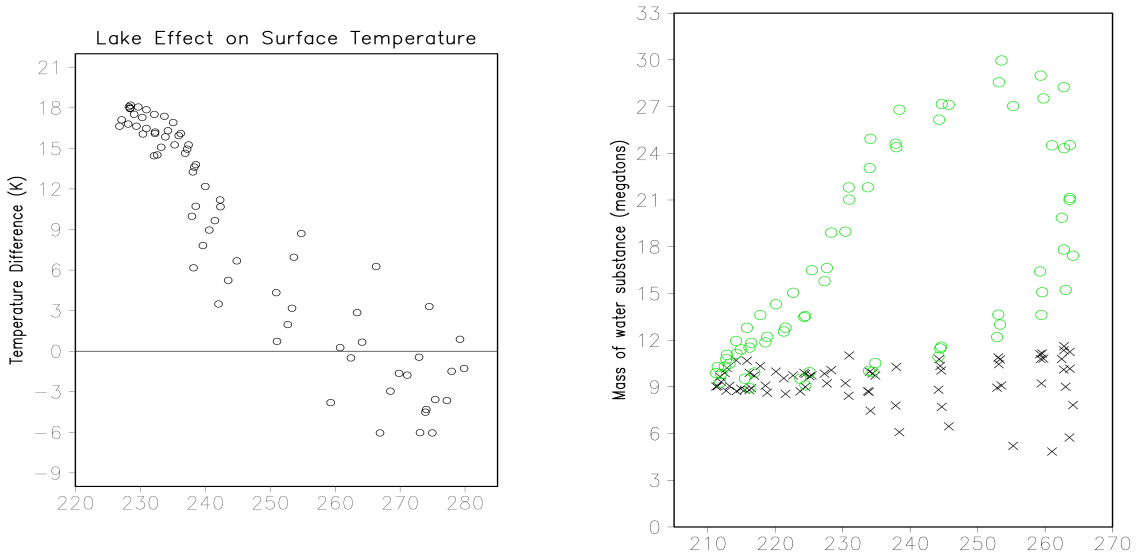

Figure 2.3 Spatially-averaged time dependencies are highly repeatable between sols. Left panel: Lake perturbation to surface temperature downwind of the lake, as a function of surface temperature in K. Right panel: Mass of water in atmosphere in 400km side square box centered on the cloud, as a function of near-surface air temperature in K. Green circles correspond to vapor mass, and black crosses correspond to ice mass.

2.4.2 Spatially-averaged time dependencies

The area of peak water-ice precipitation is immediately S of the lake. Within a square with sides ≈65km immediately S of the lake, the daily temperature cycle is regular, with little variability. Water vapor and cloud blanketing raises nighttime surface temperature by up to 18K relative to the dry run, but the net increase in daytime surface temperature due to the lake is small or negative because of ice-particle scattering (Figure 2.3, left panel). Despite ice-particle scattering, afternoon surface temperature exceeds 273K in the area of peak water-ice precipitation, so snow falling onto bare ground during the afternoon will melt. Snow falling onto ground that is cooled by the increased albedo of snow that has fallen during the night may or may not melt, depending on the grain size, thickness, and dust content of the nighttime snow layer (Clow, 1987).

To track water and ice mass budgets, we average over a square 400 km on a side which contains the lake but is centered 100km S of the lake in order to enclose the cloud. The time dependence of the water substance mass budget is dominated by a strong afternoon peak in atmospheric water vapor (∼2.5 x the predawn minimum of ∼9 Mton) at a time when atmospheric temperatures are highest (Figure 2.3, right panel). The mass of water ice in the atmosphere is independent of time-of-day and averages 10 Mton during sols 5-7. The

majority of the water vapor injected into the system precipitates as water ice during the night (see §2.4.4). Again, notice that atmospheric temperature does not exceed 273K, so liquid water aerosol is never stable.

2.4.3 Structure of the buoyant plume

Latent heat release drives plume ascent. Figure 2.4 is a predawn snapshot: water ice mass ratio in the plume core exceeds 1%. At 17.5 km elevation, more than 95% of water substance is in the condensed phase and vertical velocities reach 54 m s^{-1}. There is now little energy to be gained from further condensation, so the plume slows and broadens. Sublimation, entrainment, and especially precipitation, all lower the ratio of ice to vapor. The plume overshoots its equilibrium level, peaking near 35km.

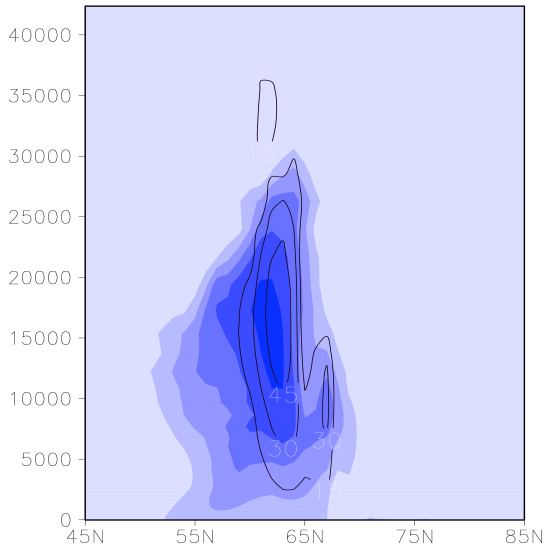

Figure 2.4 N-S cross section through lake storm above idealized lake. Blue tint corresponds to increasing water ice fraction (interval 0.002, maximum value 0.011). Labeled contours correspond to bulk vertical velocity in m s^{-1}. y-axis is vertical distance in m. x-axis is horizontal distance in simulation units: 10 simulation units = 59 km. Lake extends from 69N to 79N on this scale.

At a given altitude, plume updraft velocities are strongest just before dawn and weakest in early afternoon. This diurnal cycle in plume behavior corresponds to three related changes in the state of the atmosphere just upwind of the lake. Firstly, the Planetary Boundary Layer (PBL) pinches and swells during the diurnal cycle. The greater depth and intensity

of turbulent mixing during the day leads to more entrainment of moist air by the ambient atmosphere, where it does not contribute to the plume. Higher air temperatures disfavor crystallization at low altitudes during the day. Together, these two changes allow more vapor to escape during the day, by advection downwind within the thickened PBL, and not contribute to the plume. Finally, during the day, the excess of lake temperature over land temperature is small, and convergence is weak, so the shear velocity u_* is small. Therefore, relatively little vapor mixes from the lake surface boundary layer into the atmosphere. During the night, the greater land-lake temperature contrast is associated with stronger convergence. More vapor is mixed above the surface layer and entrained by the plume. Allowing for dynamic lake surface roughness ($z_0 \sim u_*^2$) increases the sensitivity of plume velocity to time-of-day, which confirms the effect of surface-layer dynamics on the diurnal cycle.

2.4.4 Precipitation

Precipitation is strongly peaked just downwind of the lake. Figure 2.5 shows that time-averaged snowfall is everywhere $< 0.006 \times$ its peak value at distances > 150 km from that spatial peak. Peak snowfall shows a similar, but more noisy, pattern, with peak precipitation > 4.5 mm/hr only in a small area beneath the buoyant plume. Precipitation rates increase by a factor of 4 during the night, with a rapid decline during the morning to a lower, stable afternoon rate.

Diurnally-averaged precipitation is steady in location over the 12 days of our extended `ref` simulation. The total precipitation rate increases slightly with time.

Table 2.2 Vapor fate (end of sol 6). Units are Mt (10^6 metric tons). Italicized ***dry*** run is subtracted from all other runs. See also Figure 2.6.

Run	Evaporation Rate (mm h^{-1})	Water in Atmosphere	Total Atmosphere (%)	Snow in Lake	Snow Beyond Lake	Total Snow (%)
DRY[b]	0	420	100	0	0	0
REF (sol 6)	2.5	334	26	234	741	74
REF (sol 12)	2.5	316	11	543	1942	89
LINE	3.7	1420	12	2701	7355	88
S	16.2	26	38	0.8	42.7	62
M	3.6	68	49	12	59.1	51
L	2.5	228	44	84	204	56
XXL	2.9	899	9	5030	4503	91
ROUGH	2.6	381	27	250	793	73
LO_SUN	2.8	176	12	484	820	88
HIPRESS	3.4	175	22	484	820	78

[a]End of sol 6. Units are Mt (10^6 metric tons). See also Figure 6.
[b]RUN is subtracted from all other runs.

2.4.5 Precipitation efficiency

Figure 2.6 and Table 2 show the fate of released vapor at the end of sol 6 in `ref`. The majority of the vapor precipitates <200 km from the lake. Of the vapor that reaches distances >200

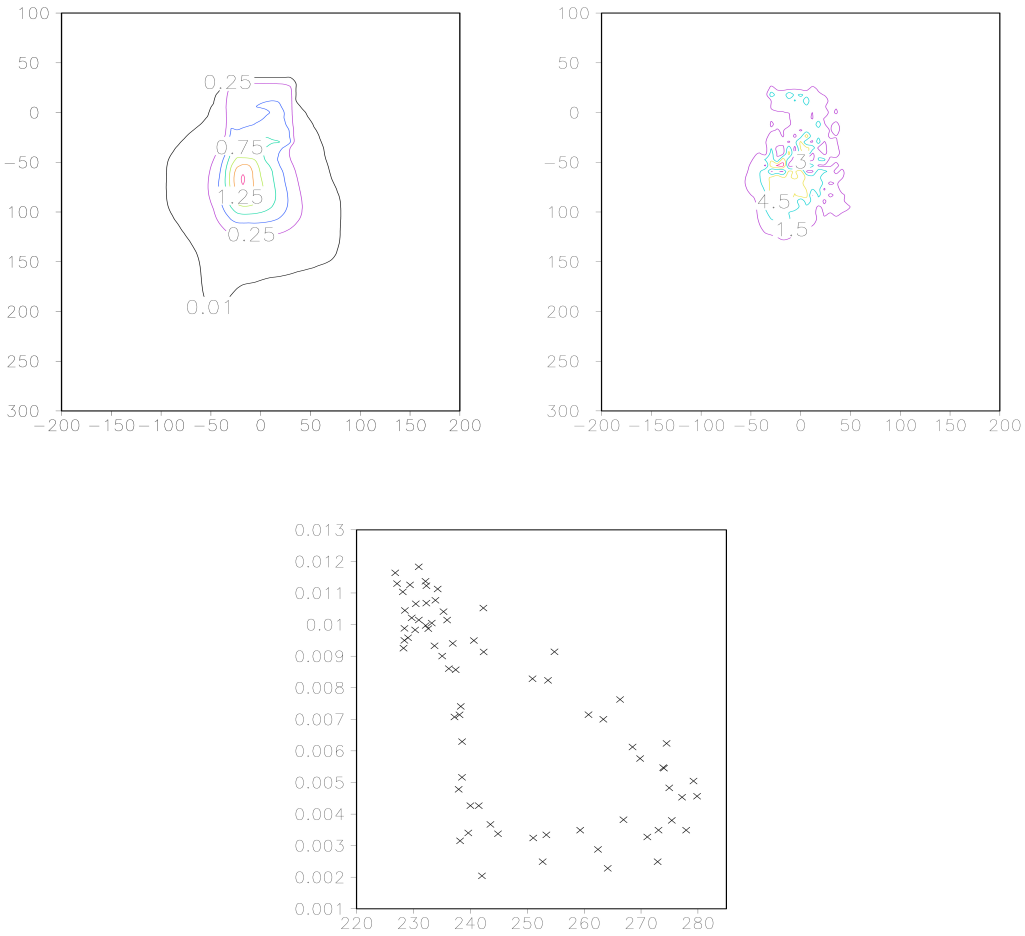

Figure 2.5 Precipitation from our `ref` simulation. Top left panel: Mean precipitation (mm/hr water equivalent) for reference simulation. Peak value is 1.5 mm/hr. Top right panel: Maximum precipitation (mm/hr water equivalent) for reference simulation. Peak value is 6 mm/hr. Bottom panel: Diurnal cycle in spatially-averaged precipitation (mm/hr) as a function of average surface temperature (K): snow falls at a high rate during the night but is reduced following sunrise (diagonal branch), leveling out at values $\sim \frac{1}{3}$ of the nighttime peak during the late afternoon (horizontal branch). Sunset permits a rapid return to high rates of snowfall (vertical branch).

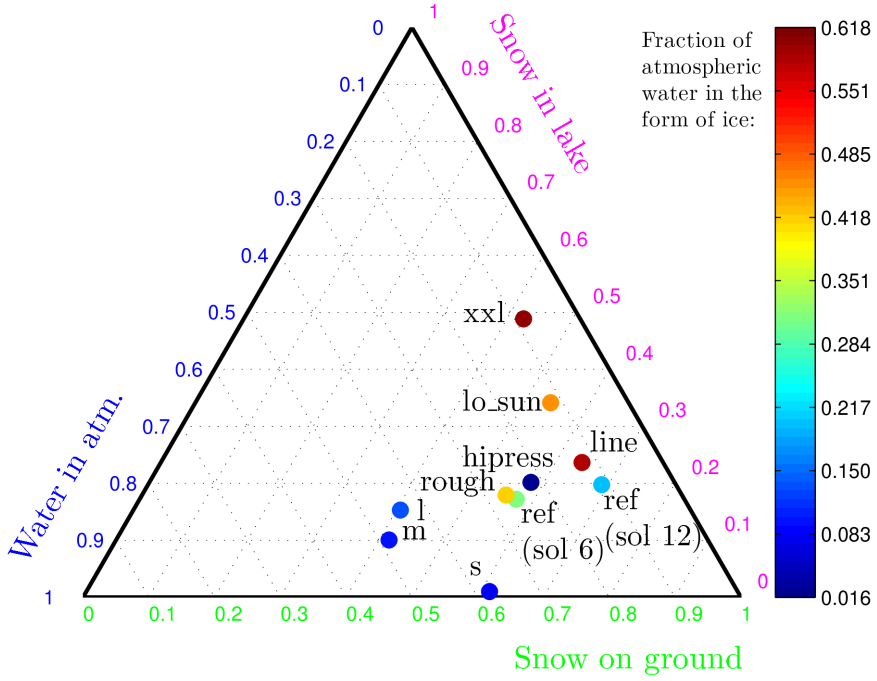

Figure 2.6 Fate of vapor released from the lake (precipitation efficiency). Colored dots corresponds to a models' inventory of water substance after 6 sols, after subtracting the inventory of a lake-free run. Color corresponds to fraction of atmospheric water in the ice phase: red is more ice-rich, blue is more vapor-rich. Only snow on ground can contribute to localized geomorphology. Water substance in atmosphere can contribute to regional and global climate change: greenhouse warming is increasingly likely as the mass of atmospheric water increases.

km from the lake, the majority is in the form of vapor at the end of the simulation.

After 6 days of the `ref` run, the outermost (hemispheric) grid contains ∼300 Mt more atmospheric water than the `dry` run (please refer to Table 1 for details of runs and parameters). This is equivalent to a global surface liquid water layer 2μm thick, or a lake depth of 7 cm. This is radiatively unimportant on the global scale, and less than the current global average (∼17 pr μm in the northern hemisphere, ∼9.5 pr μm in the South: Smith (2002)). The added vapor will presumably be cold-trapped as ice on the winter pole, which is outside the space and time limits of our simulation. If all vapor precipitates in a single season on a polar cap of area 10^6 km^2, it would form a layer 0.3 m thick. Layers of this thickness could be resolved by the HiRISE camera on a gently-sloping exposure.

Figure 2.6 understates the fraction of water that precipitates locally if the conditions that maintain a liquid surface are maintained indefinitely. This is because some of the water that is in the atmosphere at the end of sol 6 will precipitate locally. In an extended run (`ref (sol 12)` in Figure 2.6), the fraction of water that precipitates locally is increased.

2.5 Sensitivity tests

2.5.1 Vertical resolution

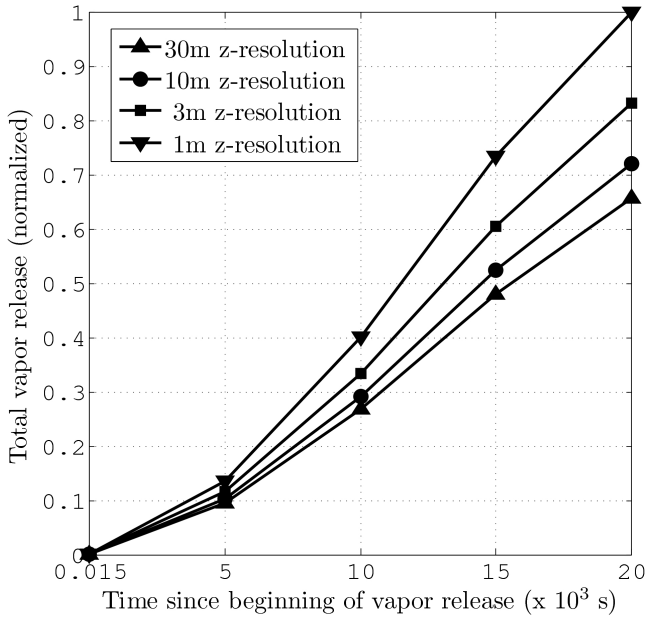

Figure 2.7 Outcome of vertical resolution sensitivity test. Values are normalized to total vapor release at the end of the 1m-resolution run.

We carried out a sensitivity test to determine model vapor release as a function of vertical resolution. The computational expense of increasing vertical resolution scales as $N\log(N)$, so runs were for only $\frac{1}{4}$ sol starting at $\sim$ 12 noon Local Solar Time. Vapor release rate is moderately sensitive to model vertical resolution. Increasing surface layer thickness by a factor of 30 decreases vapor release by 35% (Figure 2.7). Therefore, our modeled afternoon vapor release (and precipitation) rates are probably underestimates. This is conservative, in terms of driving localized precipitation.

2.5.2 Horizontal resolution

We carried out a simulation, `hires`, that added an inner grid with 2.0 km horizontal resolution. (`hires` was initialized from `ref` output after 2 days). Overall storm structure was similar, although secondary plumes developed in addition to the main plume. Peak vertical velocity increased by 34%, peak time-averaged vertical velocity by 57 %, and cloud height by 12%, relative to `ref`. When averaged to the lower resolution of `ref`, these differences decreased to 16%, 26%, and 12%, respectively (Figure 2.8). Although these differences are not negligible, we observed that our main results (strong plume and localized precipitation) were not affected by the increase in horizontal resolution. Simulations which use resolutions intermediate between eddy-resolving and the mesoscale are known to suffer from artifacts caused by aliasing of barely-resolved eddies by the grid cell size, and we observed 2Δx noise in `hires`. For these reasons, and because of the computational expense of high resolution, we held model horizontal resolution at 5.9 km for the remainder of our sensitivity tests.

2.5.3 Size of idealized lake

Small lakes in our simulations are unable to drive deep convection, and have weaker localized precipitation. We modeled square lakes with areas of $\sim$35 km^2 (`s`), $\sim$300 km^2 (`m`), $\sim$1700 km^2 (`l`), and $\sim$29000 km^2 (`xxl`), in addition to the $\sim$4000 km^2 `ref` simulation.

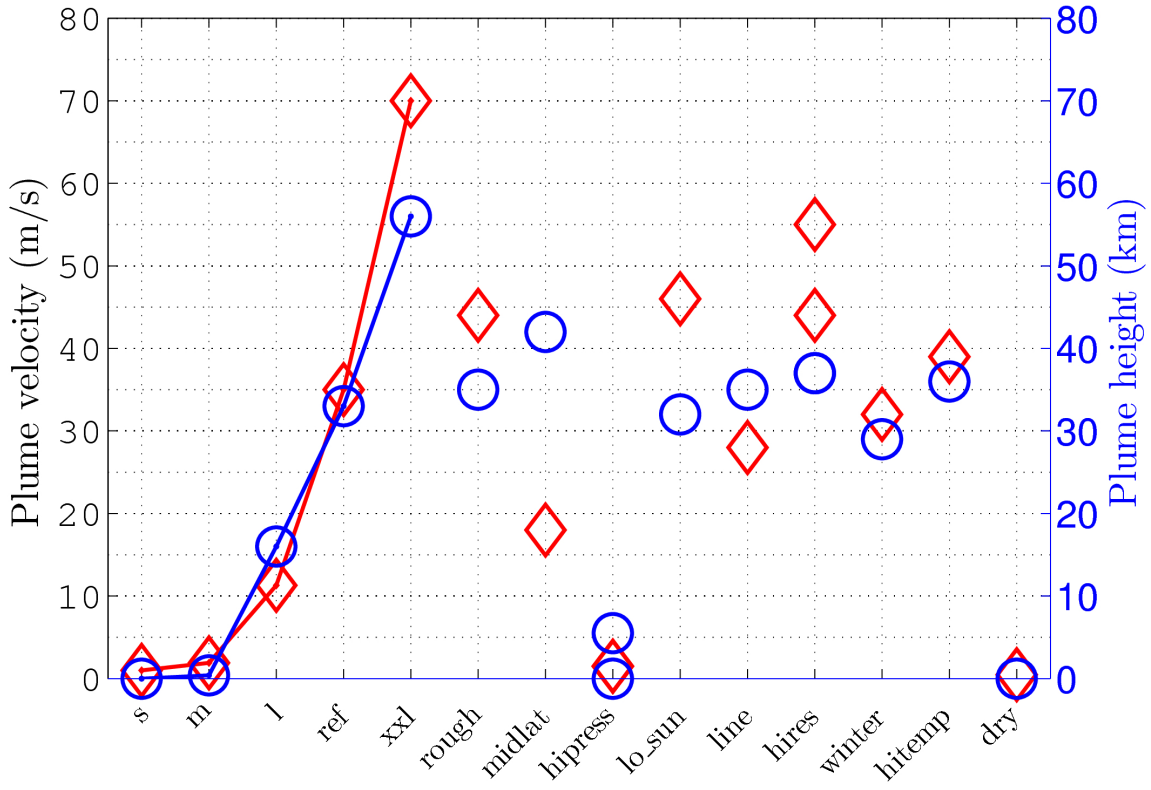

Figure 2.8 Intensity of moist convection for runs listed in Table 1. Red diamonds correspond to peak time-averaged plume velocity, blue circles correspond to plume height. Lines connect the run of 5 simulations in which only size was varied. Plume height is defined as the altitude at which the plumes' spatial peak in time-averaged ice mixing ratio falls below 10^{-3}. The two blue circles for `hipress` correspond to ice mixing ratios of 10^{-3} (lower circle) and 10^{-4} (upper circle). The two red diamonds for `hires` correspond to peak velocities at 2km resolution (upper diamond) and peak velocities smoothed to 5.9 km resolution (lower diamond).

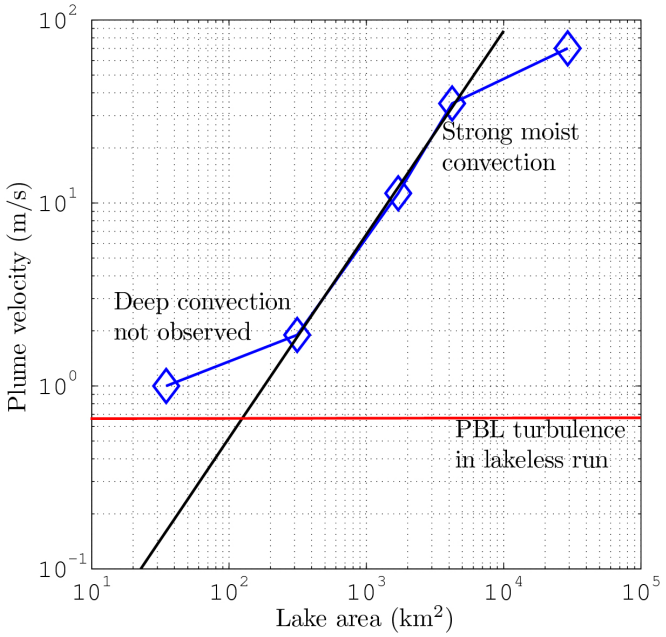

Figure 2.9 Dependence of plume convective intensity on lake size. The black line is a best-fit power law (slope = 1.11) to the three central points. It intersects the lakeless-run Planetary Boundary Layer (PBL) turbulence at a lake size of $O(10^2)$km^2; below this lake size, we would not expect to recognize a plume. Explanations of the similarity of the power-law exponent to 1, and the deviation of the largest lake from this slope, are provided in the text.

Deep moist convection was not observed in the `s` and `m` simulations. To verify that this was not an artifact of insufficient model resolution, we ran a 2km-resolution nested grid on `m`. Although peak vertical velocities did increase in the nested grid relative to the default-resolution model, lake-sourced vapor did not reach altitudes much greater than the planetary boundary layer and, as in the default-resolution model, was passively advected downwind. Given our particular choice of atmospheric boundary conditions (present day orbital conditions, low latitude, and southern Summer), lake size $>10^3$ km^2 is required for deep moist convection. If vapor is funneled to a single central plume of constant radius and entirely condensed, we would expect plume vertical velocity to scale linearly with lake area. Figure 2.9 shows that this expectation is borne out for lakes of size $10^{2.5}$ km^2- $10^{3.5}$ km^2, but overestimates lake storm convective intensity for the largest simulation. This `xxl` simulation is unusual because it has a much broader area of strong upwelling than the smaller lakes, which explains why its convective velocities are not as high as expected. In the smallest lake modeled, the lake-associated updrafts are so weak that they were difficult to separate from everyday planetary boundary layer convection.

Because lake-induced convergence (Figure 2.2d) efficiently funnels lake-released vapor into one buoyant plume, plume velocity and plume height increase with lake size (Figure 2.8). Greater plume heights promote ice formation, and the ice fraction of atmospheric water increases with lake size (colors in Figure 2.6). This is a self-sustaining feedback, because ice formation provides energy for plume ascent, which in turn creates low pressure above the lake and drives convergence.

Larger lakes inject proportionately less water into the global atmosphere. More than $\frac{1}{3}$ of the water released in the `s`,`m` and `l` simulations is in the atmosphere at the end of the simulation. <14% is in the form of ice. In the `xxl` simulation, the fraction of released water that is precipitated locally is >90%, and most of the atmospheric water is ice aerosol that would probably precipitate locally if the lake surface froze over. The `line` source has a similar lake area to the square `xxl` run, and behaves similarly in having a small atmospheric water fraction and a large ice aerosol fraction. This suggests that this trend of increased localized precipitation fraction with increased lake area does not depend on lake geometry.

2.5.4 Surface roughness parameterization

Our default run assumes fixed lake surface roughness, but water surface roughness increases with wind speed. A more realistic approximation is that of Garratt (1992) as given by Eq. 7.21 of Pielke (2002):

$$z_0 = 1 \times 10^{-4} + (0.01625u^2/g) \tag{2.7}$$

where we have added the first term to maintain numerical stability. This remains an adequate fit to the much larger datasets now available (Zeng et al., 1998). The time-average lake roughness with this parameterization is 0.0126 m, and is a factor of three higher during the night when near-surface winds are stronger.

Our time-averaged results are insensitive to this more accurate lake surface roughness parameterization (Table 2; Figure 2.6), although the very strong plumes seen during the night (when vapor injection rate is highest) increase both plume height and updraft velocity (Figure 2.8).

2.5.5 Line source

Our line source is intended to sketch an outflow channel during a channel-forming flood. It is a N-S oriented, straight trough of depth 1.5 km, floor width 30 km, wall slope 0.13, and length 880 km. The floor is flooded. Of the resulting snow, 23% falls back into the lake and a further 70% falls within 100 km of the edge of the trough. The diurnal cycle consists of a strong, steady, spatially continuous line storm on the W edge of the trough during the night, and a clumpy, broken line of weak updrafts some distance E of the trough during the day. Time-averaged vertical velocity and precipitation fields do not show this clumpiness:

instead, there is a trend of monotonically increasing vertical velocity and precipitation rates toward the north, because the background wind field advects the upper parts of the cloud toward the north.

We do not consider the influence of the flowing water on surface roughness, nor the drag of the flowing water on the atmosphere.

2.5.6 Season

In southern winter (also aphelion season) the sign of the Hadley circulation reverses. In a run at Ls = 90°, the GCM boundary conditions produced ESE-directed time-averaged winds at altitudes below $\sim$ 15 km, and SW-directed time-averaged winds at higher altitudes. The highest snowfall rates were just ESE of the lake, reflecting steering of the plume by regional winds. Total localized precipitation was the same as in `ref` to within 7%.

2.5.7 Latitude

A cyclonic circulation does not develop in our `ref` run. To determine if Coriolis effects can produce a cyclone at higher latitudes, we ran a test at 45°S latitude. As expected given the small size of the lake compared to the Rossby radius, the lake-driven circulation is too weak to restructure the background wind field and a lake-induced standing cyclone does not form.

The total localized precipitation in the midlatitude run is only $\frac{1}{3}$ of the total localized precipitation in the equatorial runs. Since vapor release is similar, vapor is being converted to localized precipitation with a smaller efficiency. Peak time-averaged column ice fractions are $< 40\%$ in the midlatitude run, compared to $> 70\%$ in the reference run (Figure 2.2e). This is because both runs are close to southern summer solstice. The southern midlatitude site, `midlat`, is in sunlight for 2/3 of each day, and has air temperatures higher by 20K on average than the equatorial site, `ref`. Because of the lower supersaturations, water in the midlatitude plume must be lifted 5 km higher to obtain a given ice fraction than in the equatorial plume. Therefore, more vapor escapes to the regional atmosphere.

2.5.8 Faint young sun

Many channel networks on Mars formed when the Sun was fainter. The solar luminosity L at the Hesperian-Amazonian boundary was 0.78-0.85 $\times$ present-day solar luminosity L_0, and L at the Noachian-Hesperian boundary was 0.75-0.77 $\times$ L_0 (Bahcall et al., 2001; Hartmann, 2005). The uncertainty is due to differences among the models that map crater density onto absolute age: the solar evolution model has much smaller error bars. The Juventae plateau channel networks (Chapter 3) could be as old as Hesperian (Le Deit et al., 2010), so we ran a test at 0.75 L_0. As well as being less luminous, the young Sun was also 1.5 % cooler (Bahcall et al., 2001). We ignore the resulting small shift in the solar spectrum, and simply reduce the flux at all wavelengths by 25 %.

Colder air temperatures under the faint young sun lower the cloud base by ~ 5 km. Peak updraft velocities are >50 m.s. in both simulations, but occur at lower elevations in the faint young sun simulation. Because supersaturations are higher at all colder altitudes, ice growth is favored and the fraction of atmospheric water that is ice increases from 32 % in `ref` to 47 % in `lo_sun`.

We conclude that localized precipitation is favored by reduced solar luminosity. However, this is not true for runoff generation and channel formation (§2.6).

2.5.9 Paleoatmospheric pressure

Figure 1 suggests that localized precipitation will not occur if atmospheric pressure is greatly increased. To test this, we increased pressure to 10x Present Atmospheric Level (PAL) on all the mesoscale grids (run `hipress`). Deep moist convection is suppressed, uplift velocities are reduced, and comparatively little vapor reaches cloud-forming altitudes. No lake-sourced ice is found above 10km, and little ice aerosol forms (1.6 % of atmospheric water mass on the inmost grid, versus 32 % in `ref`).

Precipitation is reduced by 20 %, and preliminary runs at 20x PAL lead us to expect that further increases in pressure will greatly reduce localized precipitation.

2.6 A probabilistic model of snowpack melting on ancient Mars

Localized precipitation is not occurring today, so our model can only be tested against the geologic record of past events. Geology records erosion and sediment transport, which require melting. If storm systems in a cold background climate deliver snow locally, and that snow sublimes away without melting, it will leave no geological trace. Therefore, a melting model is required to test the localized precipitation hypothesis. For a lake lifetime of 1 Earth year (similar to expected chaos outflow durations: Andrews-Hanna and Phillips (2007); Harrison and Grimm (2008)), and assuming that seasonal effects on the storm are minor, $\sim$2 m of snow is predicted to accumulate downwind of the lake by our reference simulation, assuming a snowpack density of 350 kg/m^3. Will it melt?

We expect the lifetime of snowpack against sublimation and wind erosion to be $\geq O(1)$ year, so that the annual-maximum temperature is that which is relevant for snow melting. For predicted snowpack depths $O(1)$m, this residence time is supported by GCM simulations (e.g., Table 1 in Madeleine et al. (2009)). A simple energy argument gives the same result –

$$t_{\rm s} \sim \frac{d_{\rm snow}\rho_{\rm snow}L_{\rm s}}{F_{\rm Sun}\eta f_d} \tag{2.8}$$

which with snow depth $d_{\rm snow} = 1$ m, snow density $\rho_{\rm snow} = 350$ kg/m^3, solar flux $F_{\rm Sun}$ = 300 W/m^2, fraction of solar energy used for sublimation $\eta = 0.1$, day fraction $f_d = 0.5$,

gives sublimation time $t_s = 1.0$ Mars year. With surface pressures on the plateau of ≈1000 Pa, maximum modeled surface shear stress is not sufficient to initiate motion of snow that is resting on the ground (Greeley and Iversen, 1985).

In general melting probability will depend on orbital elements including obliquity and precession, latitude, age (via solar luminosity), material properties, and the lifetime of snowpack against sublimation losses to planetary cold traps. For age ≥20 Mya, deterministic chaos makes orbital elements unreliable: as our interest is in ancient Mars our model is therefore probabilistic. We model temperatures at the equator - 64% of the sedimentary rocks on Mars are within 10° of the equator (Malin et al. (2010), `figure16.txt` in their online supporting data), and our modeling target in Chapter 3 is at 5°S.

a. Energy balance at the melting point. The energy balance of a snow-bearing surface on Mars is (Dundas and Byrne, 2010)

$$\frac{\partial U}{\partial t} = (1-\alpha)SW\downarrow + \epsilon LW\downarrow - \epsilon\sigma T^4 - SH - C_n - L_s\frac{\partial m_w}{\partial t} \tag{2.9}$$

where the left-hand side is gain of energy by the surface layer, α is surface albedo, $SW\downarrow$ is sunlight, $\epsilon \sim 0.98$ for ice is thermal emissivity, $LW\downarrow$ is the greenhouse effect, σ is the Stefan-Boltzmann constant, T is surface temperature, SH is net sensible heat flux from the surface to the atmosphere, C_n is net conductive heat flux from the surface into the ground, L_s is the latent heat of sublimation of water, and $\frac{\partial m_w}{\partial t}$ is the sublimation rate.

The minimum sublimation rate (in the absence of wind) is given by (Hecht, 2002; Dundas and Byrne, 2010)

$$\frac{\partial m_w}{\partial t} = 0.14\Delta\eta\rho_{asl}D\left(\left(\frac{\Delta\rho_{asl}}{\rho_{asl}}\right)\left(\frac{g}{\nu_a^2}\right)\left(\frac{\nu_a}{D_a}\right)\right)^{1/3} \tag{2.10}$$

where $\Delta\eta$ is the difference between atmospheric and surface gas water mass fractions, ρ_{asl} is the atmospheric density within the surface layer, D_a is atmospheric mass diffusivity, $\Delta\rho_{asl}/\rho_{asl}$ is the normalized density difference between the moist near-surface atmosphere and ambient atmosphere, and ν_a is kinematic viscosity. We parameterize the temperature-dependency of ν_a and D_a following Dundas and Byrne (2010).

Melting occurs if $\frac{\partial U}{\partial t} \geq 0$ at $T = 273.15$K. We set up optimistic conditions for melting, and ask: with what probability do orbital conditions permit melting?

Evaporative cooling is handled following (Dundas and Byrne, 2010): we obtain 165W assuming 70% humidity, atmospheric pressure 1220 Pa, and zero wind. The more sophisticated surface-layer theory of Clow and Haberle (1990) gives an evaporative cooling rate >2 times less than in Dundas and Byrne (2010) (and >4 times less than in Ingersoll (1970)) for roughnesses $z_0 < 0.3$ mm that are appropriate for polar snow (Brock et al., 2006). Therefore, our parameterization may overestimate evaporative cooling by free convection. We assume still conditions, so that cooling by wind-driven turbulent fluxes (forced convection) is negligible: this assumption is favorable for melting. We also neglect the turbulent flux of sensible

heat SH, which is a factor of >10 smaller than evaporative cooling for these conditions (Hecht, 2002). The noontime conductive heat flow $C_{\rm n}$ can be parameterized assuming the temperature falls to the diurnal average temperature at a depth equal to twice the diurnal skin depth. Assuming a diurnal-average temperature during the hottest season of 220K, this gives

$$C_{\rm n} = k\frac{\partial T}{\partial z} = k\frac{273.15 - 220}{2\sqrt{\kappa P/\pi}} \tag{2.11}$$

For thermal conductivity $k = 0.125$ W/m/K for snow (Carr and Head, 2003b), sol length $P = 88775.204$ s, and thermal diffusivity $\kappa = 2.04$ x 10^{-7} $\mathrm{m^2 s^{-1}}$ appropriate for low-density snow, we obtain $C_{\rm n} = 40.3\mathrm{W}/m^2$.

The greenhouse effect $LW\downarrow$ at the time of peak surface temperature is assumed to be $55\mathrm{W/m^2}$ (European Mars Climate Database). We do not consider the additional greenhouse forcing from the lake storm, nor from a possible past stronger greenhouse effect.

For dusty snowpack with albedo 0.28, the resulting minimum on SW is 640W.

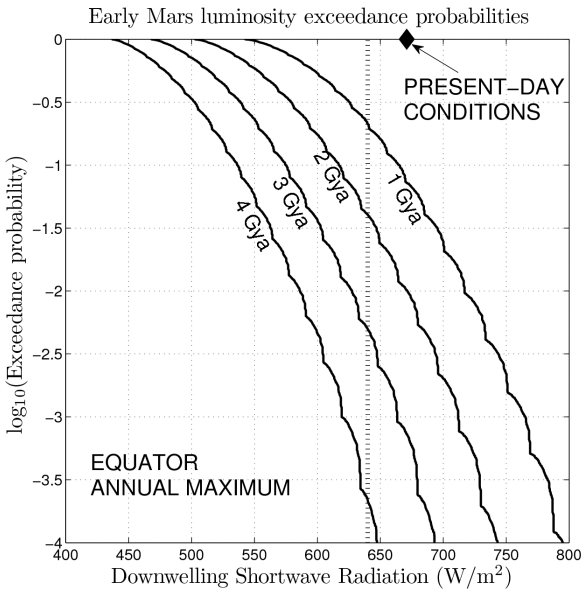

Figure 2.10 Exceedance probabilities for annual maximum sunlight at Mars' equator. Vertical dashed line is 640W/m^2, the minimum for melting (see text). Snow instantaneously emplaced at Mars' equator with the current orbital conditions and solar luminosity would melt. For progressively earlier times (reduced solar luminosity), the probability of melting decreases. The small wiggles in the solid curves are interpolation artifacts.

We calculate the maximum equatorial luminosity for all ages, seasons, and orbital conditions. The age-dependent solar luminosity is taken from the standard solar model of Bahcall et al. (2001). We then weight the annual-maximum luminosity results by the age-dependent probability densities for obliquity and eccentricity from Laskar et al. (2004), assuming that obliquity and eccentricity are not strongly correlated. (In the 0.25 Gyr solutions provided by J. Laskar at `http://www.imcce.fr/ Equipes/ASD/ insola/mars/mars.html`, obliquity and eccentricity are not strongly correlated.) 640W is exceeded with 21% probability at 1 Gya, but with only 0.5% probability 3 Gya (Figure 2.10).

b. A 1D column model. Next we calculate temperatures within snowpack for the full range of obliquities (ϕ, $0^\circ \rightarrow 80^\circ$), eccentricity ($e$, $0.0 \rightarrow 0.175$), longitudes of perihelion (L_p) and solar longitudes that are sampled by Mars (Laskar et al., 2004). We use a 1D thermal model to calculate temperature T within snowpack at a range of seasons, ignoring the greenhouse effect $LW\downarrow$. T is solved for by a Crank-Nicolson scheme for the linear (conduction) part and

iteratively for the nonlinear contribution of radiation and evaporative cooling in the topmost layer. The timestep is 12 seconds. Evaporative cooling is handled following (Dundas and Byrne, 2010) with optimistic assumptions as in the simple energy balance. Each run is initialized with surface temperature $T_{\rm s}$ at instantaneous thermal equilibrium with incoming sunlight, decaying with an e-folding depth equal to the diurnal skin depth $d = \sqrt{(k\rho)/(Pc_p\pi)}$ to an energy-weighted time-averaged equilibrium temperature at depth. (Here, k is thermal conductivity, ρ density, P the length of 1 sol in seconds, and c_p specific heat capacity of the subsurface.) We then integrate forwards in time for multiple sols, but with seasonal forcing held constant, until sol peak $T_{\rm s}$ has converged. Models that neglect the greenhouse effect provide a good approximation to Mars' observed surface temperature.

Atmospheric contributions $LW\downarrow$ are parameterized as a time-independent greenhouse temperature increase, $\Delta T_{\rm a}$. The purpose of adding the atmospheric contribution in post-processing is to allow different models of the past atmosphere to be compared to each other without rerunning the ensemble of $\sim 10^5$ column models. Typical present-day values are $\Delta T_{\rm a}$ = 5-10K (Read and Lewis, 2004). This averages over strong nighttime warming, which is irrelevant for melting, and weak afternoon warming, which is critical to melting. Setting $\Delta T_{\rm a}$ to the time average of present-day greenhouse warming will therefore lead to an overestimate of melting. Instead, we want to know the value $\Delta T_{\rm a}$ at the peak temperatures relevant to melting. We make the approximation

$$\Delta T_{\rm a} \simeq T_{\rm s,max} - \sqrt[4]{\sigma T_{\rm s,max}^4 - \frac{LW\downarrow \epsilon}{\sigma}} \tag{2.12}$$

The Mars Climate Database Mars Year 24 simulation shows $\Delta T_{\rm a}$ 5-7K at low latitudes. This excludes the dust storm season, for which the neglect of atmospheric scattering leads to an overestimate of the net atmospheric contribution. We therefore adopt 6K as our greenhouse forcing. Additional greenhouse forcing due to doubled CO_2 is small and safely neglected (Wordsworth et al., 2010).

Material properties for snowpack are taken from Carr and Head (2003a): we assume a snowpack density of 350 kg/m^3, thermal conductivity of 0.125 W/m/K, and specific heat capacity c_p of 1751 J kg^{-1}, and neglect the temperature dependence of k and c_p. We consider dirty H_2O snow albedos between 0.28 and 0.4. The smaller value is the present-day albedo of Mars' dust continents (Mellon et al., 2000), and the larger value is the upper end of the envelope that best fits the observed seasonal dependence of ephemeral equatorial snow on present-day Mars (Vincendon et al., 2010). (Chapter 3 provides a more detailed discussion of snowpack albedo).

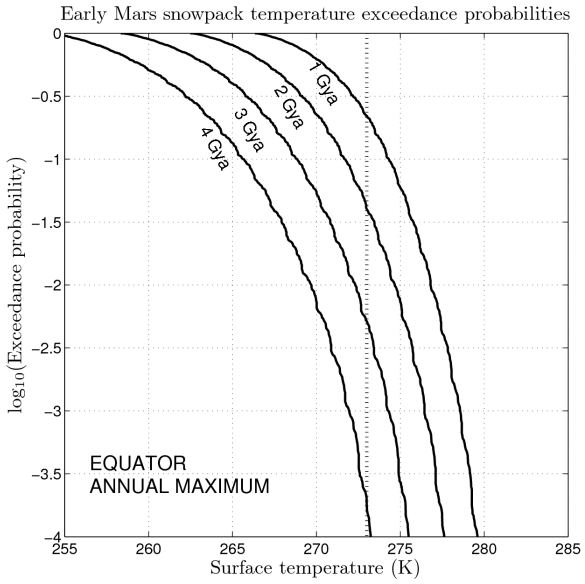

Figure 2.11 Exceedance probabilities for annual peak temperature of snowpack at Mars' equator, from our 1D column model. A dust-like albedo (0.28) is assumed. Vertical dashed line corresponds to the melting point. The small wiggles in the solid curves are interpolation artifacts. For progressively earlier times (reduced solar luminosity), the probability of melting decreases.

Maximum-temperature results are interpolated onto a finer mesh in orbital parameters (ϕ, e, L_p). We again weight the results using the probability distributions of Laskar et al. (2004). Results for albedo = 0.28 and latitude = 0° are shown in Figure 2.11. Temperatures greater than 273.15K are not realistic, because snowpack temperature will be buffered by the latent heat of melting. The agreement between the melting probabilities obtained from the 1D column model and the melting probabilities obtained from the simple energy balance argument is excellent (Figures 2.10 and 2.11). Even with the weak, present-day greenhouse effect, temperatures high enough for melting occur during 4% of the years (0.1% for albedo 0.35). With an additional 6K of greenhouse warming, melting occurs during 56% of years (12% for albedo 0.35).

Discussion. The exact melting probabilities are unlikely to be correct, but we draw three lessons from these simple models:

- The probability of low-latitude melting is certainly higher for instantaneous emplacement of snow than for gradual (e.g, orbital equilibrium) emplacement of snow, and

probably much higher. That is because gradual emplacement of annually-persistent snow at the equator is only possible at high obliquity (∼50% of the time), while instantaneous emplacement can occur at any time. In addition, gradually-emplaced snow will accumulate preferentially in areas where it is most stable: for example, shadowed areas, adverse steep slopes, and especially chasma and crater interiors where shadowing reduces peak temperature. Craters at 10°S in Sinus Sabeus appear to contain mantled, atmospherically-emplaced ice deposits, providing direct evidence that equatorial ice on Mars does preferentially accumulate in crater-interior cold traps (Shean, 2010). The most compelling evidence for low-latitude glaciation on Mars is on the flanks of the Tharsis Montes, which have the lowest atmospheric pressures on the planet (Forget et al., 2006). Liquid water exposed on the Tharsis Montes today would boil internally, leading to very rapid evaporative losses. Taken together, these observations suggest that localized precipitation is much more likely to melt than orbital-equilibrium precipitation. Today's orbital conditions would lead to melting of snowpack on the equator (diamond in Figure 2.10). However, on today's Mars, snow is almost entirely restricted to high latitudes. Snow and ice on Mars do not melt in general because the area of transient liquid water stability changes on slow, orbital timescales $O(10^{4-5})$ yr. This allows time for ice to be removed (vertically or latitudinally) from the advancing zone of increased saturation vapor pressures, towards cold traps where melting cannot occur. Therefore the areas of surface ice and of transient liquid water stability rarely intersect. Theory, experiments, and the lack of evidence for transient liquid water at the Phoenix landing site confirm this (Schorghofer, 2010; Hudson et al., 2007; Mellon et al., 2009). Steep (>20°) gullied slopes within mid- and high-latitude craters are an exception (Morgan et al., 2010), assuming that the gullies formed from liquid water flows. In contrast, localized precipitation delivers snow on timescales $O(10^{-1})$ yr to a location uncorrelated with transient liquid water stability, so a wider range of orbital conditions will then allow melting. In the case of impact-induced precipitation, snow falling on hot ejecta will melt regardless of orbital conditions.

- Because of the wide range of possible orbital states, the probability of melting is not large, but neither is it zero. The distribution of melting events ($T_s \geq$273K) with orbital parameters is shown in Figure 2.12. Relative to the cdf of obliquity, melting events are more probable at low obliquity than high; they are much more probable when perihelion occurs at equinox than when perihelion occurs at solstice; and they occur exclusively at moderate-to-high eccentricity. These results may be understood as follows. Moderate eccentricity is needed to offset the reduced solar luminosity. For example, at 3.0 Ga and e = 0.11, perihelion insolation is equivalent to insolation on a circular orbit today. Perihelion near equinox is needed to align the season when the noontime sun is highest at the equator with the peak solar flux. Increasing obliquity narrows the seasonal window during which the sun rises high enough in the equatorial sky for melting to occur. Therefore, the probability of aligning with perihelion is reduced and so the

chance of a melting event at high obliquity is lower. This distribution is almost exactly a ranking in peak solar luminosity, and is not sensitive to our model assumptions.

- Using slightly less optimistic assumptions in the energy balance approach (humidity = 0.25 and albedo 0.35), the minimum SW flux for melting rises to 882W/m^2. This is unachievable at Mars. For comparison, the sunlight striking the top of the atmosphere above North Greenland, 80N, at summer solstice during the melt season is 730W/m^2. The strength of the evaporative cooling term at low pressures strongly suppresses snowpack melting. Evaporative cooling may not be relevant for understanding the melting of small quantities of snow that is in contact with non-volatile soil, and small quantities may be all that is necessary to redistribute mobile elements and to form crusts in the global soil (Amundson et al., 2008; Arvidson et al., 2010). However, this cannot account for runoff generation and channel formation. Adding CO_2 pressure quickly damps evaporative cooling, but also increases the magnitude of sensible heat transfer to the atmosphere. There is a minimum in cooling at intermediate pressures (Hecht, 2002), but this pressure may be high enough to suppress localized precipitation (Figure 2.8). The problem is exacerbated by the threshold processes linking melting to erosion. To generate runoff, melting must outpace the sum of infiltration, sublimation and refreezing. If erosion is to occur, melt-fed streams must be at least deep and fast enough that their basal traction exceeds the threshold for bed grain motion, in order to transport eroded clasts away.

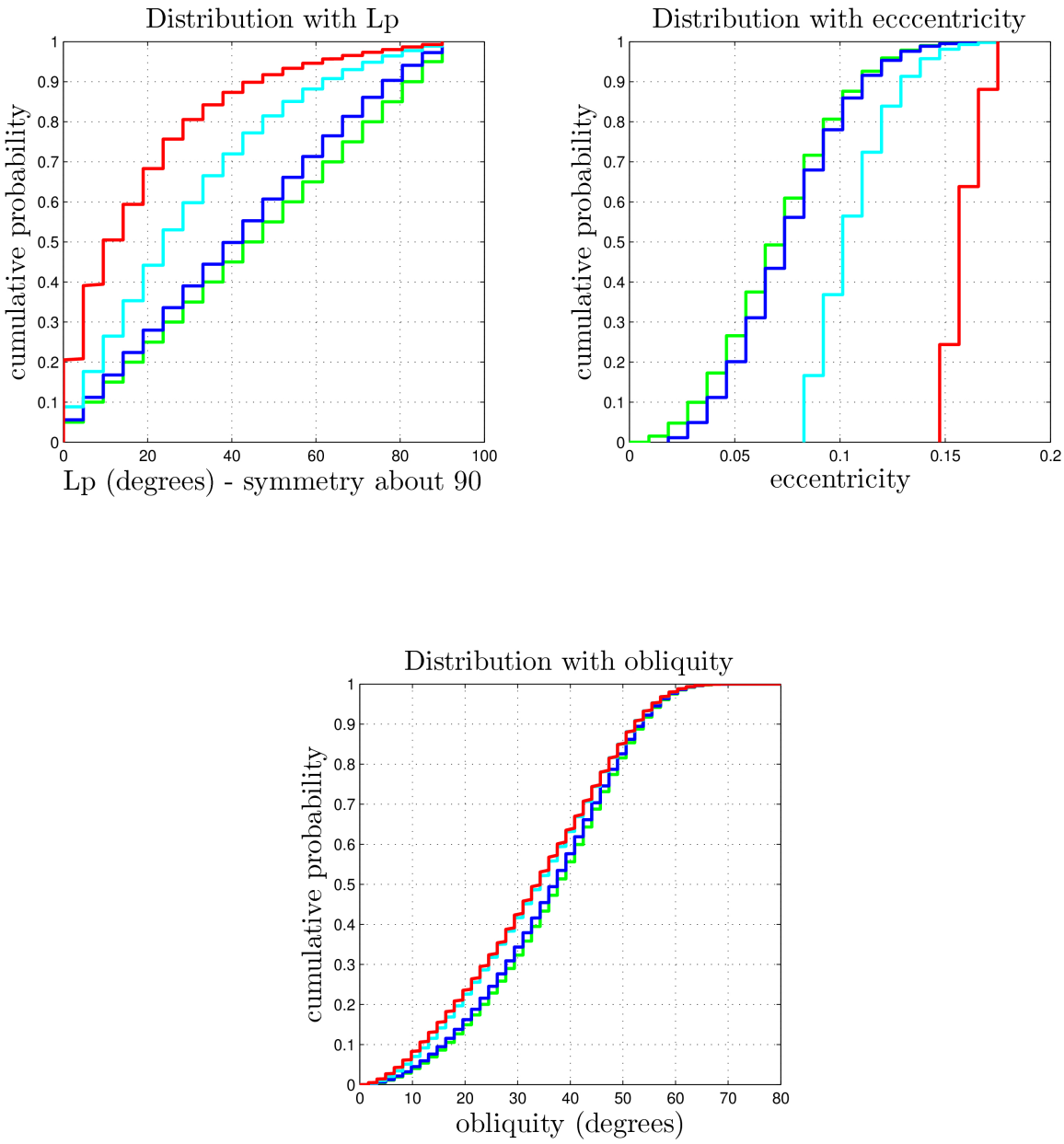

Figure 2.12 Self-normalized probability density functions for the subset of sampled orbital conditions that produce melt. Top left panel shows solar longitude of perihelion; top right panel shows eccentricity; and bottom panel shows obliquity. In all cases, albedo = 0.28, age = 1.0 Gya (other albedos and ages have very similar cdf shapes, although maximum temperatures differ). The cyan lines corresponds to 273K (melting), and the other colors are green (all temperatures), blue (268K), and red (278K).

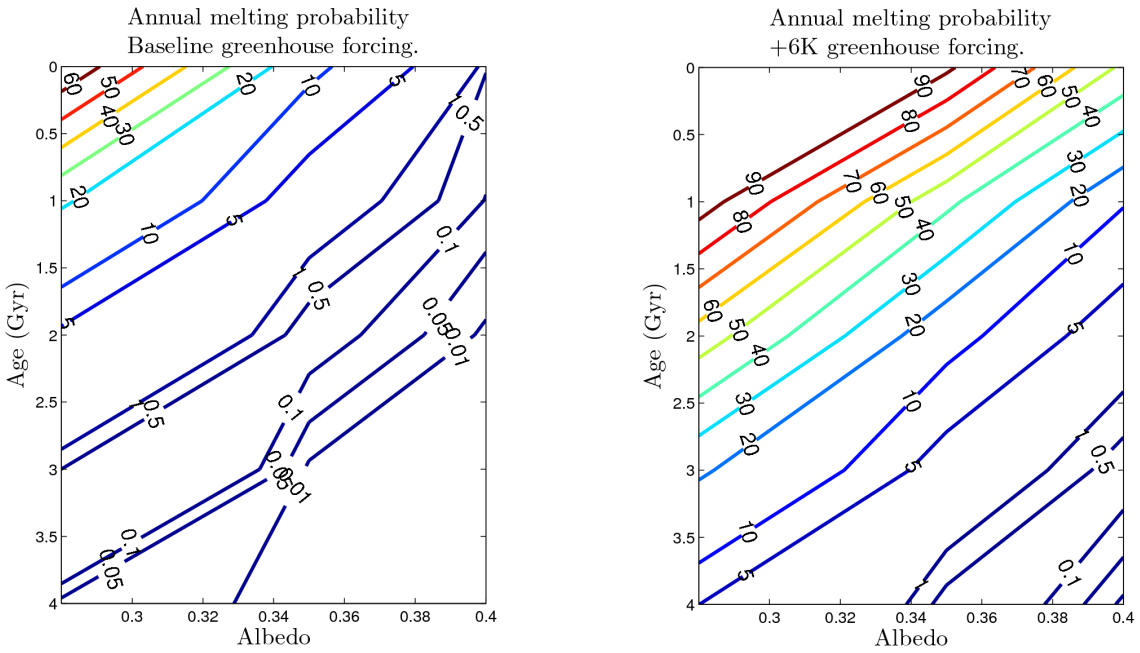

Figure 2.13 Contoured probability (percent) of melting of rapidly-emplaced equatorial precipitation as a function of albedo and solar luminosity. Left-hand panel corresponds to an atmosphere similar to today, and right-hand panel to one with 6K additional greenhouse forcing.

For Early Mars, this dilemma can probably only be resolved by an early orbital state with a smaller semimajor axis or smaller eccentricity than the current one; a multibar CO_2/H_2O atmosphere; or adding non-CO_2 greenhouse gases. In summary, our models do suggest a requirement for a different global climate state if localized precipitation is to lead to substantial runoff on gentle slopes on Early Mars, but this is only necessary to bring temperatures back up to the level of contemporary Mars: melting probabilities with present-day solar luminosity are large (Figure 2.13). To counteract the effect of the Faint Young Sun (FYS) on mean Mars surface temperature at 3.5 Gya, the required greenhouse warming is approximately

$$\Delta T_{\rm fys} = (1 - 0.77^{0.25}) T_{\rm M} \approx 13K \tag{2.13}$$

(with Mars-average surface temperature $T_{\rm M} \sim 210$K; the luminosity at 3.5 Ga is from Bahcall et al. (2001)). This is a relatively modest requirement. It does not hold for impact-induced precipitation, because snow falling on hot ejecta will melt provided that atmospheric pressure is above the triple point.

Figure 2.14 Seasonal supraglacial lakes on Greenland ice sheet. Largest lake is 4.5 km across. Note absence of clouds and precipitation at 1 bar, and high drainage density of meandering, snowmelt-fed channels feeding lake. (Image used with kind permission of I. Joughin, U. Washington Polar Science Center).

2.7 Prospectus and discussion

Our model shows lake storm ice forming at terrestrial cirrus cloud temperatures >200K, which because of the higher water vapor mixing ratio is warmer than modern Mars cloud forming temperatures ≤185K. Recent laboratory experiments (Iraci et al., 2010) show that ice nucleation at T ≤ 185K requires greater supersaturations than previously thought, while confirming that the MRAMS-CARMA parameterization of the critical supersaturation at the higher ice nucleation temperatures observed in our simulation is adequate.

We have focussed on ephemeral open-water lakes in this study, but this is not the only way of getting water into the atmosphere. Fumaroles and rootless cones inject vapor to the atmosphere, but their efficiency has not been as well studied as that of a wind-stirred lake surface (Zeng et al., 1998). Gas-charged fountains may inject vapor during the early stages of outflow channel formation (Bargery and Wilson, 2010). The mass flux we obtain in even the smallest simulation greatly exceed the greatest spring discharges on Earth. Leads in lake ice may allow deep convection to continue after the majority of the lake surface has frozen over.

2.7.1 Geomorphic paleobarometer?

Cold lakes at 1 bar on Earth do not produce vigorous storms, with convection and precipitation in a dry background atmosphere (Figure 2.14); cold lakes at 12 mbar on Mars do, at least in our model. Therefore there is a threshold atmospheric pressure, between 12 mbar and 1 bar, below which cold lakes on Mars can induce convective storms and localized precipitation (orange line in Figure 2.1). We speculate this pressure is $\sim 10^2$ mbar, because this is the pressure at which a 273K lake on Mars produces the same buoyancy flux as 299K on Earth. 299K is the lower limit of the tropical sea surface temperatures that on today's Earth are associated with deep convection (Emanuel, 1994). A preliminary run at 20x present-day pressure ($\sim$ 120 mbar) showed significant suppression of the buoyant plume, with limited localized precipitation. If a past landform on Mars could be conclusively shown to result from localized, lake-induced precipitation, that would suggest a low atmospheric pressure ($\leq 10^2$ mbar) at the time it formed. We investigate one set of candidate landforms in Chapter 3, but because of geological ambiguities it does not reach the 'conclusive' standard.

If the vapor injection mechanism is a fumarole or gas-charged fountain rather than a lake surface, then the ability to set a paleopressure constraint goes away. The potentially much higher injection rate can overcome the dilution by the thicker atmosphere.

2.7.2 Applications to the Late Hesperian and Amazonian sedimentary record

One motivation for our localized-precipitation work is to understand Late Hesperian and Amazonian fluvial features which are widespread, although rare, on the Martian surface (Figure 2.15; Chapter 3). They postdate the global decline in valley formation, aqueous mineralization and erosion rates near the Noachian-Hesperian boundary. Therefore, localized processes are *a priori* a reasonable explanation for these fluvial features. Unusual microclimates (such as nearby steep slopes) may explain some of the features (Fassett et al., 2010), but those on the Valles Marineris plateau and at Mojave Crater suggest localized precipitation (Figure 2.15; Mangold et al. (2008); Chapter 3).

Impact-induced precipitation has been proposed to explain fluvial fans at Mojave Crater, but not yet modeled (Williams and Malin, 2008). Mojave is a fresh crater whose inner terraces are dissected by channelized fans that drain hillslopes. The young fans are very rare in the region surrounding the crater, suggesting that the Mojave impact triggered the fluvial activity that formed the fans (Williams and Malin, 2008). Several other Amazonian craters show Mojave-like fans, but they are more degraded (e.g., PSP_007447_1995 in Tartarus and PSP_008669_1905 in Isidis). Mojave has been described as a 'Rosetta Stone' for decoding impact-associated fluvial features on Mars, because it is relatively young and records with high fidelity processes that are degraded in the ancient record (Segura et al., 2008; Senft and Stewart, 2008; Toon et al., 2010).

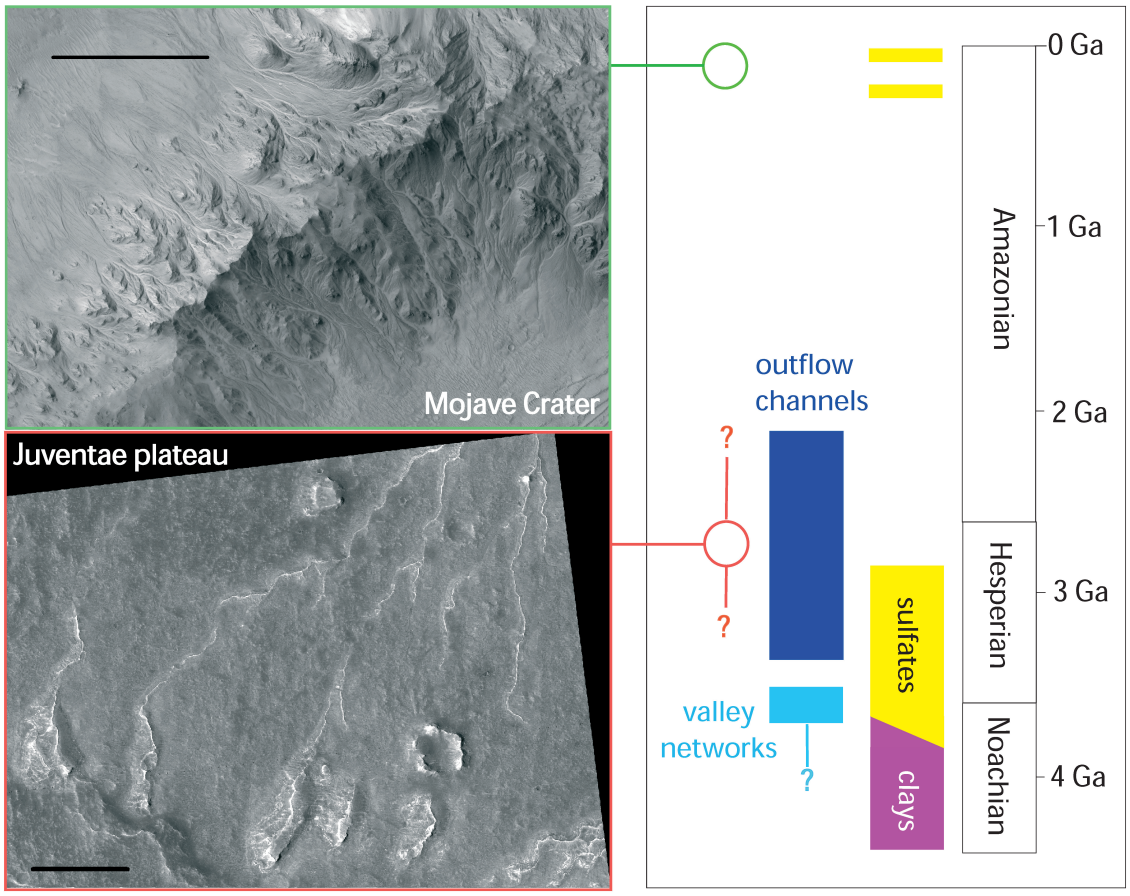

Figure 2.15 Primary motivation for this study: Two geological settings where fluvial activity postdates the Late Noachian - Early Hesperian acme of channel formation, and there is a candidate vapor source nearby. Scale bars are 500 m. *Green box:* Sub-kilometer fans resembling alluvial fans at Mojave Crater, which may be a recent impact into icy ground (7.9N 326.6E, orthorectified HiRISE image PSP_001481_1875). Channels dissect both sides of 100-200m tall ridge and channel heads are found $<$ 20m from ridgeline.; *Red box:* Inverted streams on plateau near Juventae Chasma (4.3S 296.7E, orthorectified HiRISE image PSP_003223_1755). Negligible post-Noachian erosion over most of the rest of the planet indicates that such events were localized. *Sources for stratigraphic context:* Hartmann (2005) (absolute ages); Murchie et al. (2009b) (clay and sulfate stratigraphy) Carr and Head (2010) (age of outflow channels); Fassett and Head (2008a) (age of valley networks); Massé et al. (2010) & Mangold et al. (2010) (existence of young sulfates); Le Deit et al. (2010) (age of Juventae plateau channels).

2.7.3 Can localized precipitation explain Noachian erosion?

Early Mars' geomorphic record strongly suggests that long-lived and regional/global precipitation contributed to Noachian erosion, but it is also consistent with a role for localized precipitation. The well-dated Late Noachian / Early Hesperian (Fassett and Head, 2008a; Hynek et al., 2010) peak in valley formation on Mars includes some integrated drainage networks extending over 1000s of km, that appear to have formed over a long period of time relative to crater formation (e.g., Barnhart et al. (2009)). Because localized precipitation on a cold planet is almost always short-lived precipitation (§2.1), these findings are not consistent with the model developed in this paper. In addition to this timescale problem, the rapid discharges and short formation timescales required to form some valley networks and deltas are at best marginally compatible with snowmelt (Kraal et al., 2008b; Kleinhans et al., 2010), and suggest ejecta dewatering or rain-phase precipitation. (Atmospheric liquid water aerosol is currently not included in our model.)

On the other hand, the majority of drainage systems on Early Mars are poorly integrated and localized, including most infilled crater floors and eroded crater rims. Inspired by observations at Mojave Crater (Williams and Malin, 2008), and supported by the results of the idealized model presented here, we suggest that localized precipitation is relevant to understanding these systems. Mars' deuterium-hydrogen ratio indicates that Mars has lost water over time (Jakosky, 1991). Therefore, crater lakes resulting from impacts into icy targets, wet-based ice sheets and lava-ice interactions would all have been more common on ancient Mars, and could serve as localized vapor sources. An Early Mars GCM with water sources at the valley-associated crater lakes shows precipitation only near the lakes and at planetary cold traps, consistent with our mesoscale results (Soto et al., 2010).

Any hypothesis for Early Mars erosion should explain the transition from significant crater infilling and crater rim erosion prior to the Noachian-Hesperian boundary, to minimal erosion in the Mid-Late Hesperian and Amazonian (as documented by, for example, Golombek et al. (2006); Forsberg-Taylor et al. (2004); Boyce and Garbeil (2007); Howard et al. (2005); Irwin et al. (2005a); Moore and Howard (2005)). In a localized precipitation scenario, this would correspond to a change in planetary target properties: an ice-rich crust before the erosional transition, and an ice-poor crust afterwards.

For impacts into a planetary crust containing buried ice layers, models suggest that fast-moving ice-rich debris flows cause crater infilling in the minutes after impact (Senft and Stewart, 2008). Therefore, we focus on relatively late-stage, relatively prolonged (hours to millennia) erosion of the inner slope of the crater rim.

Energy balance suggests that it is physically possible for localized precipitation to contribute to increased Noachian crater rim erosion. The energy source for the system is the heat of shocked target material. If the vapor source close to the crater center (fumarole, geyser or lake) can mine heat from deep within the shocked material, a sustained vapor source for years is possible, but the interval over which snow melts on contact with fresh ejecta on the rim is limited by conductive cooling of the surface boundary layer. However,

if snowmelt-fueled erosion removes the chilled boundary layer, hot material will again be exposed and melting can resume. Therefore, positive feedback between erosion and melting can sustain snowmelt-driven erosional activity on the crater rim. Snow can mine heat from deeper within the ejecta blanket provided that

$$(T_{\mathrm{b}} - 273.15)c_{\mathrm{b}} > \frac{Wt}{Rk}\left(L_{\mathrm{m}} + (273.15 - T_{\mathrm{sn}})c_{\mathrm{sn}}\right) \tag{2.14}$$

where Wt/Rk is the water:rock ratio required for erosion, L_{m} is the latent heat of melting, T_{sn} is snow temperature, and c_{sn} is snow heat capacity.

Ejecta blanket thickness is variable but lunar scalings suggest craters $>$ 160 km diameter have ejecta $>$ 0.6 km thick at their rim (McGetchin et al., 1973). Therefore, if ejecta temperature exceeds 900K, snow is continuously supplied at 1.25 mm/hr as found in our simulations, and the majority of eroded material is removed by debris flows with a W/R of 1.5, condition (14) is satisfied, and $>$ 0.6 km material can be eroded from the inner slope of the crater rim by localized precipitation within a decade.

This is directly relevant to three of the final four Mars Science Laboratory candidate landing sites. Gale (155 km diameter), Holden (155 km diameter), and Eberswalde (65 km diameter; immediately NE of Holden), because all three have deeply dissected rims showing evidence for aqueous transport of material from the rim to the crater floor (Anderson and Bell, 2010; Moore and Howard, 2005; Rice and Bell, 2010).

2.8 Conclusions

We conclude that:-

1. A low-pressure lake effect creates deep convection, rapid updrafts, and intense precipitation above cold liquid water surfaces on Mars. On Earth, because of much higher atmospheric pressure, this requires tropical temperatures.

2. We use MRAMS to simulate lake storms on Mars. The modeled storms have updraft velocities and plume heights which exceed the intensity of the strongest recorded thunderstorms on Earth.

3. The fraction of vapor that is trapped near the vapor source as localized precipitation increases with lake size.

4. The localized greenhouse effect of the released water vapor is too weak to cause melting of the snow.

5. Melting of equatorial, rapidly-emplaced localized snow with the albedo of dust is possible for a subset of orbital conditions, even with the present-day weak greenhouse effect.

6. Assuming that transient lakes on Mars are uncorrelated with orbital forcing, melting of rapidly-emplaced localized precipitation is more likely than melting of precipitation that has been emplaced in equilibrium with orbital conditions.

7. Taken together, localized storms, rapidly-emplaced localized precipitation, and favorable orbital conditions are an alternative to regional/global precipitation as one working hypothesis for (at least part of) the erosion and channel formation observed on pre-modern Mars.

2.9 Methods

Note: This section includes contributions from collaborator T.I. Michaels
The fully compressible dynamical core of MRAMS is derived from the terrestrial RAMS code, that has been adapted to Mars, as described in Rafkin et al. (2001). A cloud microphysical scheme derived from the Community Aerosol and Radiation Model for Atmospheres (CARMA; Toon et al. (1988)) was recently added to MRAMS, and we made use of these capabilities in Chapters 2 and 3. This cloud microphysics scheme has been used to successfully reproduce spacecraft observations of low-latitude clouds downwind of the Tharsis Montes and Olympus Mons (Michaels et al., 2006). A recent description of MRAMS capabilities is Michaels and Rafkin (2008). For the runs described in this paper, we use 20 bins in grain size for water ice aerosol. Minimum particle radius is 72.1 nm and the bins increase in mass with a fixed mass ratio of 7.2. For dust aerosol, we use 8 bins in grain size with the smallest particle radius being 50 nm and a ratio of 7.2 in mass between bins representing progressively larger grains. The initial atmospheric dust loading used by the cloud microphysics is taken from the General Circulation Model (GCM), and it is not replenished in any way throughout the MRAMS run. The initial dust number distribution is log normal with a mean radius of 1.5μm, and a geometric standard deviation of 1.8. Dust serves as water ice nuclei, and as such is scavenged during cloud formation. In addition to microphysically active dust, there is a static background dust loading that is only used to maintain nominal Mars dust opacity for the radiative transfer (RT) calculation. This background dust is based on MGS TES column dust opacity (Smith, 2004). Both the background dust and the microphysically-active dust are radiatively active.

Water ice microphysics are implemented using 18 mass bins (first mass bin corresponds to a particle radius of 0.072 μm), with the mass of each successive bin increasing by a factor of 7.2. The contact parameter for nucleation is 0.95. Microphysical dust and water ice particles are advected, gravitationally sedimented, and diffused in the model. The background dust is not altered in any way by any simulated physical process.

Atmospheric boundary and initial conditions, including dust and water vapor, are taken from the NASA Ames MGCM (Haberle et al., 1993) driven by present-day orbital parameters. The MGCM includes an active water cycle based on the microphysical scheme of

Colaprete et al. (1999) and is tuned appropriately to match the MGS-TES observed column water vapor and cloud ice abundance (Smith, 2004). Any water ice in the GCM is added to the GCM water vapor field, and this total water substance field is used by MRAMS. The mass of dust serving as nucleation cores for any GCM water ice aerosol is returned to the total GCM dust field and then used by MRAMS. Unlike the dry Martian climate which spins up rapidly within the MGCM, the water cycle requires several years or more of simulation to achieve stability. Therefore, data from the sixth Mars-year of the MGCM simulation is used.

The water ice and total dust (background plus microphysically-active) are treated as being radiatively active, using a two-stream radiative transfer algorithm based on Toon et al. (1989). The optical parameters for these aerosol particles were calculated with a Mie theory code. Aerosol particles were assumed to be spherical, and wavelength-dependent refractive indices were taken from measurements of water ice and Hawaiian palagonite.

We made minimal modifications to the MRAMS v.2.5-01 code to allow for surface liquid water. Liquid water microphysics is not included. Water vapor thermodynamics are included in the energy equation, but water vapor is not included in the mass and momentum equations – that is, we ignore pressure and virtual temperature effects. We do not permit dynamic dust lifting at the mesoscale.

Vertical resolution varied from 2.3 km at the top of the model to 30 m near the ground. We used four grids with the outermost being hemispheric and a horizontal resolution of $\sim$5.9 km on the inmost grid. Output was sampled every 1/24 sol ($\approx$ 3699 s), or 'Mars-hour.' We assume that this frequency, limited by available disk space, is enough to capture model behavior – for example, we refer to the warmest of 24 samples during a sol as the 'day's maximum temperature.' The timestep varied between runs but was never more than 3.75s on the inmost grid.

The season is southern summer (Ls $\sim 270^\circ$) for the runs, and boundary conditions are from the NASA Ames MGCM, version 2.1. We use present-day orbital conditions.

Our spinup procedure included 24 Mars-hours with no vapor release from the lake, 3 Mars-hours with vapor release but cloud microphysics off, and the remainder of the run with aerosol microphysics on. We observed that obvious spin-up transients had died away by the end of day 3. Snow albedo feedback was not considered, but would tend to increase the intensity of convergence and convective intensity by increasing the temperature gradient between land and lake.

Chapter 3

Chaos terrain, storms and past climate on Mars

This chapter was published as: Kite, E. S., S. C. R. Rafkin, T. I. Michaels, W. E. Dietrich, and M. Manga (2011), "Chaos terrain, storms and past climate on Mars," Journal of Geophysical Research, 116, E10002, doi:10.1029/2010JE003792.

Summary

We model the atmospheric response to a chaos-forming event at Juventae Chasma, northern Valles Marineris, Mars, using the Mars Regional Atmospheric Modeling System (MRAMS). Interactions between lake-driven convergence, topography, and the regional wind field steer lake-induced precipitation to the southwest. Mean snowfall reaches a maximum of 0.9 mm/hr water equivalent (peak snowfall 1.7 mm/hr water equivalent) on the SW rim of the chasm. More than 80% of vapor released by the lake is trapped in or next to the lake as snow. Radiative effects of the thick cloud cover raise mean plateau surface temperature by up to 18K locally. We find that the area of maximum modeled precipitation corresponds to the mapped Juventae plateau channel networks. At Echus Chasma, modeled precipitation maxima also correspond to mapped plateau channel networks. This is consistent with the earlier suggestion (Mangold et al., 2008) that Valles Marineris plateau layered deposits and interbedded channel networks result from localized precipitation. However, snowpack thermal modeling shows temperatures below freezing for the 12 mbar CO_2 atmosphere used in our MRAMS simulations. This is true even for the most favorable orbital conditions, and whether or not the greenhouse effect of the lake storm is included. Moderately higher CO_2 pressures, or non-CO_2 greenhouse forcing, is very likely required for melting and plateau channel network formation. Required warming is $\leq$10K – global temperatures need not be higher than today. In these localized precipitation scenarios, the rest of the planet remains dry.

3.1 Introduction

The highlands of Mars show both erosional and depositional evidence for past fluvial flow, and geochemical and textural evidence at Meridiani indicates these features were formed by liquid water (Malin and Edgett, 2003; Kraal et al., 2008a; Murchie et al., 2009b; Grotzinger et al., 2006; McLennan and Grotzinger, 2008). The distribution of fans and valleys with elevation, together with their morphology and inferred discharge, argue against groundwater as the sole source, and demand precipitation (Craddock and Howard, 2002; Carr and Head, 2003a, 2010; Hynek and Phillips, 2003). Three models may explain these observations. (1) A globally prolonged climate interval that intermittently allowed surface runoff is the most straightforward interpretation, and one that can draw on arid and polar Earth analogs (Pollack et al., 1987; Craddock and Howard, 2002; Forsberg-Taylor et al., 2004; Halevy et al., 2007; Barnhart et al., 2009). (2) Water vaporized by large impacts would briefly warm the global atmosphere, and precipitation from these transient water vapor greenhouse atmospheres could cut some valleys where there is evidence of rapid discharge (Segura et al., 2002, 2008; Kraal et al., 2008b; Toon et al., 2010). (3) Localized precipitation in a globally cold/dry atmosphere is an alternative to global wet conditions. Triggers for localized precipitation could include groundwater outbursts, volcanic plumes, or medium-sized impacts (Mangold et al., 2008; Segura et al., 2008). At least after the Noachian, valleys are patchily distributed (Williams, 2007; Weitz et al., 2008; Fassett and Head, 2008b; Hynek et al., 2010; Carr and Malin, 2000), which is consistent with localized precipitation.

Localized precipitation is especially attractive as an explanation for $\sim$ 3.0 Gya valleys exposed by aeolian erosion of layered deposits on the Valles Marineris plateau (Mangold et al., 2004; Weitz et al., 2008), and also $\sim$ 10 Mya fans at Mojave Crater (Williams and Malin, 2008). That is because these channels and fans postdate the sharp decline in globally-averaged erosion rates, aqueous alteration, and channel formation near the Noachian - Hesperian boundary (Murchie et al., 2009b; Fassett and Head, 2008a; Golombek et al., 2006). The rarity of channels, fans, fluvial erosion, or aqueous minerals of similar age suggests that the Valles Marineris plateau channel networks and Mojave Crater fans do not record global episodes of surface runoff. Localized precipitation is an alternative, with vapor sourced from a transient event such as groundwater release during chaos terrain formation (at Valles Marineris) or partial melting of an ice-silicate mixture during impact (at Mojave Crater). Simulations relevant to impact-induced localized precipitation have been reported in several conference abstracts (e.g., Segura and Colaprete (2009)) and a thesis chapter (Plesko et al., 2009). Baker et al. (1991) suggests that vapor release during outflow channel formation has global effects. Valles Marineris localized precipitation has been suggested previously (Gulick and Baker, 1989; Baker et al., 1991; Mangold et al., 2008; Williams and Malin, 2008), and Santiago et al. (2005, 2006) report preliminary Global Circulation Model (GCM) simulations of atmospheric response to outflow channel flooding. Mesoscale effects of the outflow response have not been studied previously.

Here we investigate the well-preserved layered deposits with interbedded channel net-

works on the Valles Marineris plateau west of Juventae Chasma (Malin et al., 2010; Weitz et al., 2010). Our goal is to understand these deposits and use them as a proxy for past Mars climate. Our approach iterates between modeling and geology. The Juventae plateau networks include "hillslope rills and low-order streams," leading Malin et al. (2010) to describe them as "the best evidence yet found on Mars to indicate that rainfall and surface runoff occurred." In §3.2-3.3, we summarize geologic observations: some constitute boundary conditions for the model, others are targets that the model must reproduce in order to be considered successful. In §3.4 we analyze results from Mars Regional Atmospheric Modeling System (MRAMS, Rafkin et al. (2001); Michaels et al. (2006)) simulations of chaos flood-effect precipitation that include detailed cloud microphysics (§2.9). We find excellent agreement between the model-predicted precipitation locations and the previously-mapped area of layered deposits and inverted channel networks (statistical analysis in §3.10.1). In this chapter, we concentrate on what controls the rate and location of precipitation. Chapter 2 describes idealized simulations of cloud formation and precipitation in a thin, cold atmosphere perturbed by a lake. Precipitation in our model falls as snow, but the geologic observations demand liquid water runoff. Snowpack melting on the Juventae plateau will occur under certain combinations of orbital parameters and snowpack physical properties. These are determined (§3.5, §3.10.2) by running a simple snowpack thermal model over all seasons, pressures from 12-195 mbar, all relevant solar luminosities, and for the full range of orbital conditions sampled by the chaotic diffusion of Mars' orbital parameters (Laskar et al., 2004). We calculate the probability that snowpack melting will occur as a function of solar luminosity and additional greenhouse effect. In §3.6, we evaluate multiple working hypotheses for the mechanism of channel formation against measurements from our HiRISE Digital Terrain Models (DTMs; §3.10.3). These measurements are from a small number of key localities on the Juventae Plateau. We do not attempt a comprehensive geologic analysis. Finally we test the localized-precipitation hypothesis at a second site, Echus Chasma (§3.7), and discuss the implications of our results for global excursions to conditions warmer than the present-day on Hesperian Mars (§3.8).

3.2 Geologic constraints: Valles Marineris plateau channel networks

The Valles Marineris plateau layered deposits are distinct from layered deposits elsewhere on Mars (Weitz et al., 2008; Murchie et al., 2009b; Weitz et al., 2010). Dendritic channels with both positive and negative relief are commonly found in association with the plateau layered deposits (Malin and Edgett, 2003; Edgett, 2005; Williams et al., 2005), with preserved drainage densities as high as 15 km^{-1} and commonly >1 km^{-1}. In contrast, most Mars light-toned layered deposits (LLD) have few or no channels visible from orbit. Channels at different levels within the plateau layered deposits crosscut one another (Weitz et al., 2010).

This requires that plateau channel formation was either interspersed with, or synchronous with, the depositional events that formed the layers. It suggests a common geologic scenario for plateau channel formation and plateau layered deposit formation. Opal (± hydroxylated ferric sulfate) has been reported in the plateau layered deposits (Milliken et al., 2008; Bishop et al., 2009), whereas most Mars LLD show sulfate (± hematite ± phyllosilicates) (Murchie et al., 2009b). Plateau layered deposits show no evidence for regular bedding. Most LLD, in contrast, give the visual impression of quasi-periodic bedding, and this has been statistically confirmed at many locations (Lewis et al., 2008, 2010). Because the most likely pacemaker for quasi-periodic sedimentation is orbital forcing (Kuiper et al., 2008; Lewis et al., 2008), this suggests the process that formed the plateau layered deposits was not sensitive to orbital forcing. Either stochastic processes controlled deposition, or deposition timescales were much shorter than orbital timescales (Lewis et al., 2010). The deposits are $O(10^1)$m thick (Weitz et al., 2010), in contrast to the $O(10^3)$m of sulfate-bearing deposits within craters and canyons. Opaline plateau layered deposits overly early Hesperian lavas, placing them among the youngest classes of aqueous minerals on Mars (Murchie et al., 2009b). They significantly postdate the maximum in valley formation during the Late Noachian – Early Hesperian (Le Deit et al., 2010). Taken together, these differences suggest the process which formed the Valles Marineris plateau layered deposits differed from that forming layered deposits elsewhere on Mars (Murchie et al., 2009b).

Plateau layered deposits and inverted channels formed over an extended interval of time. Tilted channels are present on downdropped fault blocks (Le Deit et al., 2010), and some channels are truncated by chasm edges - therefore, some channels formed before backwasting of the chasm to its present day form. Multiple periods of runoff are recorded on the plateau (Weitz et al., 2010).

These observations raise several questions. What was the process that formed the plateau layered deposits? What was the source of the water for channel formation, and what permitted surface liquid water at this location? Does this require atmospheric pressures, temperatures, or water vapor loading different from contemporary Mars – and if so, are the required changes global, regional or local? What were the mechanics of channel formation - for example, are these mechanically-eroded or thermally-eroded channels? Our focus in this chapter is on the first three questions. We briefly discuss channel formation mechanisms in §3.6.

Channels are usually found on plateaux immediately adjacent to chasms. Location on a plateau immediately adjacent to a chasm apparently provided a driver (limiting factor) for channel formation and/or preservation (Figure 3.1, top panel). For example, the Echus, Juventae and Ganges plateau channel networks are all immediately West (downwind) of inferred paleolakes (Figure 3.2; Coleman and Baker (2007); Harrison and Grimm (2008)). A relief-elevation plot confirms, independently, that all light-toned layered deposits are on the plateau near the edge of a chasm (Figure 3.2). To form, a channel requires water supply sufficient to balance continuous losses to infiltration and evaporation, while generating runoff. Runoff must encounter sediment that is fine-grained enough to be mobilized. Inverted channels have additional requirements: to be exposed at the surface today, an inverted channel must be preferentially cemented or indurated, and then incompletely eroded. Therefore, there are five potential limiting factors for inverted channel formation: - heat, water, sediment, cementing fluids, or erosion. Location downwind of a chasm should logically supply at least one.

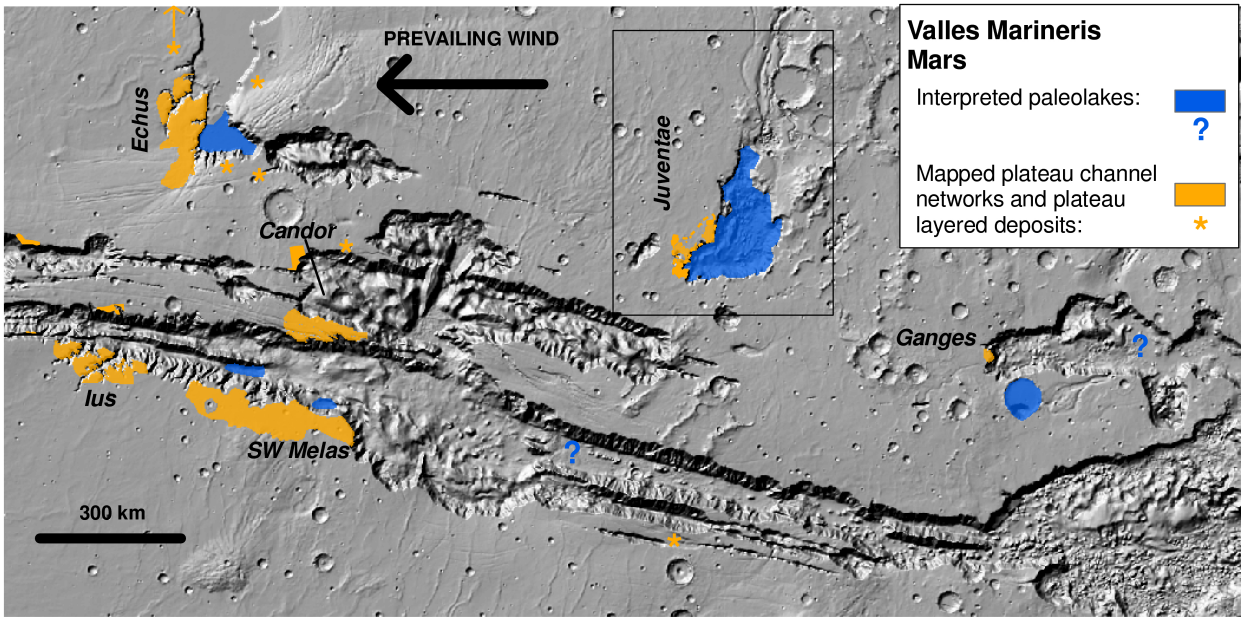
PREVAILING WIND
Echus
Juventae
Candor
Ganges
Ius
SW Melas
300 km
Valles Marineris
Mars
Interpreted paleolakes:
?
Mapped plateau channel
networks and plateau
layered deposits:

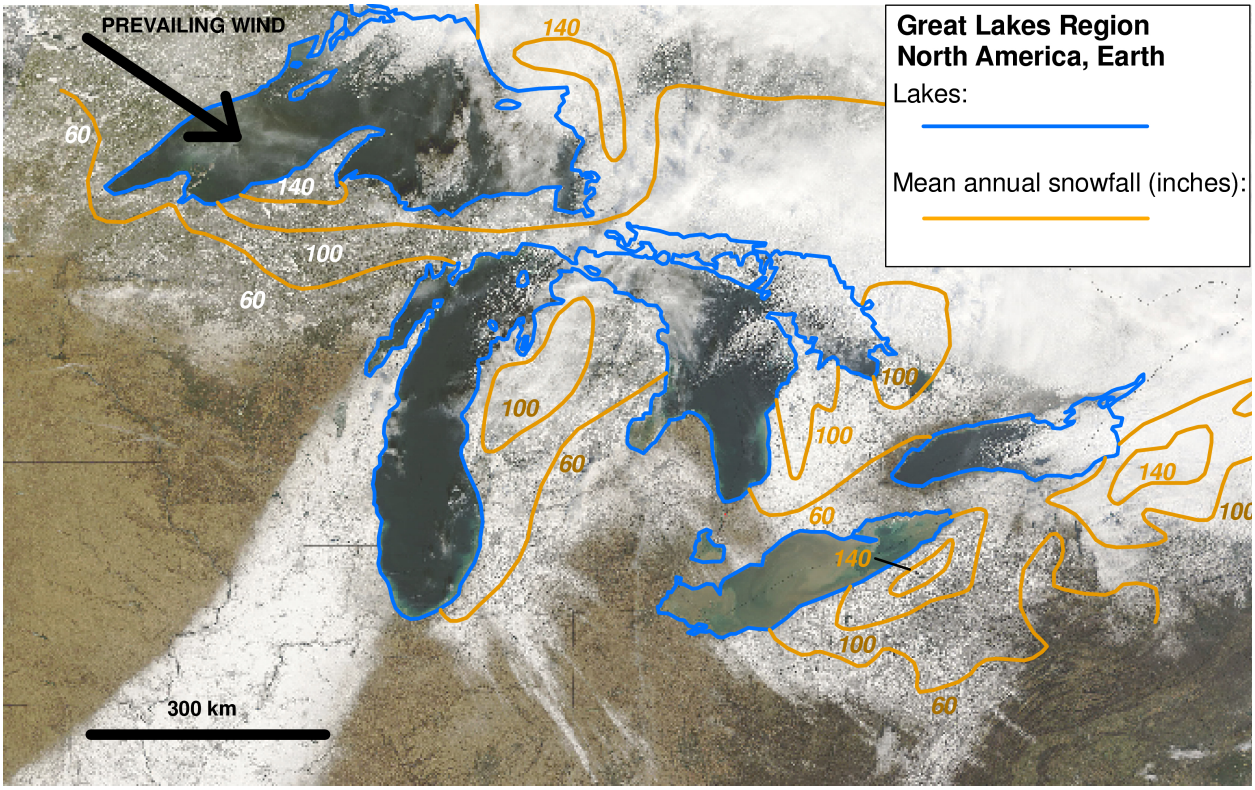
PREVAILING WIND
140
60
140
100
60
100
60
100
100
60
140
60
140
100
100
60
300 km
Great Lakes Region
North America, Earth
Lakes:
Mean annual snowfall (inches):

Figure 3.1 (Upper panel) Location of Valles Marineris plateau layered deposits and plateau channel networks downwind of paleolakes. Reported plateau layered deposits and channel networks are shown by orange shading. Asterisks correspond to isolated, or incompletely mapped, occurrences. Reported paleolakes are shaded in blue: those where we consider the evidence to be less strong are shown by question marks. Box around Juventae corresponds to Figure 3.4. Background is MOLA shaded relief. Sources:- Weitz et al. (2010) (SW Melas, S Ius, S flank W Candor, Juventae and Ganges layered deposits); Le Deit et al. (2010) (N Ius, N flank W Candor, N Tithonium and Juventae layered deposits) Mangold et al. (2008) (Echus networks); Williams et al. (2005) (Candor channel); Harrison and Grimm (2008) (questionable Candor lake); Harrison and Chapman (2008) (Juventae and Echus lakes); Metz et al. (2009a) (SW Melas lake); Roach et al. (2010) (Ius closed evaporitic basin); Komatsu et al. (2009) (Morella lake); Carr (1995) (questionable Ganges lake). (Lower panel) Location of snowbelts downwind of the Great Lakes, North America, Earth. Each local maximum in mean annual snowfall, as shown by orange contours, is downwind of a lake. Snowbelts form from the cumulative effect of lake-effect storms. Contours are from (Eichenlaub, 1979), as reproduced in Markowski and Richardson (2010). The prevailing wind direction is shown by the black arrow and the snow streaks in the background image. Background image was acquired 9 December 2006 by Terra/MODIS and shows the effects of a lake-effect storm on 7-8 December 2006 (image credit: NASA GSFC/Earth Observatory).

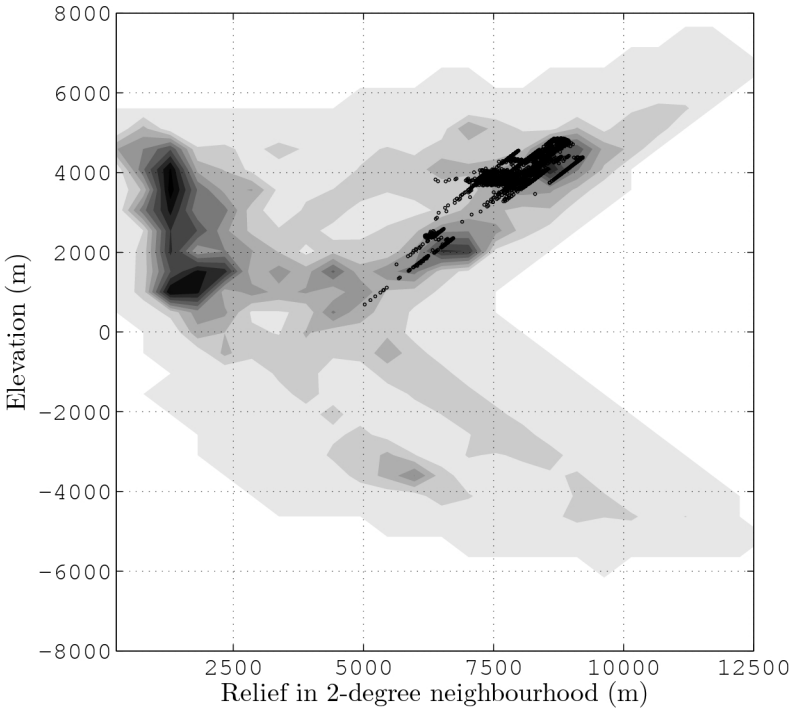

Figure 3.2 Topographic context of inverted channels. Black dots correspond to points mapped as 'light-toned layered deposit' or 'inverted channel' by Weitz et al. (2010). The association of inverted channels with light-toned layered deposits containing opal ± jarosite is only found near the rims of large canyons. Grayscale background is the probability distribution of all points, using a bin size of 500m. Relief at a point is defined as the maximum difference in elevation between that point and all other points in a neighborhood with 2-degree radius. (Points with intermediate elevation cannot have high relief with this definition.)

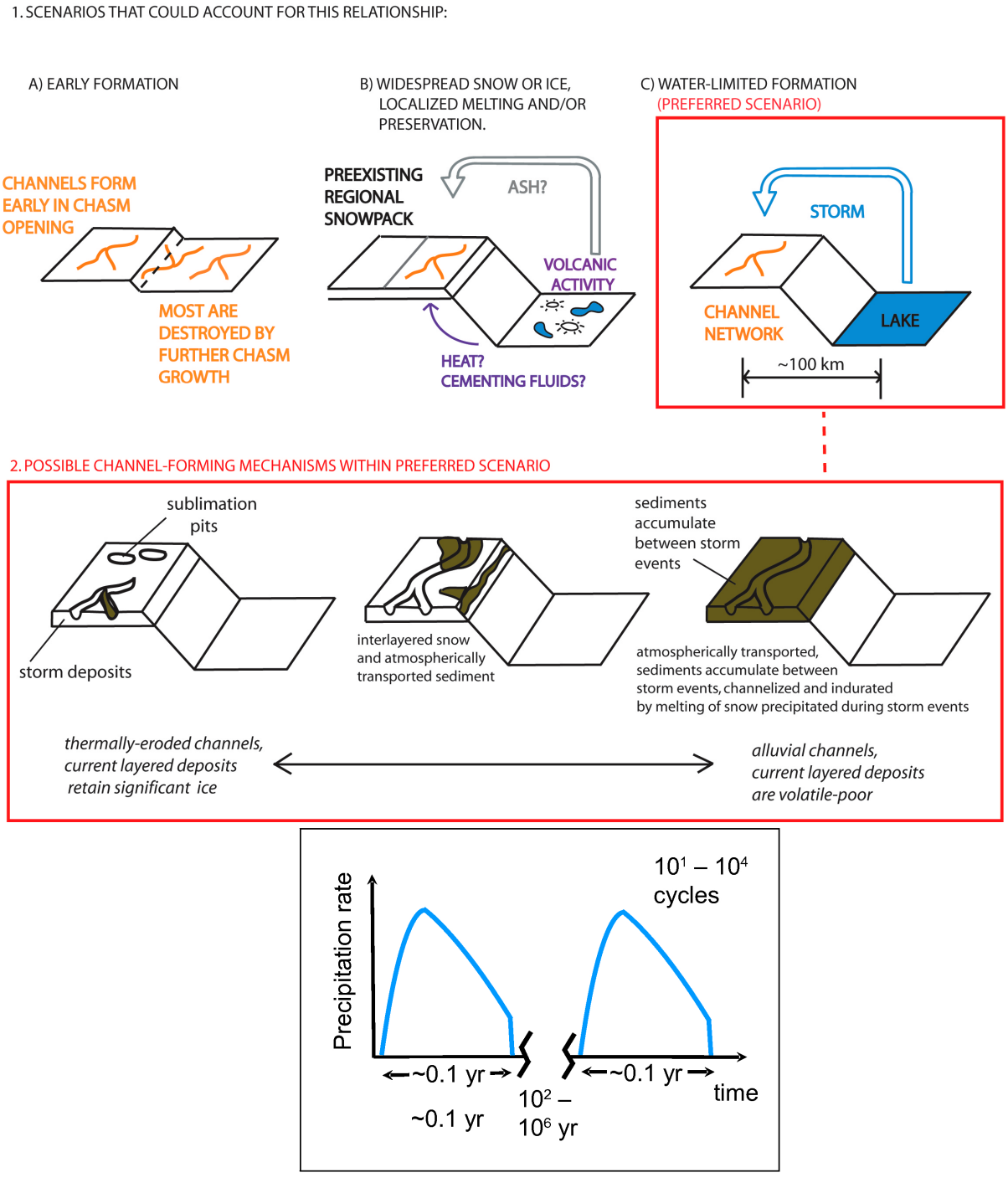
1. SCENARIOS THAT COULD ACCOUNT FOR THIS RELATIONSHIP:
A) EARLY FORMATION
CHANNELS FORM EARLY IN CHASM OPENING
MOST ARE DESTROYED BY FURTHER CHASM GROWTH
B) WIDESPREAD SNOW OR ICE, LOCALIZED MELTING AND/OR PRESERVATION.
PREEXISTING REGIONAL SNOWPACK
ASH?
VOLCANIC ACTIVITY
HEAT? CEMENTING FLUIDS?
C) WATER-LIMITED FORMATION (PREFERRED SCENARIO)
STORM
CHANNEL NETWORK
LAKE
~100 km
2. POSSIBLE CHANNEL-FORMING MECHANISMS WITHIN PREFERRED SCENARIO
sublimation pits
storm deposits
interlayered snow and atmospherically transported sediment
sediments accumulate between storm events
atmospherically transported, sediments accumulate between storm events, channelized and indurated by melting of snow precipitated during storm events
thermally-eroded channels, current layered deposits retain significant ice
alluvial channels, current layered deposits are volatile-poor
Precipitation rate
$10^1 – 10^4$ cycles
~0.1 yr
~0.1 yr
$10^2 – 10^6$ yr
time

Figure 3.3 From geologic relations (§3.2), we infer that the formation of plateau channel networks and plateau layered deposits is related to chasm opening (and associated flooding). Top panel: Sketch of scenarios that could account for this relationship. In our preferred scenario, condensation of vapor released from short-lived lake in chasm creates a snowstorm. Precipitation on the plateau next to the chasm forms channel networks. Precipitation falling back into the lake leaves no geomorphic signature. Several possible channel–forming mechanisms (middle panel) are consistent with the preferred scenario. Bottom panel: Timescales implied by published models of chaos hydrology and the thermodynamics of lake freezing: each lake event lasts $\leq$1 year (Andrews-Hanna and Phillips, 2007; Harrison and Chapman, 2008). Crosscutting channels, and discharge estimates from measurements of inner channels, require that many flood events occurred in each chaos chasm. Estimates of repose interval between groundwater outflow events center on 10^2 - 10^6 years, and are considered to lengthen with time, but are sensitive to poorly-known crustal hydrologic properties (Andrews-Hanna and Phillips, 2007; Harrison and Chapman, 2008).

We hypothesize that the Juventae, Echus and Ganges plateau channel networks and layered deposits formed downwind of ephemeral chaos lakes, through precipitation from lake-effect storms (Chapter 2, Figure 3.3). In our hypothesis, rain or snow from nearby lakes is the limiting factor for forming plateau channels and light-toned deposits - explaining the spatial association between chasm lakes and plateau channels/light-toned deposits. This is analogous to the 'snowbelts' that form downwind of the Great Lakes of N America from the cumulative precipitation of lake-effect storms (Figure 3.1, bottom panel). Our hypothesis predicts that simulations of lake-effect storms in Valles Marineris should produce precipitation that is localized to the chasm rim and in the observed locations. We test our hypothesis at Juventae Chasma, because it has the best-preserved plateau channels and the geologic evidence for a paleolake there is also compelling (Coleman and Baker, 2007; Harrison and Grimm, 2008). Other possible scenarios for forming plateau channels and plateau layered deposits (Figure 3.3) are discussed in §3.6.

3.3 Geologic constraints: Boundary conditions at Juventae Chasma

Juventae Chasma has a spillway at $\approx +1$ km elevation that is connected to the Maja Vallis outflow channel (Catling et al. (2006); Coleman and Baker (2007); Figure 3.4). The deepest point of Juventae Chasma is below -4 km. Insofar the chasm was formed by fluvial or debris-flow transport of sediment across the spillway, this suggests that a lake many km deep existed at least once in Juventae Chasma (Coleman and Baker, 2007). Evidence that multiple outbursts cut Maja Vallis also suggests that Juventae Chasma was flooded multiple times (Harrison and Chapman, 2008).

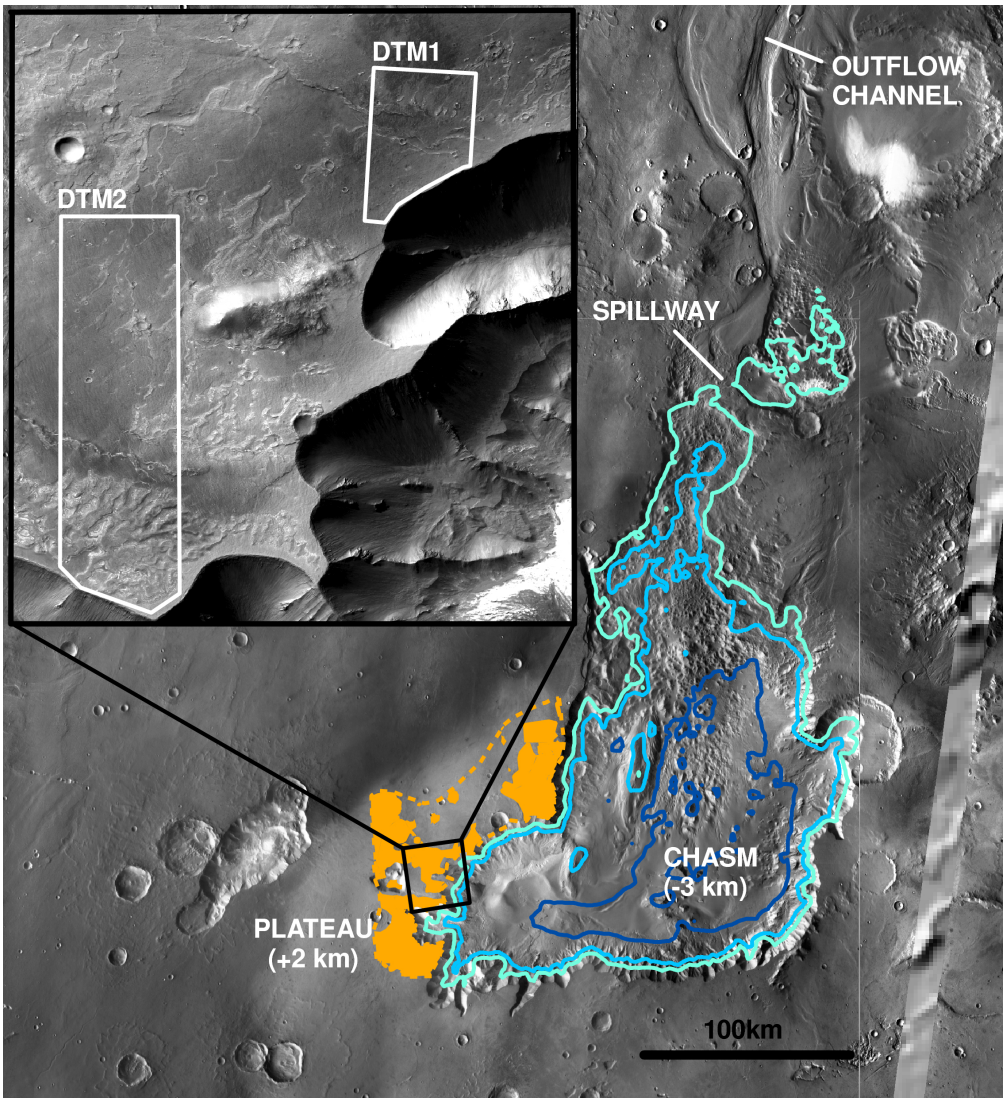

Figure 3.4 Site for our hypothesis test – Juventae. Juventae Chasma is a 5 km deep, sharp-sided chaos chasm that sources Maja Valles (outflow channel to N). *Main image:* Orange shading corresponds to the area of plateau channel networks and plateau layered deposits mapped by Le Deit et al. (2010). Orange dotted line corresponds to pre-erosion extent estimated by Le Deit et al. (2010) from outliers. Spillway to N of chasm indicates that flood level exceeded +1180m. We model flooding to depth -3000m (deep blue), -1000m (mid blue) and +0m (cyan). Main figure background is THEMIS VIS mosaic. *Inset image* shows the locations of 2 HiRISE DTMs that we constructed (§3.10.3) to characterize the inverted channel networks. Inset background is part of CTX image P18_007983_1751_XN_04S063W.

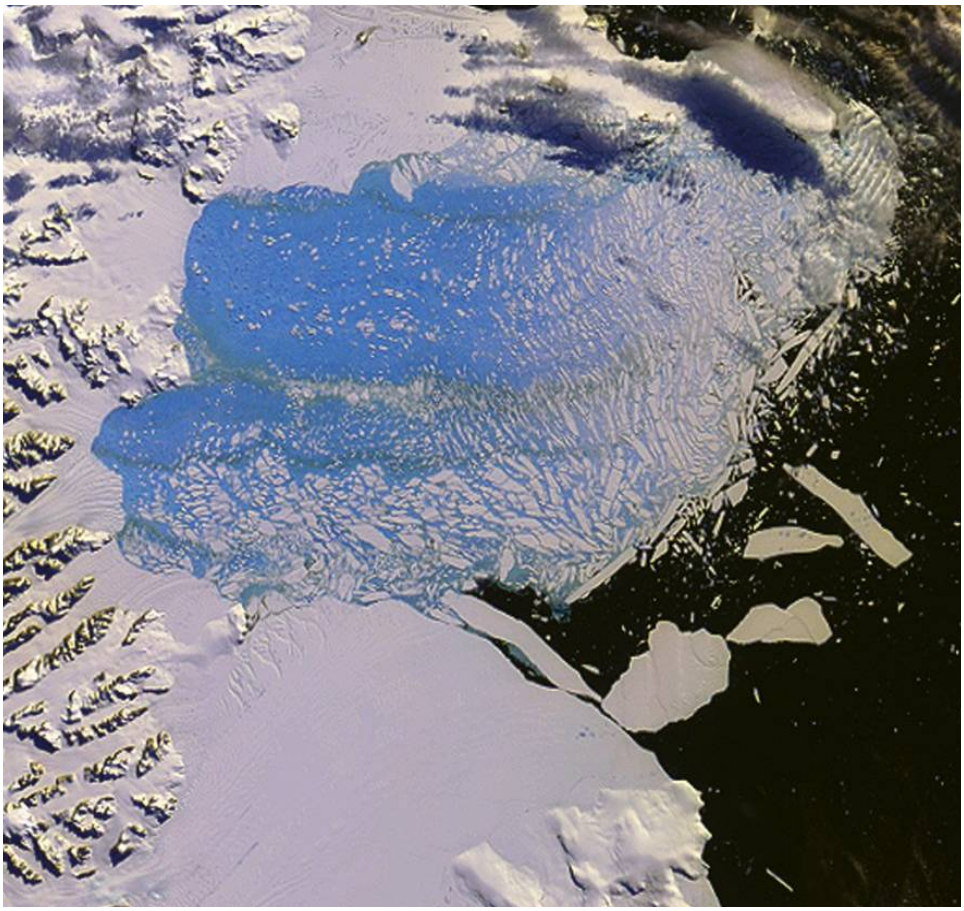

Figure 3.5 Disintegration of Antarctica's Larsen B ice shelf. Collapsed area is $\sim$3000 km^2. Acquired 7 March 2002 by Terra/MODIS. Image credit: NASA/GSFC.

The duration of surface liquid water during groundwater outburst floods is unknown. It will depend partly on the peak discharge, which is set by the permeability of the source aquifer - another unknown. Harrison and Grimm (2008) calculate a duration of 0.1 – 10^5 days per event, with $\leq$5 x 10^3 days per event preferred. The corresponding peak discharge rates are 3 x 10^5 – $>10^8$ m^3s^{-1}. When discharge falls below the evaporation rate, icing-over of the lake surface is increasingly likely. For the 140 km-diameter cylindrical chaos modeled by Harrison and Grimm (2008), and an evaporation rate of 2 mm/hr, the cryosphere fractures are frozen shut before the discharge falls below the evaporation rate. Alternatively, surface liquid water in a chaos terrain can be generated by failure of a dam confining an ice-covered lake, leading to mechanical disruption of the ice cover. For example, the 2002 stepwise collapse of Antarctica's Larsen B ice shelf took 3 weeks, with open water between collapsed ice blocks (Figure 3.5).

Boundary conditions are as follows. We impose a lake temperature of 278.15K (5°C), which is midway between dissipative throttling (Joule-Thompson) heating of aquifer water initially at 5km, and two-phase hydrostatic ascent (Gaidos and Marion, 2003). However, for the largest lake simulated (`juventae_high`, Table 3.1), we set lake surface temperature to 273.15K (0°C). This is because the high latent-energy flux associated with a relatively high temperature and a large lake area caused numerical instabilities in the model. We hold lake temperature steady. This is a reasonable assumption if the atmospheric response timescale (hours-days) is shorter than the timescale over which the chaos flood hydrograph changes, or if surface water continuously pours over the spillway, allowing the surface layer to be refreshed by warmer water from depth (see discussion in §3.4.1). Wind-dependent lake surface roughness is from equation 7.21 of Pielke (2002). The inverted streams at Juventae required surface liquid water to form, but currently the low atmospheric pressure at plateau elevation (+2 km) makes surface liquid water unstable (Conway et al., 2011). Therefore, we doubled initial and boundary pressure throughout our simulation. We will show later (§3.5) that still higher pressures are probably needed to suppress evaporative cooling and allow melting. We use present-day topography in our model, apart from flooding to the lake level within Juventae Chasma[1]. We use present-day solar luminosity in our precipitation model (but not in our melting model; §3.5). This is conservative in terms of localized precipitation, because lower atmospheric temperatures favor localized precipitation (Chapter 2). Apart from the more–realistic topographic boundary conditions, the MRAMS setup is essentially the same to that described in §2.9.

[1]A minor exception is that we remove the sulfate-bearing (Bishop et al., 2009; Catling et al., 2006) light-toned layered deposits from within the chasm, which would otherwise form islands in our ephemeral lake. This is because we agree with the geologic interpretation that these deposits largely postdate chasm formation (Murchie et al., 2009a), although there is disagreement on this point (Catling et al., 2006). The change has no effect on our best-fit model (`juventae_high`) because, in our smoothed topography, the lake level in `juventae_high` is higher than the summits of the sulfate-bearing light-toned layered deposits.

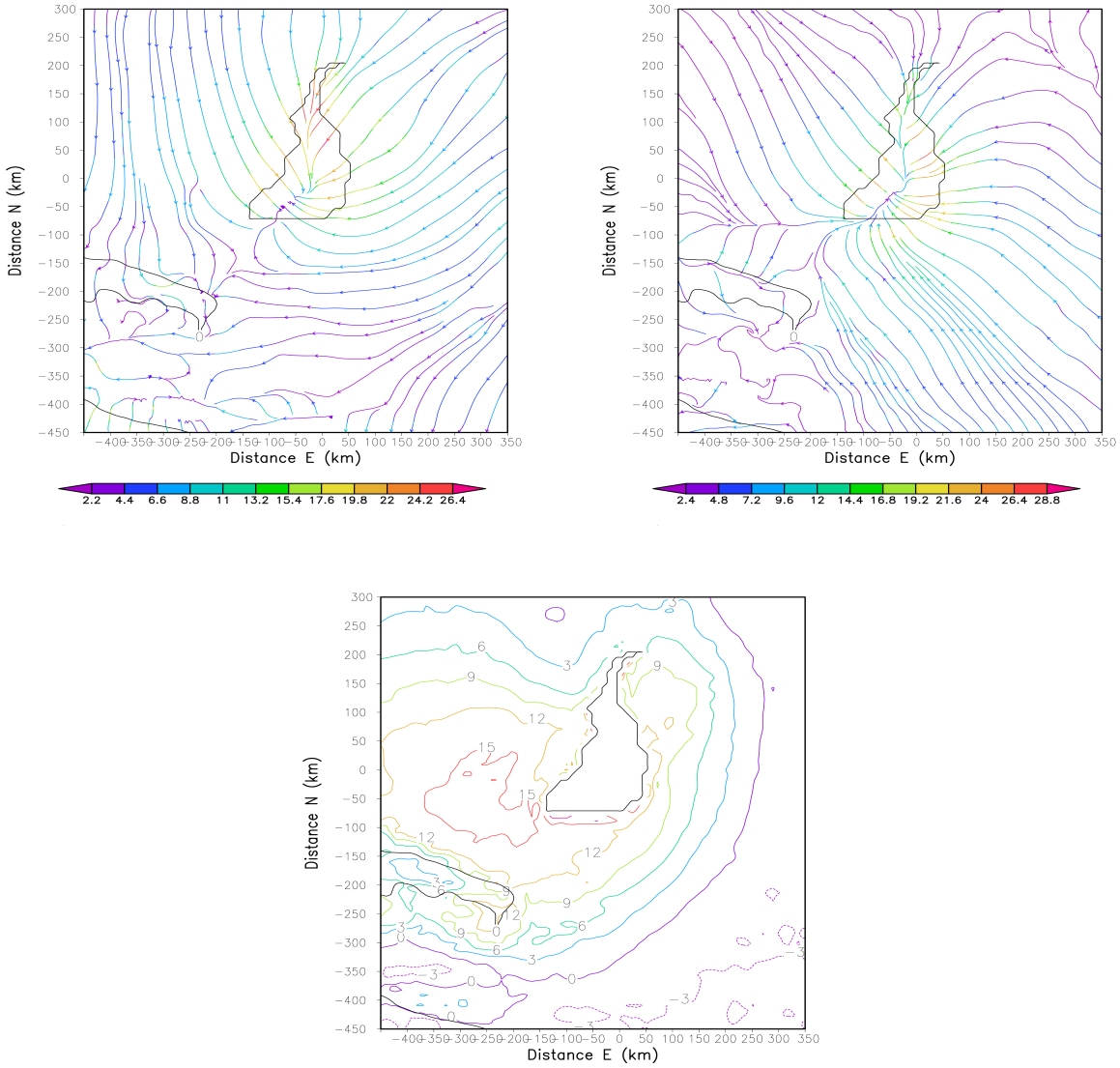

Figure 3.6 Temperature and wind field at Juventae in our best-fit lake simulation (`juventae_high`). 0m contour (black) defines canyons. Top left panel: Net time-averaged wind at 13m elevation. Overall Easterly & South-Easterly winds are reversed at Juventae Chasma because of the lake-driven circulation. Top right panel: Change in wind field due to the lake (differencing dry and wet runs). Lake storm drives low-level convergence of up to 30 m s^{-1}. Magnitude of lake-driven circulation is comparable to magnitude of non-lake circulation. Bottom panel: Temperature difference due to lake. Temperature increases by up to 18K downwind of lake. Axis tick labels correspond to distance from 3.91S 298.53E, near the lake center (Average over 3 sols, from Mars-hours 49 to 121).

3.4 Juventae mesoscale model: precipitation output

This chapter reports the results of model runs that vary lake temperature and lake level (Table 3.1), holding orbital elements and obliquity at present-day values and fixing the season at simulation start to southern Summer (Ls $\sim$ 270). An MRAMS run simulating 7 sols at Valles Marineris takes $\sim$0.5 years to complete, so we are limited in the number of parameters we can vary. In addition, we must rerun the General Circulation Model (GCM) that supplies the mesoscale boundary conditions if we wish to model a major change in pressure or dust loading. This limits the range of sensitivity tests we can practicably apply. Chapter 2 describes a wider range of sensitivity tests.

Table 3.1 Valles Marineris simulations: list of runs with parameters

Run	Full Name	Lake Level (m)	Lake Temperature (K)	Lake Area (km^2)	Description
JUVENTAE_DRY	juventae_Mar_12_2010	–	–	–	Valles Marineris topography, no lake
JUVENTAE_HIGH	juventae_May_12_2010	+0	273.15	25800	At spillway
JUVENTAE_MED	juventae_Mar_13_2010	−1000	278.15	19400	Almost fills chasm
JUVENTAE_LOW	juventae_Mar_14_2010	−3000	278.15	6400	In SE corner of chasm
ECHUS_LOW	echus_Apr_52010	−900	278.15	3600	Small equant lake
ECHUS_HIGH	echus_Mar_25_2010	−800	273.15	17100	At spillway, elongated N–S

3.4.1 Analysis of best-fit model

Lake-driven convergence. The lake perturbation to the atmosphere is superimposed on the complex, topographically driven Valles Marineris mesoscale windfield (Rafkin and Michaels, 2003; Spiga and Forget, 2009). Strong slope winds are seen at Juventae Chasma in the `juventae_dry` run, as previously described (Rafkin and Michaels, 2003; Spiga and Forget, 2009). The diurnal cycle of upslope daytime winds and downslope nighttime winds is broken by the lake, which drives low-level convergence strong enough to overcome the upslope daytime wind (Figure 3.6b). At altitudes <6 km, the convergence is toward a sheet-like time-averaged updraft running along the lake's long axis (N-S), and concentrated in the southern half of the lake. Above 10 km, wind moves out from this updraft. East-directed outflow encounters the west-directed prevailing wind and slows, allowing more time for ice crystals to precipitate out before reaching the chasm edge. West-directed outflow is much faster. Above 20 km, the windfield is increasingly dominated by radial flow away from a narrow, cylindrical updraft in the center of the lake. Lake storm effects on the background windfield are minor above 40km. A copious supply of water vapor, the availability of dust for ice nucleation, water vapor and cloud radiative effects, and induced low-level convergence combine to drive continuous precipitation.

Radiative effects. Mean temperature rises by 17K downwind of the lake, where icy scatterers have precipitated but the greenhouse effect of vapor remains (Figure 3.6c). There is a

broad region of >5K warming. On average, downwelling longwave radiation increases by 60 W m^{-2} SW of the deep pit that lies W of S Juventae. Ice cloud scattering partly compensates for this during the day, but maximum temperature also rises, by up to 8K, which is important for melting (§3.5). However, in the area of greatest modeled precipitation, maximum temperature is reduced by up to 3K because of the locally high atmospheric ice column abundance.

Water vapor and ice column abundance. The time-averaged water vapor column abundance (Figure 3.7a) shows that high vapor abundances are confined to the canyon. Ascent of vapor-laden parcels up canyon walls aids crystallization, and (ice column mass):(total water column mass) ratio increases from typically <50% within Juventae Chasma to 60-70% on the plateau. Vapor is most abundant at low elevations. Peak precipitable vapor column abundance is ∼0.27 cm and is located slightly SW of the lake's areal centroid. The peak in time-averaged ice column abundance (Figure 3.7b) is shifted 30km further WSW. This is the product of plume ascent timescales and the WSW-directed background wind speed (Chapter 2). Falloff of ice column abundance with distance from this peak is almost symmetric. This is because the outward-directed pressure gradient at the top of the buoyant plume is much stronger than that driving the background wind field. Maximum water ice column abundances away from the lake are above a promontory jutting into the lake on the SW edge of the chasm, and along the S edge of the chasm. These also correspond to the highest values of precipitation, as discussed below and shown in Figures 3.8, 3.9 and 3.10.

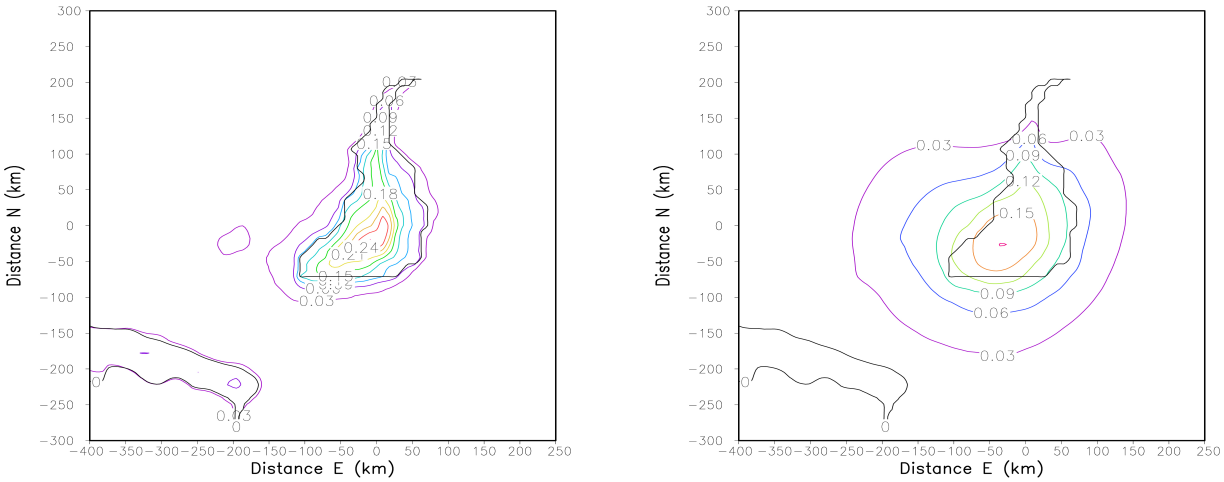

Figure 3.7 Ice and vapor columns at Juventae Chasma. Left panel: Time-averaged precipitable vapor column abundance in cm water equivalent. Right panel: Time-averaged precipitable ice column abundance in cm water equivalent. (`juventae_high`, average for 3 sols, from Mars-hours 49 to 121).

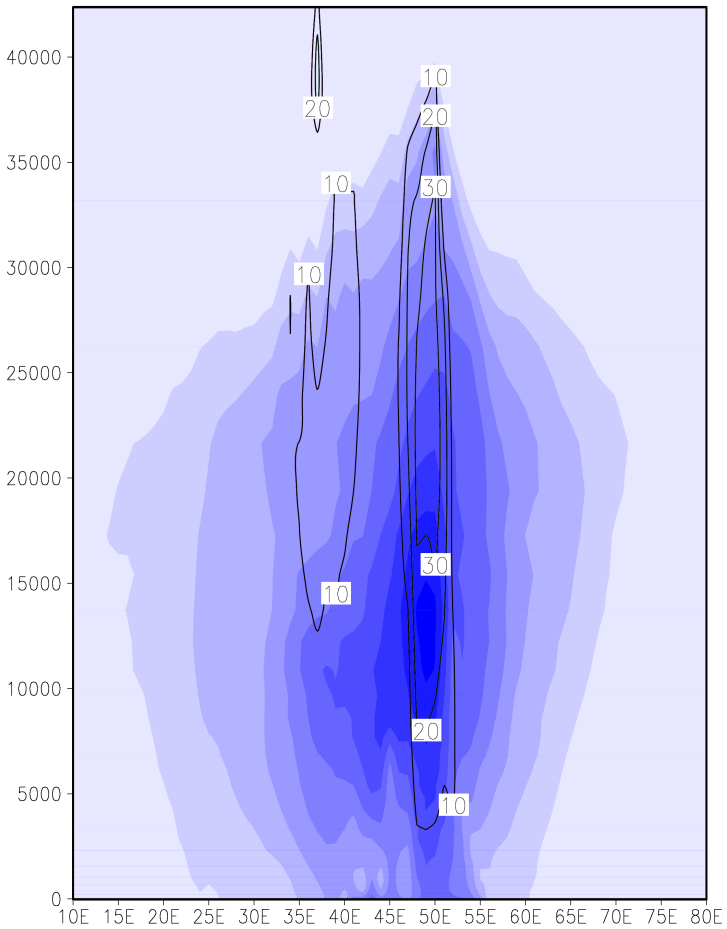

Figure 3.8 E-W cross section through lake storm. Blue tint corresponds to increasing water ice fraction (interval 0.001, maximum value 0.009). Labeled contours correspond to bulk vertical velocity in m s^{-1}, which are comparable to the most intense supercell storms on Earth. The y-axis is vertical distance in m. The x-axis is horizontal distance: 10 units = 83 km. Lake extends from 41E to 55E on this scale.

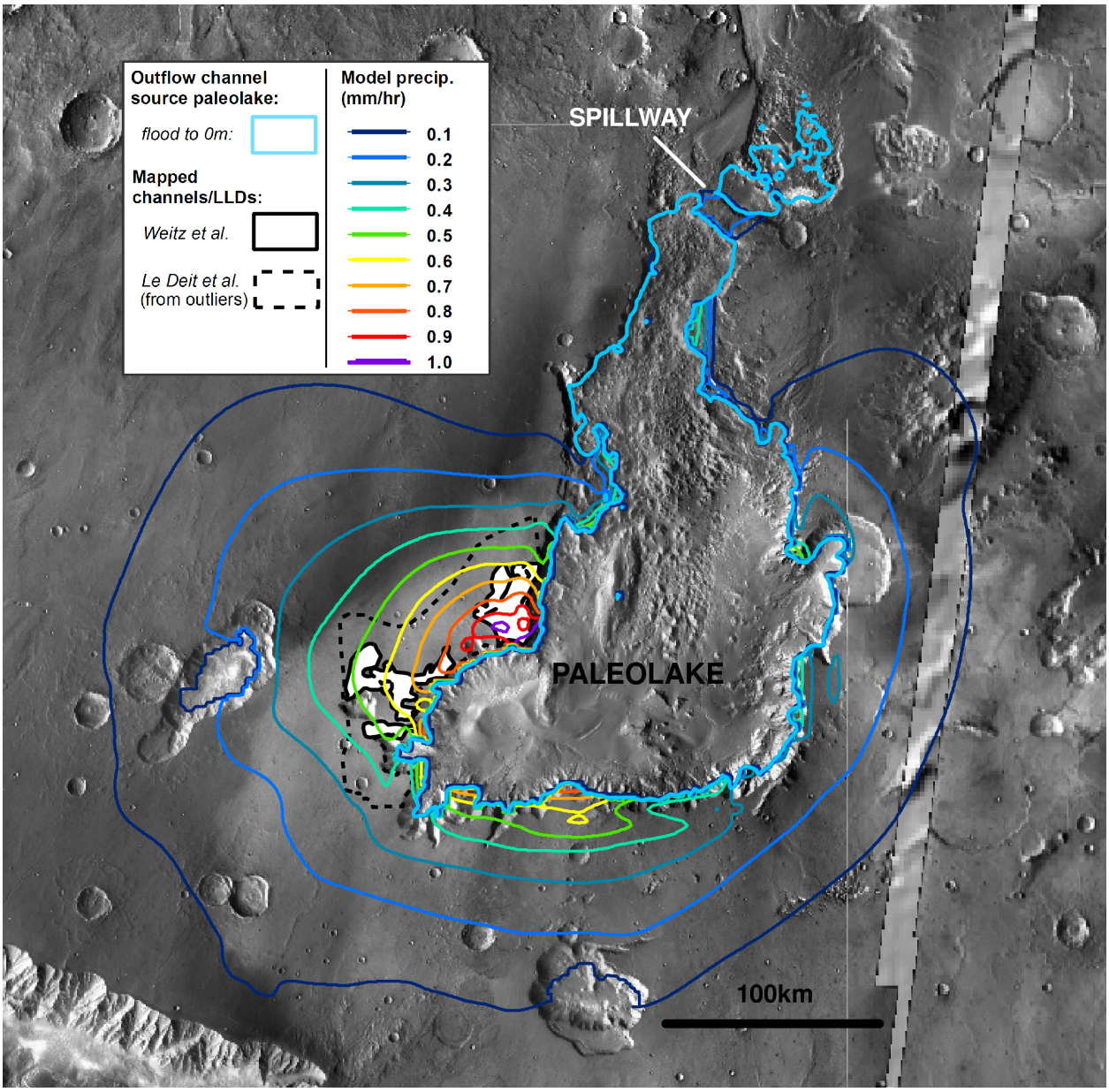

Figure 3.9 Modeled precipitation contours overlain on observed geology at Juventae. White shading with thick solid black outline corresponds to area of layered deposits and inverted channels reported by Weitz et al. (2010). The dashed black outline corresponds to the pre-erosion area of layered deposits inferred from outlier buttes and pedestal craters by Le Deit et al. (2010). The thick cyan line defines the flooded area for this simulation (the -1000m contour). The colored lines are modeled time-averaged precipitation contours at intervals of 0.1 mm/hr water equivalent. Precipitation falling back into the lake is not shown. The spatial maximum in mean precipitation is ≈1.0 mm/hr. (Note: sol 5 average).

Rate and location of snowfall. The footprint of precipitation is displaced downwind of the centroid of the lake by a distance similar to the product of vapor lifetime (loss due to ice crystal growth and subsequent gravitational sedimentation) and characteristic wind velocity at cloud height (Figure 3.10). Because the size of Juventae Chasma exceeds this distance, the peak in total precipitation (1.3 mm/hr water equivalent, w.e.) lies within the lake. This prediction cannot be geologically tested, so we focus on results for precipitation on land.

Most snow falls close to the chasm edge (Figure 3.9). Water-ice precipitation on the chasm flanks has a maximum on a promontory southwest of the lake center. Mean precipitation is >0.6 mm/hr w.e. only in a narrow belt <40 km from the chasm edge on the SW rim of the chasm. This area of high modeled precipitation corresponds to the mapped area of channels and layered deposits (Figure 3.9). In §3.10.1 (see also Table 3.3), we use four independent metrics to quantify the agreement between geologic data and precipitation model that is qualitatively apparent in Figure 3.9.

Reduction in snowfall with distance from the chasm is rapid (Figure 3.18). Decline is most rapid upwind (east) of the chasm. 200 km east of the chasm rim, peak snowfall and mean snowfall are both 1000 times less than at the chasm rim. Falloff is strongly modulated by topography: at a given distance from the lake, plateaux receive 10-100 times more snowfall than canyon floors.

Maximum precipitation on land (not shown) is 1.7 mm/hr w.e. In the area of greatest mean precipitation, maximum precipitation is 1.5-2.0× the mean precipitation rate. Transient high snowfall during model spin-up is excluded.

The inflection in precipitation contours at the chasm edge (Figures 3.9 and 3.10) is a projection effect of the steep chasm wall slopes. Fall rates per unit column atmosphere decrease smoothly with distance from the lake, but at the chasm wall the snow from this column is spread over a larger surface area.

Precipitation is localized and vapor lifetime is short, so precipitation rates are comparable to evaporation rates.

Mass & energy budgets: Mean evaporation rates found from our mass balance (∼2 mm/hr, Table 3.2) entail 1.4 kW/m^2 evaporative cooling. Is our assumption of constant lake surface temperature sustainable? An isolated, well-mixed lake of depth 5 km would cool only 0.006 K/sol through evaporative cooling, so the assumption of constant lake surface temperature over the length of our simulations is reasonable in this case. The key is the depth of mixing. 1.4 kW/m^2 cannot be supplied from the interior of a liquid lake to its surface by conduction. Thermal convection may transfer the required heat if lake temperature is above water's temperature of maximum density (277.13K) and

$$q_{convect} = 0.05 \left(\frac{\rho g \alpha \Delta T}{\kappa \nu} \right)^{1/3} k \nabla T > 1.4 \mathrm{kW/m^2} \tag{3.1}$$

where $q_{convect}$ is convective heat flow in W/m^2, $\rho = 1000$ kg/m^3 is water density, $g = 3.7$ m/s^2 is Mars gravity, $\alpha = 2$ x 10^{-4} K^{-1}, $\kappa = 1.4$ x 10^{-7} m^2/s, $\nu = 10^{-6}$ m^2/s, $k = 0.6$ W/m/K is

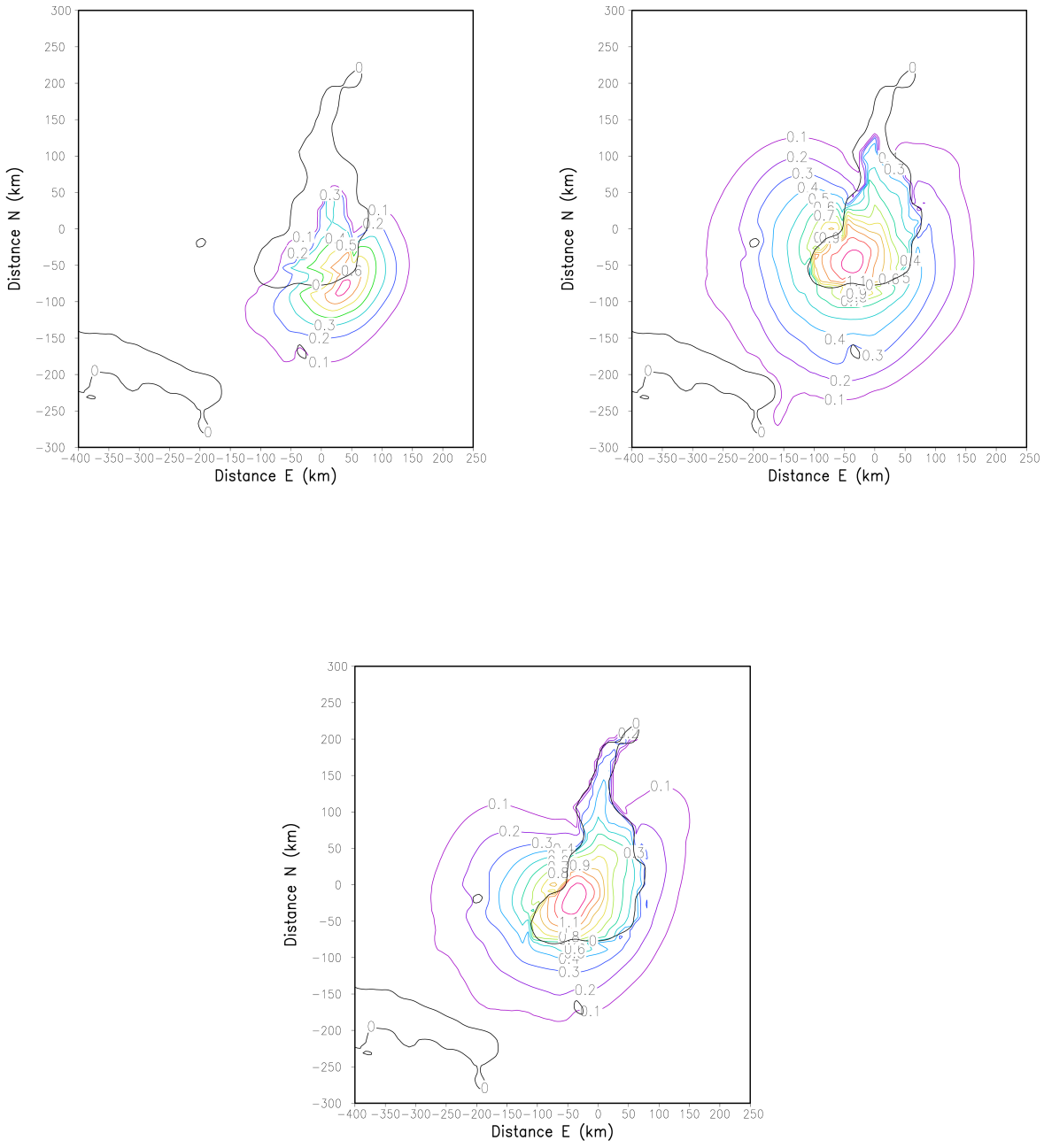

Figure 3.10 Sensitivity test comparing mean precipitation (mm/hr) for 3 different lake levels. Top left: -3000m (`juventae_low`), top right: -1000m (`juventae_medium`), bottom left: 0m (`juventae_high`).

thermal conductivity, and ∇T is the temperature gradient across the lake (Postberg et al., 2009). Even with $\nabla T = 0.25$ K/m (very steep), $q_{convect} = 180$ W/m^2, insufficient to sustain evaporation.

Therefore, in order for the lake not to freeze immediately, waves, bubbles or currents are required to stir the lake. This is reasonable, for example, if the aquifer was saturated with CO_2 by a magmatic intrusion (Bargery and Wilson, 2010). Also, the outflow itself could have disrupted the forming ice cover (Figure 5). For maximum Maja Valles outflow channel discharge $Q_{Maja} = 1.1$ x 10^8 m^3 s^{-1} (Kleinhans, 2005) and a lake surface area $A_{lake} = 25800$ km^2 (Table 3.1), maintaining a steady lake surface elevation requires a vertical current $w \sim$ 4 mm/s to the part of the lake above the spillway. The corresponding enthalpy flux to the upper part of the lake is $w\rho(c_p(T - 273.15) + L_{freeze}) = 1.42$ MW/m^2, much greater than evaporitic losses. Equivalently, suppose that we track a parcel of water upwelling near the center of the lake to the spillway. Assume that the water lying above the spillway depth is well-stirred by currents flowing toward the spillway. Then cooling during the journey from the center of the lake to the spillway is

$$\Delta T \approx 1.5\text{kW/m}^2 \frac{A_{lake}}{\rho c_p Q_{Maja}} \sim 0.1\text{K}, \tag{3.2}$$

which is small.

Evaporitic loss from a fully open lake, 1.3 x 10^4 m^{3}s^{-1} ($\equiv$ 1.9 mm/hr) in our best-fitting model, is small compared to maximum Maja Valles outflow channel discharge (1.1 x 10^8 m^3 s^{-1}; Kleinhans (2005)).

We conclude that the liquid water surface imposed as a boundary condition for the mesoscale simulation is consistent with the simulation results, provided that catastrophic groundwater discharge continues as long as the lake storm persists.

3.4.2 Sensitivity to flooding depth

The location of precipitation is sensitive to flooding depth, and flooding depths close to the spillway provide the best match to observations (Figure 3.10). As lake level rises, the offset of maximum precipitation from the lake center changes. The main change on land as the flooding depth is moved closer to the spillway is that precipitation to the S of Juventae Chasma is reduced. This is because the area of convergence shifts NW and then N, tracking the centroid of lake area.

More than 80% of vapor released by the lake is trapped in or next to the lake as snow (Figure 2.6). As plume intensity increases, so does the fraction of water vapor that snows out locally. Plume intensity - which we define using updraft velocity and cloud height - increases with increasing lake size (Chapter 2) and with increasing lake temperature. Therefore, higher flooding depths within Juventae Chasma lead to more localized precipitation. Atmospheric water does increase with increasing lake area, but slowly (Table 3.2). Only

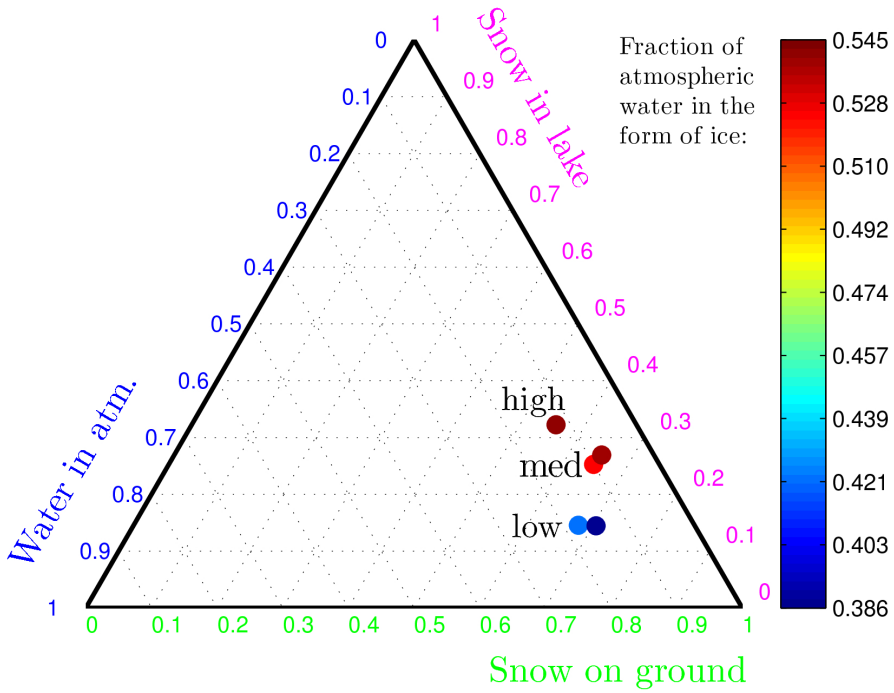

Figure 3.11 Fate of vapor released from the lake (precipitation efficiency). Colored dots correspond to the inventory of water (ice + vapor) after either 5 or 7 sols, after subtracting the inventory of a lake-free run. Color corresponds to fraction of atmospheric water in the ice phase: red is more ice-rich, blue is more vapor-rich. Only snow on ground can contribute to localized geomorphology. Water vapor in the atmosphere can contribute to regional and global climate change: global warming is increasingly likely as the mass of atmospheric water increases.

`juventae_low` and `juventae_med` are directly comparable because of the lower lake temperature in `juventae_high`.

Table 3.2 Evaporation rate and vapor fate (end of sol 5). Units are Mt (10^6 metric tons). Italicized ***dry*** runs are subtracted from the runs below them. See also Figure 2.6.

Run	Evaporation Rate (mm/h)	Water in Atmosphere	Total Atmosphere (%)	Snow in Lake	Snow Beyond Lake	Total Snow (%)
JUVENTAE_DRY	*0*	*536*	*100%*	*0*	*0*	*0%*
JUVENTAE_LOW	2.47	304	18	251	1166	82
JUVENTAE_MED	2.82	536	10	1356	3472	90
JUVENTAE_HIGH	1.88	571	12	1505	2590	88
JUVENTAE_DRY_SOL_7	*0*	*520*	*100*	*0*	*0*	*0*
JUVENTAE_LOW_SOL_7	2.54	403	15	387	1887	85
JUVENTAE_MED_SOL_7	2.90	658	8	2230	5393	92

[a]Units are Mt (10^6 metric tons). Italicized dry runs are subtracted from the runs below them. See also Figure 11.

3.5 Will snow melt?

We calculate the melting probability for snow precipitated from the storm using a 1D model (§3.10.2). This model is decoupled from the mesoscale model. We use the 1D model to assess all possible orbital states and solar luminosities. We show only the likelihood that Mars' orbital state permits melting at the equator (Figure 3.12). The top panel excludes the greenhouse effect of the storm. The bottom panel includes this additional greenhouse effect. More recent times favor melting because of increasing solar luminosity. Higher pressures favor melting, because of the suppression of evaporitic cooling and the greenhouse effect of added CO_2.

Our model will overestimate the quantity of snowmelt available to erode channels, for two reasons. Parameters are chosen (Table 3.5) to favor melting – in particular, we use a dirty snow albedo of 0.28, similar to Mars dust (Mellon et al. (2000), and discussed in §3.10.2). Also, we do not include hydrologic effects. For example, if the porous layer is much deeper than the diurnal thermal skin depth, then melt percolating from the surface will refreeze. Such effects will limit the proportion of snowmelt available for runoff (e.g., Colbeck (1976)).

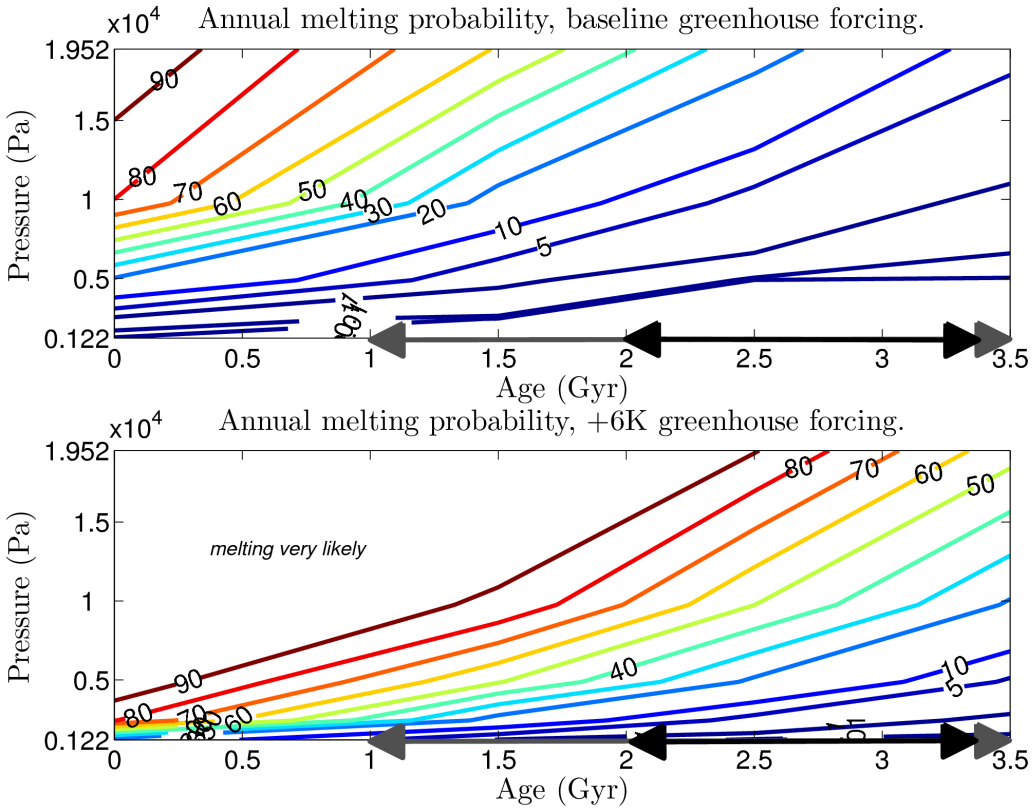

Figure 3.12 Equatorial melting probability (in %) for flatlying snowpack. The four lowest probability contours correspond to 5%, 1%, 0.1%, and 0.01%. Gray arrow on the x-axis corresponds to the range of ages for opaline layered deposits stated in the text of Murchie et al. (2009b). Black arrow corresponds to the smallest range of stratigraphic ages that could accommodate all the plateau channel networks according to Le Deit et al. (2010). Age uncertainties are large enough that it is possible that all the plateau channel networks formed at approximately the same time. Pressures on the y-axis range from 1220 Pa ($\sim$ 2$\times$ present atmospheric level) to 19520 Pa ($\sim$ 32$\times$ present atmospheric level). The thermal model in this chapter includes more terms – leading to slightly colder outcomes – than the model used in Chapter 2.

Table 3.3 Model skill using method of Pielke and Mahrer (1978). The best-fitting model for each geological target is highlighted in bold. Italicized text corresponds to the original extent of layered deposits mapped by Weitz et al. (2010), and normal text is the value for Le Deit et al. (2010). 1.0 mm/hr is not shown because there is only 1 pixel in the model output that exceeds this value.

	Skill					Coverage				
Precip. (mm/hr)	0.02	0.2	0.4	0.6	0.8	0.02	0.2	0.4	0.6	0.8
`juventae_low`	11	0	0	0	0	0.040	0	0	0	0
	11	*0*	*0*	*0*	*0*	*0.009*	*0*	*0*	*0*	*0*
`juventae_med`	5	19	50	108	122	0.020	0.071	0.185	0.403	0.455
	5	*19*	*51*	*138*	*227*	*0.004*	*0.015*	*0.041*	*0.111*	*0.182*
`juventae_high`	6	33	120	229	**269**	0.022	0.122	0.446	0.853	**1.000**
	6	*33*	*136*	*293*	***498***	*0.005*	*0.026*	*0.109*	*0.235*	***0.400***

Main results from the melting model are:

- *Boundary conditions for the mesoscale storm model are too cold for snowmelt under the Faint Young Sun.* Snow is unlikely to melt at 12 mbar (Figure 3.12). Some combination of the following is required to melt snow:- (1) higher atmospheric pressure; (2) non-CO_2 greenhouse forcing; (3) a very large number of lake storms occurred, so that a few storm deposits encountered orbital conditions that allowed melt even though the probability of melting was low; (4) transient warming from impact ejecta or a geothermal event; or (5) the deposits are younger than thought. We do not have enough information to choose between these. Absent direct warming from impact ejecta or a geothermal event, moderately higher pressures are almost certainly required (at least 50 mbar appears necessary). Strong evaporitic cooling suppresses melting at lower pressures. Transient warming from impact ejecta or a geothermal event could overcome evaporitic cooling, and it is possible that impacts or geothermal activity trigger chaos events (McKenzie and Nimmo, 1999; Wang et al., 2005).

  Localized precipitation may not be possible at 50 mbar. Certainly the updraft vertical velocities will be reduced. In an idealized simulation at 60 mbar (Chapter 2), precipitation was reduced by 20% relative to the 12 mbar case.

- *Snowmelt at low latitudes is more likely for snow that accumulates out of equilibrium with orbital forcing.* More than half of the hottest orbital conditions occur at less than median obliquity (Chapter 2). Accumulation of annually-persistent snow at the equator is only possible for median obliquity or higher. Instantaneous emplacement from lake-effect storms can occur at any obliquity. Other factors (Chapter 2) also favor melting of localized storm deposits. We do not know the frequency of localized storms,

so we cannot use this information to calculate the likelihood that an observed channel network formed from melting of instantaneously-emplaced snow.

We assume that storm deposits persist until the melt season. Is this reasonable? Low-latitude sublimation rates modeled by GCM (Madeleine et al., 2009) are ∼0.25 m/yr w.e., with wide scatter. Lakes with lifetime $>10^2$ hours generate this snowpack, given our modeled precipitation rates.

Once liquid water is flowing, feedbacks can extend its lifetime. For example, in Greenland, supraglacial channels with water depth >0.5m reduce the albedo to close to that of water ($\sim$ 0.05) (Lüthje et al., 2006). Viscous dissipation can balance evaporative cooling of the stream only if

$$S > \frac{eL}{\rho g u D} \tag{3.3}$$

where S is river slope, $e \sim 1$ mm/hr is evaporation rate, L is the latent heat of vaporization, $\rho = 1000$ kg/m^3 is density, g is Mars gravity, $u = O(1)$m/s is stream velocity, and $D = O(1)$m is stream depth (Clow, 1994). This condition is not satisfied for the Juventae plateau channel networks (which have slopes <1%; Table 3.4), so the stream will be roofed over by ice. Insulation of streams by ice can greatly extend liquid water lifetime (Clow, 1987).

3.6 Channel and layered deposit formation

We now evaluate formation mechanisms for the layered deposits and interbedded channel networks in light of our simulations. First we review constraints, including measurements from our own DTMs. We consider a series of options for the channel-forming mechanism, and test them against these constraints. These different mechanisms all assume that water is sourced from ephemeral lakes as in §3.2 - §3.5 (center row in Figure 3.3). Next we drop the assumption that water is sourced from ephemeral lakes, and describe entirely different geological scenarios (top row in Figure 3.3). We do not find decisive evidence that allows us to choose between these channel forming mechanisms or geological scenarios – we are left with multiple working hypotheses. We list future tests that could help decide among these multiple working hypotheses.

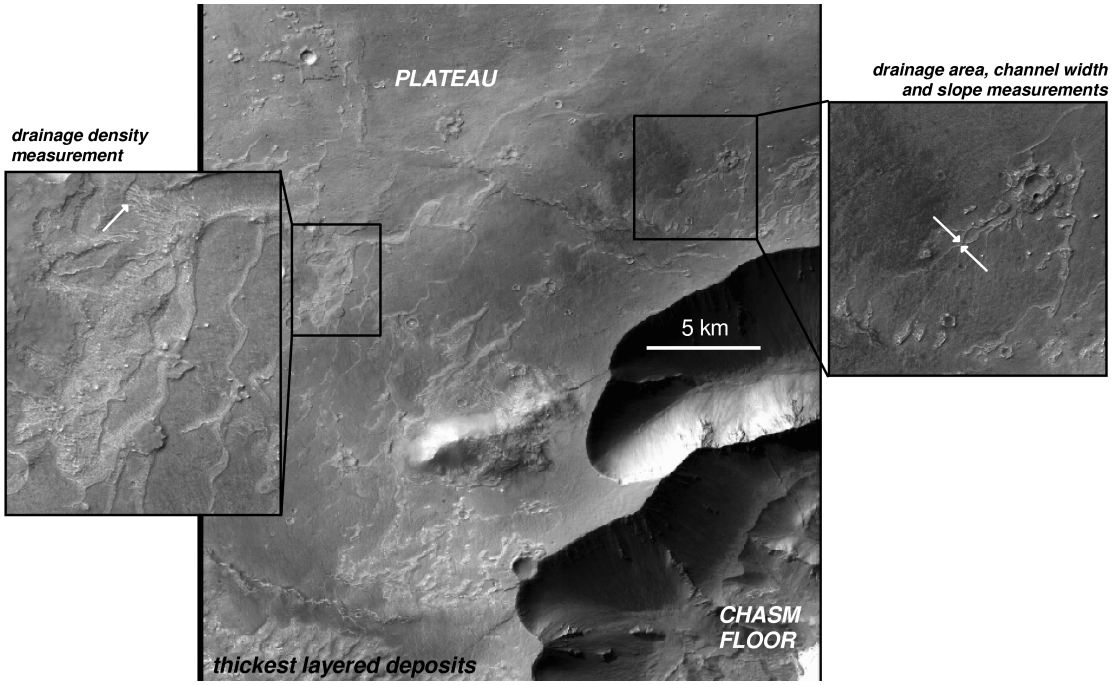

Figure 3.13 Geological context for measurements of layered deposit thickness, channel drainage density, catchment area, channel slope and channel width. White arrows in zoomed-in panels show localities. Some thickness measurements come from an area just SW of this image. Background is part of CTX image P18_007983_1751_XN_04S063W.

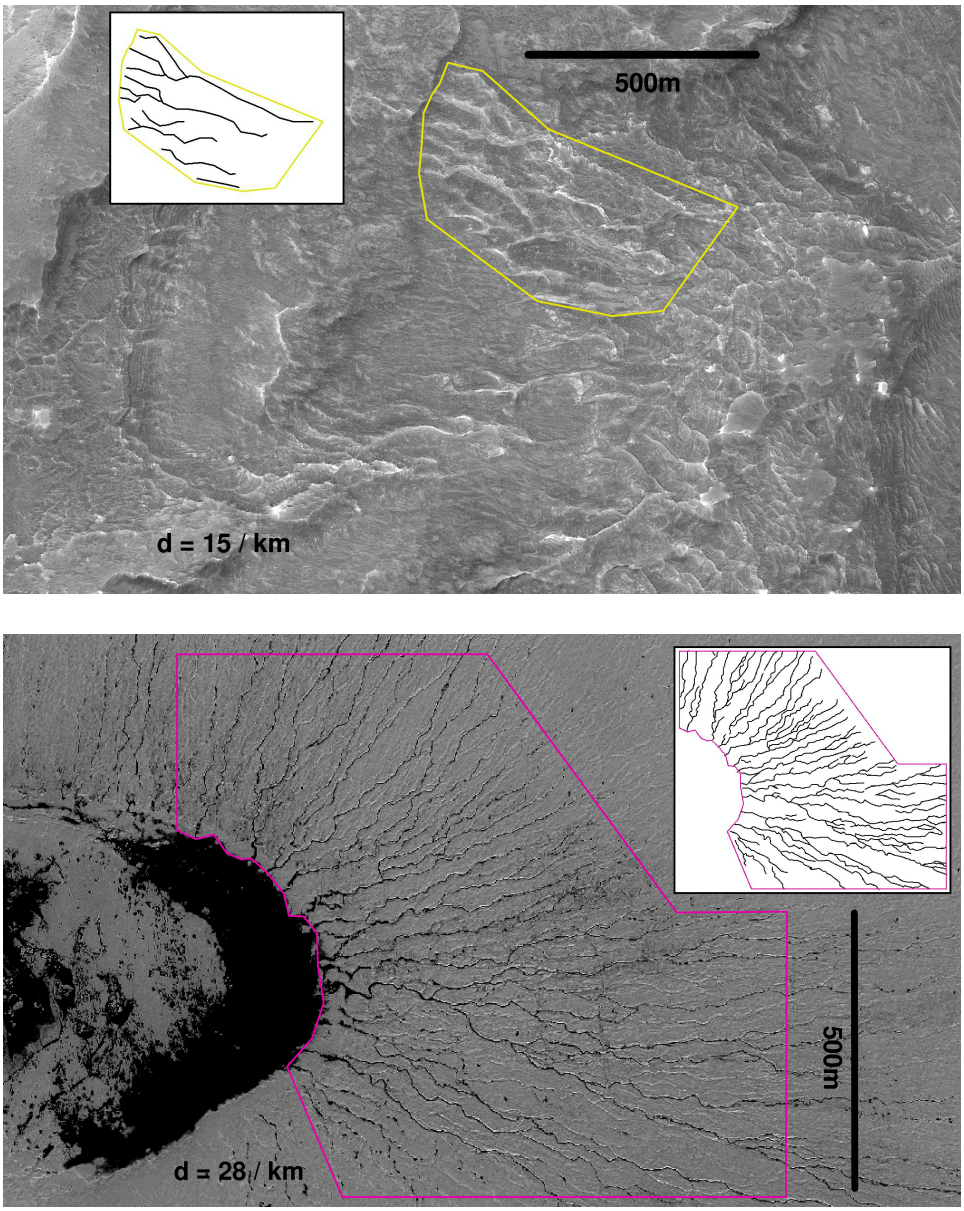

Figure 3.14 Comparison of the area of maximum drainage density at Juventae to snowmelt-carved systems on the Greenland ice plateau. Polygons enclose the area for which drainage density was measured, and the inset panels show channels which contributed to the count. *Upper panel:* PSP_005346_1755, Juventae Plateau. This locality was identified by Malin et al. (2010) as "the best evidence yet found on Mars to indicate that rainfall and surface runoff occurred." *Lower panel:* IKONOS image of Greenland ice sheet, showing snowmelt-carved channels draining into a supraglacial lake. (Image courtesy Jason Box/OSU/Discovery Channel; Box and Ski (2007)). *Details:* Greenland - length = 21.3 km, area = 0.77 km^2, giving drainage density $d = 28$/km. Mars - length = 3.4 km, area = 0.22 km, giving drainage density $d = 15$/km.

In agreement with previous work (Mangold et al., 2008; Weitz et al., 2008), we interpret the networks of sinuous ridges and troughs to be fossil fluvial channels (Figure 3.13). Juventae plateau channels have low to moderate sinuosity. We have only found 2-3 highly sinuous (meandering) channels. This should be compared to Gale-Aeolis-Zephyria, where most channels meander (Burr et al., 2009). Most channels run down the present-day 0.2° NNE regional slope (Mangold et al., 2008). Sinuous ridge width distribution appears bimodal. We suspect that the broader $O(10^2\text{m})$ sinuous ridges are inverted valleys. Given that the channel networks are fossil fluvial channels, endmember channel-forming mechanisms are thermal erosion into ice, and mechanical erosion of sediment (Figure 3.3). These have corollary implications for the composition of the light-toned layered deposits: in the thermal erosion endmember case, the present-day plateau layered deposits contain significant relict ice at depth. Relict water ice at the equator of Mars cannot be stable (Mellon and Jakosky, 1995). Nevertheless, geologic and radar evidence suggests that loss rates are sufficiently slow for ancient water ice to metastably persist in some equatorial locations (Head and Kreslavsky, 2004; Levy and Head, 2005; Shean et al., 2007; Watters et al., 2007; Mouginot et al., 2010; Warner et al., 2010; Shean, 2010). An example on Earth of the thermal erosion endmember case is the snowmelt-fed channel network that forms each summer on the Greenland ice sheet (Figure 3.14). In the mechanical erosion endmember case, the present-day plateau layered deposits are composed of (indurated) sediment grains.

3.6.1 Implications of constraints for channel-forming mechanisms

Many of the channels are preserved in inverted relief: On Earth channels can become inverted through cementation of channel fill, armoring by coarse grains of the channel floor against erosion, or infilling of the channel by an erosionally resistant material such as lava (Williams et al., 2009). Increased cementation of the channel thread, followed by differential erosion, is the most likely cause of inversion for inverted channels studied elsewhere on Mars (Williams et al., 2009; Burr et al., 2010). Juventae's inverted channel networks lack evidence (such as pitting) for sublimation. They are often horizontally or sub–horizontally layered, and the layers have variations in tone. They have well-defined, smooth, flat tops. These observations suggest that the inverted channels are composed of sediment and are not ice-cored. Sediment fill is more consistent with the mechanical erosion endmember scenario than the thermal erosion endmember scenario.

However, inverted channels on Mars do occur in ice-dominated, supraglacial and proglacial settings. Therefore, the interpretation that the inverted channels are composed of (indurated or cemented) sediment does not rule out thermal erosion of the progenitor channel. Midlatitude Amazonian glacier-associated channels at Lyot Crater (HiRISE image ESP_016339_2225) and Acheron Fossae (HiWish image ESP_018178_2165), and E of Reull Valles (HiWish image ESP_020055_1410) have become inverted (Fassett et al., 2010). The Acheron inverted channel is $\leq$80 Ma based on the age of its source glacier (Fassett et al., 2010). In each case, glacier-associated channels appear to have incised into ice, but to have

been incompletely filled with debris and sediment during or after incision. As surrounding ice retreats due to sublimation, the channel-filling sediment is left as a sinuous ridge.

The layered deposits are tens of meters thick: We measure the present-day thickness of the plateau layered deposits close to the chasm edge as 43±11 m ($n = 13$), using HiRISE DTMs. 33-39 layers are visible in HiRISE images of the thickest exposures (defining layers using laterally continuous changes in tone, slope or erosional morphology).

In the thermal erosion endmember scenario in Figure 3.3, layered deposits are primarily water ice. The deposit thickness of 44±13m then requires a minimum of 1400-2600 sols to accumulate at our peak precipitation of 0.9 mm/hr, ignoring sublimation losses. Peak Maja discharge, Q_{Maja}, is 1.1 x 10^8 m^3s^{-1} (Kleinhans, 2005). The volume of Juventae Chasma below the pour point is ∼7x10^4 km^3 (ignoring the volume of Maja Valles itself). If this missing volume is 70% rock by volume and was exported over the spillway, with a fluvial sediment concentration of 1% by volume, then the minimum cumulative time to carve Maja Valles is 740 sols. Peak discharge exceeds mean discharge, so Maja Valles operated for longer than this calculation suggests. In addition, an unfrozen lake may have remained in Juventae after the end of channel formation. Making the conservative assumption that there is only open water at the lake surface only when a catastrophic flood is occurring, the predicted deposit thickness is 28%-53% of the observed thickness. Because we are using a lower limit on lifetime, this discrepancy does not rule out the thermal erosion endmember scenario.

The thickness of the deposits is also compatible with the mechanical erosion endmember scenario (Figure 3.3), in which the present-day plateau deposits are (indurated) sediments. Enough atmospherically-transported material (sand, dust, and volcaniclastic material) must be brought in from other regions of a primarily dry Mars to account for observed thicknesses. Suppose atmospheric dust precipitable column abundance is 10μm, background regional horizontal wind speed is 10 m/s, a circular storm region of radius 200km, and complete scavenging of dust by ice nuclei in the storm region. Then mass balance requires 1600-2700 years of cumulative storm activity to build up the observed thickness of plateau layered deposits (less if precipitation is concentrated). Alternatively, sediment could accumulate on the plateau between storm events as sand, dust or volcaniclastic materials, or (less likely) be supplied from the chasm floor during the early stages of outflow events by buoyant plumes. Lake storms might be responsible for the channels in this case, but would not be the source of the material making up the layers. However, fluid released during snow melting could be responsible for the induration or cementation of these materials, and thus their long-term preservation (Figure 3.3).

It is not possible for the layered deposits to predate the channel-forming events, because channels at different levels within the deposit crosscut each other.

Drainage basin and channel dimensions and slopes: Even if the channels were cut by thermal erosion, some of them must have been infilled by sediment in order to form inverted channels (Figure 3.3). If the channels are formed in fine sediment by mechanical erosion, then sediment transport is required to form both the positive and the negative-relief channels. Therefore,

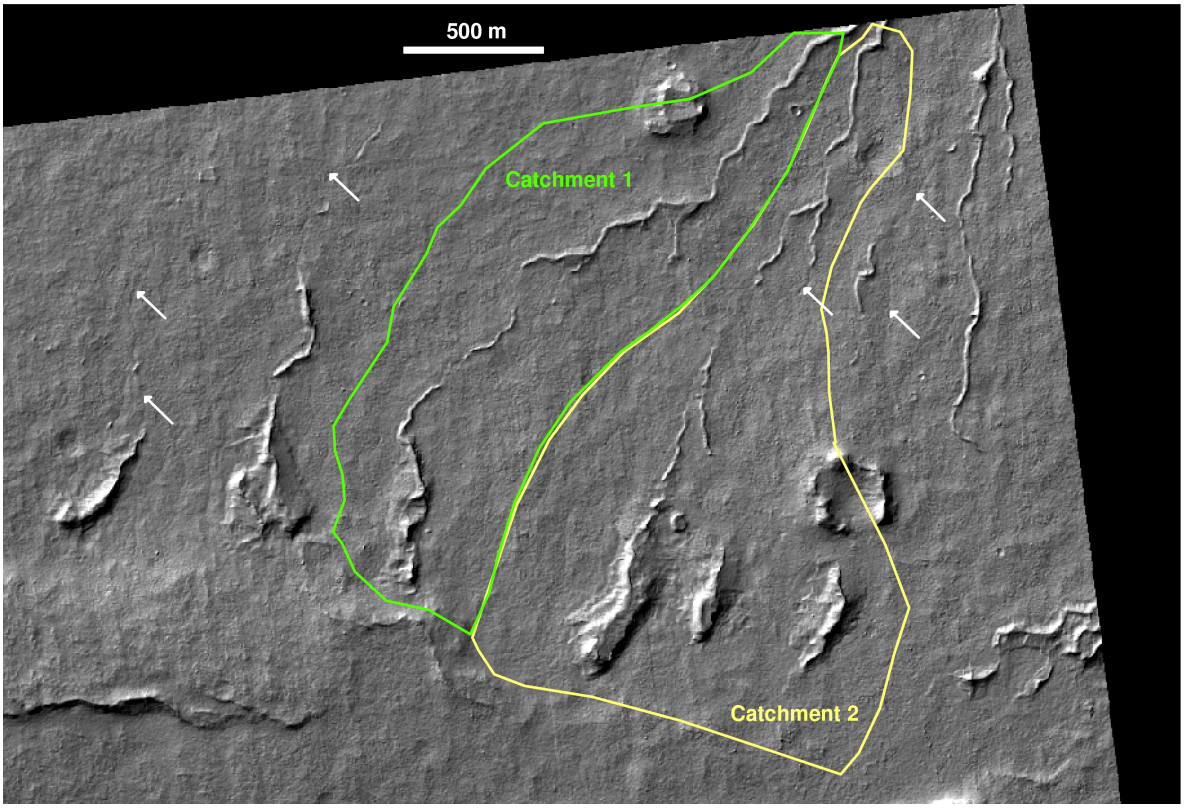

Figure 3.15 Inverted channel systems on the Juventae plateau from which hydraulic parameters were measured. Shaded relief from HiRISE stereo DTM 1 (Figure 3.4), illuminated from top left. North is up. Streams flow down present-day slope. Barely-visible striping parallel to the edge of the shaded relief raster is an artifact of stereo DTM generation. Inverted channel heights are typically 2-5m. Shallow negative-relief channels (white arrows, depth $<$ 1m from DTM) join some inverted channel segments. The corresponding HiRISE image pair is PSP_003223_1755 and PSP_003724_1755.

in either endmember case, sediment must be transported through the observed channel network. The critical runoff R needed to initiate sediment transport in a preexisting channel is (Perron et al., 2006):

$$R_{crit} = \frac{1}{A}\frac{w^2\rho'\tau_c^* D}{wS - 2\rho'\tau_c^* D}\left(\frac{8\rho' g\tau_c^* D}{f}\right)^{\frac{1}{2}} \tag{3.4}$$

where R_{crit} is the critical runoff rate, A is drainage area, w is channel width, $\rho' = (\rho_s/\rho_f) - 1$ is the normalized density, ρ_s is sediment density, ρ_f is fluid density, $\tau_c^* \approx 0.05$ is the critical Shields number, D is sediment grain diameter, S is slope, g is Mars gravity, f is the Darcy-Weisbach friction factor, and all units are mks. We assume basaltic sediment, with $\rho_s = 3000$ kg/m^3, and water density $\rho_f = 1000$ kg/m^3. In alluvial streams, f is closely related to grainsize, but no similar relationship has been published for thermally-eroded channels. A, w, and S are taken from our DTMs, as shown in Figure 3.15, tabulated in Table 3.4, and described below. *Area:* Erosion has scoured the deposits between preserved inverted channels, removing the drainage basins that once sourced those channels. We therefore divide the area between channels by equidistance. Because there have been multiple episodes of crosscutting flow, some truncation of channels by subsequent generations of channel may have occurred, which may lead to a systematic underestimate of A and corresponding overestimate of R_{crit}. *Width:* We measure channel widths using the distinctive, light-toned region at the top of the sinuous ridges visible in HiRISE images. DTMs confirm that this light-toned strip forms the summit of the much broader ridge, and often resolve a break-in slope near the top of the ridge approximately corresponding to the light-toned strip in the red-filter HiRISE images. This is frequently much narrower than the total ridge width visible in shaded-relief DTM images such as Figure 3.15. By analogy with inverted channels near Green River, Utah (Williams et al., 2007), these observations suggest that the bright region whose width we are measuring corresponds to an erosionally resistant and vertically thin channel-fill deposit capping underlying weaker material. The channel widths we obtain are several meters for drainage areas $O(1)$ km^2 (Table 3.4). These widths may correspond to indurated channel fill (or valley fill) sediments that are wider than was the instantaneous channel. Much wider ridges are seen elsewhere, but these are the largest channels for which we have area and DTM slope constraints. *Slope:* We take an average slope along the exposed length of the channel. There is no visually obvious evidence of major post–depositional tilting of the plateau - the channels run approximately down the present-day slope.

Table 3.4 Measurements relevant to hydrology for 2 adjacent inverted channels (Figure 3.15).

			Catchment 1	Catchment 2
A	area	km^2	1.6	2.1
w	width	m	3.3±0.8	3.2±0.47
S	slope	Δz:Δx	0.82°	0.96°

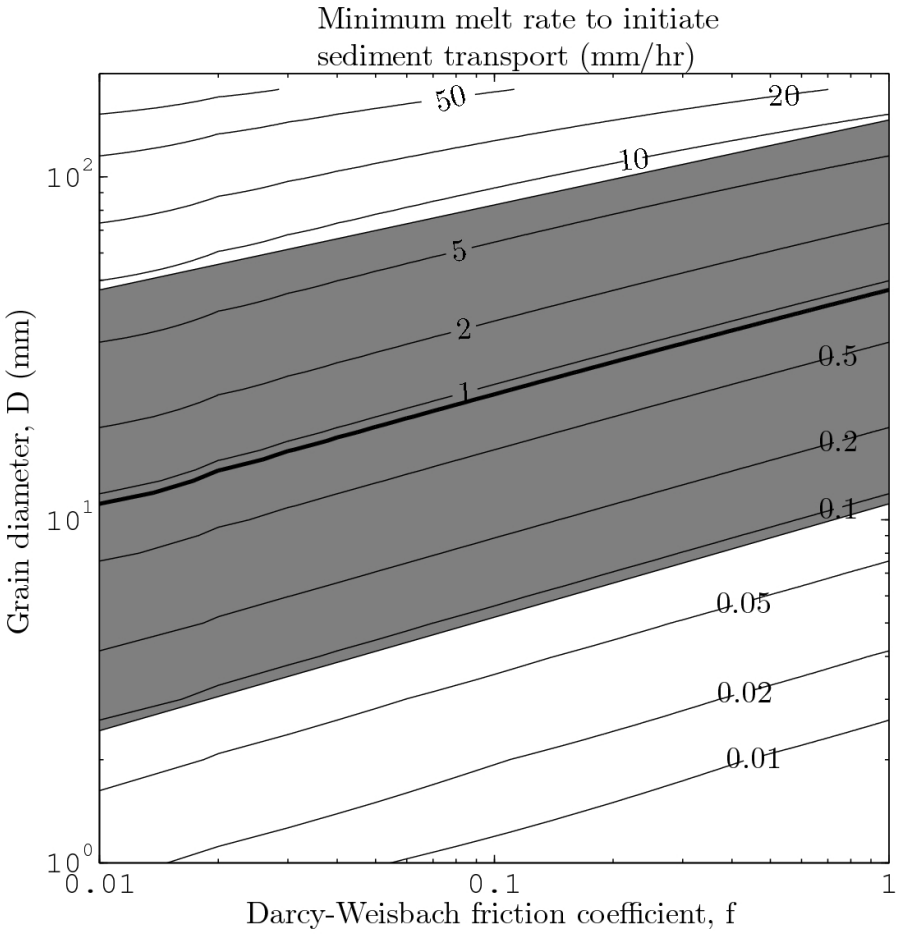

Figure 3.16 Grain sizes that can be mobilized by the modeled precipitation. The central black line corresponds to the modeled snowfall rate, 0.9 mm/hr. Because we consider the modeled precipitation rate to be only an order-of-magnitude guide to the true precipitation rate, the gray envelope shows order-of-magnitude uncertainties in both directions. The melting rate will be lower than the precipitation rate, and in our probabilistic discharge model the exceedance probability for a melt rate of 1.0 mm/hr is extremely low. Melt rates of 0.09 mm/hr (lower end of gray envelope) are more likely, and are sufficient to mobilize sand and gravel.

R_{crit} for a catchment of area 1.6 km^2 and slope 0.8° feeding a channel of width 3.3 m is shown in Figure 3.16. The adjacent catchment of area 2.1 km^2 produces almost indistinguishable results. Both networks are from DTM1 (§3.10.3). We assume $R \approx M$, where M is the melt rate. R will only approach this upper bound if there is a shallow impermeable ice table, or if the substrate is covered with fine-grained material that has a low infiltration rate. An upper limit on M is if all precipitation melts upon reaching the ground. Then the resulting runoff can mobilize coarse gravel (thick black line in Figure 3.16). However, a more realistic melt rate is 0.1 mm/hr. This is still capable of initiating the transport of coarse sand and fine gravel through the network (lower bound of gray envelope in Figure 3.16). The upper limit on the gray envelope in is an order-of-magnitude error intended to capture errors in the precipitation model, weather, and especially the width and area measurements discussed above. We conclude from the area covered by this gray envelope that if boulder-sized (>256 mm diameter) clasts have been transported through these Juventae channel networks, that would be strong evidence against localized precipitation. Howard et al. (2007) provides criteria for distinguishing fluvially-transported boulders from post–depositionally cemented blocks. Any clast that can be resolved by HiRISE is a boulder.

3.6.2 Alternative interpretations and tests

In §3.2, we inferred that location adjacent to a chasm supplies one or more limiting factors for inverted channel formation. Likely limiting factors included availability of snow or rain, sufficient heat for melting, availability of sediments that can be mobilized, cementing fluids, and incomplete erosion. In §3.3 - §3.5, we developed and tested the hypothesis that precipitation is limiting. Results are consistent with the hypothesis. What about heat, sediment, cementing fluids, and erosion? Can we rule any or all out?

Precipitation on the Valles Marineris plateau sourced from ephemeral chaos lakes is one model compatible with data, but other scenarios are also possible (Figure 3.3, top row). For example, we cannot currently rule out a scenario where the observed narrow, extended Valles Marineris cloud trails (0.4 micron effective diameter; Clancy et al. (2009)) increase spectacularly in mean grain size and move closer to the canyon edge during different orbital conditions or dust loading, permitting regional precipitation. Near-surface water-ice morning fog occurs in Valles Marineris today (Möhlmann et al., 2009), and OMEGA has detected surface water ice on the northern wall of Coprates Chasma (Vincendon et al., 2010). Net annual ice accumulation within the Valles Marineris occurs in GCMs at high and moderate obliquity (Madeleine et al., 2009), although this is largely due to the high thermal inertia of the chasm walls (J.B. Madeleine, via email). Taken together, this evidence suggests that Valles Marineris is a preferred site for equatorial ice precipitation, which is important at high obliquity (Jakosky and Carr, 1985; Jakosky et al., 1995; Mischna et al., 2003; Forget et al., 2006). Mischna and Richardson (2005) point out that polar sublimation rates – and thus equatorial precipitation rates – will decline at high obliquity when and if a sublimation lag deposit has grown thicker than the seasonal thermal skin depth. In this high-obliquity

precipitation scenario, snowpack is broadly distributed in the Valles Marineris region, but generally does not melt. This possibility is discussed by Le Deit et al. (2010). The limiting factor provided by the chaos regions is then airborne darkening agents (ash and/or debris) sourced from the chasm floor and lofted by buoyant plumes ("dirty thunderstorms"; van Eaton et al. (2010)), which lead to patchy melting or patchy preservation of a broadly distributed, preexisting snowpack. Alternatively, ash and/or debris forms a cast of the channels, which form over a broad region but disappear elsewhere when the snowpack sublimes. A weakness of this scenario is that both the observed fog and surface ice, and the predicted high-obliquity net ice accumulation, are on the chasm floor and walls and not the adjacent plateau. Opal-bearing layered deposits and channel networks are overwhelmingly found on the plateau, not the floor and walls (Figure 3.2). Another weakness is that no geomorphic evidence for explosive volcanism has been found on the floor of Juventae Chasma.

Another alternative source of water is springs. Before chasm opening had begun, drainage from aufeis blisters, or groundwater, could source springs (Gaidos and Marion, 2003; Murchie et al., 2009a). In this scenario, the layers and channel networks predate outflow channel formation. This would not explain the downwind preference for channel networks, but there is a 7% possibility that this could be due to chance (§3.4, Figure 3.19).

Among these three scenarios, our preference for the late formation model is tentative, but testable. First, a more complete study of the plateau channel networks, using HiRISE DTMs where possible, and using channel width as a proxy for discharge (Montgomery and Gran (2001) and references therein), would test the spring hypothesis and the precipitation hypotheses. If plateau channels were fed by a small number of point or line sources, channel widths should be constant between confluences (and channel sources should correlate to linear fractures, shear bands, or mineralogical anomalies). If precipitation or distributed groundwater flow fed the channels, channel widths should increase with contributing area as seen on Earth, and channel sources should not be correlated with fractures or mineralogical anomalies. Second, further tests of the localized-precipitation model at other sites might uncover inconsistencies that would weaken the model's application at all sites including Juventae. Possible sites include Ganges Chasma, Cerberus Fossae and Mangala Fossae. We report initial results from one such test (at Echus) in §3.7.

Additional predictions are specific to the thermal-erosion endmember scenario (Figure 3.3): failure of these predictions would not rule out the mechanical-erosion endmember scenario (Figure 3.3). The thickness of the layered deposits should decrease away from the chasm edge in proportion to the mean precipitation rates predicted by localized precipitation models (e.g., Figure 3.9). Finally, SHARAD observations can test if the light-toned layered deposits have a vertically-averaged dielectric constant consistent with relict ice, as is required by the thermal-erosion endmember scenario. SHARAD has a free-space wavelength of 15 m (9 m in water ice), so the light toned layered deposits are thick enough for this test.

3.7 Echus plateau

The greatest of the outflow channels is Kasei Valles (Williams et al., 2000). Kasei's source is lava-floored Echus Chasma. Beyond the 5km-high chasm wall, on the Hesperian plateau, dendritic channel networks are abundant (Figure 3.17a, Chapman et al. (2010a,b)(Mangold et al., 2004, 2008). The floor of Echus Chasma is now 200m below a saddle that marks the start of the main channel. Regional topography suggests that the floor of Echus was once much deeper (Harrison and Grimm, 2008).

Although no opal or hydroxylated sulfates have been reported on the Echus plateau (Milliken et al., 2008), the erosional properties of the substrate for the Echus channel networks resembles the erosional properties of the Juventae plateau layered deposits. Material on the SE rim of Echus is relatively thinly layered, relatively light-toned in outcrop, and recessed from the chasm edge, suggesting a sedimentary or volcaniclastic origin (CTX image P14_006586_1800_XN_00N079W). It is cut by very broad valleys, which bottom out on more resistant basalt, suggesting it is less resistant to fluvial erosion (P02_001839_1806_XN_00N079W).

Our simulations of the Echus plateau channel networks, which are preserved in negative relief, show peak non-lake precipitation in the densest area of observed channels, at 0.7 mm/hr (Figure 3.17a). Because of the interaction of lake convergence, topography, and the regional windfield, precipitation is also predicted S and E of the chasm beyond the existing mapped area of channels. THEMIS and CTX show extensive channelization in these areas (dotted lines in Figure 3.17a), which die away on a length scale similar to the length scale of predicted precipitation (Figure 3.17b). Cursory inspection of CTX images further away from the channel edge does not show channelization. These results are consistent with localized precipitation. Incomplete geomorphic mapping of the Echus headwaters currently prevents more thorough hypothesis testing, but this is a promising initial result that suggests our ability to match observations at Juventae with only localized precipitation can be reproduced elsewhere.

The Echus plateau channel networks are deep and extensive. It isn't clear whether the cumulative duration of outflow channel activity within Echus Chasma is long enough for lake storms to deposit enough water to produce the Echus plateau channel networks. Chapman et al. (2010b) gives 82 km^3 total erosion over an eroded outcrop of $\sim$ 30000 km^2, corresponding to an average of 2.7m material removed. With a melt season length of 30 sols, melting of 1 mm/day, and a fluvial sediment:water ratio of 100:1, 9000 years would be required to cut the observed channels.

We predict that future simulations of lake-effect storms in Ganges Chasma should produce precipitation that is concentrated near the Ganges plateau inverted channels. However, not every post-Noachian paleolake on Mars has associated inverted channel networks (Mangold and Ansan, 2006; Dehouck et al., 2010). Possible limiting factors include low atmospheric pressure (§3.5, Figure 3.12), a lack of mobilizeable sediment (§3.2), or a lack or currents, bubbles or wind to mix the lake and prevent rapid freezing-over of the lake (§3.4.1).

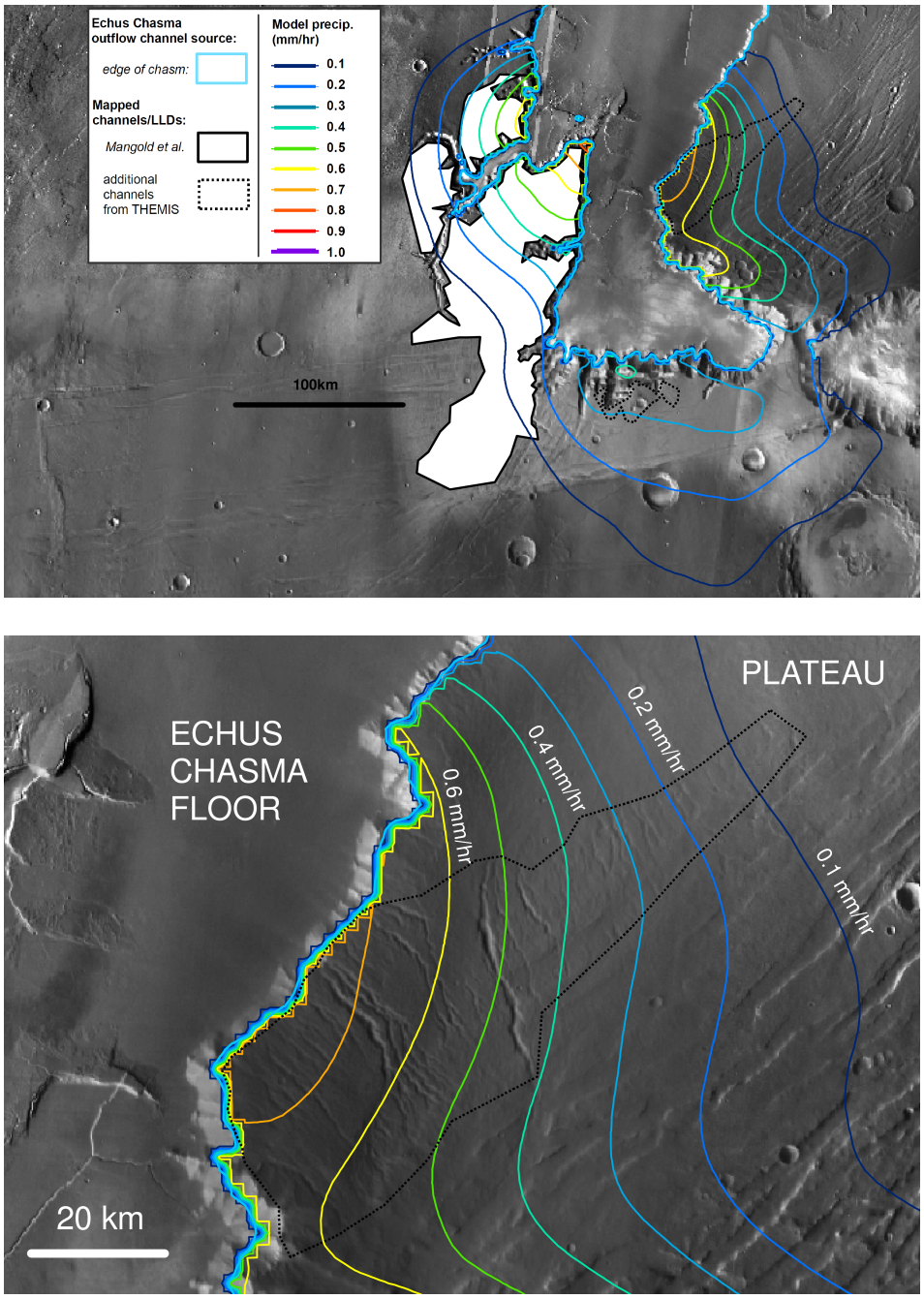

Figure 3.17 a) Modeled precipitation contours overlain on observed geology at Echus. White shading with thick solid black outline is the perimeter of channels reported by Mangold et al. (2008). The dotted black line corresponds to additional channels observed in the THEMIS Day IR 100m per pixel global mosaic. The colored lines are modeled mean precipitation contours at intervals of 0.1 mm/hr water equivalent. Precipitation falling into the lake is not shown. b) Focus on area where channels have not been previously mapped. The dotted line encloses the area of channels visible in THEMIS IR mosaics. The depth and width of the observed channels decreases away from the chasm edge in step with the decline in modeled precipitation.

3.8 Implications for regional and global climate change

Most water vapor released in our simulations is trapped by localized precipitation near the lake, and so is unavailable for broader climate change (Figure 2.6). Remaining atmospheric vapor load is less than present-day global loads (Smith, 2002), and we do not expect a global excursion to wet conditions (the MEGAOUTFLO hypothesis; Baker et al. (1991); Baker (2001); Quantin et al. (2005)) to result from water vapor release during chaos events (Fig 2.6). There are four caveats: (1) Simultaneous triggering of chaos events in multiple chasms, or the broad area of outwash at the terminus of the outflow channels, would provide a larger interface for water vapor injection to the atmosphere than is simulated here. Supposing an evaporation rate of 2 mm/hr, for 5% global water cover, and in the absence of precipitation, the atmosphere will contain 6 mbar water in 70 sols. Water vapor is a powerful greenhouse gas and 6 mbar of water vapor would cause noticeable global warming. But precipitation will occur, and it is likely that outwash freezes over in $<<$70 sols. Inner channels within the outflow channels indicate that the outflow channels were incised by much lower discharge rates than previously thought (Williams et al., 2000). This does not support the hypothesis of large Late Hesperian and Amazonian seas: at low discharges, water would freeze and perhaps sublime, redepositing at planetary cold traps. (2) Noncondensible gases such as CO_2 or CH_4, stored in cryosphere clathrates (or deep aquifers) and outgassed during chaos events (Bargery and Wilson, 2010), could provide warming. (3) If chaos events are triggered by magma bodies laden with CO_2, SO_2, and halogens, then chaos events and transient greenhouse warming could occur simultaneously (e.g., Johnson et al. (2008)). (4) If atmospheric pressure was much higher (e.g. hundreds of mbar) this would suppress the buoyant instability that leads to localized precipitation, allowing more water vapor to escape to the background atmosphere (Chapter 2).

Our model indicates that regional or global temperatures warmer than today are not required to explain snowmelt at the location of the outflow-channel associated valley networks (§3.5, §3.10.2, Figure 3.12). However, the present atmospheric state is incapable of allowing melt under the Faint Young Sun $\sim$3.0 Gya when the channels formed (Figure 3.12). Channel formation requires either a change in background atmospheric state, or transient heating from impact ejecta or geothermal activity. If transient heating did not occur, then atmospheric pressure $>$50 mbar, non-CO_2 greenhouse forcing, or both, are very likely required to raise the melting probability.

If melting probability $<$1 during plateau layered deposit deposition, why are channels found throughout the stratigraphic column? We suggest three possible explanations. (1) Melting is needed to produce water that indurates the sediment. Since induration increases resistance to aeolian erosion, the stratigraphic record on the Juventae plains preferentially records chaos storms that were accompanied by melting. (2) Runoff accompanied only a few layer-forming events, but the channels cut from the top to the bottom of the sedimentary stack. Meltwater percolated through the stack and cemented all layers. Deeply-incising, rather than superficial, channels are suggested by the observation of negative-relief channel

continuous with channel-topped ridges (Figure 3.15). If the 33-39 layers identifiable in the stratigraphic column correspond to 33-39 lake events, and modeling melt events as a Poisson process, the probability of melting occurring on the plateau at some point in the year following at least one chaos event is 49% - 54% for a one–time melting probability of 2%. (3) The chaos events were correlated with orbital conditions, with chaos events preferentially occurring during times that favored melt.

Movement of the melt pulse through the watershed is not considered here. However, discharge of <0.05 m^3/s is sufficient to move fine sediment through the km-scale drainage networks visible in our DTM (Figure 3.15). With DTM drainage network and channel geometries, runoff of 0.1 mm/hr is approximately the required runoff for mobilization of fine gravel/granules, and runoff of 1.0 mm/hr will mobilize medium gravel (Figure 3.16).

The dendritic channels provide strong evidence for water runoff, and are *prima facie* evidence that global temperatures and pressures permitting surface liquid water runoff persisted (or were revived) well after the Late Noachian/Early Hesperian maximum in valley network formation. However, our melting scenarios are consistent with a transient and localized response to disequilibrium forcing from catastrophic groundwater release – weather, not climate.

3.9 Conclusions

We conclude that:-

1. In mesoscale simulations of lake storms during chaos formation at Juventae Chasma, peak precipitation over land occurs to the SW of the chasm. This corresponds to the location of the observed Juventae plateau channel networks. The location is sensitive to lake surface elevation;

2. Peak snowfall of 1.7 mm/hr water equivalent (w.e.) and mean snowfall of 0.9 mm/hr w.e. occurs at the location of the observed plateau channel networks. These rates are sensitive to lake surface elevation and lake temperature;

3. Mesoscale model output is consistent with a model in which material lofted from Juventae Chasma and transported W by the background wind field contributed to channel formation on the Juventae plateau;

4. The minimum background atmospheric temperature to allow melting of localized snowstorm deposits is sensitive to snowpack albedo, solar luminosity, atmospheric pressure and orbital conditions. Melting is impossible under the Faint Young Sun with today's atmospheric composition. Higher atmospheric pressure, and a modest non-CO_2 greenhouse contribution, are both probably required for melting under the Faint Young Sun;

5. Juventae's plateau channel networks could have formed from localized precipitation, and do not require global warm/wet conditions;

6. The majority of water vapor released to the atmosphere during chaos flooding is trapped by localized precipitation at the chasm edge, and is not available to drive global climate change;

7. This model is not unique. Alternative explanations of channel formation that are compatible with stratigraphic constraints include patchy melting of broadly distributed equatorial snowpack, and spring discharge of groundwater on the plateau early in the formation of Juventae Chasma;

8. Our model strongly predicts that plateau channel networks will not be found > 250 km from a water vapor source. It also predicts that additional plateau channel networks and plateau layered deposits should be identified downwind of large, localized vapor sources elsewhere on Mars.

3.10 Methods

3.10.1 Comparison between area of modeled precipitation and area of observed channels

Because (i) channels are exposed by incomplete erosion of the plateau layered deposits, (ii) the inverted channels are themselves layered, and (iii) channels are found wherever layered deposits are incompletely eroded on the Juventae plateau, we assume that areas containing light-toned layered deposits also contain channels.

We compared model predictions to geologic data in four ways:-

- *Method of Pielke and Mahrer (1978).* Following Pielke (2002), let A_4 be the area of the inmost grid in the MRAMS domain, $P_{i,t}$ be the area of precipitation predicted by meteorological model i above some threshold value t, and G_j be the area of channels and light-toned layered deposits (collectively referred to as "geology", for brevity) mapped using criteria j. Then the skill of the model in predicting geology is

$$skill = \frac{F_E}{F_M} = \frac{(P_{i,t} \cap G_j)/G_j}{P_{i,t}/A_4} \tag{3.5}$$

  where F_E is the fraction of the geology in areas with model precipitation above the threshold, and F_M is the fraction of the model domain over which the model precipitation is above the threshold. The fraction of the model-predicted area that is occupied by geology, or coverage

$$coverage = (P_{i,t} \cap G_j)/P_{i,t} \tag{3.6}$$

is a measure of the tendency of the model to overpredict the observed geology (where a value of 1 corresponds to no overprediction). Here, the null hypothesis is that the association between model and data is due to chance. *skill* and *coverage* are shown in Table 3.3. `juventae_high` shows the greatest skill, for both j. We obtain *skill* values >200 for `juventae_high` and $t = 0.8$ mm/hr. For these cases, the area of overlap between prediction and data is >200 times that expected by chance, showing that the agreement is almost certainly not due to chance.

- *Monte Carlo.* For this metric, we determine the fraction of randomly placed precipitation templates that provide a better fit to the geologic observations than the modeled precipitation. We take the predicted precipitation P for each model i, including snow falling back into the lake (the precipitation 'template'), and randomly translate it in latitude and longitude, wrapping around the boundaries of the inmost model grid (∼1300 km x ∼870 km). This creates a new modeled precipitation grid Q_i. A data grid G_j is constructed by assigning 1 to areas containing mapped inverted channels or light-toned layered deposits and 0 otherwise. We then calculate the cross-correlation as

$$X = G'_j * Q'_i \tag{3.7}$$

where the primes denote normalization (for each trial) by subtracting the nonlake mean and dividing by the nonlake standard deviation. The area of the lake (which is not translated) is masked out in all cases. We repeat this 10^4 times per model. Here, the null hypothesis is that the geology formed from a localized source of some kind, but that the location of this source was uncorrelated with present-day Juventae Chasma. The resulting p-values are 0.005 for `juventae_high` (nominal $X = 0.476$), 0.009 for `juventae_med` (nominal $X = 0.365$), and 0.058 for `juventae_low` (nominal $X = 0.044$). These are for the map of Le Deit et al. (2010). The null hypothesis is rejected at the 99.5% level for `juventae_high`: if the observed channels and layered deposits formed from a localized source of some kind, it was almost certainly close to the present-day center of Juventae Chasma.

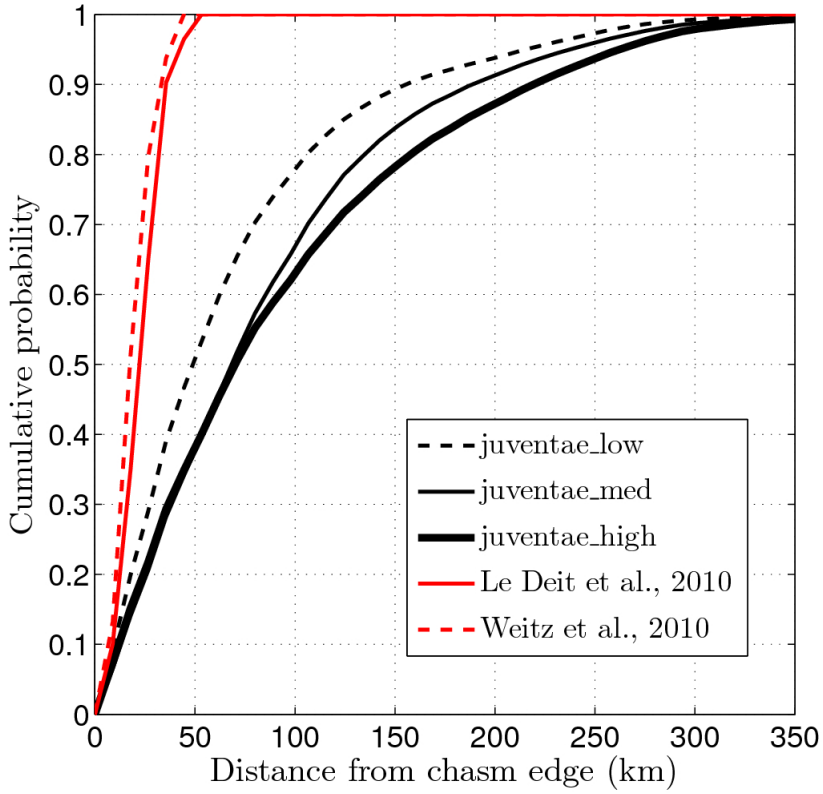

Figure 3.18 Comparison of falloff of precipitation with falloff of mapped area of channels and layered deposits. Because of an arbitrary mapping cutoff, layered deposits likely extend further than shown.

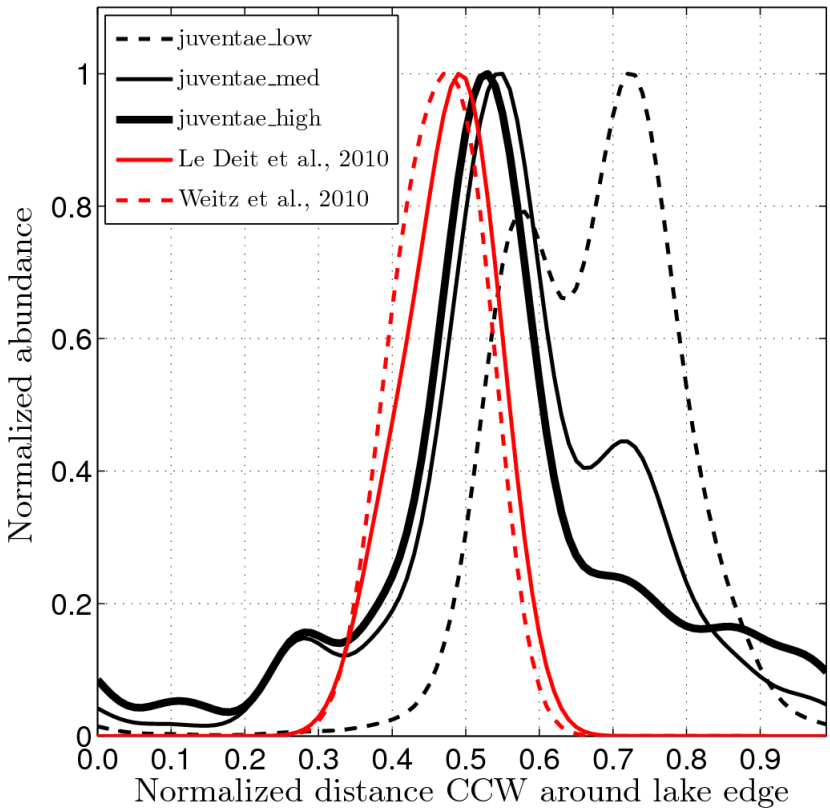

Figure 3.19 Comparison of azimuth of precipitation with azimuth of mapped channels.

- *Azimuth.* We assign each land pixel to its nearest pixel on the perimeter of the lake. We then assign each perimeter pixel to its normalized distance along the circumference. Both the perimeter-matched geologic data and the perimeter-matched model output are then smoothed with a gaussian kernel of full width at half maximum equal to 5% of lake circumference. The results are shown in Figure 3.19. All models produce a broader distribution of snowfall with azimuth and are also biased counterclockwise (from SW to S) with respect to the data. This bias is least severe for `juventae_high`. `juventae_high` also shows the best overall fit to the data. By cyclic translation of the smoothed and area-normalized precipitation pattern (the "prayer-bead" method, described for exoplanet data analysis by (Southworth, 2008)), we can find the percentage of perturbed patterns that would provide a better least-squared fit to the smoothed data than our actual model. For the Le Deit et al. (2010) geology, this percentage is 7% for `juventae_high`, 12% for `juventae_med`, and 36% for `juventae_low`. The corresponding values for the Weitz et al. (2010) geology are 10%, 16%, and 39%. Note that the azimuthal distributions shown in Figure 3.19 are maximum-normalized, not area-normalized.

- *Falloff of precipitation.* Figure 3.18 shows cumulative distribution functions (CDFs) of geology and precipitation. All geology is found within 60 km of the chasm edge, but the e-folding distance of the cumulative precipitation is significantly larger, 70-110 km. $\sim$95% of snow is found within 250 km of the chasm edge.

All these metrics show that the area of precipitation is more extensive than the mapped area of channel networks. This may be an artifact of incomplete preservation and incomplete high-resolution imaging. For example, there is a 25km-diameter ejecta blanket in our area of highest modeled precipitation that may be obscuring underlying channels. If precipitation is necessary to form or indurate plateau layered deposits, decline in the precipitation at 100-200 km from the chasm (Figure 3.18) will create thin, or weakly-indurated deposits. These could easily be missed during mapping, removed by the wind, or both. It is possible that the relatively low horizontal resolution of our simulations is artificially broadening our modeled precipitation. Alternatively, there may be a threshold precipitation level to produce layered deposits and channels. For example, sublimation losses may occur during the months between deposition and the beginning of the melt season. These sublimation losses are not included in our simulations, and will thin the snowpack everywhere while reducing the area of remaining snow. Sediment mobilization is very sensitive to small changes in runoff:

$$Q_{sed} \propto (\tau_b - \tau_{crit})^{3/2} \tag{3.8}$$

where Q_{sed} is sediment flux, $\tau_b \propto H$ is bed shear stress and is proportional to flow depth H, and τ_{crit} is critical bed shear stress. If snow availability is a limiting factor, this will focus channel incision on areas with high precipitation rates.

3.10.2 Snow melting model

We use a simple probabilistic melting model to determine the likelihood of melting for the range of orbital conditions possible on pre-modern Mars.

We simulate the temperatures within snowpack using a 1D column model that includes radiative, conductive, and turbulent cooling fluxes. Obliquity ϕ, eccentricity e, solar longitude of perihelion L_p, season L_s, atmospheric pressure P_{atm}, and geologic age τ are varied – the ranges swept are given in Table 3.5. We calculate the annual maximum surface temperature that the snow would reach *ignoring buffering at the melting temperature* - if this temperature >273.15K, melting should occur sometime during the year. Orbital parameters are not known deterministically for ages $\gg$10 Mya (Laskar et al., 2004). However, the probability distribution for orbital elements as a function of time has been calculated (Laskar et al., 2004). Therefore, we calculate temperatures for all orbital states and multiply each by the probability of that state. The Juventae channels are at 4°S, and all our calculations are for the equator.

Within the snowpack, material properties are assumed uniform with depth and heat flow is by conduction only. Energy balance at the surface is given by

$$\left(\frac{1}{\rho c_p \Delta z}\right)\frac{\partial T}{\partial t} = -k\frac{\partial T}{\partial z} - \epsilon\sigma T^4 + LW\downarrow + (1-RCF)(1-\alpha)L \\ -SH_{free} - SH_{forced} - LH_{free} - LH_{forced}$$

where ρ is snow density, c_p is snow heat capacity, Δz is the thickness of the subsurface layer whose upper boundary is the surface ($\sim$2.5mm for our nominal parameters), T is the surface temperature, k is snow thermal conductivity, $LW\downarrow$ is downwelling longwave radiation, RCF is the Rayleigh-scattering correction factor (the difference between insolation reaching the surface in the presence of an atmosphere and in the absence of an atmosphere), α is snow albedo, SH_{free} corresponds to free sensible heat losses driven by atmosphere-surface temperature differences, SH_{forced} corresponds to forced sensible heat losses caused by cool breezes over warm ground, LH_{free} corresponds to evaporative cooling by free convection when the atmosphere has relative humidity <1, and LH_{forced} corresponds to additional evaporative cooling when the wind is nonzero. Table 3.5 lists parameters used.

The initial condition at the surface is slightly cooler than radiative equilibrium, decaying with an e-folding depth equal to the diurnal skin depth to the energy-weighted diurnal average temperature at depth. For a range of L_s, we integrate forwards in time for several sols using constant seasonal forcing until the day's maximum surface temperature has converged to <0.025K. The subsurface is assumed to be in equilibrium with the radiative forcing for a given L_s - month-to-month thermal inertia is not considered.

Radiative terms: We use a 1D radiative-convective column model of the atmosphere to populate look-up tables of $LW\downarrow$ as a function of surface temperature and surface pressure,

and RCF as a function of atmospheric pressure and solar zenith angle. (Both look-up tables were provided by Itay Halevy from output of a column radiative transfer calculation; Halevy et al. (2009)). The atmosphere is assumed to be entirely CO_2. P_{atm} in our calculations is for the elevation of the Juventae plateau (+2km). This is 20% lower than P_{atm} at datum.

Free convective terms: Our treatment of turbulent fluxes closely follows Dundas and Byrne (2010). We set

$$SH_{free} = 0.14(T - T_a)k_a \left(\left(\frac{C_p \nu_a \rho_a}{k_a} \right) \left(\frac{g_{Mars}}{\nu_a^2} \right) \left(\frac{\Delta\rho}{\rho_a} \right) \right)^{1/3} \tag{3.9}$$

where T_a is the atmospheric temperature, k_a is the atmospheric thermal conductivity, C_p is heat capacity of air, ν_a is temperature-dependent viscosity of air, $\rho_a \propto P_{atm}$ is density of air, g_{Mars} is Mars gravity, and $\Delta\rho/\rho_a$ is the density contrast between air in equilibrium with the ground and air overlying the surface layer.

$\Delta\rho/\rho_a$ is given by

$$\frac{\Delta\rho}{\rho_a} = \frac{(m_c - m_w) e_{sat} (1 - r_{humidity})}{m_c P_{atm}} \tag{3.10}$$

Here, m_c is the molar mass of CO_2 and m_w is the molar mass of H_2O. $r_{humidity}$ is the relative humidity of the overlying atmosphere. $e_{sat} = 3.69 \times 10^{12} e^{(-6150/T)}$ is the saturation vapor pressure over water ice, from Cuffey and Paterson (2010) equation 4.5. This agrees to within 1% with the Hardy (1998) ITS 90 curve fit for 175K $< T <$ 298K. Equation 3.10 assumes that water vapor pressure is a minor component of the overall atmospheric pressure, and is simpler but less accurate than Eq. 10 in Dundas and Byrne (2010).

T_a is parameterized as (Dundas and Byrne, 2010)

$T_a = T_{min}^{b_{DB}} T^{1-b_{DB}}$

where T_{min} is the coldest (nighttime) surface temperature experienced by the model, and b_{DB} is the Dundas-Byrne 'b', a fitting parameter. As P_{atm} increases the turbulent coupling between the surface and atmosphere becomes stronger, so b_{DB} decreases. We obtain $b_{DB}(P_{atm})$ by fitting to the globally-averaged noontime atmosphere-surface temperature difference from GCM models (values provided by Melinda A. Kahre; Kahre and Haberle (2010)).

We let

$$LH_{free} = L_{subl} 0.14 \Delta\eta \rho_a D_a \left(\left(\frac{\nu_a}{D_a} \right) \left(\frac{g_{Mars}}{\nu_a^2} \right) \left(\frac{\Delta\rho}{\rho} \right) \right)^{1/3} \tag{3.11}$$

where L_{subl} is the latent heat of sublimation of ice, $\Delta\eta$ is the difference between atmosphere and surface water mass fractions, and D_a is the temperature-dependent diffusion coefficient of H_2O in CO_2.

Forced convective terms: We parameterize

$$SH_{forced} = \rho_a C_p u_{wind} A(T_a - T) \tag{3.12}$$

where C_p is the atmospheric heat capacity and u_{wind} is the near-surface wind speed. The drag coefficient A is given by

$A = \frac{K_{vonk}^2}{log(z_{anem}/z_o)^2}$

where K_{vonk} is von Karman's constant, z_{anem} is anemometer height and z_o is surface roughness.

Near-surface wind speed u_{wind} in Mars GCMs is expected to decrease with increasing pressure and decreasing solar luminosity. The four-season average of European Mars Climate Database (E-MCD; Millour et al. (2008)) "MY24" simulation globally-averaged near-surface wind speeds at the present epoch is 3.37 m/s. We extrapolate this to pressures up to 250 mbar using a logarithmic falloff of mean wind speed with increasing pressure calibrated using GCM model output for pressures between 6 and 80 mbar (supplied by Melinda A. Kahre). We lower the wind speeds by a factor of 1.08 for the faint young Sun using the ratio of wind speeds for two 60 mbar simulations that differ only in solar luminosity. Simulations also suggest u_{wind} depends on orbital parameters (Haberle et al., 2003), but we ignore this.
We set

$$LH_{forced} = L_{subl} \frac{M_w}{kT_{bl}} u_{wind} e_{sat} (1 - r_{humidity}) \tag{3.13}$$

where M_w is the molecular mass of water, and k is Boltzmann's constant.

Albedo: The probability of melting depends on snow albedo, which is high for pure snow but much lower for realistic, dust-contaminated snow. Warren and Wiscombe (1980) show that 1000 ppmw of Saharan dust can reduce ice albedo from >0.9 to 0.3. In the words of Langevin et al. (2005), "Water ice is very bright in the visible spectrum when clean, but even a small amount of dust contamination can reduce the albedo to values close to that of the dust itself if the dust grains are embedded in ice grains." Clow (1987) shows that 1000 ppmw dust reduces snow albedo to 0.45-0.6 for ice grain sizes 400μm - 100μm, respectively. This is for precipitation grain sizes in our model; metamorphism will increase grain size and decrease albedo. The mean bolometric albedo of bright regions in Mars' North Polar Residual Cap is inferred to be 0.41 from energy balance (Kieffer et al., 1976). Near-infrared spectroscopy has identified seasonal water ice layers up to 0.2 mm thick on pole-facing slopes in the Mars low latitudes (Vincendon et al., 2010). Analysis of the spatial and seasonal dependence of these detections indicates that low-latitude surface water ice has albedo 0.3 – 0.4 (Vincendon et al., 2010). Modeling of OMEGA data indicates that water-rich terrains in the South Polar Layered Deposits have albedo $\sim$ 0.3 – 0.4 (Figure 7 in Douté et al. (2007)). Measurements of the gray ring component of Dark Dune Spots in Richardson Crater at 72°S show it to be composed of seasonal water ice deposits with an albedo of 0.25 – 0.30 (Kereszturi et al.,

2011). When melting starts, the albedo of dust-contaminated ice remains low because "when snow melts, the impurities often tend to collect at the surface rather than washing away with the meltwater" (Warren, 1984), forming a lag. Water has a low albedo, so stream and melt pond albedo is lower than unmelted surface albedo. Gardner and Sharp (2010) show that 2 ppmw soot can greatly reduce snow albedo. Soot is 200× more optically effective than Earth crustal dust, and presumably more effective than Mars dust. We use an albedo of 0.28 (the albedo of Mars' dust continents; Mellon et al. (2000)). This corresponds to very dirty snow. Higher albedos will lead to lower melting probabilities (Chapter 2).

The melting is also sensitive to orbital conditions. For example, at the equator, high eccentricity is more favorable for melting than is low eccentricity (Chapter 2).

3.10.3 HiRISE stereo DTMs

HiRISE DTMs were generated using SOCET SET following USGS recommended procedure.

DTM1: Juventae1, PSP_003223_1755/PSP_003724_1755

DTM2: Juventae2, PSP_004423_1755/PSP_005412_1755

DTM3: Ganges1, PSP_005161_1720/ESP_016237_1720

All DTMs, together with the corresponding orthorectified HiRISE images, can be obtained for unrestricted further use from Edwin S. Kite.

In addition, we made use of PDS released files for a Juventae plateau stereopair, PSP_003434_1755 / PSP_003579_1755.

Table 3.5 Parameters used in the melting model (§3.5, §3.10.2).

Symbol	Parameter	Value and units	Notes/Reference
ϕ	obliquity	0° - 80°	[Laskar et al., 2004]
e	eccentricity	0 - 0.16	[Laskar et al., 2004]
L_p	solar longitude of perihelion	0° - 180°	symmetry at equator
L_s	season	0° - 360°	
P_{atm}	atmospheric pressure	1220 - 19520 Pa	2-32× present CO_2
α	albedo of dusty snowpack	0.28	Very dusty snow
τ	time of interest	0 - 3.5 Gyr ago	[Mangold et al., 2004]
σ	Stefan-Boltzmann constant	5.67 x 10^{-8} J s^{-1} m^{-2} K^{-4}	
$sollength$	duration of 1 Mars sol	88775 s	
R_{gas}	gas constant	8.3144 J/(mol K)	
g_{Mars}	Mars surface gravity	3.7 m/s^2	
m_c	Molar mass of CO_2	0.044 kg	
m_w	Molar mass of H_2O	0.018 kg	
M_w	Molecular mass of H_2O	2.99 x 10^{-26} kg	
ρ_{now}	Density of atmosphere, present-day	0.02 kg/m^3	NSSDC
$P_{atm,now}$	Pressure of atmosphere, present-day	610 Pa	NSSDC
M_w	Molecular mass of H_2O	2.99 x 10^{26} kg	
K_{vonk}	von Karman's constant	0.4	
z_o	Roughness length	0.1 mm	Polar snow. [Brock et al., 2006.]
z_{anem}	Anemometer height	5.53 m	E-MCD
u_{wind}	Reference near-surface wind speed	3.37 m/s	E-MCD (4 season "MY24" average)
$r_{humidity}$	Relative humidity	0.25	
C_p	Specific heat of Mars atmosphere	770 J/kg/K	
k_b	Boltzmann's constant	1.381 x 10^{23} m^2 kg s^{-2} K^{-1}	
L_{subl}	Latent heat of sublimation	2.83 x 10^6 J/kg	
ϵ	Thermal emissivity of snow	0.98	
ρ	Density of snowpack	350 kg/m^3	[Carr & Head, 2003]
C_p	Specific heat capacity of snow	1751 J/kg/K	[Carr & Head, 2003]
k_{snow}	Thermal cond. of snowpack	0.125 W/m/K	[Carr & Head, 2003]

Chapter 4

Snowmelt-limited formation and distribution of sedimentary rocks on Mars.

This chapter describes collaborative work by Edwin S. Kite, Michael Manga, Itay Halevy, and Melinda A. Kahre. Authors' contributions were as follows: E.S.K. conceived, designed and carried out research, and wrote the chapter except as described below. M.M. supervised research. I.H. and M.A.K. contributed results from atmospheric models.

The first paragraph on "Radiative terms" in Section 4.4.2 was drafted by coauthor Itay Halevy, and describes work done by him. The rest of the chapter was written by Edwin S. Kite.

Summary

Martian sedimentary rocks record surface runoff and aqueous mineralization ∼3.8-3.0 billion years ago (Ga) (Malin and Edgett, 2000; McLennan and Grotzinger, 2008; Murchie et al., 2009b; Lewis et al., 2008). The water source, environment, and paleoclimatic context of these rocks remain unclear, especially in light of the difficulty of achieving warm temperatures on early Mars (Tian et al., 2010). Here we use an energy-balance model of snowmelt on Early Mars, integrated over all possible orbital forcings (Laskar et al., 2004), to model the spatial distribution of sedimentary rocks formed by localized snowmelt-processes at average temperatures little higher than today. The preference of sedimentary rocks for low elevations suggests atmospheric pressures not much greater than 100 mbar at the time of formation, consistent with snowmelt on a marginally warmer planet. Geochemical evidence (Elwood Madden et al., 2009; Berger et al., 2009; Ming et al., 2008; Hurowitz and McLennan, 2007; Amundson et al., 2008), channel discharge estimates (Irwin et al., 2005b), and total water

requirements are also suggestive of snowmelt-limited rock-forming processes and a top-down water source. Our results suggest intermittency of snowmelt and long globally-dry intervals, unfavorable for past life on Mars. This model is testable with the Mars Science Laboratory rover, Curiosity, at Gale Crater.

4.1 Introduction

What environmental conditions allowed widespread dendritic valley networks and sedimentary rocks to form on Early Mars, a planet in a distant orbit around the Faint Young Sun? What caused that environment to deteriorate? The simplest solution to this *Early Mars climate problem* is that Early Mars had a multibar CO_2-H_2O greenhouse atmosphere (Haberle, 1998). Multibar atmospheres can produce annual mean surface temperatures $\bar{T} > 273$K, but only for the thickest atmospheres and if there is a hemispheric ocean (Wordsworth et al., 2010; Wordsworth, 2010). Multibar CO_2 atmospheres also tend to collapse irreversibly onto the poles at low obliquity (Soto et al., 2011). SO_2 is a stronger greenhouse gas than CO_2, and sulphates are abundant in Mars soils and sedimentary rocks, but volcanogenic SO_2 is quickly removed by liquid in the Mars atmosphere (Tian et al., 2010). An alternative is rainout from ephemeral steam greenhouses produced by basin-forming impacts into icy crust (Segura et al., 2002, 2008; Toon et al., 2010). Another alternative is seasonal snowmelt (Clow, 1987; Squyres and Kasting, 1994; Gaidos and Marion, 2003). Seasonal snowmelt requires annual maximum surface temperature $T_{max} > 273$K on Early Mars, which requires more modest changes to the present greenhouse forcing than $\bar{T} > 273$K. Low abundance of surface-formed weathering minerals (Ehlmann et al., 2011), the immaturity of Martian drainage networks (Aharonson et al., 2002), and the absence of surface carbonate sinks large enough to account for an early multibar CO_2 atmosphere, suggest globally cold surface conditions with minimal runoff. This motivates a new look at seasonal-snowmelt environmental models.

In this chapter we model the formation and distribution of sedimentary rocks of Early Mars. Formation of light-toned, layered and frequently sulfate-bearing sedimentary rocks peaked in the Hesperian, which is relatively late in stratigraphic sequence of evidence for stable surface liquid water on Mars (Carr and Head, 2010; Murchie et al., 2009b). The sedimentary rocks are clearly preceded by most clay formation on Mars (Ehlmann et al., 2011; Fassett and Head, 2011). Sedimentary clays are found interbedded with the oldest sulfate-bearing sedimentary rocks on Mars, but these clays may be reworked (Barnhart and Nimmo, 2011). Although the sedimentary rocks do contain some channels preserved in inverted relief, the sedimentary rocks are spatially separated from and mostly postdate the large-scale, regionally integrated valley networks of the Late Noachian/Early Hesperian (Carr and Head, 2010; Fassett and Head, 2011; Andrews-Hanna and Lewis, 2011). Therefore, the observed sedimentary rocks are not simply the terminal deposits of the classic valley networks, and the climate that created the classic valley networks could have been different from the climate

that subsequently created the sedimentary rocks (Andrews-Hanna and Lewis, 2011). Most sedimentary rocks also postdate the large impacts of the Late Heavy Bombardment. Many have quasi-periodic bedding suggesting orbitally-paced deposition (Lewis et al., 2008, 2010). These observations are inconsistent with brief bursts of rapid sedimentary rock formation during impact-induced greenhouse events. The main sulfate-bearing sedimentary rocks occur relatively late in the stratigraphic sequence of evidence for stable surface liquid water on Mars: they are postdated only by opaline silica deposits on the Valles Marineris plateau (Chapter 3), relatively minor fluvial channels associated with ice deposits and volcanoes, and rare young sulfate deposits.

Observations suggest liquid water availability was limiting for sedimentary rock formation on Mars. Geochemistry strongly suggests low water:rock ratios (Berger et al., 2009; Hurowitz and McLennan, 2007), and that the cumulative duration of water-rock interaction was short (Elwood Madden et al., 2009; Hausrath et al., 2008). The present day extent of sulfate-bearing sedimentary rock outcrops is small, and the persistence of opal, jarosite and olivine indicates minimal water-rock interaction since exposure (Tosca and Knoll, 2009; Olsen and Rimstidt, 2007). Away from the sedimentary rocks themselves, there is little evidence for aqueous mineralization and especially clay formation elsewhere on the planet at the time when most sulfate-bearing sedimentary rocks formed (Murchie et al., 2009b; Mustard et al., 2009; Fassett and Head, 2011). Low specific grind energy of sandstones indicates weak cementation (Herkenhoff et al., 2008a). Elemental profiles indicate downward mobilization of soluble elements, and globally soils formed "with little aqueous alteration under conditions similar to those of the current Martian climate" (Amundson et al., 2008; Bandfield et al., 2011). Dividing the total thickness of sedimentary rock deposits by the thickness of quasi-periodic layers and multiplying by the Milankovitch periods thought to indicate that the sedimentary rocks formed in 1-10 Ma Lewis et al. (2010). This is a small fraction of Mars' history. Geomorphic evidence that the Mars surface environment has only marginally melted since the Noachian includes mean erosion rates $\sim 10^{-10}$ m/yr (Golombek et al., 2006), and very minor crater infilling and post-Noachian valley network formation (Fassett and Head, 2008a) relative to Noachian and pre-Noachian crater infilling and valley network formation. These data argue for a short-lived and downward-infiltrating post-Noachian water supply, suggestive of transient liquid water that is generated only during a brief melt season.

If surface liquid water availability was limiting for sedimentary rock formation, then a map of liquid water availability is also a map of sedimentary rocks. Maxima in liquid water availability should also correspond to maxima in sedimentary rock thickness. In the only previous global model of sedimentary rock formation on Mars, Andrews-Hanna et al. (2007) tracked groundwater flow in a global aquifer that is recharged by a broad low-latitude belt of precipitation. Groundwater upwelling is focussed in low-lying, low-latitude areas, generally consistent with the observed distribution of sedimentary rocks. This model assumes $\bar{T} > 273$K, in order to avoid the development of an impermeable cryosphere. Especially in light of the Faint Young Sun predicted by standard solar models, temperatures this high require greenhouse forcing much stronger than today's Mars. Our model also assumes that

liquid water is limiting for sedimentary rock formation, but that it is supplied from locally-derived snowmelt, rather than a deep global aquifer. Groundwater flow is confined to shallow, local aquifers perched above the cryosphere. This allows annually– and planet–averaged temperatures similar to today's Mars, and reduces the required change in climate forcing from the present state. If Mars climate once sustained $\bar{T}$ >273K, then it must have passed through climate conditions amenable to snowmelt en route to the present state.

4.2 Snowmelt hypothesis and test

We hypothesize that Early Mars' sedimentary rocks are atmospherically-transported sediments that were indurated by snowmelt-limited processes, such as vertical infiltration and shallow groundwater flow, seasonal rivers and streams, and chemical precipitation beneath ice-covered lakes.

We assume that sedimentary rock formation on Mars requires water, and was limited by the availability of water to form aqueous cements. At the Opportunity landing site, evaporitic sandstones (60% chemical precipitates, 40% siliciclastic by weight) record multiple episodes of groundwater recharge and aqueous cementation. Sulphates and hematite are present in sedimentary rocks throughout Meridiani and Valles Marineris (Bibring et al., 2007), suggesting that aqueous cementation as observed by Opportunity was widespread. Pressure-solution recrystallization can occlude porosity and lithify weak evaporites at $P \sim$ 30 bars, without aqueous cementation (Warren, 2006). However, water is still required in order to form the evaporites.

Sediment availability is unlikely to have limited sedimentary rock formation on Mars, because transport rates for atmospherically-transported sediment on today's Mars are comparable to past accumulation rates of sedimentary rocks. Observations of Mars dust storm deposits and lander observations suggest a gross deposition rate of dust of a few μm/yr (Arvidson et al., 1979; Geissler, 2005; Geissler et al., 2010). These accumulation rates are a factor of 1-10 less than the accumulation rate inferred for sedimentary rocks: 20-50 μm/yr at the best-measured site (Lewis et al., 2008), or >2.2 μm/yr in E Meridiani (Zabrusky et al., 2011). Given the difference in age, this is not a large difference. Despite the low atmospheric pressure, some aeolian bedforms are active today or have been in the recent past (Bourke et al., 2008; Chojnacki et al., 2011; Hansen et al., 2011; Silvestro et al., 2010). Aeolian transport and dust lifting on Mars is very sensitive to small increases in atmospheric pressure (Newman et al., 2005). Because Mars has lost atmospheric CO_2 over time (Barabash et al., 2007; Phillips et al., 2011), gross dust deposition rates were probably >> a few μm/yr on Early Mars. Present-day reservoirs of atmospherically-transported sediment are large: for example, dust deposits at high elevations on Tharsis are >6m thick (Bridges et al., 2010) and tens of meters thick at E Arabia Terra (Mangold et al., 2009). Sedimentary rock formation is probably not limited by fluxes or reservoirs of atmospherically-transported sediment. The difficulty is instead to pin the sediment in place for >3.3 Gyr.

Antarctica's McMurdo Dry Valleys are a terrestrial analog for fluvial erosion and melt-limited sedimentary rock formation in a $\bar{T} < 273$K environment (Doran et al., 2010). Temperatures are well below freezing at depth, and weathering and mineralization is confined to lakes, hyporheic zones, and a shallow active layer. However, seasonal river discharges reach 20 m^3 s^{-1} (McKnight, 2011), fluvial valleys incise up to 10m deep (Shaw and Healy, 1980), and annually-averaged weathering intensity within the hyporheic zone is greater than in temperature latitudes (Nezat et al., 2001). Outcrops of gypsum, carbonate evaporites, and algal limestone sediments show that sediments have accumulated at the base of perennial lakes for 300,000 years (McKay et al., 1985; Hendy, 2000).

The snowmelt hypothesis predicts that Early Mars should have encountered orbital conditions that were favorable for snowmelt at observed sedimentary rock locations. This should be robust to reasonable variations in past climate parameters. Maxima in snowmelt should also correspond to maxima in sedimentary rock thickness. To test this prediction, we do the following:– For a given trial set of past climate parameters and orbital parameters, we calculate potential snow temperature for all seasons and latitudes using a 1D surface energy balance model. Using the 1D model output for a range of pressures, we map the potential annual maximum snow temperatures and annual-average snow sublimation rates onto topography. We assign warm-season snow to locations most favorable for interanually persistent snow: spatial minima in annual-average potential sublimation rates. Snowmelt occurs if any of the warm-season snow locations have maximum temperature >273.15K. We thus obtain maps of snow stability and snowmelt (if any) for the given climate parameters and orbital parameters. Mars has a very wide range of orbital forcing – and a correspondingly wide range in tendency to melt – so modeling average orbital conditions is neither sufficient nor appropriate. Instead, we repeat this for all possible Early Mars orbital parameters, convolving the outputs with the Early Mars probability distribution function for Early Mars (Laskar et al., 2004; Laskar, 2008). The output is a map of predicted snowmelt on Mars integrated over geologic time, which can be compared to observed sedimentary rock abundance and thickness data. We repeat this entire sequence for all plausible past climate parameters. Marginalizing over climate parameters quantifies the robustness of the match between data and model to uncertainties in Mars' past climate. Assuming the snowmelt model is correct, the combination of climate parameters that produces the best correlation between model predictions and data is the best-fit Early Mars climate.

4.3 Data

The distribution of sedimentary rocks on Mars suggests that surface water availability was narrowly concentrated near the equator and at low elevations. The Mars Orbiter Camera Narrow Angle (MOC NA) took 97,000 images of Mars between 1997 and 2006 (Malin et al., 2010). 4% showed "layered rock outcrops of probable or likely sedimentary origin" (Malin et al., 2010). Of those, 64% are within 10° of the equator (60% when the Valles Marineris

region is excluded) (Figure 4.1). Blanketing by young midlatitude mantling deposits may contribute to the paucity of sedimentary rocks poleward of 35°, but cannot explain the rarity of sedimentary rocks at 10-35° latitude relative to the equatorial belt. The +/- 10° band is not unusual in thermal inertia, dust cover index, albedo, or surface age distribution, so a dependence of sedimentary rock on these parameters could not explain the latitudinal distribution. Sedimentary rocks are also biased low by 2km in median elevation (Figure 4.2), although this does not account for the equatorial concentration. The Valles Marineris are a unique tectonic feature containing many sedimentary rocks. To make sure that our conclusions are insensitive to this unique tectonic feature, we defined a large "Valles Marineris box" from 260E - 330E, 20S - 20N. Excluding all data within this box does not change our conclusions. Dividing the number of sedimentary rock images by the total number of MOC NA images within a given latitude bin also does not affect the conclusion that there is a strong equatorial concentration of sedimentary rocks in the MOC NA database.

Locations in the MOC NA sedimentary rock database are likely to be strongly correlated with the true distribution of sedimentary rocks on Mars, even though MOC NA did not sample the planet completely or uniformly. MOC NA imaged only 5.5% of Mars' surface (Malin et al., 2010), but the Mars Reconnaissance Orbiter Context Camera (CTX) has since surveyed >40% of the planet at comparable resolution to MOC NA (Edgett and Malin, 2008) and has not found large areas of sedimentary rock missed by MOC NA. MOC NA targets were selected on a 1-month rolling cycle on the basis of Viking imagery, previous MOC images, and the demands of other Mars missions (Malin et al., 2010). Sedimentary rocks were among the highest scientific priorities of the MOC investigation (Malin and Edgett, 2000; Malin et al., 2010), so there is a high density of MOC NA footprints in areas of sedimentary rocks identified early in the mission. Maps of the relative abundance of sedimentary rocks are only slightly broader when defined using the fraction of MOC NA images showing sedimentary rocks within a given spatial bin than when defined using the absolute number of sedimentary rock observations in a given spatial bin, with the largest broadening in Northern Hellas. We use the absolute distribution of sedimentary rock images as our modeling target, because high relief near canyons and craters is important to the model output, but is smeared out by the spatial averaging necessary to calculate a fraction of all images. The definition of sedimentary rock used by the MOC NA team excludes two areas, the Terra Sirenum drape deposit and a large part of the Medusae Fossae Formation, both of which are sedimentary in origin (Grant et al., 2010). However, the Terra Sirenum drape deposit has a phyllosilicate-rich mineralogy that is distinct from the sulphate-bearing sedimentary rocks that are the focus of this paper (Ehlmann et al., 2011), and the entire area of the Medusae Fossae Formation is consistently predicted to be a global near-maximum in sedimentary rock accumulation by our orbitally-integrated model output. Therefore, neither of these omissions from the database is important to our results.

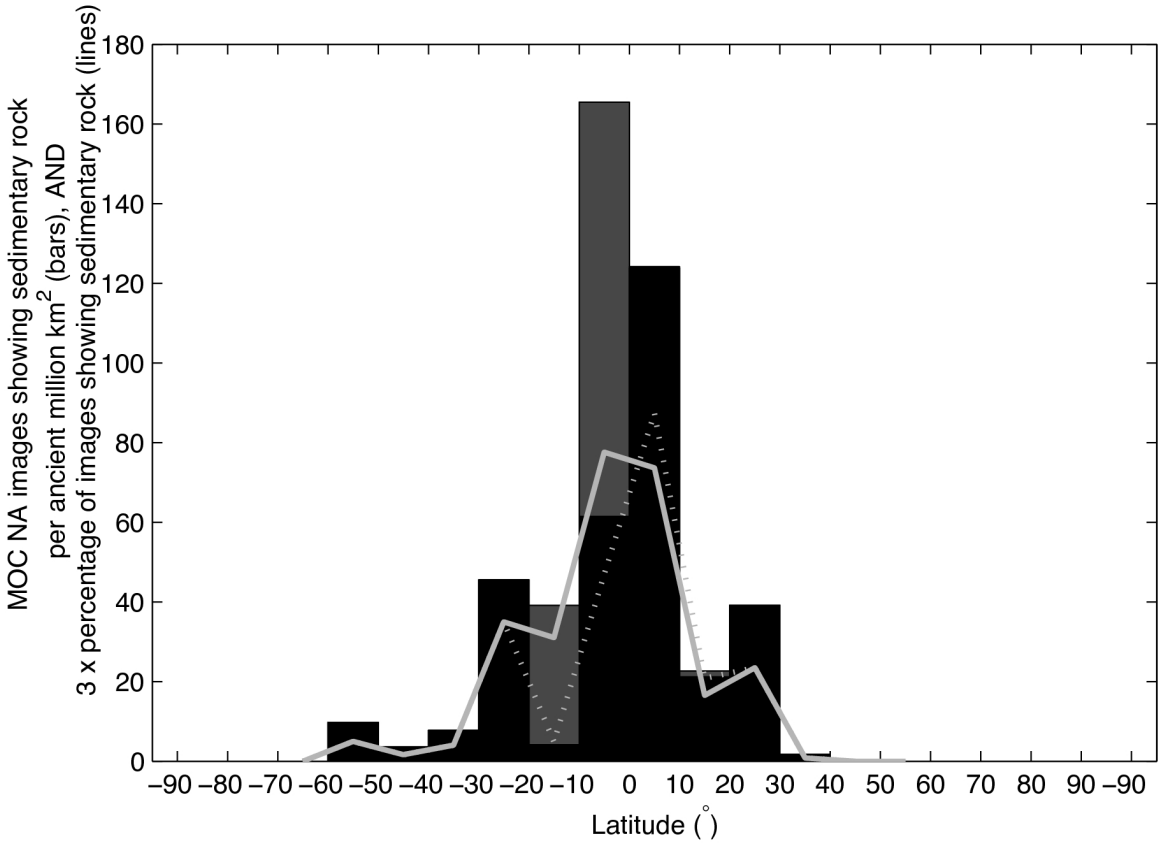

Figure 4.1 Latitudinal dependence of sedimentary rocks, masking out recently resurfaced terrain. The bar graph corresponds to sedimentary rock observations per million km^2 of ancient terrain. For the histogram, dark gray blocks are the contribution from the Valles Marineris region, and black blocks are the contribution from all terrain outside Valles Marineris. The line graph corresponds to the percentage of all ancient-terrain MOC-NA observations showing sedimentary rock, as a function of latitude. The solid gray line corresponds to the percentage of all ancient-terrain MOC-NA observations showing sedimentary rock, and the dashed gray line is the same but with observations near Valles Marineris excluded.

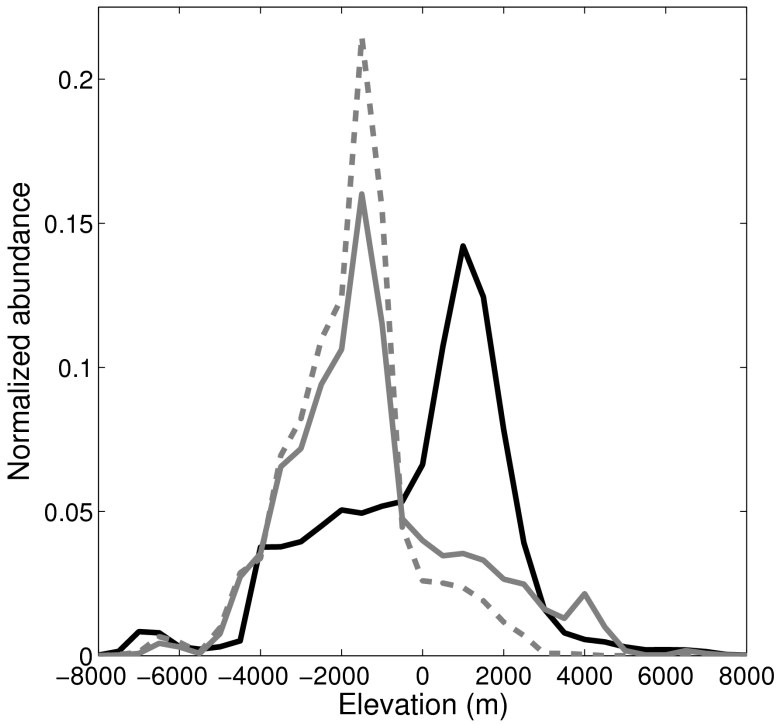

Figure 4.2 Elevation dependence of sedimentary rocks, masking out recently resurfaced terrain. Elevation bin size is 500m. Gray line is normalized histogram of terrain with sedimentary rocks, and black line is histogram of all ancient terrain. Dotted gray line is the normalized histogram of terrain with sedimentary rocks, after masking out Valles Marineris. Median sedimentary rock elevation is ∼2km lower than median ancient terrain.

We exclude from our analysis areas that have been resurfaced since the Hesperian peak of sedimentary rock formation. This is because resurfacing would conceal older rocks. The best available global geological map of Mars dates from the Viking era. Instead of using the old map, we hand-georeferenced Figure 2 from Nimmo and Tanaka (2005) onto MOLA topography, and traced areas mapped as Late Hesperian or Amazonian materials (34% of the planet). These areas contain 141 images of sedimentary rocks (3.5% of total), mostly from the Medusae Fossae Formation and the plateaux surrounding Valles Marineris. We interpret these rocks as a late tail in sedimentary rock formation, and retain them in the plots of elevation and latitude dependence. Omitting them does not change our conclusions. Because we assume image center coordinates are close to the locations of sedimentary rocks, we exclude images from orbits early in the mission, when image footprints could be large

(the Science Phasing, FHA, and Aerobraking phases). This leaves $n = 3965$ sedimentary rock images from the M,E,R, and S phases.

Changes in Mars' topography since 3.5 Gya have been minor (Werner, 2009; Kite et al., 2009; Matsuyama and Manga, 2010), with one exception being the growth of the sedimentary mounds themselves.

To be successful, any model for the origin of the sedimentary rocks must also match sedimentological and paleodischarge constraints from the same time interval and location, including the total thickness of observed deposits, and accumulation rate data.

4.4 Model

We hypothesize that the distribution of sedimentary rocks on Mars is an orbitally-integrated, wet-pass-filtered record of snowmelt-limited processes. To predict past snowmelt distribution on Mars, we need to know (i) where the snow is and (ii) whether it melts.

Because Mars has a very wide range of orbital forcing (Touma and Wisdom, 1993) – and a correspondingly wide range in tendency to melt – evidence that the sedimentary rocks formed in a small fraction of Mars' history (Lewis et al., 2010) implies that negligible melting occurred under mean orbital conditions. Water-limited sedimentary rock formation is a wet-pass filter of Mars climate history that only records environmental conditions when orbital conditions are near-optimal for melting. Modeling average orbital conditions is neither sufficient nor appropriate.

It is not practical to run 3D Global Climate Models (GCMs) for all possible orbital forcings. Instead, we solve a 1D snowpack-energy-balance equation for all locations: this accounts for evaporative cooling, Rayleigh scattering, and a simplified greenhouse effect, but neglects horizontal transport of energy by the wind and local slopes. The greenhouse effect parameterization uses a simplified atmospheric thermal structure, with an adiabatic lapse rate pinned to the surface temperature and to an isothermal stratosphere. We set an upper bound on the error introduced by this approximation in the section on "Radiative terms" below. We use the results to mask out locations where snow is unstable to sublimation, and seek annual maximum temperatures T_{max} >273K in the locations where snow is most stable. We weight the resulting snowmelt maps by the probability of the corresponding orbital forcing (Laskar et al., 2004), and compare the rock distribution predicted for snowmelt-limited rock-forming processes to observations (Section 4.5).

Mars' environment has two special features that should be addressed by any snowmelt model in order for it to be compared to observations: –

- Interannually-persistent surface water ice on Mars covers only ∼1% of the planet's surface area today, all in cold traps near the poles. The location of cold traps varies with orbital parameters and atmospheric pressure, and a Mars snowmelt model must track these shifts. Migration of ice to cold traps disfavors melting. Our approach is

to (1) assume that snow persists everywhere on Mars, and calculate its temperature, then (2) identify which of these locations actually have interannually-persistent snow, by finding global minima (or near-minima) in annual-average mean sublimation rate.

- Mars has a very wide range of orbital variability, and a correspondingly wide range in tendency to melt. Orbital changes cannot be known deterministically prior to ∼50 Ma (Laskar et al., 2004). Our approach is to run a snowpack energy balance model for all possible orbital states. For each orbital configuration, we assume that interannually-persistent snow only exists at locations that are minima, or near-minima, in annual-average sublimation rate. Finally, we weight the snowmelt predictions for each orbital state by the time-dependent probability of that state.

Because we assess melting to have been marginal, we merely track melting events, not the subsequent path of water. In this idealized model, we do not track the location or temperature of seasonal snow (because melting only occurs at annual-maximum temperatures if melting is just marginal). We make the approximation that snow which persists through the warm season will persist through the year.

More details are given in subsequent sections.

4.4.1 Framework

The climate of Mars is controlled by Mars spin-orbit parameters **E**, atmospheric composition **A**, solar luminosity L, and surface material properties **M**. Local climate also depends on geographic position **G**, local slope and relief **T**, and horizontal atmospheric transport **R**. Climate acts on **M** to produce melt at rate $D_{\mathbf{G}}$, which in most cases is zero.

In order to use the geologic record of Mars to place quantitative constraints on past climate, we need a forward modeling framework that predicts $D_{\mathbf{G}}$ for a given **E**, **A** and L. (**R** and **T** are neglected, for reasons explained later).

This paper uses proxy observations of $D_{\mathbf{G}}$ for a particular time, $\tau \sim 3.5$ Gya (Hesperian), to constrain $\mathbf{A}_\tau$. Our proxy for $D_{\mathbf{G}} > 0$ is thick accumulations of sedimentary rock, catalogued by (Malin et al., 2010). Although sulfate-bearing sedimentary units formed over a wide range of time, they appear to peak in the Hesperian (Carr and Head, 2010). Lithification requires water, so the sedimentary rock record acts as a wet-pass filter, and the sedimentary rocks could have formed in a small fraction of Mars' total history (Lewis et al., 2010). Liquid water availability is very sensitive to **E**. Therefore, modeling average orbital conditions is neither sufficient nor appropriate. Our hypothesis in this paper is that unusual orbital conditions can produce snowmelt on Early Mars at observed sedimentary rock locations, without requiring a multibar atmosphere.

To evaluate this hypothesis for a given atmospheric composition **A**, our approach is to model the temperature of snowpack on Mars for the full range of **E** plausibly sampled by Mars since the Late Heavy Bombardment. There is not enough water ice on Mars to cover

the whole planet, so we use the annual-average sublimation rate to determine the **G** that have interannually-persistent snow for a given **E**. For our global model we approximate the water source and sedimentary rock as being collocated (in the same ∼30 km × ∼30 km grid cell). This is clearly appropriate for vertical infiltration. Even when there is some horizontal runoff, the collocation assumption is justified because the sedimentary rocks contain only small inverted channels that indicate relatively small-scale fluvial transport – for example, tens of km for the outward-directed drainage on the Gale Crater mound (Anderson and Bell, 2010). The sedimentary rocks mostly postdate the regionally integrated valley drainage networks of the Noachian (Fassett and Head, 2011).

The Mars surface environment appears to have only marginally permitted melting since the Noachian. Overall, post-Noachian erosion/degradation and aqueous mineralization rates appear to have been extremely slow. These slow rates suggest transient liquid water that is generated only during a brief melt season. In this case, the governing physical processes are the same as for the Antarctic Dry Valleys, although the mineralogy of Antarctic Dry Valleys lake evaporites differs from Mars sedimentary rock evaporites.

We make several simplifications. First, we neglect **R** because meridional heat transport is minor in the thin atmospheres presumed by our hypothesis. This allows us to run computationally efficient 1D models. We set **T** aside because the most extensive sedimentary rock deposits are flatlying in broad chasms and large craters, where slope and shadowing effects are minor. We ignore non-CO_2 gases, currently only ∼5% of the atmosphere, and which are diluted by pCO_2 increases. We ignore changes in **G** due to true polar wander and other tectonics, both of which are thought to have been small since the sedimentary rock era (Matsuyama and Manga, 2010). The equatorial alignment of sedimentary-rock data and our model predictions provides further evidence that changes in **G** were small.

4.4.2 Thermal model

We simulate the temperatures within snowpack using a surface energy balance model. We calculate the maximum surface temperature that the snow would reach *without* buffering at the melting point - if this is greater than 273.15K, melting should occur. Within the snowpack, material properties are assumed uniform with depth and heat flow is by conduction only. Energy balance at the surface is given by

$$\rho c_p \frac{\partial T}{\partial t} = k\frac{\partial^2 T}{\partial z^2} - \underbrace{\epsilon\sigma T^4 + LW\downarrow + (1-s_r)(1-\alpha)SW\downarrow}_{radiative\ terms} - \underbrace{S_{fr} - L_{fr}}_{free\ convection} - \underbrace{S_{fo} - L_{fo}}_{forced\ convection} \quad (4.1)$$

for temperatures within the snowpack, all but the first term on the right–hand–side are zero. Here, ρ is snow density, c_p is snow heat capacity, Δz is the thickness of the subsurface layer whose upper boundary is the surface, ϵ is the longwave emissivity of ice, T is the surface temperature, k is snow thermal conductivity, $LW\downarrow$ is downwelling longwave radiation, s_r

is the Rayleigh-scattering correction factor (the difference between insolation reaching the surface in the presence of a pure-gas atmosphere and in the absence of an atmosphere), α is snow albedo, $SW\downarrow$ is solar flux per unit surface area. We use the standard solar model of Bahcall et al. (2001) to correct $SW\downarrow$ for the faint young sun).

S_{fr} corresponds to free sensible heat losses driven by atmosphere-surface temperature differences, L_{fr} corresponds to evaporative cooling by free convection when the atmosphere has relative humidity <1, S_{fo} corresponds to forced sensible heat losses caused by cool breezes over warm ground, and L_{fo} corresponds to additional evaporative cooling when the wind is nonzero. Of the convective terms, L_{fr} is most important at low pressure, and S_{fo} is most important at high pressure. We sum the free and forced terms together, rather than considering only the dominant term. This is the standard approach in Mars research (Dundas and Byrne, 2010; Williams et al., 2009; Toon et al., 1980) and matches the functional form of Mars-chamber data (Chittenden et al., 2008). However, summing the terms is an idealization that may overestimate cooling. In our case the idealization is conservative, because overestimating cooling will tend to understate the ability of a thin atmosphere to support melting.

The initial condition at the surface is slightly cooler than radiative equilibrium, decaying to the energy-weighted diurnal average temperature at depth, with an e-folding depth equal to the diurnal skin depth. We integrate forwards in time for several sols using constant seasonal forcing until the day's maximum surface temperature has converged (to <0.025K). Seasonal thermal inertia (and seasonal changes) are not considered directly - instead, for each $\mathbf{G}$, we run the model for many solar longitudes (L_s) and interpolate the output on a grid equally spaced in time to obtain time-averaged annual means.

Conductive cooling is solved for using a Crank-Nicolson scheme. We use a vertical resolution of ≈2.5mm for our nominal parameters, which is 0.033× the analytic diurnal skin depth. Time resolution is 12 s.

Radiative terms.
We use a 1D line-by-line radiative transfer model of the atmosphere (Halevy et al., 2009) to populate look-up tables of $LW\downarrow$ as a function of surface temperature and surface pressure, and $SW\downarrow$ as a function of atmospheric pressure and solar zenith angle. The model, which assumes a clear-sky, pure CO_2 atmosphere with no clouds or dust, is not run to radiative-convective equilibrium. Instead, for each combination of surface P, T, α and solar zenith angle we prescribe an atmospheric pressure-temperature structure and calculate the resulting radiative fluxes. The fluxes calculated in this way represent the instantaneous response of the atmosphere to short timescale (<diurnal) changes in the surface temperature. Following the approach of (Kasting, 1991), the tropospheric lapse rate is dry adiabatic and the stratosphere is approximated as isothermal with a temperature of 167 K. A two-stream approximation to the equations of diffuse radiative transfer (which accounts for multiple scattering) is solved over a wavelength grid with a spectral resolution of 1 cm^{-1} at frequencies lower than 10,000 cm^{-1} and a spectral resolution of 10 cm^{-1} at higher frequencies. The error induced

by this spectral resolution relative to high resolution calculations is small compared to the uncertainties in the other model parameters (Halevy et al., 2009).

The assumption of instantaneous atmospheric thermal response will overestimate $LW\downarrow$ during the hottest part of the day. To set a bound on this error, we also ran the model for the case where the atmospheric thermal structure is pinned to the energy-weighted diurnal average surface temperature, which will underestimate $LW\downarrow$ during the hottest part of the day. The correct $LW\downarrow$ will be in between these bounds. The difference in maximum surface temperature between the two cases is 3-4K, for orbital conditions and surface material properties chosen to be favorable to melting. The assumption of instantaneous atmospheric thermal response likely introduces an overestimate of 2-3K in the surface temperature.

Free convective terms.
Our treatment of turbulent fluxes closely follows Dundas and Byrne (2010). We set

$$S_{fr} = 0.14(T - T_a)k_a \left(\left(\frac{C_p \nu_a \rho_a}{k_a} \right) \left(\frac{g_{Mars}}{\nu_a^2} \right) \left(\frac{\Delta\rho}{\rho_a} \right) \right)^{1/3} \tag{4.2}$$

where T is the surface temperature T_a is the atmospheric temperature, k_a is the atmospheric thermal conductivity, C_p is heat capacity of air, ν_a is viscosity of air, ρ_a is density of air, g_{Mars} is Mars gravity, and $\Delta\rho/\rho_a$ is the difference in density between air in equilibrium with the ground and air overlying the surface layer.

$\Delta\rho/\rho_a$ is given by

$$\frac{\Delta\rho}{\rho} = \frac{(m_c - m_w)e_{sat}(1 - r_h)}{m_c P}$$

Here, m_c is the molar mass of CO_2 and m_w is the molar mass of H_2O. r_h is the relative humidity of the overlying atmosphere and P is the atmospheric pressure. $e_{sat} = 3.69 \times 10^{12}$ $\exp(-6150/T)$ is the saturation vapor pressure over water ice (Cuffey and Paterson, 2010). This agrees to within 1% of Hardy (1998) for 175K $< T <$ 298K. This expression for $\Delta\rho$ assumes that water vapor pressure is a minor component of the overall atmospheric pressure and is simpler but less accurate than Eq. 10 in Dundas and Byrne (2010).

T_a is parameterized as (Dundas and Byrne, 2010)

$$T_a = T_{min}^{b_{DB}} T^{1 - b_{DB}}$$

where T_{min} is the coldest (nighttime) surface temperature experienced by the model, and b_{DB} is the Dundas-Byrne 'b', a fitting parameter. This is an empirical model motivated by Viking 2 measurements (Dundas and Byrne, 2010). As P increases the turbulent coupling between the surface and atmosphere becomes stronger, so b_{DB} decreases. We obtain $b_{DB}(P)$ by fitting to the globally-averaged noontime atmosphere-surface temperature difference from GCM models (unpublished work by Melinda A. Kahre, using the model described in Kahre et al. (2006)).

We let

$$L_{fr} = L_e 0.14 \Delta\eta \rho_a D_a \left(\left(\frac{\nu_a}{D_a} \right) \left(\frac{g_{Mars}}{\nu_a^2} \right) \left(\frac{\Delta\rho}{\rho} \right) \right)^{\frac{1}{3}} \tag{4.3}$$

where L_e is the latent heat of evaporation, $\Delta\eta$ is the difference between atmosphere and surface water mass fractions, and D_a is the diffusion coefficient of H_2O in CO_2.

Forced convective terms.
We set

$$S_{fo} = \rho_a C_p u_s A (T_a - T) \tag{4.4}$$

where C_p is the atmospheric heat capacity and u_s is the near-surface wind speed. (Because these near-surface winds are controlled by planetary boundary layer turbulence which serves to mix the atmosphere vertically, $S_{fo} \neq 0$ is consistent with our assumption of $\mathbf{R} = 0$.) The drag coefficient A is given by

$$A = \left(\frac{K_{vonk}^2}{(log(z_{anem}/z_o)^2} \right)$$

where K_{vonk} is von Karman's constant, z_{anem} is anemometer height and z_o is surface roughness.

Near-surface wind speed u_s in Mars GCMs is expected to decrease with increasing pressure and decreasing solar luminosity. The four-season average of European Mars Climate Database ("MY24" simulation) globally-averaged near-surface wind speeds at the present epoch is 3.37 m/s (Millour et al., 2008). We extrapolate this to pressures up to 290 mbar using a logarithmic dependence of mean wind speed on pressure obtained using GCM model output for pressures between 6 and 80 mbar. We lower the wind speeds by a factor of 1.08 for the faint young Sun using the ratio of wind speeds for two 60 mbar simulations that differ only in solar luminosity. Simulations suggest u_s also depends on $\mathbf{E}$ (Haberle et al., 2003), but we ignore this.

Finally we set

$$L_{fo} = L_e \frac{M_w}{kT_{bl}} u_s (e_{sat}(1 - r_h)) \tag{4.5}$$

where M_w is the molecular mass of water, and k is Boltzmann's constant.

4.4.3 Snow location prescription

For realistic greenhouse forcings, we only predict temperature above freezing within Mars snowpack during the warmest season, and within a diurnal skin depth (mm-cm) of the

surface. Experiments, observation and theory show that warm-season snow within this depth range is in equilibrium with orbital forcing (Mellon and Jakosky, 1995; Hudson and Aharonson, 2008; Hudson et al., 2009; Boynton et al., 2002; Schorghofer and Aharonson, 2005; Boynton et al., 2002). For example, thermal inertia and spectroscopic surveys of Mars rule out warm-season snow and ice within 60° of the equator today.

For each **E**, we use the output of the thermal model for all **G** and season (L_s) to determine the **G** where snow is most likely to be present during the melt season. We assume that melt-season snow is only found at locations **G** where the annually-averaged sublimation is minimized. Figure 4.3 shows an example, for a planet without topography.

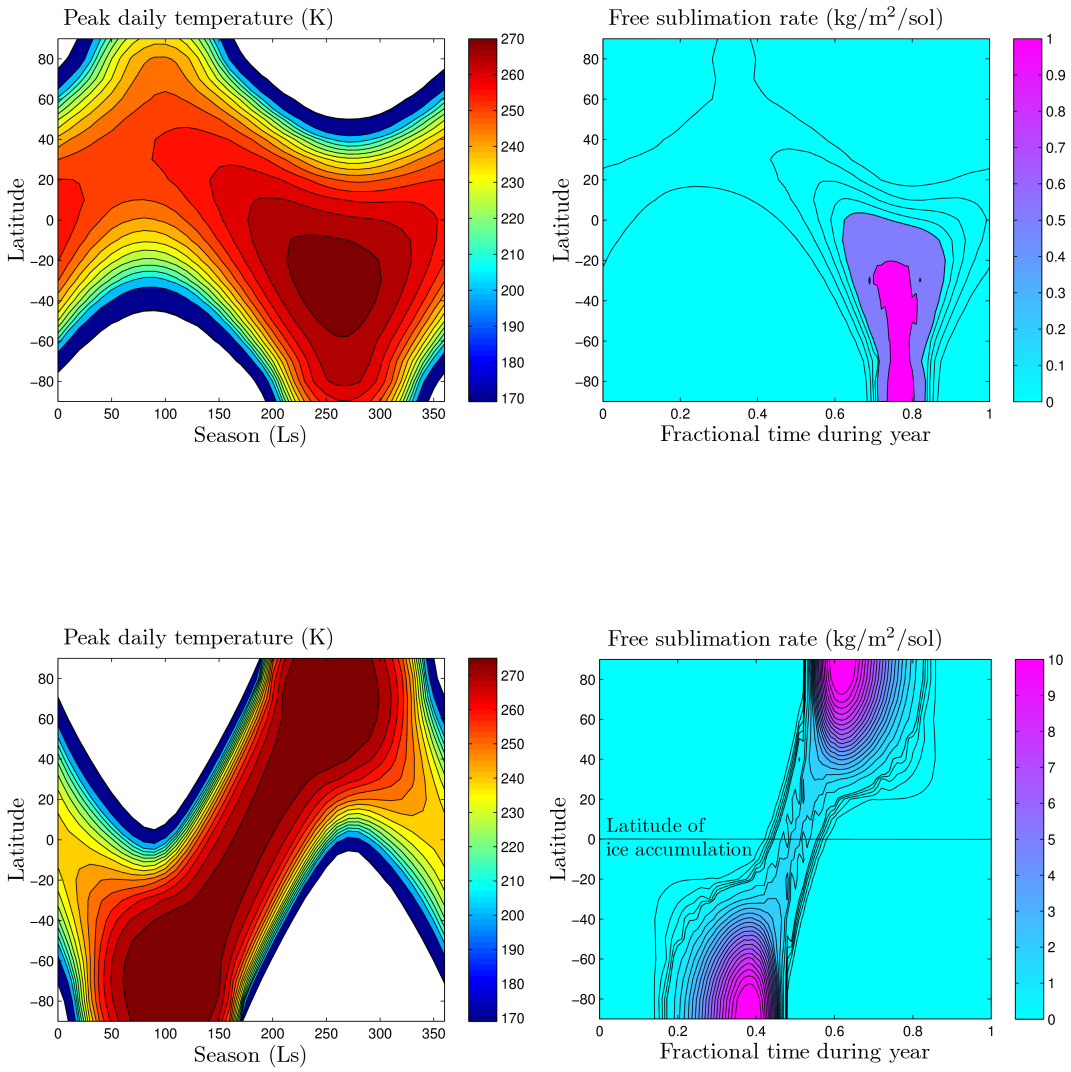

Figure 4.3 Seasonal cycle of diurnal–peak temperature and diurnal–mean free sublimation rate for 3.5 Gya insolation and 195 mbar pure CO_2 atmosphere, assuming flat topography. **Upper row:** present-day orbital forcing ($e = 0.093$, $\phi = 25.2°$, $L_p = 251°$); **Lower row:** optimal conditions for melting – high-obliquity, moderate eccentricity, and L_p aligned with equinox conditions ($e = 0.15$, $\phi = 50°$, $L_p = 180°$). Temperature contours are drawn at 170K, 200K, and 210K and then at intervals of 5K up to a maximum of 275K, only reached for optimal conditions. White-tinted areas approximately correspond to seasonal CO_2 condensation. Sublimation–rate contours are drawn intervals of 0.1 kg/m^2/sol up to 0.5 kg/m^2/sol and then at intervals of 0.5 kg/m^2/sol up to a maximum of 10 kg/m^2/sol. At low eccentricity and low obliquity (upper row), ice is stable at the poles, where temperatures never exceed freezing. Under melting-optimal conditions (lower row), ice is most stable at the equator, and annual peak temperature exceeds freezing everywhere at some point during the year.

Spatially varying precipitation is ignored. This is justified because: (1) to track precipitation we would, at a minimum, have to couple our thermal models seasonally and latitudinally. This would make the model inappropriately complicated, because we do not understand the release rates of water and its transport pathways even at the present orbital conditions. (2) Full GCMs show great inter-model variability in accumulation predictions (Mischna et al., 2003; Madeleine et al., 2009). (3) On Earth, "[a]dvances and retreats of glaciers are broadly synchronous" (Cuffey and Paterson, 2010), because small changes in Earth **G**, L, and lately **A** overwhelm regional variations in precipitation. This ablation sensitivity is what makes glaciers good dipsticks for Earth's paleoclimate. (4) On Mars, recent glaciations have laid down geomorphic strips near-parallel to lines of latitude (Kreslavsky and Head, 2003; Kadish et al., 2010), suggesting that longitudinally variable precipitation is less important than insolation in controlling precipitation and snowmelt. (5) The ancient conditions we find suitable for melting involve higher obliquity (ϕ) and higher P. At higher ϕ, water ice is at the equator and is systematically warmer, leading to much higher water vapor loading. The saturation level in the atmosphere moves close to the ground, and there are correspondingly more widespread water ice clouds. At higher P, water ice crystal terminal velocity is reduced by drag. These two effects should lead to slower falls of snow spread over a broader area than for present-day conditions. In addition, high P and ϕ both strengthen solstice winds that should generate dust storms (Haberle et al., 2003; Newman et al., 2005). Small increases in mean shear stress over current values lead to enormous increases in dust lifting. The greater availability of ice nuclei in a dusty atmosphere will reduce snow grain size for a given scavenging efficiency, again reducing fall speed. Water ice precipitation on Mars was observed directly by the Phoenix lander (Whiteway et al., 2009).

For eccentric orbits, L_s does not increase linearly in time during the year. Therefore, we first assign an L_s to each of 100 equally-spaced times during the year (mean anomalies, M) using Kepler's equation. Next we linearly interpolate the converged thermal output for L_s onto M, giving an unbiased run of temperature during the year. Finally, we apply Equations 4.3 and 4.5 to this unbiased run of temperature to calculate the annual total mass of snow lost by sublimation for each **G**. (We make simplified assumptions about T_a in this last step). We ignore losses due to melting, which are assumed to be small in the annual mean compared to sublimation losses.

All geographic locations **G** are assigned an area-weighted rank, r, scaled from 0 (global minimum in sublimation - most favorable for snow accumulation) to 1 (global maximum in sublimation - least favorable to snow accumulation). We assume that warm-season snow does not occur above a critical r. (In general, the critical r for interannually-persistent snow will be less than the critical r for warm-season snow, but we ignore this). This critical r is the fractional area of the planet covered with interannually persistent snow, f_{snow}.

A complication is that the most favorable places for snow accumulation will tend to develop ice sheets (through net accumulation of snow, plus compaction). An ice sheet distances surface melt from soil by its own thickness, but sediment-water interactions are needed. The best places for aqueous alteration and fluvial transport of sediment are at the margins of

ice sheets, where a thin layer of snow survives through the hottest part of the year but has vanished (partly by melting) before the coldest part of the year, leaving bare soil. These are not the most favorable places for snow accumulation - they have no net accumulation. Therefore, the critical r is only an approximate guide to where sedimentary rocks should form.

Melting is almost certain to occur when orbital forcing leads to annual-maximum temperatures above freezing at all latitudes. Twice-yearly transfer of the water ice reservoir across the equator to the cold high-obliquity winter pole would require seasonally reversing mean wind speed >160 m/s.[1] Thermal barriers >10cm thick can damp the diurnal thermal wave, but a sublimation lag covering all ice is logically impossible,[2] and a debris lag covering all ice is unlikely. The albedo of pure, fresh, fine-grained snow is high enough to prevent melting, but contamination with dust at the hundreds of ppmw level is very likely. The impact of parts-per-thousand levels of dust on snowpack albedo and runoff is severe (Warren and Wiscombe, 1980). Present day observed and calculated Mars seasonal H_2O snow albedo is 0.25-0.4 (Vincendon et al., 2010; Kereszturi et al., 2011) and water ice albedo on the South Polar cap is 0.30 (Titus et al., 2003). To allow melting to create gullies, snowpack albedo must have been as low as 0.12. Dust storms and dust devils occur every year, and caused major changes in regional and global albedo between 1978 and 2000 (Geissler, 2005) and between 2003 and 2007 (Putzig and Mellon, 2007). Global dust storms, which now occur every few years, are likely to occur every solstice at high obliquity (Haberle et al., 2003; Newman et al., 2005). Therefore, it is reasonable to expect snowpack at high obliquity to be contaminated with dust, especially since dust is required to supply ice nuclei for heterogenous nucleation. "When snow melts, the impurities often tend to collect at the surface rather than washing away with the meltwater" (Warren, 1984).

[1]For example, shifting the present-day polar layered deposits (combined volume 2.7 x 10^6 km^3) across the equatorial circumference twice per year requires a mass flux of $4.2x10^3$ kg/s/m across the equator. At a conservatively high mean temperature of 250K, H_2O saturation vapor pressure is 0.95 mbar, for an atmospheric column mass of 26 kg/m^2 under Mars gravity. This leads to a required mean wind speed of 161 m/s.

[2]The atmosphere is a negligible reservoir of water, so the ice that is removed into the atmosphere to form any sublimation lag must be deposited elsewhere on the surface. Currently the atmosphere contains $<10^{-6}$ $\times$ the quantity of water in the polar layered deposits.

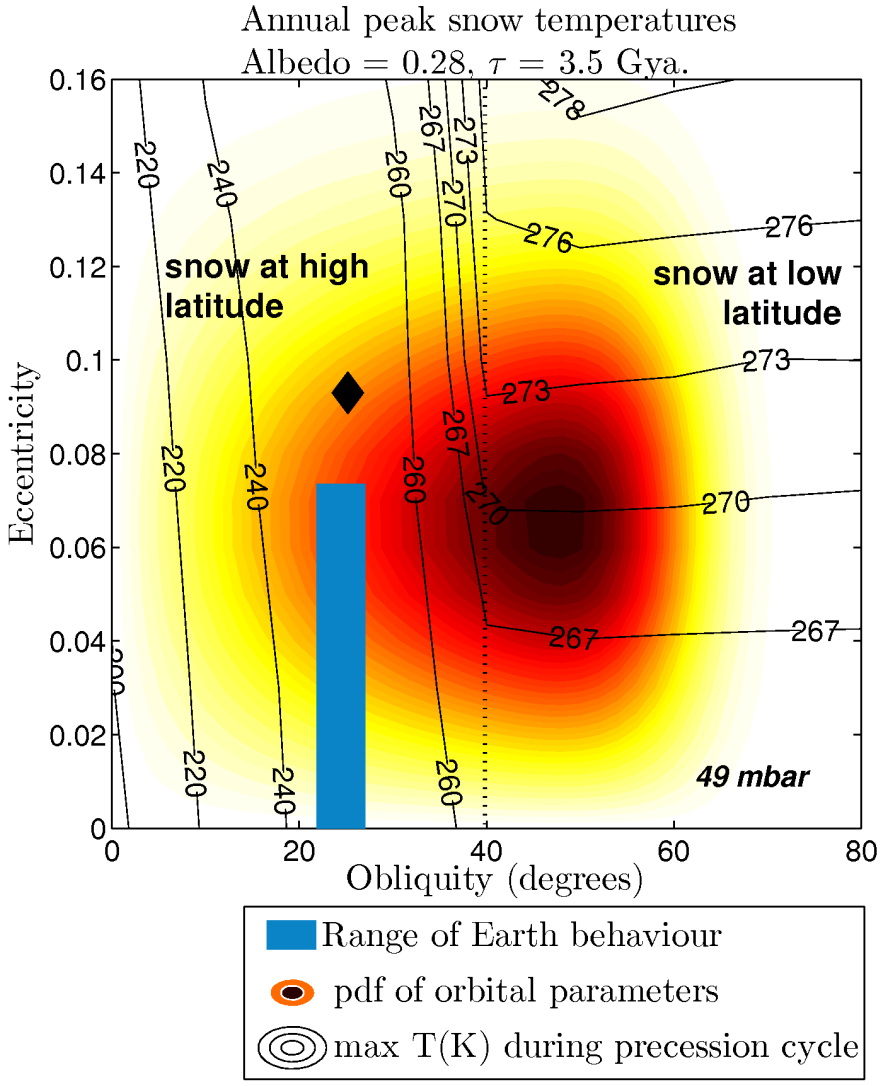

Figure 4.4 Sensitivity of peak snowpack temperature to orbital forcing on an idealized Mars lacking topography. ΔT_{GH} = 5K, P = 49 mbar, snowpack albedo 0.28, Faint Young Sun. Maximum snowpack temperatures over a precession cycle (black contours) are highest for high obliquity and moderate eccentricity. Mars orbital elements probability distribution (warm shading, with darker colors more probable) is much wider than Earths orbital elements probability distribution (blue box). Black diamond corresponds to Mars orbital elements today. Vertical dashed line divides obliquities <40° for which warm-season snow is generally found at high latitude, from obliquities >40° for which warm-season snow is generally found at low latitude. Temperatures ignore buffering at the melting point.

4.4.4 Integrating over all orbital states

Because Mars' spin pole precesses at a frequency close to one of the eigenfrequencies of the Solar System, Mars undergoes chaotic obliquity (ϕ) variations with a likely range (for billion-year intervals) 20 $\times$ that of Earth (Laskar et al., 2004). In addition, the long-term variance of Mars' eccentricity (e) is twice that of Earth (Laskar, 2008). These wide swings in $\mathbf{E} = \{\phi, e, L_p\}$ cause correspondingly large insolation variations. (Here, L_p is the solar longitude of perihelion. Inclination has no effect on insolation and is ignored; the true anomaly ν is broken out of $\mathbf{E}$ and treated separately as a seasonal parameter, L_s.)

For each $\mathbf{E}$, we obtain r for each $\mathbf{G}$, together with T_{max} – the annual-maximum temperature that would be experienced by snow at that location. In practice, we use a mesh of runs in P and latitude to interpolate onto Mars Orbiter Laser Altimeter topography. We interpolate r and T_{max} onto a denser mesh in $\mathbf{E}$ and $\mathbf{G}$. f_{snow} allows us to map out the snow distribution, and f_{snow} and ΔT_{GH} together allow us to map out the snowmelt distribution. ΔT_{GH} is a fixed increase in maximum temperature above that given in the model, or a decrease in the melting point below 273.15K. It can be interpreted as due to:- non-CO_2 greenhouse forcings such as water vapor, clouds, or SO_2; freezing-point depressants; a younger age and correspondingly higher solar luminosity; or stochastic fluctuations in parameters around those assumed in Table 1. Alternatively, it can be thought of as a measure of the mismatch between the model assumptions and the data – very high values of ΔT_{GH} require a different (warmer, wetter) climate system than assumed by our framework.

We weight the resulting maps of snow and snowmelt using the probability distributions given by Laskar et al. (2004) and sum the weighted maps. In order to use Laskar et al. (2004)'s probability distributions, we assume that the instantaneous values of e, ϕ and L_p are independent. Although the classical secular equations show precession rate is a function of ϕ, and that ϕ is a function of e, 250 Myr numerical integrations of Mars' secular equations by Laskar et al. (ref. 7, and `http://www.imcce.fr/Equipes/ASD/insola/mars/mars.html`) do not show a strong correlation between e and ϕ. This is because the secular frequencies that modulate e and ϕ are not in resonance, and the long term evolution of ϕ is dominated by chaotic transitions which smear out remaining correlation between ϕ and e. While mean probabilities exceed median probabilities, over 4 Gya, the exceedance probability for $e = 0.15$ is $\sim$0.8 (Laskar, 2008).

To remove longitudinal stripes of high snow probability in the Northern Plains that are artifacts of finite model resolution in $\mathbf{E}$ and latitude, we replace the Heaviside weighting function in $(f_{snow} - r)$ with a linear ramp in $(f_{snow} - r)$. The ramp is chosen so that it does not extend the region of predicted snow (or melt) beyond that in the unsmoothed map, but it does slightly soften spatial peaks in probability within the region where snow (or melt) is predicted. This is a minor adjustment.

Table 4.1 Snowmelt model: parameters, choices, and rationale.

Symbol	Parameter	Value and units	Source
α	albedo	0.28	Albedo of very dusty snow
b_{DB}	Dundas-Byrne "b"	f(P)	Extrapolation from GCM runs
σ	Stefan-Boltzmann constant	5.67 x 10^{-8} mks	
τ	time of interest	3.5 Gyr ago	(Murchie et al., 2009b)
sol length	duration of 1 Mars sol	88775 s	
R_{gas}	gas constant	8.3144 mks	
g_{Mars}	Mars surface gravity	3.7 m/s^2	
m_c	Molar mass of CO_2	0.044 kg	
m_w	Molar mass of H_2O	0.018 kg	
M_w	Molecular mass of H_2O	2.99 x 10^{26} kg	
ρ_0	Density of atmosphere now	0.02 kg/m^3	NSSDC
$P_{atm,0}$	Pressure of atmosphere now	610 Pa	NSSDC
M_w	Molecular mass of H_2O	2.99 $\times$ 10^{-26} kg	
K_{vonk}	von Karman's constant	0.4	
$\Delta T_{air-surf}$	Atmosphere-surface ΔT	20 K	only used to rank sublimation rates
z_o	Roughness length	0.1 mm	Polar snow (Brock et al., 2006)
z_{anem}	Anemometer height	5.53 m	(Millour et al., 2008)
u_s	Reference near-surface wind speed	3.37 m/s	(Millour et al., 2008) "MY24" average
f_{snow}	Interannual snow areal fraction	variable	see Notes
r_h	Relative humidity	0.25	see Notes
ν_{air}	Kinematic viscosity of air	6.93 $\times$ 10^{-4} mks	(Hecht, 2002)
D_{air}	Mechanical diffusivity of air	14 $\times$ 10^{-4} mks	(Hecht, 2002)
C_p	Specific heat, Mars air	770 mks	MRAMS
k_b	Boltzmann's constant	1.38 $\times$ 10^{23} mks	
L_e	Latent heat of sublimation	2.83 $\times$ 10^6 J/kg	(Hecht, 2002)
ϵ	Thermal emissivity of ice	0.98	
ρ	Density of snowpack	350 kg/m^3	(Carr and Head, 2003a)
C_p	Specific heat capacity of snow	1751 J/kg/K	(Carr and Head, 2003a)
k_{snow}	Thermal cond. of snowpack	0.125 W/m/K	(Carr and Head, 2003a)

Notes to Table 4.1:

f_{snow}: f_{snow} is small, O(1%), today. However, geological evidence and models indicate that f_{snow} may have been as large as 40% in the Amazonian (Kadish et al., 2010). Geological and isotopic evidence also indicates that Mars had more water in the past, and a correspondingly larger f_{snow}. The fraction of the planet's surface on which water ice is present during *part* of the year can be very large indeed: seasonal snow has been detected spectroscopically near the equator (Vincendon et al., 2010), and nighttime water frost has been imaged at the equator (http://photojournal.jpl.nasa.gov/catalog/pia07108). We treat f_{snow} as an unknown free parameter, but find good agreement with data for $f_{snow} \sim 15\%$.

r_h: We assume $r_h = 0.25$. Because free convection increases with humidity contrast only as the cube root, decreasing r_h to zero would have little effect on our results.

Peak temperatures and P dependency are affected by material properties such as albedo and, especially, thermal inertia. High (icelike) thermal inertia suppresses the diurnal thermal wave and reduces the probability of melting. Low (snowlike) thermal inertia (Carr and Head, 2003a) is used here because water ice precipitation is predicted by all General Climate Models (GCMs) at high obliquity (e.g., Fastook et al. (2008); Mischna et al. (2003); Madeleine et al. (2009)) and was observed on Mars by the Phoenix lander (Whiteway et al., 2009)

4.4.5 Comparison of model to data at global scale

We assigned the sedimentary-rock data to $1/2^\circ \times 1/2^\circ$ spatial bins, coding each bin for presence or absence of sedimentary rock. We then thresholded the model-predicted probability for a year with some melting at 0.1% (10^6 years with some melting during a 1 Gyr interval) and 1% (10^7 years with some melting during a 1 Gyr interval). This reflects the assessment that the sedimentary rocks could have formed during a short fraction of Mars history (Lewis et al., 2010). We normalized the model predictions by subtracting the mean and dividing by the standard deviation.

We also tested non-thresholded data and models (separately and together). In the P-ΔT_{GH} plane, these climate solutions tend to favor lower pressures more strongly than the thresholded data and models, but are otherwise broadly similar to those with thresholded data and models. Because adjacent sedimentary rock outcrops record similar depositional events, the number of degrees of freedom of the Mars sedimentary rock system is clearly much less than the number of observations. However, we are not aware of work that identifies a decorrelation length scale for Martian sedimentary rock characteristics. Therefore, we tested 1°, 2°, and 5° tiles, finding only a mild trend to higher ΔT_{GH} with increasing tile size. Finally, we tested normalizing both data and model, finding very similar results. We conclude that our broad conclusions are insensitive to the choice of correlation procedure. Different melting-probability thresholds can shrink or enlarge the exclusion zone of very poor correlation at low P and low ΔT_{GH}. The existence of a band of high correlation with data for near–minimum melting is robust to different fitting procedures.

4.5 Results

Snowmelt is controlled by processes that set the location of snow and its peak temperature. In our results, four controls are the most important:

i. Orbital change: water migrates to latitudes which have the lowest annual-average sublimation rate. For obliquity $> \sim 40^\circ$, water ice precipitation at the equator forms snowpack that persists throughout the year (Jakosky and Carr, 1985; Mischna et al., 2003; Fastook et al., 2008) (Figures 4.4 and 4.3).

ii. Atmospheric pressure (P): raising P above 6 mbar (the current value) initially suppresses evaporative cooling of snowpack, favoring melting. Increasing P also strengthens the CO_2 greenhouse effect, which decreases the relative humidity above the warmed snow and increases sublimation rates. This competition defines an optimal $P \sim 100$ mbar that minimizes sublimation rate. Given a low average P, Mars snow is most stable at low elevations (Fastook et al., 2008), but for higher average P snow accumulates on mountaintops. Sedimentary rocks cluster 2 km lower than average ancient terrain (Figure 4.2). In contrast, the older valley networks cluster $\sim$0.6 km higher than average ancient terrain (Section 4.3), consistent with a more dense atmosphere lost over time.

iii. Water availability: Small f_{snow} concentrates snowmelt into deep canyons, and deep crater such as Gale. Current surface ice volume is 3 x 10^6 km (Plaut et al., 2007; Selvans et al., 2010), and would have been higher in the past. Snow accumulation is the balance between precipitation and ablation. Higher P and especially high obliquity raise atmospheric water abundance (Jakosky and Carr, 1985; Mischna et al., 2003), broadening cloud distribution and probably increasing f_{snow}. $f_{snow} \gg 1\%$ is needed for snowmelt in Meridiani Planum.

iv. Snow darkening by dust: small mass ratios ($<10^{-3}$) of dust darken snow and favor melting on Earth and Mars today (Warren and Wiscombe, 1980). Dust contamination lowers the albedo of water ice exposed near Mars south pole today to 0.30 (Titus et al., 2003), and present day observed and calculated Mars seasonal H_2O snow albedo is 0.25-0.4. Dust lofting would have been more intense at the orbital conditions and pressures relevant to melting on ancient Mars, and we set snowpack albedo to that of Mars dust continents (0.28). Increasing albedo to 0.35 is sufficient to shut down melting.

Our model results demonstrate that as greenhouse forcing and pressure increase, the first locations for snowmelt are at low elevation and at the equator (e.g. Gale Crater, Valles Marineris, Meridiani Planum) (Figures 4.5 and 4.6). These are also the locations of the thickest accumulations of sedimentary rock – for example, 5 km at Gale (Anderson and Bell, 2010), 5 km within the Valles Marineris, and 0.8 km at Meridiani Planum. In particular, the Gale Crater floor and lower mound are hemispheric maxima in snowmelt for many parameter choices. Optimal orbital forcing for melting involves the rare alignment of high obliquity, high eccentricity, and solar longitude of perihelion near equinox (Figure 4.4). This places the Sun near the zenith above equatorial snowpack at noon, during an unusually close approach to the Sun. Higher temperatures would occur for polar snowpack during high obliquity summer, but this snow cannot be in equilibrium with orbital forcing.

For low P and ΔT_{GH}, there is a good correspondence between the location of predicted snowmelt and the distribution of sedimentary rocks (Figure 4.5). For $P \gg 100$ mbar, high ΔT_{GH}, or both, this fit between model and data is much less good. The effect of changes in P, ΔT_{GH} and f_{snow} on the spatial distribution of predicted snowmelt is shown in Figure 4.6.

Total mass balance constraints are also consistent with marginal snowmelt: if the formation of Meridiani Planum was snowmelt-limited, we estimate ∼4 Myr of wet conditions, as follows. Estimated upper limits on water/rock ratio range from 1-300 (Hurowitz and McLennan, 2007; Berger et al., 2009). Taking the logarithmic mean, lithifying 800 meters of Meridiani sediments requires no more than 40 km of water. Conservatively assuming 1 mm/day of snowmelt infiltration, a melt season of 50 days, and that melting occurs during 20% of the precession cycle, only 40 precession cycles at high obliquity and moderate eccentricity (representing a total of ∼4 Myr) are needed to generate enough water to form the stack of Meridiani sediments. Runoff generation R_{melt} ∼0.3±0.2 mm/hr from channel dimensions (Irwin et al., 2005b) sets a hard lower limit on billion-year peak snowmelt energy E_{melt}

>30±20 W/m^2 (given that $E_{melt} > R_{melt}/L_{melt}$, where L_{melt} is the latent heat of melting for liquid water. In addition to low water:rock ratios, geochemistry suggests brevity of post-depositional water:rock interaction (Elwood Madden et al., 2009; Hurowitz and McLennan, 2007), downward mobilization of soluble elements (Amundson et al., 2008), and soils formed with little aqueous alteration under conditions similar to those of todays Mars (Bandfield et al., 2011). These are all compelling arguments for a short-lived and downward-infiltrating water supply.

Snowmelt-limited water supply is sufficient to indicate $\bar{T} < 273$, but the distribution of snowmelt depends critically on non-CO_2 greenhouse forcing (ΔT_{GH}, from e.g. other greenhouse gases or CO_2 ice clouds) and on P, and further implies an ancient Mars climate system that only marginally allowed melting. At high obliquity snow accumulates mostly in the hemisphere whose winter occurs at perihelion. Averaged over the precession cycle, this builds up a broad band of low-latitude snow deposition (±30°). As ΔT_{GH} and P increase beyond the minimum energy needed for melting, melting occurs over a wider range of elevations and latitudes. High P and high ΔT_{GH} would lead to a broader distribution of sedimentary rocks than is observed, suggesting that energy, rather than snow availability, limited melting (Figure 4.5). In addition, $P > 250$ mbar drives snow to high ground, leading to melting predictions that are incompatible with sedimentary rock being found at low elevation (Figure 4.6). Candidate greenhouse gases other than CO_2 and H_2O are not stable in the atmosphere, making long-term $\Delta T_{GH} \gg 5$K improbable and leaving intermediate pressures ($\geq 10 \times$ the Present Atmospheric Level (PAL) of CO_2, but much less than 1000 × PAL) as the best fit to the data. $P \sim$100 mbar is consistent with upper limits from estimated volcanic degassing (Grott et al., 2011) and from isotopic lower limits on the fraction of degassed volatiles that escaped to space (Marty and Marti, 2002). Given the long timescale for chaotic diffusion of orbital forcing, the probability distribution of past orbital forcing for the actual history Mars must have been less smooth than the ensemble probability distribution used here (Laskar et al., 2004). Therefore, the ΔT_{GH} needed to reach the >10^6-10^7 years cumulative years of snowmelt thought necessary to form sedimentary mounds (Lewis et al., 2010) could be somewhat higher (or lower) than inferred here.

Outflow channel formation could have removed sedimentary rocks in northern Margaritifer Terra, which is the only region where the model predicts snowmelt but few sedimentary rocks are observed (Figure 4.5) and also contains the largest outflow channels on Mars. Buried sediments are predicted to underlie lava in Isidis and Elysium Planitia, perhaps fueling mud volcanism there (Skinner and Tanaka, 2007), but the thickness of cover is probably too great for orbital radar sounding to test this hypothesis. Alignment of Meridiani Planum with snowmelt maximum is robust, implying True Polar Wander <10° since sediment deposition (Matsuyama and Manga, 2010). The snowmelt model shows snow, but little snowmelt, in the belt of large alluvial fans including Eberswalde around 30°S. This leaves open the question of whether the fan water source was impact-triggered ice melting (Senft and Stewart, 2008), or snow melting under unusually warm conditions or orbital disequilibrium.

The end of sedimentary rock formation can be explained by loss of CO_2 through escape to space, carbonate formation, and burial by condensation onto the polar caps or within the martian regolith. For P much less than 50 mbar, evaporative cooling prevented snowmelt on flat surfaces even under optimal orbital conditions. Limited snowmelt continued to the present era, but only for steep slopes and favorable sun angles, or disequilibrium conditions.

We favor the snowmelt model for the sedimentary-rock water source over previous global groundwater models, mainly because it arises from a self-consistent climate solution (Figure 4.5), and because the equatorial concentration of sedimentary rocks emerges naturally from any marginal-snowmelt model. Groundwater models require removal of $>2\times10^6$ km^3 of siliciclastic rock to an unknown sink (Zabrusky and Andrews-Hanna, 2010), which is not necessary in the snowmelt model. Regional groundwater flow may still be required to recharge outflow channel source regions and some evaporite-lined craters (Wray et al., 2011a), even if it is not the major process responsible for sedimentary rock formation.

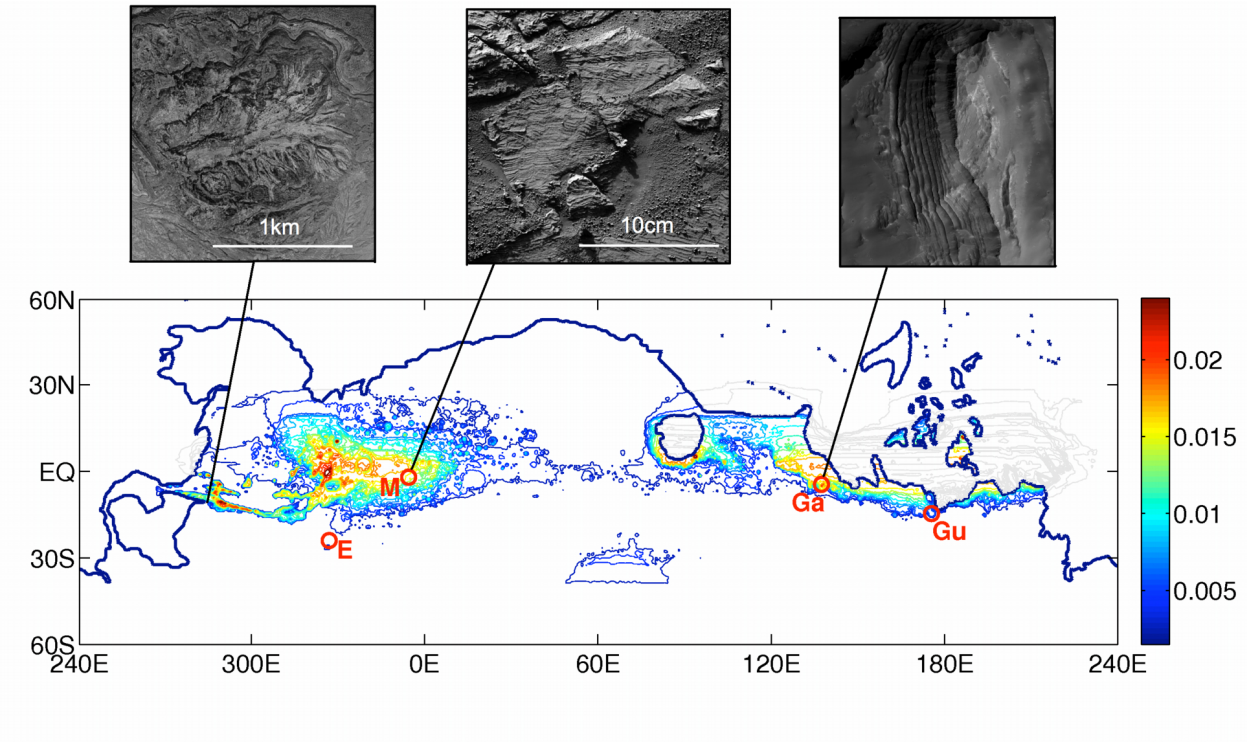
1km
10cm
60N
30N
EQ
30S
60S
240E
300E
0E
60E
120E
180E
240E
M
E
Ga
Gu
0.02
0.015
0.01
0.005

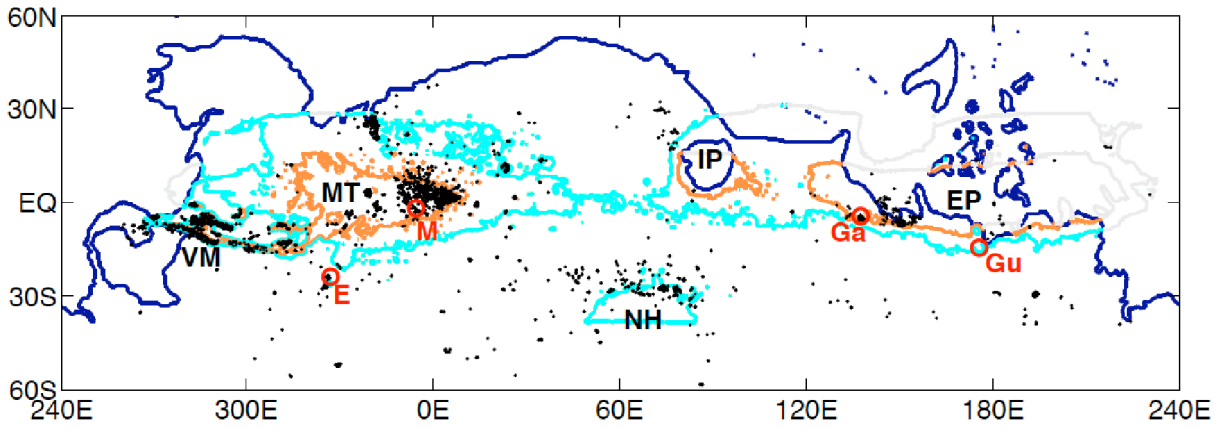
60N
30N
EQ
30S
60S
240E
300E
0E
60E
120E
180E
240E
MT
VM
M
E
IP
NH
Ga
EP
Gu

Figure 4.5 Modeled distribution of snowmelt, and Mars sedimentary rock data. Top panel: Probability of snowmelt (thin blue colored contours) for ΔT_{GH} = 5K, P = 49 mbar, and warm-season snow areal coverage f_{snow} = 15%. Colors run from blue (low probability) to red (high probability). Snowmelt predictions on recently resurfaced terrain (dark blue outline) are shaded gray. Sedimentary rock outcrops (black dots) are targets for long-range rovers. Current and planned long-range rover sites shown by red circles; Gusev Crater (Gu), Meridiani Planum (M), MSL runner-up Eberswalde Crater (E), and MSL final target Gale Crater (Ga). The inset boxes show examples of sedimentary rock morphology. From left to right, sublacustrine fans at SW Melas Chasma (HiRISE image PSP_007667_170); fluvial ripples at Meridiani Planum (Opportunity rover, Erebus Crater); rhythmic bedding at Gale Crater (HiRISE image ESP_016520_1750). Bottom panel: Comparison of predicted snowmelt to observed sedimentary rock locations. Melt probabilities of 0.15% (cyan) 1% (orange) are shown. The (ΔT_{GH},P,f_{snow} shown in this figure were selected by maximizing the correlation of the ancient terrain enclosed by the 1% contour with the ancient terrain bearing sedimentary rocks. Locations referred to in the text are VM (Valles Marineris), MT (Margaritifer Terrra), IP (Isidis Planitia), EP (Elysium Planitia), and NH (Northern Hellas).

a) $P = 49$ mbar, $\Delta T_{GH} = 5$K, $f_{snow} = 15\%$.

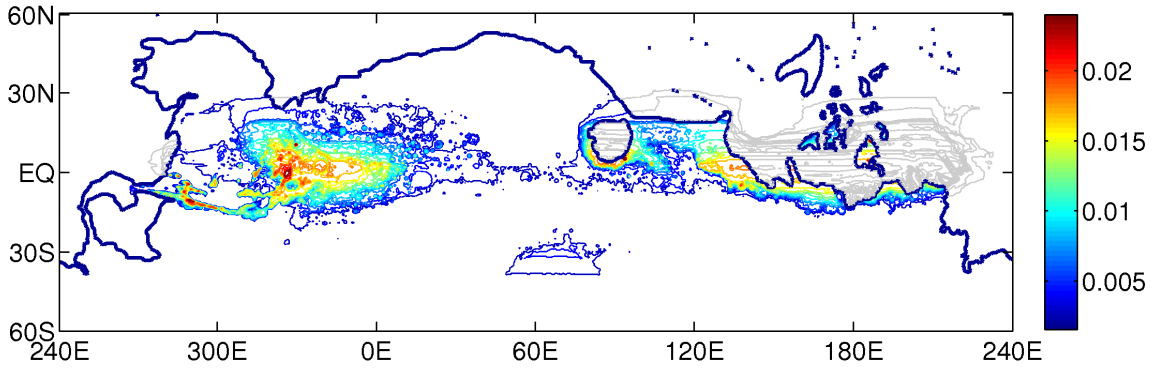

b) $P = 49$ mbar, $\Delta T_{GH} = 5$K, $f_{snow} = 0.5\%$.

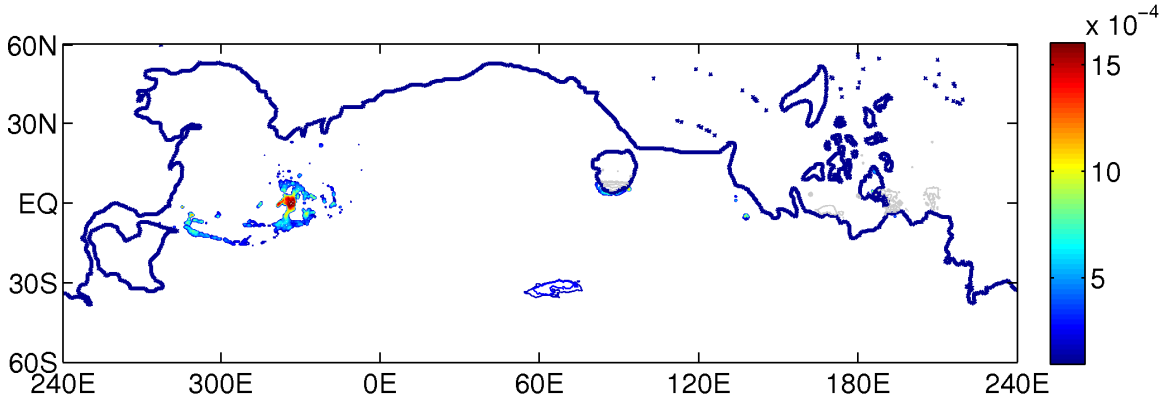

c) $P = 293$ mbar, $\Delta T_{GH} = 3$K, $f_{snow} = 5\%$.

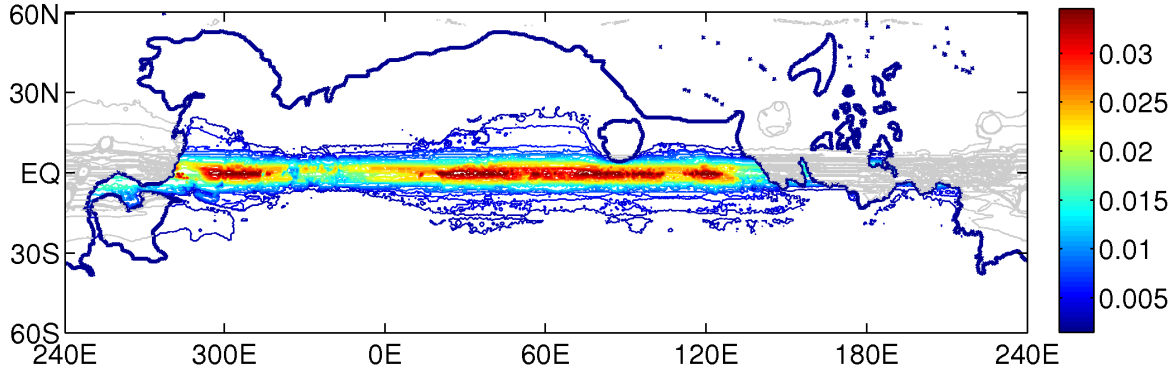

d) $P = 49$ mbar, $\Delta T_{GH} = 5$K, $f_{snow} = 35\%$.

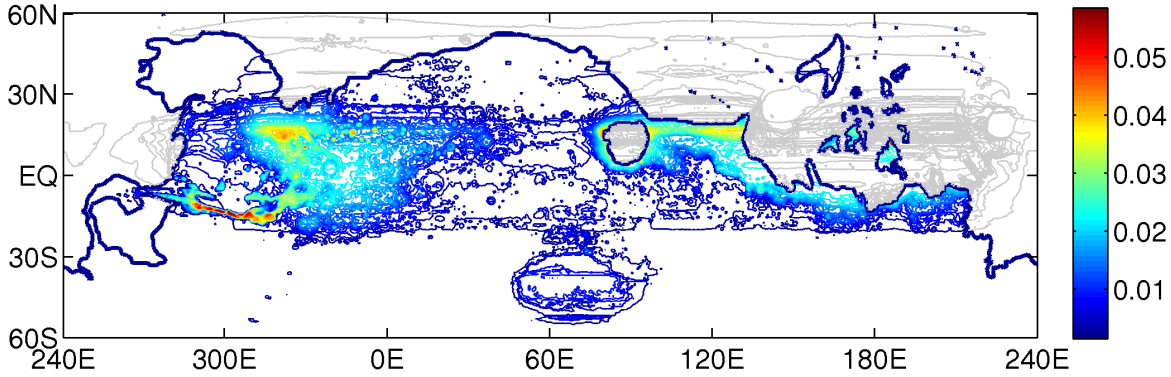

Figure 4.6 Sensitivity of snowmelt maps to extreme variations in model parameters. Colored contours correspond to snowmelt probabilities on ancient terrain. Thick blue line corresponds to border of ancient terrain, and grayed-out contours are snowmelt probabilities on recently-resurfaced terrain. **(a)** Parameters that give a good fit to the observed distribution of sedimentary rocks: $P = 49$ mbar, $\Delta T_{GH} = 5$K, $f_{snow} = 15\%$. **(b)** Parameters that allow only marginal melting: $P = 49$ mbar, $\Delta T_{GH} = 5$K, $f_{snow} = 0.5\%$. This favors snowmelt in Gale Crater, Valles Marineris, Northern Hellas, and the S Isidis Rim. Gale Crater (blue-green spot near 6S, 135E) is usually a hemispheric maximum in snowmelt for marginal-melting cases. **(c)** High pressure drives snow (and melt) to high ground: $P = 293$ mbar, $\Delta T_{GH} = 3$K, $f_{snow} = 5\%$. This is inconsistent with the observed concentration of sedimentary rock at low elevations. **(d)** Very high f_{snow} leads to a latitudinally broader distribution of sedimentary rocks than observed: $P = 49$ mbar, $\Delta T_{GH} = 5$K, $f_{snow} = 35\%$. This is slightly inconsistent with the observed concentration of sedimentary rocks at equatorial ($\pm 10°$) latitudes.

4.6 Discussion

4.6.1 Assessment of snowmelt-limited sedimentary rock formation hypothesis against geochemical and textural data at key sites

Consistent with concentration of wet conditions near the equator, three of the most spectacular exposures of sedimentary rock on Mars – Meridiani, SW Melas Chasma, and Gaza-Aeolis-Zephyria – are all within 10° of the equator. We now turn to the specific constraints provided by those deposits.

Current Rover Target: Meridiani Planum (2S 354E). The ∼10m stratigraphic section that has been explored by the Opportunity rover at Meridiani shows evidence for at least four distinct episodes of liquid water influx (McLennan and Grotzinger, 2008). Total exposure to liquid water is constrained to < 100 Kyr since jarosite formation (< 0.003% of time since 3.5 Ga; Laskar et al. (2004)), perhaps as little as 20 yr (Berger et al., 2009). Weathering at Meridiani was either isochemical or at low water/rock ratio or both, consistent with a rare trickle of snowmelt (Ming et al., 2008). Hematite concretions form a lag deposit covering the Meridiani plains surface (McLennan and Grotzinger, 2008). Because the observed volumetric abundance of hematite concretions within the underlying bedrock is ∼2% (Squyres et al., 2004), this lag deposit indicates that those rocks were buried to and then exhumed from a depth more than 50 times the blueberry radius of 0.6–4.8mm (Squyres et al., 2009). Burial allows our model, which predicts wet conditions 1% of the time, to be reconciled with mineralogical constraints that require wet conditions to be even less common. The water requirements to lithify the total thickness of sedimentary rock at Meridiani Planum (800m) is also consistent with snowmelt under unusual orbital conditions (§4.5).

Sulfate formation occurs near the surface of ice sheets on both Earth and Mars, and ice-sheet processes have previously been proposed as the source of the sulfate-rich layered deposits at Meridiani (Niles and Michalski, 2009). < 100 Myr sulfates in Noctis Labyrinthus show that layered sulfates can form in the present-day, cold dry conditions (Mangold et al., 2010).

Southwest Melas Chasma (10S 283E). Southwest Melas Chasma is a depositional basin ringed by >20° slopes with 3 km of relief. It contains sublacustrine depositional fans just downslope from densely-branching valley networks (Metz et al., 2009a). The chasm is one of the ancestral basins of Valles Marineris, thought to predate opening along the main Ius/Central Melas/Coprates axis. Chezy-type discharge estimates for the SW Melas sublacustrine fans indicate discharges of 3-98 m^3/s [Joannah Metz, via email]. Ignoring topographic effects on insolation, this requires peak snowmelt energy >1-40 W/m^2 for the ∼800 km^2 area draining into the SW Melas Chasma west fans. This is plausible for $\bar{T} << 273K$, provided that losses

to infiltration are minimal and that flow is swiftly routed into ice-capped channels to slow evaporation.

Next Rover Target: Gale-Aeolis-Zephyria. The Mars Science Laboratory's Curiosity rover will explore the ∼5km thick sedimentary sequence (Milliken et al., 2010) at Gale Crater (5S 138E). Tests of our model at this site are discussed in the main text. The adjacent Aeolis-Zephyria Planum shows numerous sinuous ridges, including meandering river systems recording avulsions and gooseneck cutoffs. Inverted river channels at Zephyria show width-discharge and meander-width relations suggesting discharges of 10 – 1000 m^3/s (Burr et al., 2010). Erosion and deflation prevent reconstruction of the watersheds that fed these channels, and because it is not known if channel threads were simultaneously active plausible values range up to the size of the western lobe of the Medusae Fossae Formation (10^5 km^2). Although 10^4 km^2 is more likely, even this sets only a weak lower bound on runoff, equivalent to >0.1 W/m^2 ignoring infiltration and hydrology.

4.6.2 Other data sets: valleys and chlorides

Chloride deposits ($n = 634$), which are generally older than the sedimentary rocks, are not concentrated near the equator (Osterloo et al., 2010) [Mikki Osterloo, via email]. This excludes an erosional mechanism for the latitudinal distribution of sedimentary rocks. Chlorides are extremely soluble, rare in the equatorial sedimentary rock bracelet, and regionally anticorrelated with sedimentary rock. We propose that they were dissolved in the equatorial band during the wet events that lithified the sedimentary rocks, and that the wet events rarely occurred far from the equator.

A new global map of Mars valley networks (Hynek et al., 2010) shows an elevation distribution biased high by 600m relative to ancient terrain. Given that the valley networks are mostly older than the sedimentary rocks (Fassett and Head, 2011), we tentatively interpret the progression from highland valley networks to lowland sedimentary rocks as a shift from a thick early atmosphere (with snow most stable on high ground) to a thinner later atmosphere (with snow most stable on lower ground). However, this elevation distribution may also reflect the generally higher elevation of mid-Noachian (as opposed to Early Hesperian) outcrop. To obtain this elevation bias, we used a 'valley index' defined to be the total length of valley within 30km-radius circles spaced every degree. More research is needed to determine if the valley networks are consistent with incision by snowmelt runoff.

4.6.3 Extensions

Three main improvements to the model are envisioned, relaxing some of the restrictive assumptions made in the current version.

1. *Improved treatment of the atmosphere:* Currently, the greenhouse effect is calculated

using an atmospheric thermal structure equilibrated to the instantaneous surface temperature. This underestimates nighttime greenhouse warming but also overestimates peak greenhouse warming, most likely giving a surface temperature overestimate of 2-3K, so a more accurate parameterization would disfavor melting. Currently, the free and forced turbulent cooling terms are summed, following Dundas and Byrne (2010). A more accurate Monin-Obukhov parameterization (Pielke, 2002) would reduce the amplitude of the cooling, favoring melt.

2. *Melt tracking:* Currently, the model assumes that all melt generated is available for sedimentary rock formation, but in reality some or all of the melt will refreeze within the snowpack or sublimate back into the atmosphere before contributing to sedimentary rock formation. An improved model would include refreezing. Including this effect would raise the threshold temperature required to generate enough melt to leave a geological trace.

3. *Disequilibrium ice:* For a given insolation at the equator, it is easier to melt snow than ice because of the lower thermal inertia of snow. However, the migration of thick ice accumulations can significantly lag orbital forcing. If ice that has been deposited in mid southern latitudes when northern summer solstice is aligned with perihelion has not been completely removed when southern summer solstice is aligned with perihelion, then melting is favored. This is attractive as an explanation for the sedimentary rock/alluvial fan belt between 25°S–30°S, which is not well fit by the current model with snow in equilibrium with orbital forcing.

4.7 Predictions for the MSL Curiosity rover at Gale Crater

When Curiosity lands at Gale (Milliken et al., 2010; Anderson and Bell, 2010), we can relate the fraction of stratigraphic section that must have formed under wet conditions to the warmth of the background climate, as follows. At a given location, orbital forcing imposes large-amplitude insolation variations on 10^4-10^5 yr timescales. These variations are recorded by bedding variations on a length scale of meters (Lewis et al., 2008, 2010). The snowmelt model predicts that melting (wet conditions) only occurs near the hot peak of these cycles. However, a warm-wet Mars would allow wet conditions throughout, either (i) by damping orbital oscillations through the homogenizing effect of a thick atmosphere's stronger winds and increased thermal inertia, or (ii) by raising the planet-averaged temperature to the point where even the coldest part of an orbital cycle is warm enough to allow melting. Therefore, a strong prediction of our marginal-melting model is wet-dry cycles on orbital timescales. Early in the wet phase of a wet-dry cycle, infiltration can provide water for diagenetic alteration of layers that were deposited under dry conditions. The depth reached by infiltrating water will

depend on porosity, permeability, and temperature of underlying layers. As cementation reduces permeability, infiltration will decline and runoff will be increasingly favored. Therefore, the best indicator of which strata were actually deposited under wet conditions is sedimentary textures such as small-scale trough cross-lamination, as observed by Opportunity at Meridiani Planum (McLennan and Grotzinger, 2008). Slow, orbitally-paced sedimentation and oscillation between reducing and oxidizing conditions would disfavor preservation of organic carbon.

As soon as Curiosity starts to ascend the Gale mound, it will gather geochemical and mineralogical data that can provide a strict test of the snowmelt model versus the global–groundwater model (Andrews-Hanna and Lewis, 2011) of the water source for cementation of the sedimentary rocks. If the snowmelt model is correct, then layer geochemistry should be a succession of closed systems, because the maximum infiltration depth of downward-infiltrating snowmelt is small compared to the height of the mound. If instead the global–groundwater model is correct, then the layers deposited at the base of the mound should be modified by open-system alteration associated with subsequent generations of fluid moving upward through the mound to cement and indurate the overlying layers.

4.8 Conclusions

We conclude that:-

1. The equatorial concentration of sedimentary rocks on Mars can be explained if sedimentary rocks form through snowmelt-limited processes under orbital conditions, with snow and ice migrating in equilibrium with orbital forcing.

2. Provided that snow and ice migrate to annually-averaged potential sublimation minima in equilibrium with orbital forcing, the concentration of Mars sedimentary rocks at low elevation can be explained by snowmelt at pressures too low for the surface temperature to couple strongly to the atmospheric adiabat ($O(10^2)$ mbar or less).

3. These results are consistent with a model in which Mars' sedimentary rocks formed during localized wet intervals, whose cumulative duration was a small fraction of Mars' history.

Chapter 5

Geodynamics and volcanism on Super-Earths.

This chapter was published as: Kite, E.S., M. Manga, and E. Gaidos (2009), "Geodynamics and rate of volcanism on massive Earth-like planets", Astrophysical Journal 700, 1732 doi:10.1088/0004-637X/700/2/1732

The second and third paragraphs in §5.3.4 were written by coauthor Eric Gaidos. All other sections were written by Edwin S. Kite.

Summary

We provide estimates of volcanism versus time for planets with Earth-like composition and masses 0.25 - 25 M_{Earth}, as a step toward predicting atmospheric mass on extrasolar rocky planets. Volcanism requires melting of the silicate mantle. We use a thermal evolution model, calibrated against Earth, in combination with standard melting models, to explore the dependence of convection-driven decompression mantle melting on planet mass. We show that (1) volcanism is likely to proceed on massive planets with plate tectonics over the main-sequence lifetime of the parent star; (2) crustal thickness (and melting rate normalized to planet mass) is weakly dependent on planet mass; (3) stagnant lid planets live fast (they have higher rates of melting than their plate tectonic counterparts early in their thermal evolution), but die young (melting shuts down after a few Gyr); (4) plate tectonics may not operate on high mass planets because of the production of buoyant crust which is difficult to subduct; and (5) melting is necessary but insufficient for efficient volcanic degassing – volatiles partition into the earliest, deepest melts, which may be denser than the residue and sink to the base of the mantle on young, massive planets. Magma must also crystallize at or near the surface, and the pressure of overlying volatiles must be fairly low, if volatiles are

to reach the surface. If volcanism is detected in the 10 Gya τ Ceti system, and tidal forcing can be shown to be weak, this would be evidence for plate tectonics.

5.1 Introduction

Theory predicts the existence of rocky planets having 1-10 Earth masses (e.g. Ida and Lin (2004)). Planets in this mass range are now being detected (Rivera et al., 2005), and next-decade observatories, such as *James Webb Space Telescope* and *Giant Magellan Telescope*, may be able to detect any atmospheres. A planet's atmosphere will consist of gas (1) accreted from the nebula, (2) degassed during impact accretion, and (3) degassed during subsequent geologic activity. (1) will depend on the lifetime of the nebula, (2) and (3) will depend on the volatile abundance of material (Elkins-Tanton and Seager, 2008a), and all will be modified by atmospheric escape. Very large planets far from their parent star will retain primitive gas, but smaller planets closer to their parent star will not. Loss rates vary between gases, so planetary atmospheres could be a mixture of gases left over from the initial atmosphere, and those replenished by volcanism. Thermal emission phase-curves gathered from extrasolar planets can set bounds on atmospheric mass. Spectral observations of atmospheric constituents with short photochemical lifetimes, such as SO_2, would require an ongoing source – most likely, volcanic degassing.

Volcanism results from partial melting of upper mantle. (Planetary mantles can cool convectively without volcanism - present-day Mercury is almost certainly an example). Partial melting occurs when the adiabat crosses the solidus. Assuming that the adiabat is steeper than the solidus, this requires that the potential temperature of the mantle T_p exceed the zero–pressure solidus of mantle rock (e.g., peridotite) (Figure 5.1, left panel):

$$T_p = T_{m,r} - P_r \frac{\partial V}{\partial S} \geq T_{sol}(0), \tag{5.1}$$

where $T_{m,r}$ is the mantle temperature evaluated at some reference pressure P_r, $\frac{\partial V}{\partial S}$ is the adiabat, potential temperature is defined as the temperature a parcel of solid mantle would have if adiabatically lifted to the surface, and T_{sol} is the solidus, evaluated here at zero pressure. On planets with plate tectonics, the thickness of the crust (the crystallized melt layer) is a convenient measure of the intensity of volcanism. The rate of crust production is the product of crustal thickness, plate spreading rate, and mid-ocean ridge length. The pressure at the base of the crust is the product of crustal thickness, the planet's surface gravity, and crustal density. A reasonable approximation to the pressure at the base of the crust is the integral of the fractional-melting curve from great depth to the surface (Figure 5.1, left panel).

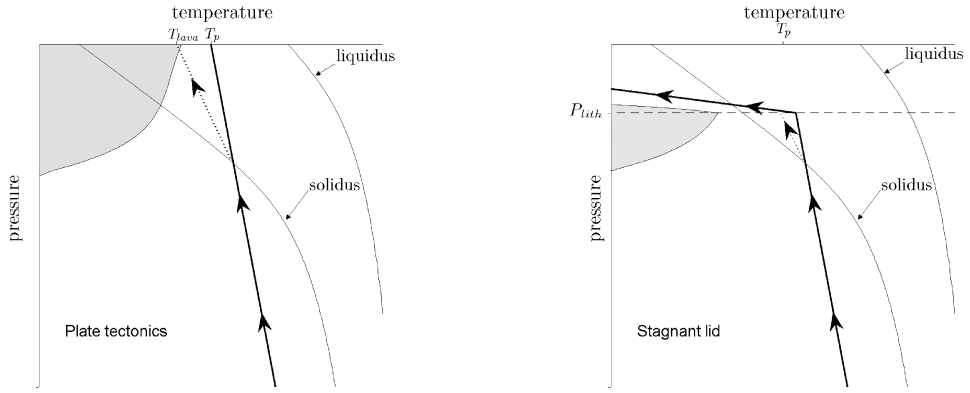

Figure 5.1 Sketches of pressure-temperature paths for passively upwelling mantle, and resulting melt fraction. In each sketch, the shaded area corresponds to the partial melt fraction as a function of pressure. Left panel: Plate tectonics. Thick solid line is the adiabatic decompression path for solid mantle. Actual path taken by upwelling mantle, traced by arrows, differs above the solidus because of latent heat of fusion. Right panel: Effect of a stagnant lid, whose base corresponds to the dashed line. Ascending mantle tracks the conductive geotherm within the lid (arrowed path). Melt generated at $P < P_{lith}$ in the stagnant lid case is a small fraction of total melt, and we ignore it in this paper.

Venus and Mars lack plate tectonics: their mantles are capped by largely immobile, so-called 'stagnant lid' lithospheres, which cool conductively. Because mantle cannot rise far into the stagnant lid, melting can only occur if the temperature at the base of the stagnant lid exceeds the local solidus of mantle rock:

$$T_{m,r} - (P_r - P_{lith})\frac{\partial V}{\partial S} \geq T_{sol}(P_{lith}), \tag{5.2}$$

where $P_{lith} = \rho_{lith} g Z_{lith}$ is the pressure at the base of the stagnant lid, ρ_{lith} is lithospheric density, g is gravity, and Z_{lith} is stagnant lid thickness. This is a more stringent condition than Equation 5.1 if the adiabat is steeper than the solidus (Figure 5.1, right panel). Io shows yet another style of rocky-planet mantle convection: magma pipe cooling (Moore, 2003).

Previous studies have examined both rocky planet atmospheres and massive-earth geodynamics. Elkins-Tanton and Seager (2008a) estimate the mass and composition of super-Earth atmospheres degassed during accretion. Complementary to that study, we emphasize long-term geological activity. There is disagreement over whether plate tectonics will operate on massive planets. One previous study uses scaling arguments to argue that higher gravity

favors subduction (Valencia et al., 2007). Another study shows that subduction might never begin if the yield stress of old plate exceeds the stresses imposed by mantle convection, which fall steeply with increasing planet mass (O'Neill and Lenardic, 2007). We do not consider yield stresses in this paper. Instead, we analyze five possible volcanism-related limits to plate tectonics, tracing the consequences in more detail than Valencia et al. (2007). The approach of Papuc and Davies (2008) is most similar to that taken here. We differ from Papuc and Davies (2008) in that we neglect the pressure dependence of viscosity, use more realistic melting models, and account for energy advected by magma.

Here we examine (1) the history of partial melting on planets with either plate tectonics or stagnant lid convection, and (2) the effect of melting and crust production on the stability of plate tectonics. Our method is given in §5.2. We use three different melting models to compute the intensity of volcanism for massive Earth-like planets of different ages. Our results are given in §5.3, for both plate tectonic (§5.3.2) and stagnant lid (§5.3.3) modes of mantle convection. We also trace the implications of galactic cosmochemical evolution for heat production and planetary thermal evolution (§5.3.4). We find that results differ greatly depending on the mode of convection. Massive Earths with plate tectonics will produce melt for at least as long as the age of the Galaxy, stagnant lid planets will not. In §5.4, we analyze the effect of melting on the style of mantle convection. We show that plate buoyancy is likely to be a severe problem, and may be limiting for plate tectonics. In §5.5, we relate our results to atmospheric degassing, and discuss the possible suppression of degassing (and, perhaps, melting) by the higher ocean pressures expected on massive Earth-like planets. Finally, in §5.6, we summarize our results; justify our approximations and model limitations; and compare our results to solar system data.

5.2 Model description and inputs

We use a model of internal structure (§5.2.1) to set boundary conditions for a simple model of mantle temperature evolution (§5.2.2), which in turn forces a melting model (§5.2.3). Greenhouse-gas regulation of surface temperature could allow melting and degassing to feed back to mantle thermal evolution (e.g. Lenardic et al. (2008)), but we neglect this. Throughout, we assume whole-mantle convection. Rather than attempt to predict exoplanet properties solely from basic physics and chemistry, we tune our models to reproduce the thickness of oceanic crust on present-day Earth.

5.2.1 Radius and mantle depth

Given our assumption of whole-mantle convection, we need to know only the mantle's outer and inner radii. The crust is thin, so the top of the mantle is $\approx$ the planet's radius, R. Valencia et al. (2006) propose the scaling $R/R_{Earth} = (M/M_{Earth})^{\simeq 0.27}$. Here, we use instead the 'modified polytrope' of Seager et al. (2007) (their equation (23)) to set planet

radius. However, we take $R/R_{Earth} = (M/M_{Earth})^{\sim 0.25}$ in our scaling relationships 5.13 – 5.14 and 5.21. To find the Core-Mantle Boundary (CMB) radius for the Seager et al. (2007) scaling, we set mantle mass $M_{mantle} = 0.675\ M_{planet}$ and numerically integrate inward using a pure magnesioperovskite mantle composition, a 4th-order Burch-Murnaghan equation-of-state, and material properties from Seager et al. (2007). Core-mantle boundary pressure is calculated to be 1.5 Mbar for 1 M_{Earth}, and 2.9 (6.9, 14, 40) Mbar for 2 (5, 10, 25) M_{Earth}.

5.2.2 Thermal model

For a convecting mantle with a mobile lithosphere, if heat is generated solely by mantle radioactivity and is equal to heat lost by cooling at the upper boundary layer,

$$Q = \frac{M_{mantle}}{A} \sum_{i=1}^{4} H_0(i) e^{-\lambda_i t} = Nu \frac{k(T_m - T_s)}{d} \tag{5.3}$$

$$Nu \approx \left(\frac{g\alpha(T_m - T_s)d^3}{\kappa\nu(T) Ra_{cr}} \right)^{\beta} \tag{5.4}$$

$$\nu(T) = \nu_0 e^{(A_0/T_m)} = \nu_1 e^{(-T_m/T_\nu)}, \tag{5.5}$$

where Q is lithospheric heat flux, A is the planet's surface area, H is the radiogenic power per unit mass, i = 1-4 are the principal long-lived radioisotopes (^{40}K, ^{232}Th, ^{235}U, ^{238}U), λ is the decay constant, t is time, Nu (Nusselt number) is the dimensionless ratio of total heat flow to conductive heat flow, k is thermal conductivity, T_m is mantle temperature, T_s is surface temperature, d is the depth to the core-mantle boundary, g is gravitational acceleration, α is thermal expansivity, κ is thermal diffusivity, ν is viscosity, Ra_{cr} is the critical Raleigh number with value $\sim 10^3$, β is 0.3 (Schubert et al., 2001), A_0 is activation temperature, and T_ν is the temperature increase (decrease) that decreases (increases) viscosity by a factor of e (Schubert et al., 2001). Equation (5) contains two equivalent parameterized expressions for T. Values used for these parameters are given in (Table 2).

We neglect the pressure dependence of viscosity (Papuc and Davies, 2008), which cannot be fully captured by parameterized models. In effect, we assume that the viscosity beneath the upper boundary layer, rather than some volume- or mass-averaged mantle viscosity, determines the properties of the flow.

We use the canonical values for H_i given by Turcotte and Schubert (2002), who estimate that 80% of Earth's current mantle heat flux is supplied by radioactive decay. Although Earth's surface heat flux is well constrained, the fraction of the flux out of the mantle that is due to radiogenic heat production is not. Literature values vary from $\leq$0.2 (Lyubetskaya and Korenaga, 2007) to 0.8 (Turcotte and Schubert, 2002), with low values increasingly favored (Loyd et al., 2007). Variability in H_i could swamp any size signal in rates of volcanism, an important uncertainty addressed in §5. 3.4. A useful rule of thumb is that a doubling a

planet's concentration of radiogenic elements makes it behave like a planet with double the radius (Stevenson, 2003).

Equations (3) – (5) can be solved directly for T. It is then easy to find the mass dependence of temperature (§5.3.1; Figure 5.2). However, secular cooling significantly contributes to the heat flux at the bottom of the lithosphere, so at a given time a planet will have a higher internal temperature and a higher heat flow than these thermal equilibrium calculations would suggest. Planets of different masses follow parallel cooling tracks (Stevenson, 2003), and internal temperature is regulated by the dependence of mantle viscosity on temperature (Tozer, 1969). A very simple model for mantle thermal evolution with temperature-dependent viscosity in plate tectonic mode is (Schubert et al., 2001): -

$$\frac{\partial T}{\partial t} = \frac{H}{c} - k_1 (T_m - T_s)^{(1+\beta)} exp\left(\frac{-\beta A_0}{T_m},\right) \tag{5.6}$$

where

$$k_1 = \frac{Ak}{cdM_{mantle}} \left(\frac{\alpha g d^3}{\kappa \nu_0 Ra_{cr}}\right) \tag{5.7}$$

and c is the specific heat capacity of mantle rock.

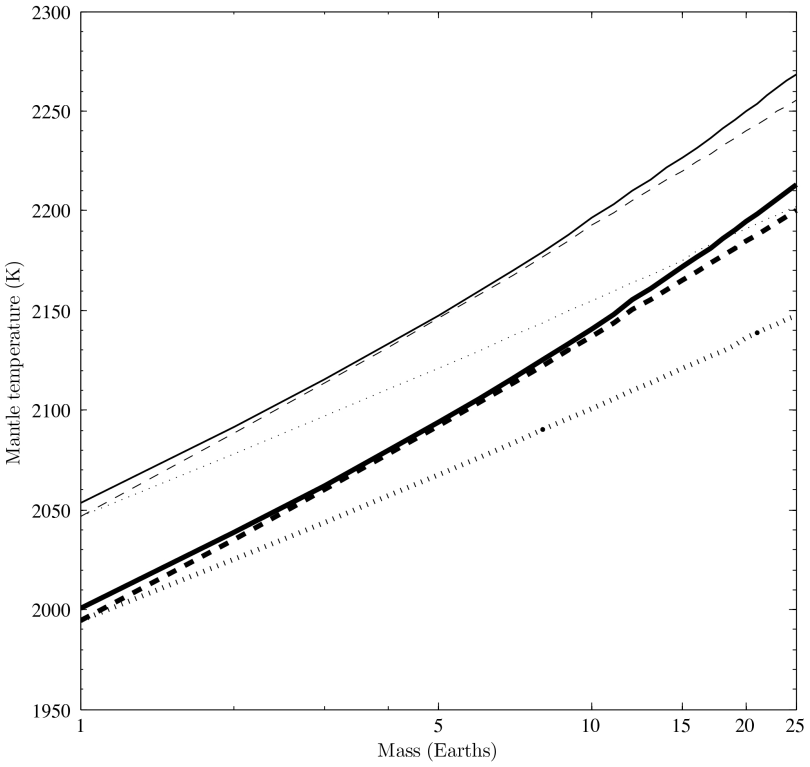

Figure 5.2 Effect of mass on mantle temperature for a planet in thermal equilibrium with a specific radiogenic power appropriate for today's Earth. Thick lines correspond to a surface temperature of 273 K, thin lines correspond to a surface temperature of 647K. The solid line uses the scaling of Seager et al. (2007), and the dashed lines use the scaling of Valencia et al. (2006): note that the latter is only valid for $M < 10\ M_{Earth}$. The dotted lines use constant-density scaling. Seager et al. (2007) model cold exoplanets, leading to an underestimate of Earth's radius by 3 %. The omission of thermal expansion leads to a smaller surface/area volume ratio than the other models, so the Seager et al. (2007) curves plot above those for Valencia et al. (2006) at low mass.

We integrate this model forward in time from a hot start, using a fourth-order Runge-Kutta scheme. Because of the exponential temperature dependence of convective velocity, the transient associated with the initial conditions decays on a 100 Myr timescale, provided that the planet has a 'hot start'. Hot starts are overwhelmingly likely for differentiated massive rocky planets. Our initial condition is $T_m = 3273$ K, but our results are insensitive to increases in this value.

For planets in stagnant lid mode, we use the scaling of Grasset and Parmentier (1998): -

$$T_c = T_m - 2.23\frac{T_m^2}{A_o}, \tag{5.8}$$

where T_c is the temperature at the base of the stagnant lid; plausible values lead to $(T_m - T_c) \ll T_m$. Then:

$$Nu \approx \left(\frac{g\alpha(T_m - T_c)d^3}{\kappa\nu(T)Ra_{cr}}\right)^{\beta}. \tag{5.9}$$

Since $T_c > T_s$, stagnant lid convection is less efficient at transporting heat than plate tectonics.

5.2.3 Melting model

Earth generates 34 km^3 yr^{-1} crust of which 63% is by isentropic decompression melting at mid-ocean ridges (Best and Christiansen, 2001). This percentage understates the contribution of mid-ocean ridge melting to overall mantle degassing, because most of the volatile flux at arcs is just recycled from subducting crust. After four decades of intensive study, mid-ocean ridge melting is also the best-understood melting process (Juteau and Maury, 1999). Beneath mid-ocean ridges, the mantle undergoes corner flow. Melt is generated in a prism with triangular cross-section, ascends buoyantly, and is focused to a narrow magma lens beneath the ridge. Petrological systematics require (Langmuir et al., 1992), and most melting models assume (Ghiorso et al., 2002) that the source magmas for mid-ocean ridge basalt melt fractionally or with small residual porosity, separate quickly, and suffer relatively little re-equilibration during ascent. For more massive planets, these remain robust assumptions. Buoyancy forces driving segregation are stronger and, because the pressure at which the solidus and adiabat intersect is at a shallower absolute depth, the ascent pathways are shorter. Because of these attractive simplifications and because mid-ocean ridge melting dominates Earth's crust production budget, we focus on mid-ocean ridge melting in this paper.

Isentropic decompression melting pathways are distinguished by their values of potential temperature, T_p. Actual temperatures of near-surface magmas are lower because of the latent heat of melting, the greater compressibility of melts with respect to solids, and, usually less important, near-surface conductive cooling. All mid-ocean-ridge melting schemes are very sensitive to T_p, especially just above the zero-pressure solidus. That is because increasing T_p both increases the pressure at which melting first occurs (lengthening the 'melting column') and also increases the mass fraction of melting (X) suffered by the top of the melt column (Figure 5.1c).

With the above assumptions,

$$P_{crust} = -\int_{P_o}^{P_f} X(T,P)dP \tag{5.10}$$

$$T(P) = T\left(P + \delta P\right) - \left(\frac{\partial V}{\partial S}\right)\delta P + \left(\frac{\partial X}{\partial P}\right)L \tag{5.11}$$

$$T(P_o) = T_p + P_o\frac{\partial V}{\partial S}, \tag{5.12}$$

where $P_f = 0$ in the case of plate tectonics or $P_f = P_{lith}$ (the pressure at the base of the lithosphere) in the case of stagnant lid convection; P_o is given by the intersection of the adiabat with the solidus, which is the point on the adiabat $\left(\frac{\partial V}{\partial S}\right)$ where $X = 0$; L is the latent heat of melting; and S is entropy.

We use three models for $X(T, P)$. In order of increasing complexity, they are those of McKenzie (1984) as extended in McKenzie and Bickle (1988) (henceforth MB88), Katz et al. (2003) (henceforth K03), and (for plate tectonic models only) Ghiorso et al. (2002), with the Smith and Asimow (2005) front-end (henceforth pMELTS). MB88 and K03 are similar in that they fit simple functional forms to experimental data, with MB88 more widely used although it is constrained by fewer data. pMELTS is a state-of-the-art model of phase equilibria for compositions similar to Earth's mantle. We use pMELTS throughout the predicted melting range, even though the model is only calibrated for use in the range 1-3 GPa. For pMELTS, we assume continuous melting with a residual porosity of 0.5% (that is, melt fractions greater than 0.5% are evacuated from the melting zone), and we use the mantle composition inferred to underly Earth's mid-ocean ridge system (Workman and Hart, 2005) with 500 ppm water. Representative results with all these models are shown in Figure 5.3.

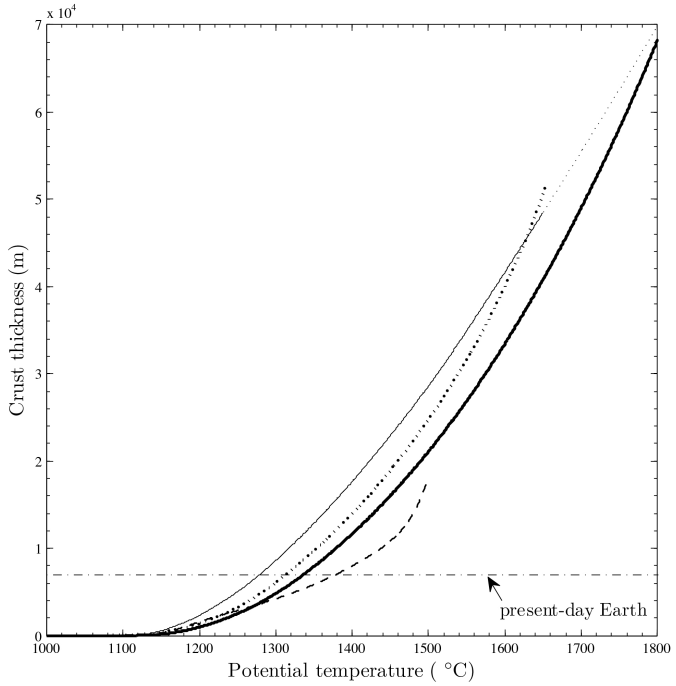

Figure 5.3 Crustal thickness as a function of potential temperature for $M_{Earth} = 1$. Thick line corresponds to the model of Langmuir et al. (1992), which has a similar functional form to the models used by Sleep (2007) and Papuc and Davies (2008). Thin solid line corresponds to MB88 model, thick dotted line to K03 model, and dashed line to pMELTS model. Thin dotted line is a cubic extrapolation of MB88 beyond its range of validity. pMELTS results are only shown where first melt occurs at < 3 GPa. MB88 results are only shown where melt fraction is zero at 8 GPa. Horizontal dash-dot line is observed crustal thickness on today's Earth.

Each model is required to produce 7 km thick basaltic crust, which is the observed value on Earth (White et al., 2001), after 4.5 Gyr on an Earth-mass planet undergoing plate tectonics. We adjust the offset between potential temperature in the melting models, and the characteristic mantle temperature used in the thermal model, to obtain the observed crustal thickness. The required offset $T_m - T_p$ is 741 K, 707 K, and 642 K, for the MB88, K03, and pMELTS models, respectively (Figure 5.3).

5.3 Model output

5.3.1 Simple scaling laws from thermal equilibrium calculations

The simplest possible rocky planet model assumes that the ratio of radiogenic heat production to lithospheric heat flux (the convective Urey number), $Ur = 1$. We take the radiogenic-element concentrations given by Turcotte and Schubert (2002) (Table 1) and use 5.3 – 5.5 to set mantle temperature. This is greater for more massive planets because their decreased surface area/volume ratio requires higher heat fluxes (& more vigorous convection) to dispose of the same heat flux. From Equations 5.3–5.5, but neglecting the dependence of Q on T_m:

$$\left(\frac{Ra}{Ra_{Earth}}\right)^{\beta} = \left(\frac{M}{M_{Earth}}\right)\left(\frac{A}{A_{Earth}}\right)\left(\frac{d}{d_{Earth}}\right) \tag{5.13}$$

which with $R \propto M^{0.25-0.28}$ (Valencia et al., 2006) gives $Ra \propto M^{\approx 2.45}$; using this simplification leads to a relation between temperature and mass

$$\nu(T) \propto M^{-5/4} \tag{5.14}$$

— which when inserted into Equation (5) gives a good fit to the results shown in Figure 5.2. Similar scaling arguments with $R \propto M^{1/3}$ give $\nu(T) \propto M^{-8/9}$, i.e. an approximately straight line on a linear-log graph of temperature versus mass (Figure 5.2).

Table 5.1 Radioisotope data: half lives, specific power W, and concentrations $[X](i)$ (ppb) after 4.5 Gyr.

Parameter	^{40}K	^{232}Th	^{235}U	^{238}U	Reference
$t^{1/2}$ (Gyr)	1.26	14.0	0.704	4.47	
Specific power ($\times 10^{-5}$ W kg^{-1})	2.92	2.64	56.9	9.46	
Concentrations					
"Mantle"	36.9	124	0.22	30.8	Turcotte & Schubert (2002)
"Undepleted Earth"	30.7	84.1	0.15	21.0	Ringwood (1991)
CI chondrites	71.4	29.4	0.058	8.1	Anders & Grevesse (1989)
EH chondrites	147.8	2.8	5.8	13.0	Newsom (1995)

Note. $H_i = [X](i)W_i$.

5.3.2 Plate tectonics

We now turn to our time-dependent results.

Table 5.2 Parameters used in interior and thermal models.

Parameter	Symbol	Value	Units	Reference
Thermal expansivity, mantle	α	3×10^{-5}	K^{-1}	1
Thermal conductivity	k	4.18	W m^{-1} K^{-1}	1
	β	0.3		1
Thermal diffusivity	κ	10^{-6}	m^2 s^{-1}	1
Critical Raleigh number	Ra_{cr}	1100		1
Gas constant	R	8.31	J K^{-1} mol^{-1}	2
Specific heat capacity, mantle	c	914	J K^{-1} kg^{-1}	1
Density, mantle	ρ_{mantle}	3400	kg m^{-3}	1
Density, crust	ρ_{crust}	2860	kg m^{-3}	3
Reference viscosity	ν_0	165	m^2 s^{-1}	1
Gravitational constant	G	6.67×10^{-11}	m^3 kg^{-1} s^{-2}	2
Core mass fraction	f_{core}	0.325		2
Earth radius	$R_\oplus$	6.372×10^6	m	2
Earth mass	$M_\oplus$	5.9742×10^{24}	kg	
Mantle temperature, initial	T_m $(t = 0)$	3273	K	
Temperature change causing e-folding in viscosity	T_ν	43 or 100	K	1 or 4

References. (1) Turcotte & Schubert 2002; (2) de Pater & Lissauer 2001; (3) Carlson & Herrick 1990; (4) Sleep 2007.

- *Thermal evolution.* As anticipated (Stevenson, 2003), mantle temperatures for planets of different masses follow ∼parallel cooling curves. Planets with M = 2 (5, 10, 25) M_{Earth} have potential temperatures 39 K (97 K, 146 K, 221 K) greater than Earth after 4.5 Gyr (Figure 5.4). There is little difference in thermal evolution between internal structure models: the temperature difference between Valencia et al. (2006) and Seager et al. (2007) is always <15 K (Figure 5.2). The constant-density planet runs significantly (up to 100K) colder since it has a much larger surface area, but the same radiogenic-element complement. From now on we use only the thermal evolution calculations for the Seager et al. (2007) internal-structure model.

- *Simple melting models, MB88 and K03.* Potential temperature increases monotonically with mass, so the pressure at the base of the crust also increases monotonically (Figure 5.3). However, the absolute thickness of the crust also scales as the inverse of gravity. In other words, although bigger planets run hotter, higher surface gravity moves the solidus and suppresses melting. For temperatures close to the solidus, the first effect dominates, and increasing planet mass increases crustal thickness (Figure 5.5). Young and/or large planets show the opposite trend, with crustal thickness decreasing as planet mass increases. Crustal thicknesses are within a factor of two of each other for 1 – 25 M_{Earth} until 8.6 Gyr. After that, the ratio of crustal thicknesses diverges, as melting begins to shut down on the lowest-mass planets. In both models, for planets of intermediate mass and with ages slightly greater than the Solar System, increasing mass

has only a small (and negative) effect on crustal thickness. However, crust production per unit time increases with increasing mass, because more massive planets have more rapid plate spreading: see §5.5.1.

- *pMELTS, a more complex melting model.* pMELTS predicts crustal thickness will increase rapidly with increasing planet mass for massive planets with ages comparable to the Solar System (Figure 5.5d). Potential temperatures for these planets are > 1500 °C. The crustal-thickness result at this temperature should be treated with suspicion, because when $T_p > 1460$ °C, pMELTS predicts melting will occur to pressures greater than those for which it has been experimentally calibrated (< 3 GPa). Crustal thickness is > 1 km even after 13 Gyr in the pMELTs model, even for masses of 1 M_{Earth}. This is because pMELTS-predicted crustal thickness ramps up slowly to 7 km crustal thickness as temperature increases (Figure 5.3), so contours of constant crustal thickness are spaced more widely in temperature (equivalently, time) than with the other models. As with the other melting models, the planet mass that produces the thickest crust at a given time increases as the planets age.

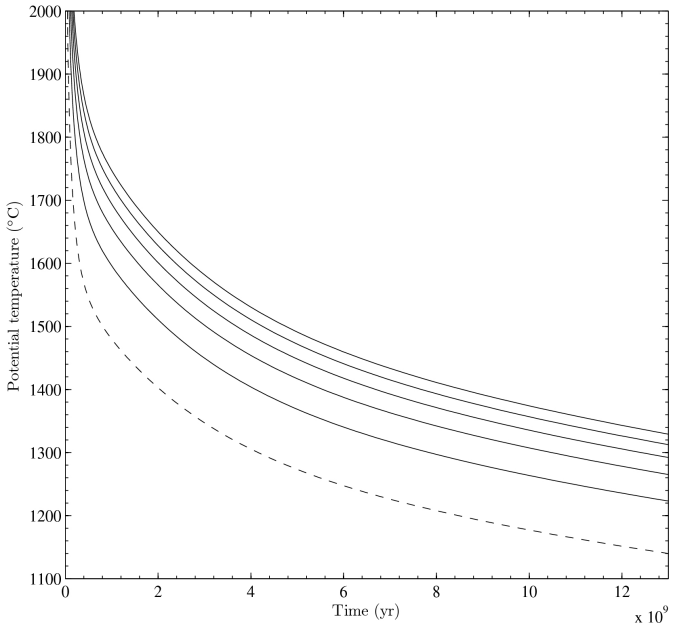

Figure 5.4 Effect of increasing planet mass on thermal evolution. Mantle temperatures are adjusted to produce 7 km thick crust with plate tectonics under MB88 melting model at 4.5 Gyr for 1 M_{Earth}. Dashed line is 1 M_{Earth}; solid lines are for 5, 10, 15, 20 and 25 M_{Earth}, with temperature increasing with increasing mass. $T_\nu = 43$ K.

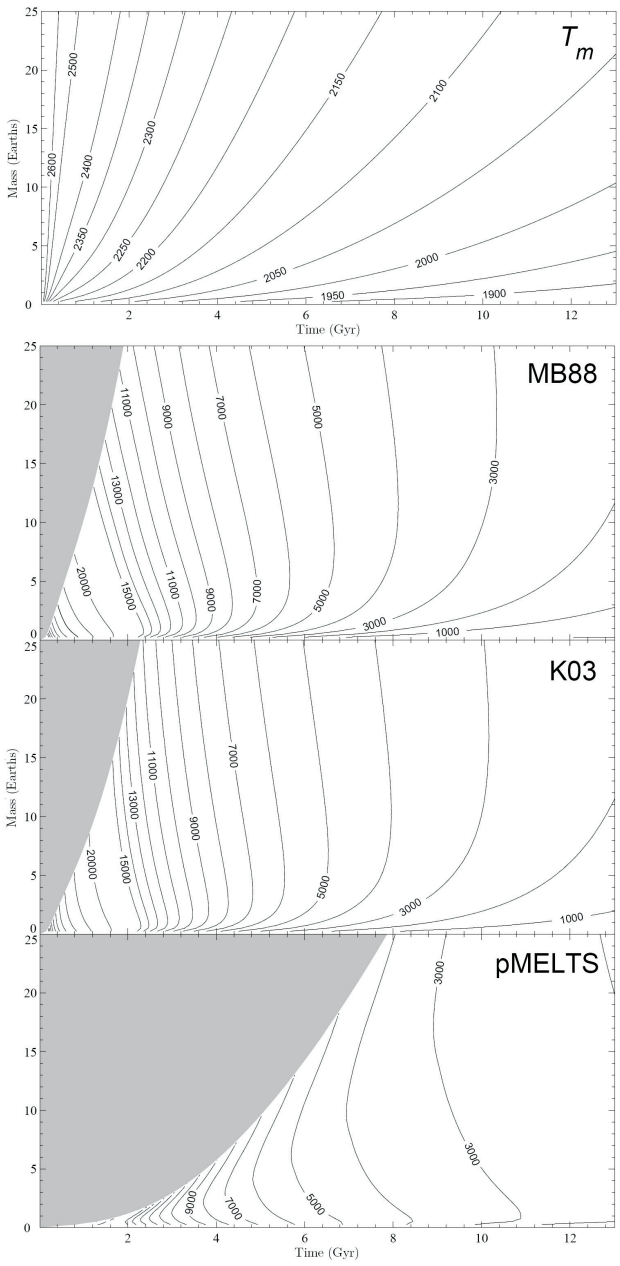

Figure 5.5 (Uppermost panel) Evolution of mantle temperature (°C) with time under plate tectonics. Seager et al. (2007) internal structure model. Initial temperature for all models is 3273 K. (Lower panel, top to bottom) Corresponding crustal thicknesses in meters for MB88, K03 and pMELTS melting modes. Contour interval is 1000m from 0 to 15000m, and 5000m for larger values. Light grey regions are where melting models are extrapolated beyond their stated range of validity. Horizontal line at bottom right of MB88 pane corresponds to cessation of volcanism on 0.25 M_{Earth}planets after $\sim$ 12 Gyr (see text).

To summarize, mass dependence increases with time as planets cool toward the solidus, and (for a given mass range) the sign of mass dependence changes with time. This is because of the strongly nonlinear behavior of melt production near the solidus; melting goes from zero to significant over a small range in potential temperature. Low-mass planets approach this temperature by 7-8 Gyr. Their crustal thickness declines more rapidly than on high-mass planets.

5.3.3 Stagnant lid

- *Thermal evolution.* Because stagnant lid convection is less efficient at transferring heat than plate tectonics, a planet in which plate tectonics is suddenly halted will heat up (the thin solid line in Figure 5.6). This temperature rise reduces mantle viscosity, so Ra increases. Temperature converges on the evolutionary track of a planet that has always been in stagnant lid mode, with a characteristic convergence timescale of $(H\Delta T_{mode})/cM_{mantle} \sim 1$ Ga. A similar argument explains the temperature changes associated with going from stagnant lid mode to plate tectonics. The temperature difference between the tracks is $\Delta T_{mode} \approx 160$ K for all masses. This is roughly $T_0\ ln\left((T_m - T_s)/(T_m - T_c)\right)$, which can be understood by equating the RHS of Equations 5.4 and 5.9. Therefore, the thermal evolution of stagnant lid planets follows Figure 5.5a, but $\approx$ 160K hotter.

- *Stagnant lid melting – live fast and die young.* Melt production within an ascending column of mantle in stagnant lid mode is truncated at the base of the lithosphere. For the same mantle temperatures, predicted erupted thickness is much smaller (Equation 5.10).This effect opposes the increased temperature of stagnant-lid mantles. To produce Figure 5.7 we use the same mantle-potential temperature offsets as in plate tectonic mode (so the model is still 'tuned to Earth'). Most planets run hotter in stagnant-lid mode to the extent that pMELTS cannot be used, as T_p exceeds the range over which it is calibrated. The MB88 and K03 models show roughly the same behavior in stagnant lid mode (Figure 5.7). For young (<2-3 Gyr) planets, an ascending column of mantle produces more melt in a stagnant lid mode than in plate tectonic mode – the higher temperature matters more than the (small) lithospheric thickness. For somewhat older planets, an ascending column of mantle produces less melt in stagnant lid mode than in plate tectonic mode. The temperature difference is much the same, but the growing lithosphere increasingly truncates the melting column. At a mass-dependent age much less than the age of the Galaxy, melting ceases.

- *What controls cessation of melting?* For a given melt production function, all planets in plate tectonics mode will cease volcanism at the same potential temperature. Consequently, a planet's volcanic lifetime is delineated by an isotherm (T_p = 1080 - 1193 °C, depending on the melting model). For planets in stagnant lid mode, this is not

the case. There is still a one-to-one relationship between temperature and the absolute thickness of the lithosphere. However, the absolute thickness of the melt zone at fixed temperature decreases with increasing gravity, but z_{lith} does not. Thus, z_{lith} increasingly truncates the melt zone as gravity increases. As a result, there is a temperature range for which low-mass planets can sustain melting in stagnant lid mode, whereas high–mass planets cannot. Over the mass range 1 – 25 M_{Earth}, this temperature range is $\sim$ 180K. Consequently, in stagnant lid mode, more massive planets run much hotter but cease melting only moderately later than smaller planets (Figure 5.7).

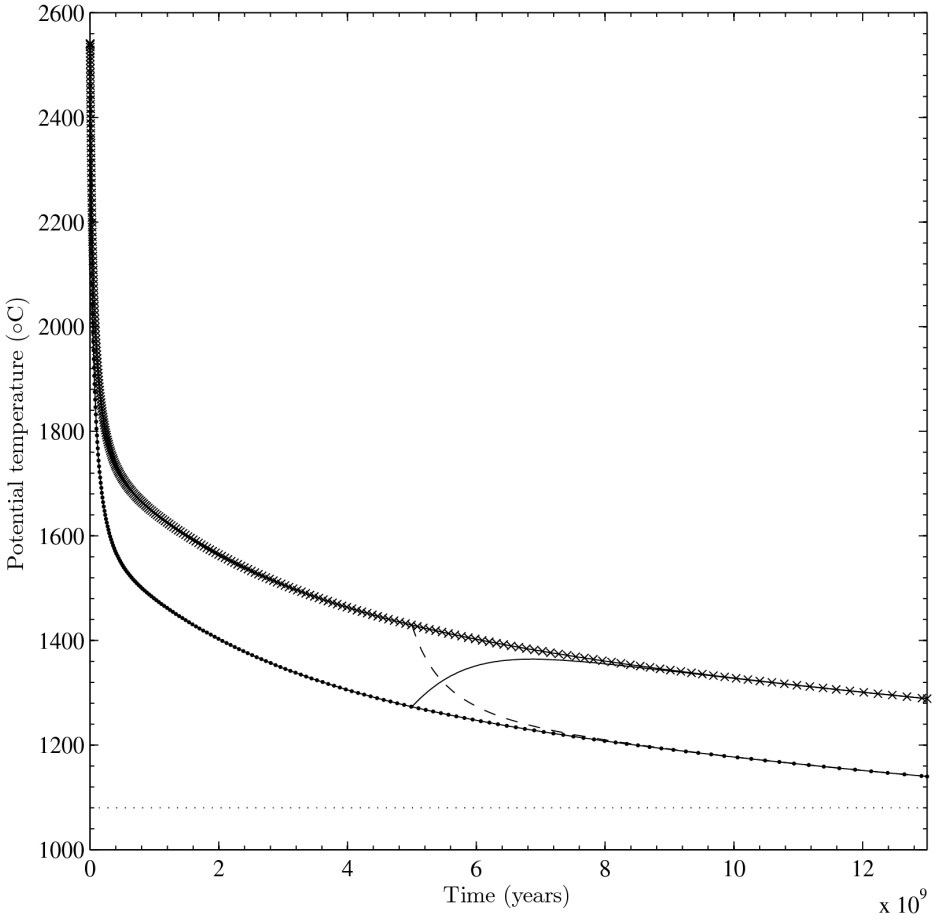

Figure 5.6 Effect of mode of mantle convection on thermal evolution. Crosses joined by solid line correspond to stagnant lid mode. Dots joined by solid line correspond to plate tectonics mode. Thin solid line shows thermal evolution when an instantaneous switch to stagnant lid mode is imposed, after 5 Gyr, on a planet undergoing plate tectonics. The dotted line corresponds to the thermal evolution following an instantaneous switch to plate tectonics. For equivalent radiogenic complements, a planet in plate tectonics mode will have a lower potential temperature than a planet in stagnant lid mode. The difference is comparable to the range in potential temperatures due to mass.

5.3.4 Initial bulk-chemistry and initial radiogenic-power variations

'Non-canonical' initial radiogenic element complements have been suggested for Earth. To evaluate this possibility, we show 1 M_{Earth} thermal evolution tracks with radioisotope complements appropriate to 'undepleted' Earth (Ringwood, 1991), CI chondrites (Anders and Grevesse, 1989), and EH chondrites (Newsom, 1995) (Table 1; Figure 5.8). The CI and 'undepleted' tracks show similar behavior to T&S, but the U^{235}-rich, U^{238}-poor EH chondrite track shows more rapid cooling. Since we use Earth's observed oceanic crust thickness to tune mantle temperature, it is not particularly important to get the absolute values right, and three of the four radiogenic-element complements tested have similar behavior over geological time.

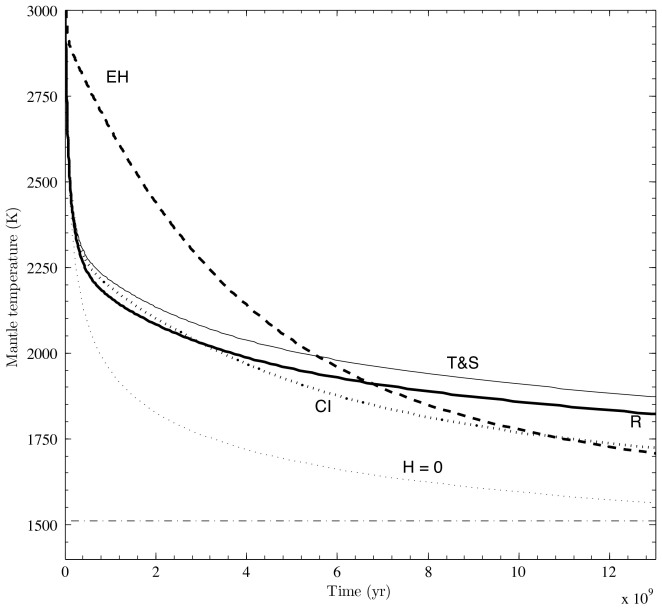

Figure 5.8 Effect of different radiogenic-element complements on thermal evolution. Initial mantle temperatures are identical; all runs are with T_ν = 43 K. Thick lines correspond to various chondritic scenarios: thick dashed line is EH chondrite; thick dotted line: CI chondrite; thick solid line: Ringwood, 1991. The thin solid line is for Turcotte and Schubert (2002), and the thin dotted line is for no radiogenic elements in the mantle. This could correspond, for example, to early and complete differentiation of the mantle to produce a thick crust, which is then swiftly removed by impacts. The horizontal dash-dot line at 1510 K corresponds to $Nu = 1$ (no convection, no large-scale mantle flow, and no potential for sustained melt production).

The long-term thermal evolution of rocky planets depends on the abundance of the long-lived radioisotopes ^{232}Th, ^{235}U, and ^{238}U at the time of planet formation. These are produced only by the rapid neutron capture process (r-process) acting on the iron-peak isotopes. This

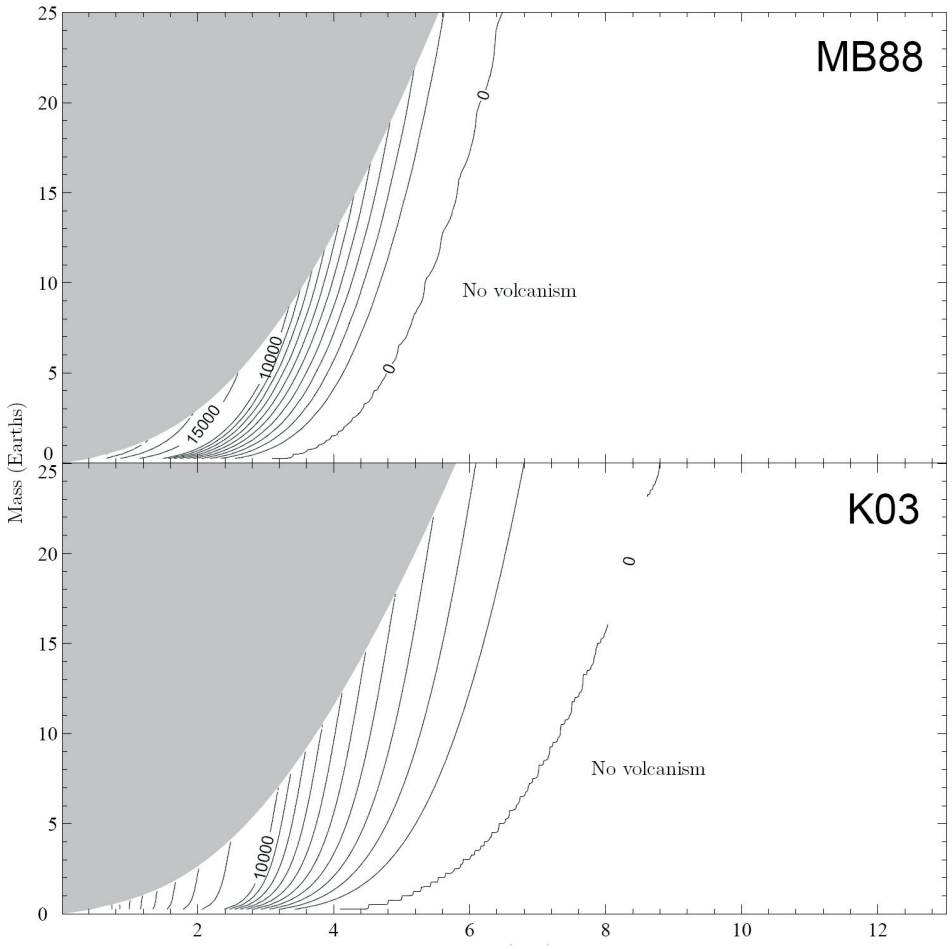

Figure 5.7 Evolution of crustal thickness with time in stagnant lid mode, for MB88 (top) and K03 (bottom) melting models. Wiggles in the $Z_{crust} = 0$ contour are interpolation artifacts.

is thought to occur only during explosive nucleosynthesis in stars with $10-20M_{\odot}$ (Chen et al., 2006). In contrast, Si is produced during α-chain process by the whole range of massive stars. Th, and especially U, are difficult to detect in stars but europium (Eu), another exclusively r-process element, can be readily measured. The average observed stellar abundance of Eu to silicon decreases by a factor of 0.63 as the abundance of heavy elements or metallicity (represented by iron Fe) increases by a factor of 100 to the solar value (Cescutti, 2008). The r-process appears to be universal and all r-process elements scale closely with solar values (Frebel, 2008). Therefore the average abundance of ^{232}Th, ^{235}U and ^{238}U isotopes can be predicted using the trend of Eu with abundance or metallicity, the age-metallicity relationship of the Galaxy, the star formation history of the Galaxy, and the half life of each isotope. We adopt a simple linear age-metallicity relationship with an increase of 1 dex (factor of 2.5) over the age of the Galaxy, with solar metallicity occurring 4.6 Gyr ago (e.g. Pont and Eyer (2004)). Figure 5.9 plots the predicted abundance of the three isotopes using the observed trend of Eu and the Prantzos & Silk (1998) parameterization of the star formation history of the Galaxy. (The predictions are only weakly sensitive to the model of star formation). The age of the Galaxy is taken to be 13.6 Gyr. All abundances are normalized to the value at the formation of the Sun.

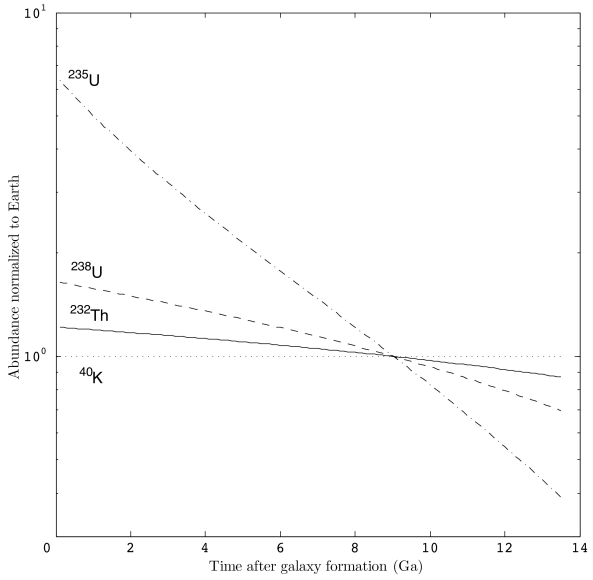

Figure 5.9 Abundance, relative to silicon and normalized to conditions at the time of the protosolar nebula, of the principal long-lived radionuclides in rocky planet mantles.

Planets forming early in the history of the Galaxy would have 50% more ^{238}U, but 6 times more ^{235}U, than Earth. The higher abundance is because the amount of radioisotopes

in the interstellar medium only reflects massive star formation over a few half-lives, whereas ^{28}Si and other stable isotopes accumulate over the history of the Galaxy. Therefore these systems are not U- and Th-rich, they are Si-poor. The high abundance of ^{235}U could have an important role in the *early* thermal history of such planets.

The effect of these trends on *present-day* planet temperatures, while still significant, is more modest. Figure 5.10 plots planet temperature against the age of the host star. Comparison with Figure 5.5 shows that inclusion of cosmochemical trends in H_i lowers T_m by up to 50 K for young planets, while raising T_m by up to 40 K for old stars, compared to their present-day temperature had they formed with an Earthlike inventory of radiogenic elements.

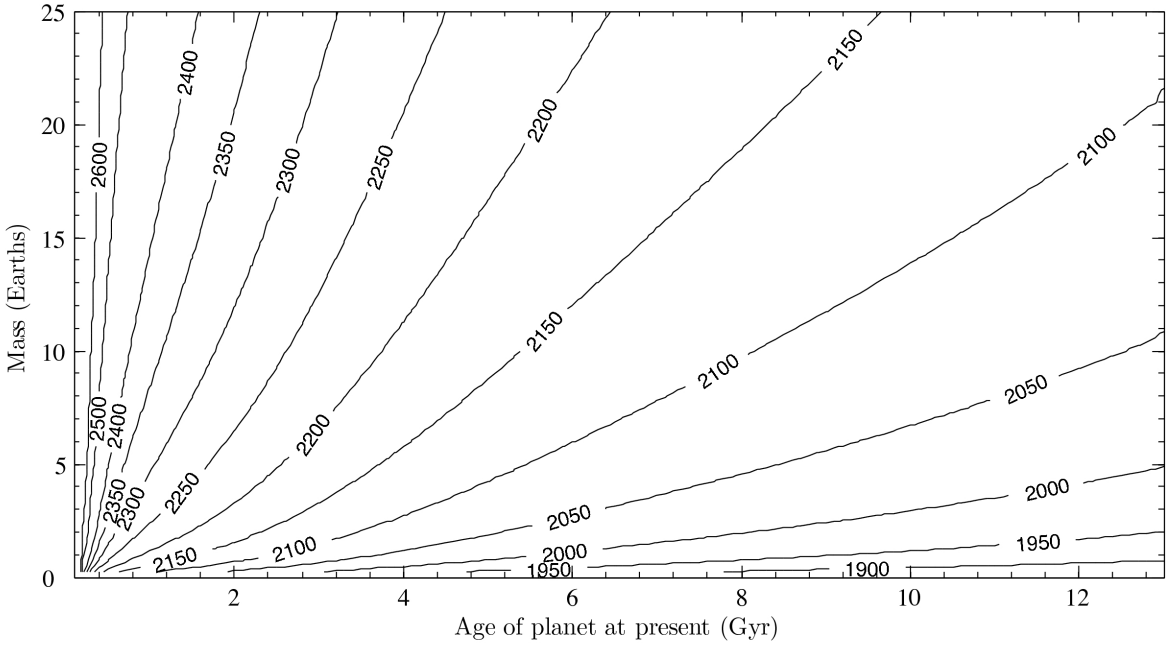

Figure 5.10 Temperature at the present epoch, tracking the effect of galactic cosmochemical evolution on initial radioisotope complement. Planets plotting to the left orbit young stars, planets plotting to the right orbit old stars. Compare with top panel of Figure 10. Note that the abscissa is not time, but the age of planet at the present day.

We have assumed that the major-element composition of planetary mantles is similar

everywhere and at all times. This is unlikely to be true in detail: for example, it has been proposed that on early Earth the mid-ocean-ridge-basalt source was more depleted than at the present day (Davies, 2007). Earth's continent mass fraction may be higher (Rosing, 2006), or lower than is typical. More severe variations in major-element composition, with correspondingly major shifts in rheology and in the solidus, can be imagined (e.g., Gaidos (2000); Kuchner and Seager (2005)). Even highly oxidized 'coreless' planets have been modeled (Elkins-Tanton and Seager, 2008b). We leave the geodynamic consequences of such variations as an open subject: a future objective will be to use geodynamic observables to constrain internal structure and bulk composition.

5.4 Effect of melting on style of mantle convection

We have shown that transitions between plate tectonics and stagnant lid mode have an impact on thermal evolution comparable to that of mass over the range of masses considered in this paper. With this motivation, we now assess whether plate tectonics is viable on more massive Earth-like planets. Our approach will be to use our comparatively robust understanding of melting to examine conditions under which other forms of heat transfer supplant Earthlike plate tectonics. Vertical tectonics, as seen on Io (Moore (2003); Lopes and Spencer (2007)) may be thought to take over from horizontal (plate) tectonics when either:– (1) the thickness of the crust becomes comparable to that of the lithosphere; (2) heat lost by magma transport dominates over conduction, or (3) the crust delaminates. We also assess the likelihood that (4) continental growth or (5) greater plate buoyancy prevents subduction. We present results only for our fiducial calculation with MB88 melting and radiogenic-isotope complements following Turcotte and Schubert (2002).

We assume throughout that surface water is available to hydrate lithosphere rock. Weakening the lithosphere by hydration is thought to be a prerequisite for plate tectonics.

5.4.1 Crust thicker than lithosphere

If the crustal thickness Z_{crust} is comparable to the lithospheric thickness Z_{lith}, the lower crust is likely to melt and form buoyant diapirs. Widespread intracrustal diapirism within the oceanic crust is not known on Earth and, if it were a major heat sink for the mantle, would be a substitute for plate tectonics. Z_{lith} scales as Q^{-1}, and on Earth the equilibrium value of Z_{lith} is ~ 110 km (McKenzie et al., 2005). Therefore,

$$\left(\frac{Z_{crust}}{Z_{lith}}\right) = \frac{7}{110}\left(\frac{Q}{Q_{Earth}}\right)\left(\frac{Z_{crust}}{Z_{crust,Earth}}\right). \tag{5.15}$$

We find $Z_{crust}/Z_{lith} < 1$ for all planets > 2 Gya (Figure 5.11), so intracrustal diapirism is unlikely within equilibrium lithosphere. Intracrustal diapirism is unlikely to be the limiting factor for super-Earth plate tectonics.

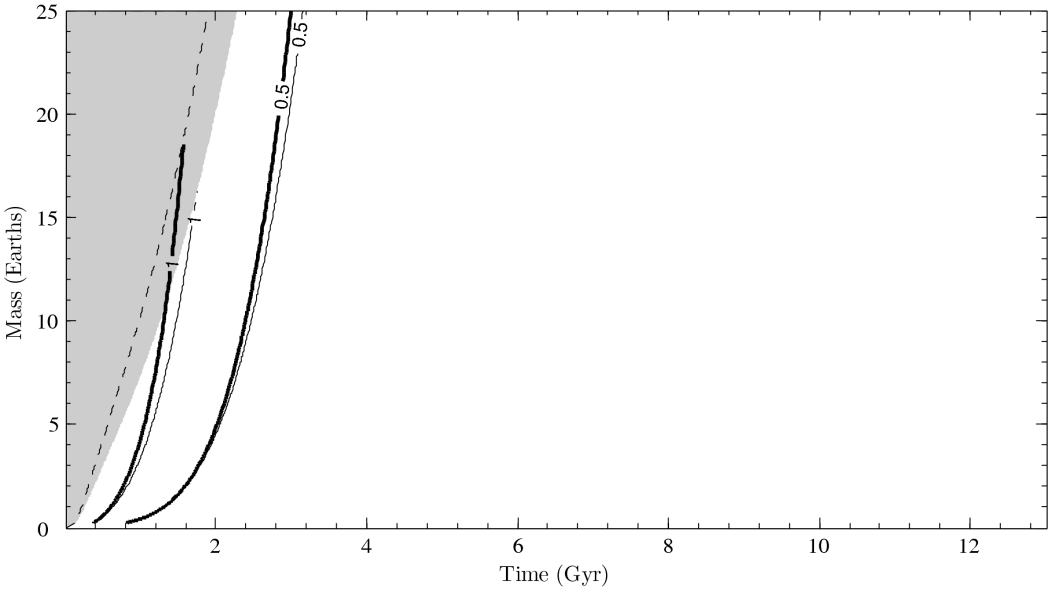

Figure 5.11 Possible limits to plate tectonics. Thick solid lines correspond to crust–to–lithosphere thickness ratios of 0.5 and 1.0 for MB88 melting model; thin solid lines are the same, but for K03 melting model. Points to the left of these solid lines may be subject to vertical (Io-type) tectonics. Dotted line is the limit of validity of the MB88 melting model. Results not shown for pMELTS melting model because solid lines fall in the temperature region for which pMELTS is not valid.

5.4.2 Magma-pipe transport energetically trumps conduction

On Earth, heat lost by conduction through thin lithosphere near mid-ocean ridges greatly exceeds heat lost by advection of magma. On Io, the opposite is true: most internally-deposited heat is lost by advection of magma through lithosphere-crossing magma conduits – 'magma pipes' (Moore, 2001). Such a planet, although it may have limited plate spreading, is not in plate tectonic mode; vertical rather than horizontal motion of the material making up the lid is the more important process.

We introduce the dimensionless 'Moore number', Mo, in appreciation of the work of Moore (2001, 2003), which we define to be the ratio of magma-pipe heat transport, Q_{magma}, to heat lost by conduction across the lithosphere, Q_{cond}. To calculate how this number (analogous to a Peclet number) scales with increased mass, we specify that total heat loss

(magma pipe transport plus conduction across the boundary layer) adjusts to match the heat loss across the boundary layer prescribed by the thermal evolution model:

$$Mo = \frac{Q_{magma}}{Q_{cond}} = \frac{Q}{Q_{cond}} - 1 \tag{5.16}$$

An upper bound on magma-pipe transport is to assume that all melt crystallizes completely and cools to the surface temperature. In that case:

$$Q_{magma} = \rho_{crust}(c_b \Delta T_1 + E_{lc}) Z_{crust} l_r s \sim c_1 s. \tag{5.17}$$

where ρ_{crust} is crustal density, c_b is the specific heat of basalt, ΔT_1 is the temperature contrast between lava and the surface, E_{lc} is the latent heat of crystallization, l_r is ridge length and s is spreading rate. Provided that half-space cooling is a good approximation to the thermal evolution of plates,

$$Q_{cond} = 2k\Delta T_2 \left(\sqrt{\frac{A_{oc} l_r}{\pi \kappa}} \right) \sqrt{s} \sim c_2 \sqrt{s}, \tag{5.18}$$

where A_{oc} is the area of the ocean basins only, which we take to be $0.6 \times A$ as on Earth. We can now solve the quadratic in s —

$$Q^2 = c_1^2 s^2 + c_2^2 s. \tag{5.19}$$

Finally we obtain an expression for Mo:

$$Mo = \frac{Q_{magma}}{Q_{cond}} = \left(\frac{\rho_{crust}(c_b \Delta T_1 + E_{lc}) Z_{crust} l_r}{2k\Delta T_2 \sqrt{A l_r}/(\sqrt{\pi \kappa})} \right) \sqrt{s}. \tag{5.20}$$

Here l_r is ridge length and s is spreading rate. We assume a latent heat of crystallization E_{lc} = 550 kJ/kg, a specific heat of basalt c_b = 0.84 kJ/kg/K, crustal density ρ_{crust} of 2860 kg/m^3 (Carlson and Herrick, 1990), base lithosphere temperature of 1300 °C, and lava temperature of 1100 °C and surface temperature of 0 °C giving ΔT_1 = 1100 K and ΔT_2 = 1300K. This gives 4.2 x 10^{18} J in melt/km^3 plate made. As an illustration, for Earth (mid-ocean-ridge crust production 21 km^3 yr^{-1}), Q_{magma} is 2.8 TW. The total oceanic heat flux is 32 TW, so today's Earth has a $Mo \sim 0.10$.

Therefore, given the one-to-one relationship between Q and T_p, we can solve for spreading rate (Figure 5.12). As $Mo \to 0$, $s \to Q^2$ (Sleep and Zahnle, 2001). Notice that the characteristic age at subduction $\tau = A/(2l_r s)$. As a consequence, the Moore number does not vary with different possible scalings of ridge length (equivalently, plate size) with increased planet mass. As planet mass increases, we hold plate area (rather than the number of plates) constant to produce Figure 5.12. If one instead holds the number of plates constant, l_r falls and s increases, but, because τ is unchanged, our subsequent buoyancy and rate of volcanism calculations (§5.4.4 & §5.5) are not affected. For Earth, (18) gives $s \sim 5$ cm yr^{-1}, a good

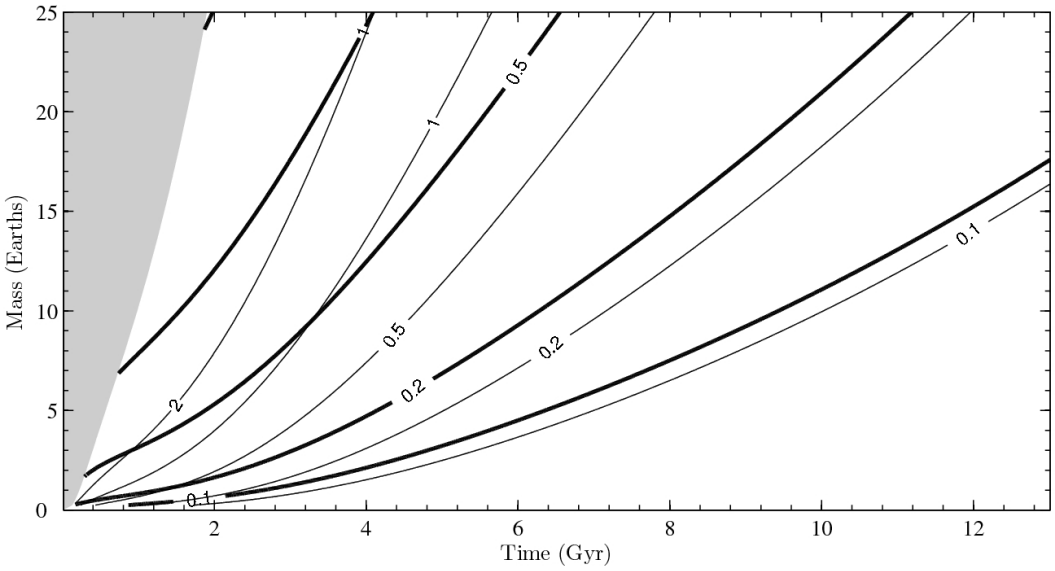

Figure 5.12 Plate spreading rate (m/yr) as a function of time. Thick lines correspond to solution including heat transport through magma pipes. Thin lines correspond to conduction-only solution. MB88 melting model.

Reaching $Mo \sim 1$ requires temperatures near or beyond the limit of validity of our melting models. Coincidentally, $Mo = 1$ plots close to $Z_{crust}/Z_{lith} = 1$ on a mass-time graph. We conclude that heat-pipe cooling is not dominant for Earth-like planets > 2 Gyr old.

5.4.3 Phase transitions within crust

Basalt, which is less dense than mantle rock, undergoes a high-pressure exothermic phase transition to eclogite, which is more dense than mantle rock (Bucher and Frey, 2002). Except during subduction, the pressures at the base of Earth's basaltic crust are too low to make

eclogite. However, the pressures at the base of the crust on massive Earth-like planets are far greater. If the crust of a massive earth-like planet includes an eclogite layer at its base, this may delaminate and founder, being refreshed by hotter mantle (Vlaar et al., 1994).

We tracked temperature and pressure at the base of the crust for planets in plate tectonics mode, and compared these with the phase boundaries for eclogite plotted in Fig. 9.9 of Bucher and Frey (2002). We assumed uniform thermal conductivity within the thermal boundary layer. We found that eclogite is not stable for $M < 25\ M_{Earth}$. As planet mass increases, the ratio of crustal to lithospheric thickness increases, while mantle temperature also rises. Consequently, the temperature at the base of the crust rises, inhibiting the exothermic eclogite-forming reaction.

5.4.4 A continental throttle?

Continental crust may sequester radiogenic elements, inhibiting plate tectonics and melting by imposing more rapid mantle cooling. The limit is a fully differentiated planet, in which successive melting events have distilled nearly all radiogenic elements into a thin shell near the surface. Independent of this effect, too great an area of nonsubductible, insulating continents may itself be enough to choke off plate tectonics - a limit of 50% of total area has been suggested (Lenardic et al., 2005). Which limit is more restrictive to plate tectonics? On Earth, continents contain (26-77)% of the radiogenic complement of Bulk Silicate Earth (Korenaga, 2008), and cover $\sim 40\%$ of the planet's surface area. If the threshold value for a significant nonsubductible-cover effect on mantle dynamics is 50% (Lenardic et al., 2005), this limit will be passed before complete differentiation occurs. However, all radiogenic elements would be sequestered in continental crust before continental coverage reached 100%. We expect that the thickness contrast between continental and oceanic crust will scale as the inverse of gravity. This is because crustal thickness variations are limited by crustal flow (and brittle failure down gravitational-potential-energy gradients). If in addition the radiogenic-element content of continental crust does not vary, then we can relate the two limits by expressing the fraction of planet surface area covered by continents as

$$f_{area} = \frac{V_{cont}}{AZ_{crust}} \propto \frac{f_{radio}M}{M^{1/2}M^{-1/2}} \propto f_{radio}M. \tag{5.21}$$

using the approximation $R \propto M^{\sim 0.25}$. This implies that continental coverage will be the more severe limit for massive planets as well. A massive planet will enshroud itself with nonsubductible crust before it sequesters a substantial fraction of its radiogenic elements into crust.

Provided that crustal flow limits continental thickness, a representative calculation shows that continents will spread out to coat the surface of an Earth-like planet $> 3\ M_{Earth}$ in much less than the age of the Earth (Figure 5.13); this is because continental production rate scales roughly as planet mass, but planet area increases only as the square root of mass. To produce this figure, we set net continental growth to zero for the first 1 Gyr of each

planet's evolution (guided by the age of the oldest surviving continental blocks on Earth). From 1 Gyr forward, we set continental growth to be proportional to crustal production rate, with a proportionality constant picked to obtain 40% coverage on Earth today.

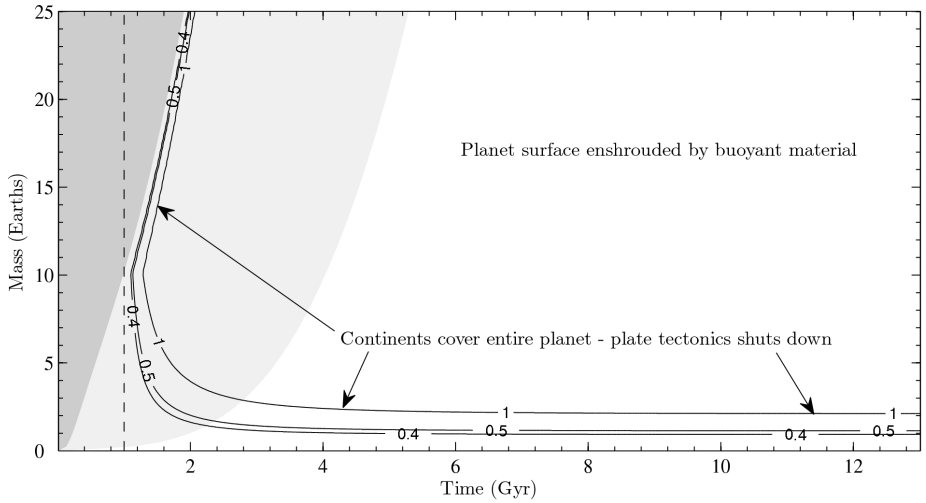

Figure 5.13 Fractional area covered by continents, versus time. MB88 melting model. The dark shaded region is that for which the melting model is invalid. The light shaded region is that for which buoyancy stresses probably prevent plate tectonics. The vertical dashed line is the time after which continental growth is permitted (1 Gyr; Condie and Pease (2008)). For $M_{Earth}> 10$, continents choke plate tectonics ≤ 0.3 Gyr after continent growth is permitted.

5.4.5 Will trenches jam?

Subduction will cease if the relative buoyancy of crust, less dense than mantle, exceeds that of the colder and denser lithospheric mantle. Provided that thermal conductivity and crustal density are constant, the subduction condition is

$$\Delta\rho \cong -\rho_{lith} + \frac{1}{Z_{lith}} \left(\rho_{lith}(1 + \alpha\Delta T_3)(Z_{lith} - Z_{crust}) + (\rho_{crust} Z_{crust})\right) < 0 \qquad (5.22)$$

where

$$\Delta T_3 = \frac{1}{2}\left(1 - \frac{Z_{crust}}{Z_{lith}}\right)\Delta T_2 \tag{5.23}$$

and $\Delta\rho$ is the density difference favoring subduction, ρ_{lith} is the reference density of mantle underlying the plate, Z_{lith} is lithospheric thickness, ΔT_3 is the average cooling of mantle lithosphere, all evaluated at subduction.

Hotter – that is, bigger or younger – planets must recycle plate faster, so a plate has less time to cool. In addition, higher potential temperatures produce a thicker crust. Both factors tend to produce positively buoyant plate, which is harder to subduct. This effect is more severe for massive planets because of their greater gravity.

Once subduction is initiated the basalt-to-eclogite transition can sustain subduction. However, it is not clear that subduction initiation is possible if plate is positively buoyant everywhere, as seems likely for Early Earth (Davies, 1992; Sleep, 2000). The geological record is neither mute nor decisive. All but the last Gyr of Earth's tectonic history is disputed, but evidence is accumulating that subduction first occurred at least 2.7 Gya (1.8 Ga after formation), and perhaps earlier than 3.2 Gya (1.3 Ga after formation) (Condie and Pease, 2008). Taking buoyancy stress per unit length of trench to be the appropriate metric for buoyancy, we can relate Archean observations to high mass planets (Figure 5.14). For example, the buoyancy stress that had to be overcome on Earth after 1.8 Ga is the same as that on a 16 M_{Earth} planet after 4.5 Ga. Here we have assumed that all plate reaches the subduction zone at a characteristic age, τ, that the temperature distribution within the plate is described by half-space cooling (so $Z_{lith} = 2.32\ \kappa^{0.5}\tau^{0.5}$), and that k and ρ_{crust} (2860 kg m^{-3} ; Carlson and Herrick (1990)) are constant. This gives a negative (subduction-favoring) buoyancy stress of 38 MPa at the characteristic age of subduction on the present Earth. The much more sophisticated model of Afonso et al. (2007) yields 21 MPa, so our estimate probably understates forces retarding subduction. However, the base of a thick, water-rich crust may be at temperatures/pressures permitting amphibolite-grade metamorphism, producing dense crust. (In addition, the crust-mantle density contrast declines with increasing melt fraction as the olivine content of the crust increases). For this reason, we also plot results for a constant crustal density of 3000 kg m^{-3}, intermediate between the densities of amphibolite (3000 – 3300 kg m^{-3}; Cloos (1993)) and unmetamorphosed crust. Whether or not amphibolitization is considered, our assessment is that plate buoyancy raises a severe hurdle for plate tectonics on massive Earths, and may well be limiting.

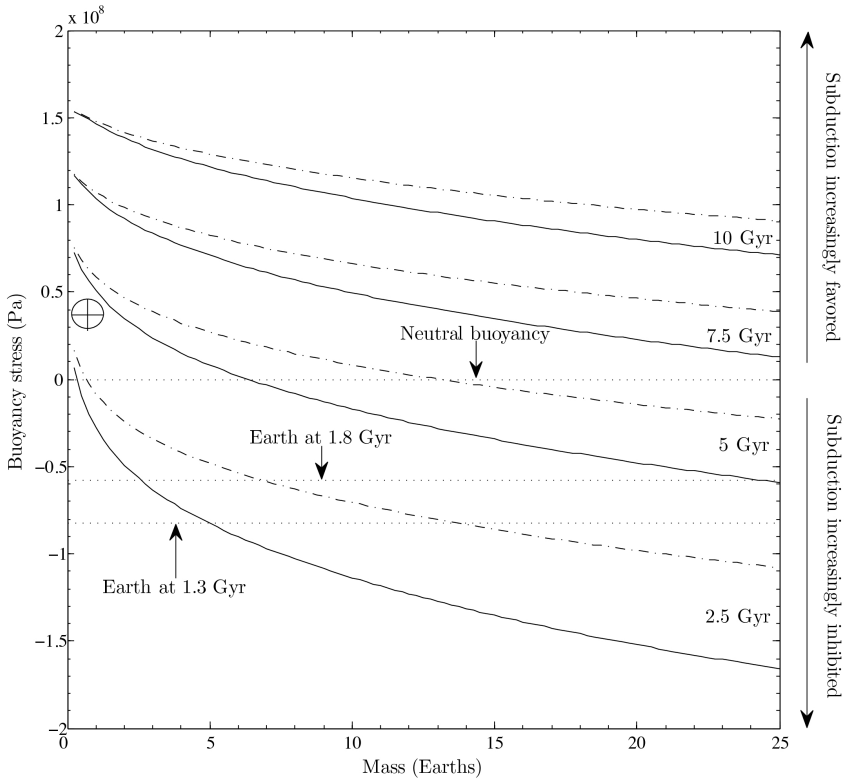

Figure 5.14 Buoyancy stresses as a function of thermal evolution and planet mass. Buoyancy stress is the product of density contrast, gravity, and lithospheric thickness. Positive values denote plate denser than underlying mantle, favoring subduction; negative values denote plate more dense than underlying mantle, retarding subduction. Solid lines connect buoyancy values for planets of different masses 2.5 Gyr, 5 Gyr, 7.5 Gyr and 10 Gyr after planet formation, for constant crustal density of 2860 kg m^{-3}. Dash-dot lines are for a crustal density of 3000 kg m^{-3}, as might be the case for partial amphibolitization. Dotted lines are possible lower limits to plate tectonics based on Earth's (disputed) geological record; arguably, subduction must be possible on planets whose buoyancy forces plot above these lines. The Earth symbol is the model calculation for present day conditions on Earth.

5.5 Rate of volcanism and implications for degassing

5.5.1 Degassing rate

In plate tectonics mode, for 'Earth-like' planets with oceans and some land, we calculate the rate of volcanism by multiplying spreading rate (§5.4.3), mid-ocean ridge length, crustal thickness (§5.3), and crustal density, then dividing by planet mass (Figure 5.15). Our model gives 1.2 x 10^{-11} yr^{-1} by mass for Earth, observations give 1.1 x 10^{-11} yr^{-1} (Best and

Christiansen, 2001). The discrepancy is mainly due to our model's higher-than-observed spreading rate (§5.4.3). For comparison, Earth's total observed present-day rate of volcanism is 1.7 x 10^{-11} yr^{-1} by mass, and 3.1 x 10^{-11} yr^{-1} by volume (Best and Christiansen, 2001). This includes arc and ocean-island volcanoes, which are not modeled in this paper. Rate per unit mass increases monotonically with increasing mass, for all times. Per unit mass, rates of volcanism vary only by a factor of three on planets < 3 Gyr old and > 1 M_{Earth}, but a stronger mass dependence develops for older planets (Figure 5.15). Melting in plate-tectonic mode ceases when potential temperature falls below the zero-pressure solidus, but this only occurs for small (0.25 M_{Earth}) planets ≥ 10 Gya (Figure 5.5).

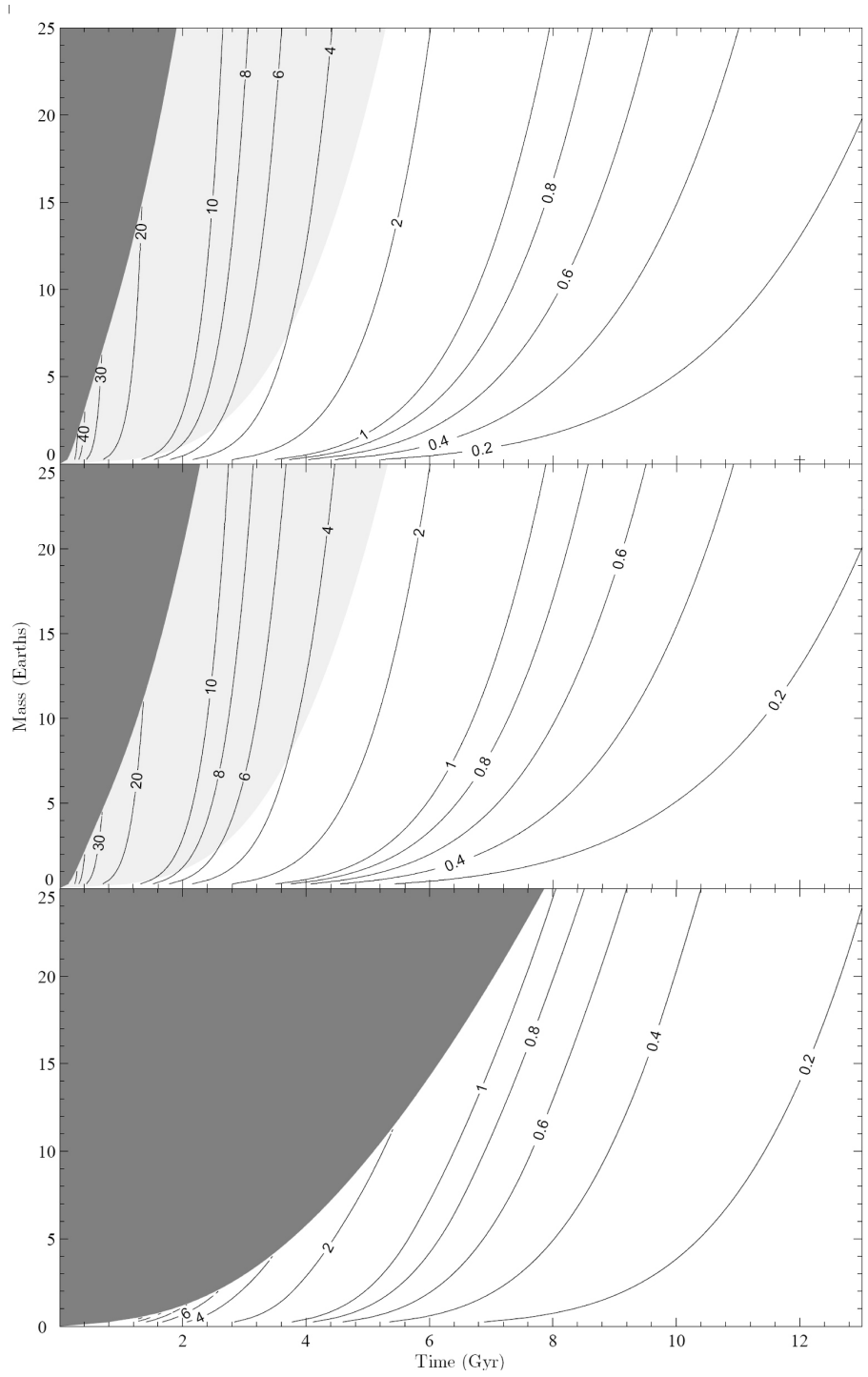

Figure 5.15 Rate of volcanism per unit mass on massive Earth-like planets experiencing plate tectonics, normalized to calculated rate on the Earth (3.75 x 10^{-19} s^{-1}, equivalent to 24 km^3 yr^{-1}), for MB88 (top), K03 (middle) and pMELTS (bottom) melting models. Light grey shaded regions correspond to negative buoyancy stresses with magnitudes in excess of 50 MPa, which would markedly inhibit subduction. Dark grey shaded regions correspond to mantle temperatures too high for a reliable crustal thickness calculation.

In plate tectonic mode, the flux of mantle into the melting zone balances spreading rate To calculate the rate of volcanism on a planet in stagnant lid mode (Figure 5.16), we must first find the flux of material into the upper boundary layer as a function of Ra. We define a near-surface convective velocity such that all heat flow in excess of the conductive heat flow is advected: -

$$Nu - 1 = \frac{u\Delta T_{conv}\rho c}{2\left(\frac{k\Delta T_{cond}}{d}\right)} = \frac{u\rho cd}{2k}\left(\frac{T_m - T_c}{T_m - T_s}\right)$$

$$u = 2(Nu - 1)\left(\frac{k}{\rho cd}\right)\left(\frac{T_m - T_s}{T_m - T_c}\right) \tag{5.24}$$

where the factor of 2 takes account of the need for downwelling material to balance upwelling. The crust production mass flux, normalized to planet mass, is

$$R = \frac{Au\rho}{M_{planet}}\left(\frac{\rho_{crust}Z_{crust}g}{P_f - P_o}\right), \tag{5.25}$$

where R is the rate of melt generation per unit mass, Z_{crust} is obtained from our models in §5.3, and the bracketed term is the mean melt fraction. This sets an upper limit to the rate of volcanism (Figure 5.16) because it assumes that all melt generated reaches the surface, and that all ascending mantle parcels reach P_o. The first assumption is probably safe because of the large forces driving magma ascent on massive planets, and the short absolute distances they must ascend. With these assumptions, we find that the rate of volcanism on stagnant lid planets initially exceeds that on their plate tectonic counterparts but this contrast soon reverses as the stagnant lid thickens. The predicted shutdown of non-plume melting on stagnant lid planets shows remarkably weak dependency on mass and melting model, as explained in §5.3.3.

We consider the rate of crust production to be a good proxy for the rate of degassing. But because volatiles are incompatible, they partition almost quantitatively into even small fractions of melt. Therefore, a more accurate statement is that degassing should be proportional to the flux of mantle processed through melting zones (Papuc and Davies, 2008). We had great difficulty in determining this processing flux because of the 'solidus rollover' problem (§5.6.2). (Because of volatile incompatibility, order-unity differences in the volatile concentrations of planetary mantles should not make much of a difference to our melting curves. Wet parcels of ascending mantle soon 'dry out'.) In addition to lavas that are extruded at the surface, magmas that crystallize below the surface as intrusions – such as the sheeted dykes and gabbros of Earth's oceanic crust – are assumed to degas fully and are referred to as 'volcanism'.

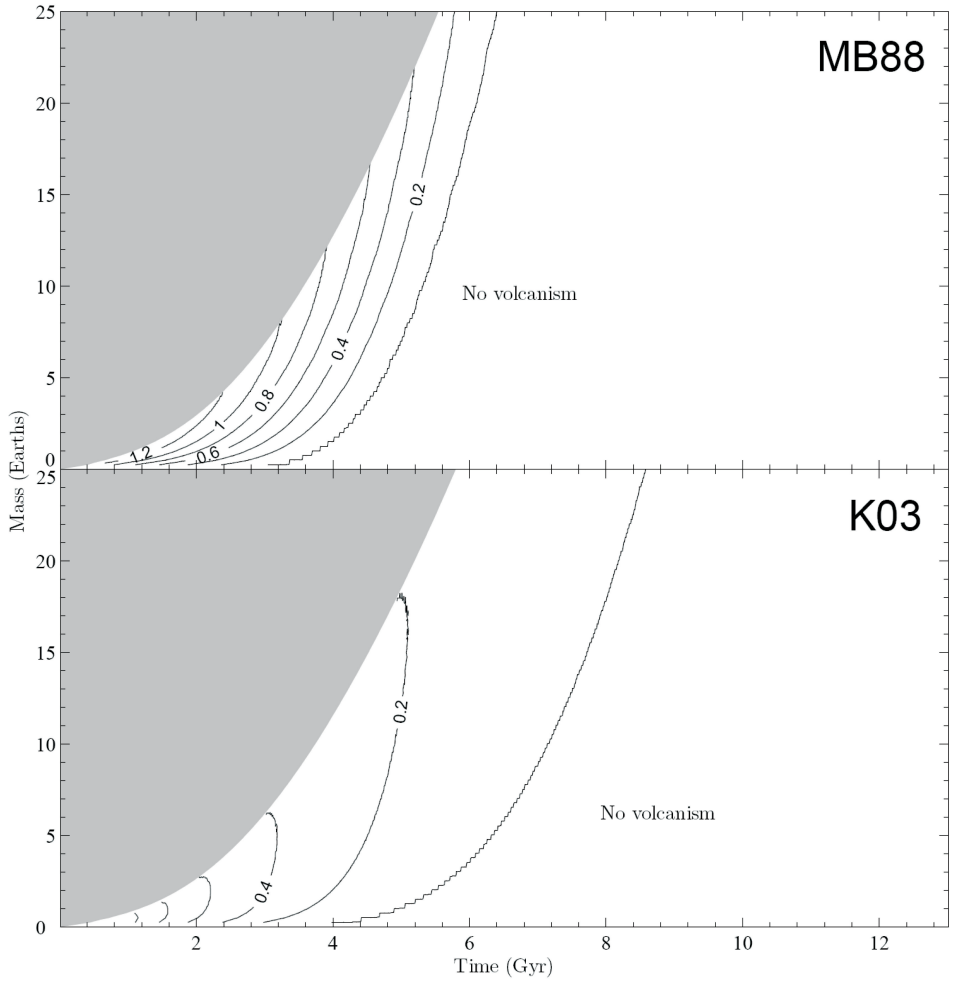

Figure 5.16 Rate of volcanism on massive Earth-like planets undergoing stagnant lid convection, normalized to calculated rate on a plate-tectonic Earth, for MB88 (top) and K03 (bottom) melting models. Dark grey shaded regions correspond to mantle temperatures too high for a reliable crustal thickness calculation. Contours are at 0, 0.2, (0.4, 0.6, ...) $\times$ Earth's rate.

The implications for greenhouse-gas release of our results depend on the water and CO_2 contents of extrasolar planet mantles. These will depend on the mantle's oxidation state (Elkins-Tanton and Seager, 2008b), the range of semimajor axes from which the growing planet draws material, and the extent of volatile loss on the planetesimals which collide to form the planet. The water and CO_2 contents of terrestrial magmas are our only empirical guide. At mid-ocean ridges, these range from 0.1% – 1.5% for H_2O, and 50-400 ppm for CO_2 (Oppenheimer, 2003). Taking the upper-limit values (which is appropriate, given that additional volatiles are almost certainly present in an unmeasured fluid phase), assuming that all mantle fluxing through the melting zone is completely degassed, and ignoring overburden pressure, our model yields 6 x 10^{13} mol a^{-1} for H_2O and 7 x 10^{11} mol a^{-1} for CO_2. This is within the range of uncertainty of observational estimates. Because our model is not 'tuned' to observed rates of volcanism, but only to crustal thickness, this lends some credence to our results for other Earth-like planets.

5.5.2 Overburden pressure

The rate of degassing from seafloor volcanoes will also be regulated by the thickness of the volatile overburden. A volatile envelope can have two effects: –

(1) through a greenhouse effect, a volatile envelope can raise surface temperatures, and increase partial melting. This is shown for our thermal-equilibrium model in Figure 5.2. Here, we show the internal temperature needed to drive convection when the surface temperature is 647K, the critical point of water (q.v. 273 K for the baseline model). In thermal equilibrium, the reduced mantle-surface temperature difference demands more vigorous convection to drive the same heat flux across the upper boundary layer. The increase in mantle temperature is 50-55K (Figure 5.2), which has a significant feedback effect on melting (Figure 5.3). Such high surface temperatures are classically considered to be encountered only for brief intervals on the path to a runaway greenhouse (Ingersoll, 1969), but if this catastrophe is suppressed for massive Earths (Pierrehumbert, 2007), then massive Earths will experience these temperatures for geologically significant intervals. The sign of this feedback is positive; higher mantle temperatures increase crustal thickness, and the associated degassing would enhance the greenhouse effect. We do not consider still higher temperatures, relevant for close-in rocky exoplanets (Gaidos et al., 2007), because plate tectonics is thought to require liquid water. (2) through overburden pressure, a volatile envelope can suppress degassing (and melting for sufficiently thick volatile layers). Water degassing is readily suppressed by 0.1-0.2 GPa of overburden (Papale, 1997), although joint-solubility effects allow some water to degas at higher pressures in association with other gases (Papale, 1999). CO_2, an important regulator of climate on the known terrestrial planets, has a solubility of 0.005% GPa^{-1}. Therefore, an overburden pressure of 1 GPa is enough to suppress CO_2 degassing from a magma containing 0.5 wt % CO_2. A planet with a massive ocean cannot degas. However, it can regas, provided that hydrous/carbonated minerals pass the line of arcs at

subduction zones. This suggests a steady state ocean mass over geodynamic time.

Much more pressure is needed to shut down melting than is needed to shut down degassing (Figure 5.17). However, numerical simulations of water delivery during late-stage accretion (Raymond et al., 2004, 2006) produce some planets with the necessary ocean volumes to shut down melting – the stochastic nature of late-scale accretion introduces a great deal of scatter. The largest planets we consider may accrete and retain a significant amount of nebula gas (Ikoma et al., 2001), which would also frustrate melting.

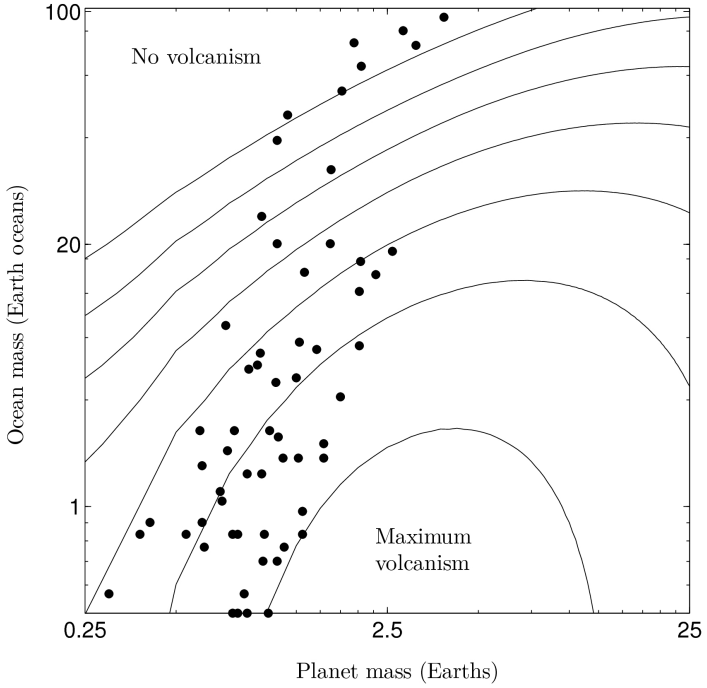

Figure 5.17 Crustal thickness as a function of planet mass and ocean mass for planets with plate tectonics, after 4.5 Gyr. K03 melting model. Solid lines are contours of crustal thickness at 1km intervals. Small fluctuations in the contours are interpolation artifacts. Black circles correspond to simulated planets in habitable zone from Raymond et al. (2004, 2006), assuming (following Raymond et al. (2006)) that volatiles are partitioned between surface and mantle reservoirs in the same proportions as on Earth. We treat the effect of the volatile overburden on melting as being equivalent to that of a stagnant lid with the same basal pressure.

Note that even for an ocean of constant depth, land is unlikely. Gravity defeats hypsometry. For example, doubling Earth's gravity would reduce the land area by a factor of eight.

This is important for climate-stabilizing feedback loops involving greenhouse-gas drawdown (Walker et al., 1981). Submarine weathering is probably less dependent on surface T than subaerial weathering, so in the case of a water-covered planet we would expect a weaker stabilizing feedback on planet temperature from CO_2–silicate weathering.

5.5.3 Melt-residue density inversion: decoupling melting from mantle degassing?

Melts are more compressible than mantle minerals, so at sufficiently high pressures melt will be denser than its residue; for example, mid-ocean ridge basalt becomes denser than garnet at 12.5 – 19.5 GPa (Agee, 1998). If the sinking rate exceeds mantle velocities, these denser melts may accumulate at the base of the mantle (Ohtani and Maeda, 2001). Meanwhile, the residue will continue to rise to shallow pressures, where it will eventually generate melt less dense than itself. That melt will segregate, ascend, and form a crust. However, because atmosphere-forming volatiles are highly incompatible, they will partition into the early-stage (sinking) melt. Because erupted melts will be volatile-poor, planets subject to this process will be unable to balance atmospheric losses to space. Generating melt at sufficiently high pressures for the density inversion to come into play requires very high potential temperatures. In our modelling, these are not encountered for planets in plate tectonic mode (except during the first 1 Gyr, which is a transient associated with cooling from our high initial temperature; initial conditions are thus very important). But the density crossover is encountered for $> 5\ M_{Earth}$ and < 3 Gyr in stagnant lid mode. We speculate that in these planets, melting is decoupled from mantle degassing.

5.6 Discussion and conclusions

5.6.1 Summary of results

- *Modest effect of planet mass on temperature and crustal thickness:* Scaling analysis predicts T_m should only be weakly dependent on planet mass (Stevenson, 2003). Because of the exponential dependence of viscosity on temperature, modest variation in T_m can accommodate the range of heat flows generated by planets of varying masses. Our more detailed study confirms this, and although the nonlinearity of mantle melting leads to greater variations in crustal thickness, these are still of order unity (§5.3.2; §5.3.3; Figure 5.5). However, planet mass can determine which mode of mantle convection the planet is in (§5.4), which in turn determines whether melting is possible at all (§5.3.3).

- *Challenges for plate tectonics on massive Earths:* Plate buoyancy is an increasingly severe problem for plate tectonics as planet mass increases (§5.4.5). Because Early

Earth faced the same challenge, geologic fieldwork may determine the threshold beyond which plate tectonics shuts down (§5.4.5). Middle-aged super-Earths may suffer from continental spread, which could choke off plate tectonics (§5.4.4). Shutdown of plate tectonics could place a planet in stagnant lid mode.

- *Shutdown of melting on old, stagnant lid planets:* All our melting models predict that stagnant lid planets older than Earth cease melting and volcanic activity (§5.3.3-5, but see caveats in §5.6.2). Therefore, observed volcanism on rocky planets > 8 Gya would provide some support for plate tectonics – if and only if tidal heating could be shown to be small.

- *Implications for the stability of atmospheres, climate, and habitability:* The atmospheres of Venus, Earth and Mars were produced by release of gases dissolved in partial melts, as well as temperature-dependent exchange of volatiles between the atmosphere and surface rocks. Planets lacking dynamos and on close orbits around their parent stars may experience high rates of atmospheric erosion due to stellar winds and coronal mass ejections (Khodachenko et al., 2007), and their atmospheres would persist on main sequence timescales only if maintained by mantle melting. Under more benign conditions, crust formation may establish the long-term carbon dioxide content of Earth-like atmospheres; CO_2 released in volcanism is sequestered as carbonates produced during the low-temperature weathering of that crust (Walker et al., 1981). Volcanism may underpin the long-term habitability that the fossil record teaches us is a prerequisite for advanced life (Butterfield, 2007).

5.6.2 Overview of approximations and model limitations

In this paper we assume whole-mantle convection. Layered mantle convection can alter the volcanic history of a planet by introducing long-term sensitivity to initial thermal conditions. For a phase boundary to form a barrier to flow its Clapeyron slope must be strongly endothermic. Historically, the $sp \rightarrow pv$ transition was thought to have this character but this is now known not to be the case. Deeper phase transitions are either exothermic ($pv \rightarrow ppv$) or very gradual (Seager et al., 2007). In spite of these arguments against layered mantle convection, barriers to flow are possible if stable deep mantle layers arise during or shortly after fractional crystallization of the primordial magma ocean. Although CMB pressures reach 14 Mbar for 10 M_{Earth} and 40 Mbar for 25 M_{Earth}, we have not considered metallized silicates (Umemoto et al., 2006), nor the possibility that lower-mantle convection is extremely sluggish (even isoviscous; Fowler (1983)) due to low homologous temperatures, nor pressure dependent viscosity (Papuc and Davies, 2008). Our parameterized treatment of mantle convection assumes the solid state and is inappropriate for very high temperatures, when the greater part of the lithosphere is underlain by a magma ocean. For almost all cases, however, the transition to a magma ocean takes place at temperatures beyond the

range of validity of our melting models, so magma ocean development is not the limiting consideration in interpreting our results.

Our model does not consider tidal heating, which may be important for Earthlike planets on close eccentric orbits about low-mass stars (Jackson et al., 2008), nor does it take into account the energetics of the core (Nimmo, 2007). Because the magnitude of core cooling is set by mantle cooling, core energetics only dominate mantle thermal evolution in Earthlike planets as $t \rightarrow \infty$ and $H \rightarrow 0$. Surface temperature is assumed to be constant, which is likely to be a good approximation except for close-in exoplanets with thin atmospheres in a 1:1 spin-orbit resonance (Ganesan et al., 2008).

All our melting models show 'solidus rollover' at high P - that is, $\frac{T_{sol}}{P} \rightarrow \frac{\partial V}{\partial S}$. As a consequence, plots of X versus P at high T_p have a long, thin high-pressure tail, and the pressure of first melting diverges at finite T_p. Although solidus rollover is a real effect, resulting from the greater compressibility of silicate melts versus solids (Ghiorso, 2004), infinite pressures of first melting are unphysical. In particular, phase transitions near 14 GPa introduce unmodeled kinks of the solidus. To sidestep the solidus rollover problem, we truncate our melting integration at 8 GPa, and do not plot model output where melting models predict nonzero X at 8 GPa. But this solution has costs: 1) we cannot model hot planets (grayed-out regions in Figures 5.5 & 5.7), and 2) because pressure at first melting is so sensitive to solidus rollover, we have little confidence in our model output for the rate of processing of the mantle through the melt zone. Melting models calibrated to higher pressures and temperatures would remove this impediment to progress. One such model (xMELTS), based on a high-pressure equation-of-state for silicate liquids (Ghiorso, 2004), will soon become available (Ghiorso et al., 2007). Because crustal production rate is proportional to the integral under the curve of X versus P, rather than the pressure at which $X = 0$, it is much less sensitive to this problem. Representing the solidus as a straight line in T-P space (Papuc and Davies, 2008) is geologically not realistic, but has the advantage that both crustal thickness and the pressure of first melting are finite for all T_p.

We calculate crustal thickness as the integral of melting fraction from the surface to great depth. In plate tectonic mode this corresponds to the observable (seismically-defined) crustal thickness. But in stagnant lid mode, the observable crustal thickness need not be the same everywhere (because melting will only occur above mantle upwellings). Also, the observable crustal thickness may be everywhere greater than the integral of melting fraction from the surface to great depth, because crust generated in previous melting events is located directly underneath 'fresh' crust. This situation is described in the context of Io by Moore (2001).

On stagnant lid planets, volcanism may be episodic (as on Mars; Wilson (2001)) and absent for long periods. This means that an observed lack of compounds with a short photochemical lifetime would not preclude a high level of volcanic activity averaged over a sufficiently long period ($\geq 10^{\sim 8}$ yr). Volcanism is not the only possible source of degassing. Metamorphic decarbonation (Bickle, 1996), and the episodic release of deep-seated volatiles as on the Moon (Gorenstein and Bjorkholm, 1973), could permit (low) rates of degassing on non-volcanic worlds.

By assuming that all melt reaches the surface, we have ignored the distinction between extrusion and intrusion. However, extrusion can alter the reflectance properties of the planet without sustaining an atmosphere – consider the Moon – and it may eventually be possible to discriminate between the two possible fates for melt.

5.6.3 Comparison with Solar System data

Thermal evolution, with an emphasis on Earth

Four decades since plate tectonics became widely accepted, geologists have not determined the detailed thermal history of the Earth, neither have we even produced a model that satisfyingly accounts for the few data points in hand. The model of Korenaga (2006, taking a parameterized approach) may be an exception, but this model assumes that present-day observed averages are valid for the past, and is probably not portable to other Earth-like planets. Complicating the picture are two sharp-edged lower mantle anomalies mapped by seismic tomography under Africa and the S. Pacific, which are likely distinct in composition and radiogenic-element density from the rest of the mantle, are probably not sampled in our collections of mantle rocks brought up by volcanoes and which may be persistent, ancient features that have interfered in mantle convection since more than 2.5 Gyr ago. Their origin is unknown (Garnero and McNamara, 2008). Geoneutrino detectors will break some of these degeneracies before 2020 [E.S. Kite and V. Lekic, "Feasibility of mantle radiogenic power determination with geoneutrinos," manuscript in revision, 2011], and continued field mapping of ancient tectonic features will sharpen the history of past dynamics of plate deformation (Condie and Pease, 2008). But using simple models and making changes along one dimension only – the approach taken here – is still a meaningful approach because the more complex models introduce many more free parameters, and it is not clear how these free parameters vary with mass. By contrast, our approach involves only one 'tuning' parameter, the offset $T_m - T_p$.

The situation for the other terrestrial planets – single plate planets with stagnant lithospheres - is in many ways better. Parameterized cooling fits all the observations. This is not just because of a lack of data: stagnant lid planets seem to be truly simpler, and the relevant fluid physics is probably better understood than the 'viscoelastoplastic plus damage' phenomenology needed to accommodate the observed geological motions of the Earth's plates. On Earth, mantle heat loss is largely by conduction aided by hydrothermal convection at mid-ocean ridges, but mantle heat loss on stagnant lid planets should be less sensitive to the details of surface deformation.

The degree to which the mantle cools over geological time depends on the activation energy for deformation of mantle rock, which is known only imprecisely (Karato, 2008). We take $T_\nu \cong 43$ K, for which $A_0 = 7$ x 10^4 K, giving an order-of-magnitude viscosity change for each 100K temperature increment (although T_ν could be as high as 100K) (Sleep, 2007). This is conservative (but not necessarily more correct) in terms of the effect of

mass on temperature, because small values of T_ν allow mass (heat flux) variations to be accommodated by small changes in temperature (Figure 5.18).

The range of mantle states that permit plate tectonics to continue will differ from the range of states permitting plate tectonics to initiate, and ongoing plate tectonics will alter the state of the mantle.

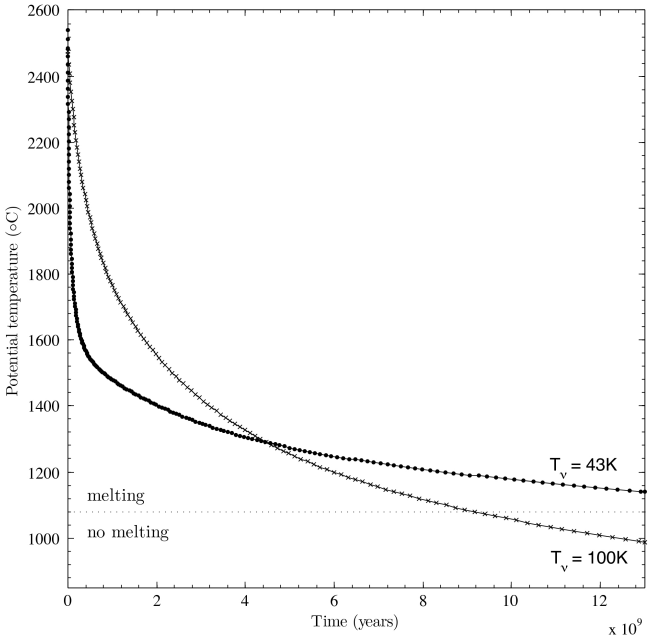

Figure 5.18 Effect of changes in activation energy for temperature-dependent viscosity on thermal evolution. Turcotte and Schubert (2002) radiogenic-element complement (M_{Earth}= 1). Mantle temperatures are adjusted to produce 7 km thick crust under MB88 at 4.5 Gyr. Dots correspond to results with T_ν = 43K. Stars correspond to results with T_ν = 100K. Note that the cooling rate at 4.5 Gyr is 71 K/Gyr for T_ν = 100K, more than double that for T_ν = 43 K (33 K/Gyr). Cessation of melting (dashed line) occurs around 9 Gyr for T_ν = 100K, but takes longer than the age of the Universe for T_ν = 43K.

Continents affect thermal evolution (§5.4.4). However, continent growth and survival is not well understood. Hydration of the oceanic crust at mid-ocean ridges, and subduction of this H_2O, is probably required for continental growth (Campbell and Taylor, 1983). There is geological and isotopic evidence for episodic continental growth (Condie and Benn, 2006). Durable continents may require photosynthetic life both in the oceans (Rosing, 2006) and on land (Lee et al., 2008). None of these effects are straightforward to model. So, though excessive continental surface area and radiogenic-element sequestration both have the potential to throttle our predicted increase in mantle melting on high-mass Earths, we consider this

only a tentative prediction.

Melting: constraints from Venus, Mars, Io, and the Moon

If massive Earth-like planets are in heat-pipe mode for ~ 1 Gya (§5.4.2), a substantial fraction of the census of nearby massive Earth-like planets would be in heat-pipe mode. And if Io is any guide (e.g., Lopes and Spencer (2007)), dramatic spatial and temporal variations in thermal emission should be present. However, the relatively slow cooling in our thermal evolution model is inappropriate for magma oceans (Sleep, 2007), because our parameterization of viscosity does not include the fifteen-order-of-magnitude decrease associated with melting. Planets with $Mo > 1$ are likely to cool quickly to $Mo < 1$; we suspect that Io-type cooling is unsustainable for geologically significant periods without a nonradiogenic source of energy.

Our melting model is tuned to Earth only, but fits Venus observations reasonably well. With the MB88 model, our calculations show that volcanism on a planet in stagnant lid mode and with Venus' mass ($M_{Earth} = 0.85$) will cease after 3.9 Gyr, which is consistent with observations (Schaber et al., 1992).

However, when decompression melting of mantle material at background temperatures cannot sustain volcanism on Earth-like planets undergoing whole-mantle convection, other mechanisms may take over. Plumes rising from the core-mantle boundary, or from a compositional interface within the mantle, can have temperatures up to several hundred degrees greater than that of passively upwelling mantle. This requires a more detailed treatment of thermal evolution than we have taken in this paper, and could be the basis of a more detailed study.

In particular, Mars' continuing – although fitful and low-rate – volcanic activity (Borg and Drake, 2005) indicates that volcanic activity can continue on planets in stagnant-lid mode for longer than our simple models predict, perhaps as the result of plumes in a compositionally-layered mantle (Wenzel et al., 2004) or a thick, thermally insulating crust (Schumacher and Breuer, 2007). On Venus, mantle fluxing by sinking delaminated lithosphere has been proposed as a mechanism that would allow volcanism to continue through to the present day (Elkins-Tanton et al., 2007), although there is no robust evidence of ongoing volcanism. Continued Solar System exploration is needed if we are to fully exploit nearby constraints on the geodynamic window for life.

Chapter 6

Climate destabilization on planets with large day-night temperature contrasts

This chapter was published as: Kite, E.S., E. Gaidos and M. Manga (2011), "Climate destabilization on tidally locked exoplanets," Astrophysical Journal, 743:41, doi:10.1088/0004-637X/743/1/41

Summary

Feedbacks that can destabilize the climates of synchronously-rotating rocky planets may arise on planets with strong day-night surface temperature contrasts. Earth-like habitable planets maintain stable surface liquid water over geological time. This requires equilibrium between the temperature-dependent rate of greenhouse-gas consumption by weathering, and greenhouse-gas resupply by other processes. Detected small-radius exoplanets, and anticipated M-dwarf habitable-zone rocky planets, are expected to be in synchronous rotation (tidally locked). In this paper we investigate two hypothetical feedbacks that can destabilize climate on planets in synchronous rotation. (1) If small changes in pressure alter the temperature distribution across a planet's surface such that the weathering rate goes up when the pressure goes down, a runaway positive feedback occurs involving increasing weathering rate near the substellar point, decreasing pressure, and increasing substellar surface temperature. We call this feedback *enhanced substellar weathering instability* (ESWI). (2) When decreases in pressure increase the fraction of surface area above the melting point (through reduced advective cooling of the substellar point), and the corresponding increase in volume of liquid causes net dissolution of the atmosphere, a further decrease in pressure will occur. This *substellar dissolution feedback* (SDF) can also cause a runaway climate shift. We use an idealized energy balance model to map out the conditions under which these instabilities may

occur. In this simplified model, the weathering runaway can shrink the habitable zone, and cause geologically rapid 10^3-fold atmospheric pressure shifts within the habitable zone. Mars may have undergone a weathering runaway in the past. Substellar dissolution is usually a negative feedback or weak positive feedback on changes in atmospheric pressure. It can only cause runaway changes for small, deep oceans and highly soluble atmospheric gases. Both instabilities are suppressed if the atmosphere has a high radiative efficiency. Our results are most relevant for atmospheres that are thin, have low greenhouse-gas radiative efficiency, and have a principal greenhouse gas that is also the main constituent of the atmosphere. These results identify a new pathway by which habitable-zone planets can undergo rapid climate shifts and become uninhabitable.

6.1 Introduction

Exoplanet research is driven in part by the hope of finding habitable planets beyond Earth (ExoPlanetTaskForce, 2008). Demonstrably habitable exoplanets maintain surface liquid water over geological time. Earth's long-term climate stability is believed to be maintained by a negative feedback between control of surface temperature by partial pressure of CO_2 (pCO_2), and temperature-dependent mineral weathering reactions that reduce pCO_2 (Walker et al., 1981). There is increasing evidence that this mechanism does, in fact, operate on Earth (Cohen et al. (2004), Zeebe and Caldeira (2008), but see also Edmond and Huh (2003)). The Circumstellar Habitable Zone hypothesis (Kasting et al., 1993) extends this stabilizing feedback to rocky planets in general, between top-of-atmosphere flux limits set by the runaway greenhouse (upper limit) and condensation of thick CO_2 atmospheres (lower limit). H_2-H_2 collision-induced opacity can extend the habitable zone further out, in theory (Pierrehumbert and Gaidos, 2011; Wordsworth, 2011). Currently the best prospects for finding stable surface liquid water orbit M stars (Tarter et al., 2007; Deming et al., 2009). Planets in M-dwarf habitable zones are close enough to their star for tidal despinning and synchronous rotation (Murray and Dermott (1999), Chapter 5). Nearby M-dwarfs are the targets of several ongoing and proposed planet searches. Rocky exoplanets in hot orbits have recently been confirmed (Léger et al., 2009; Batalha et al., 2011; Winn et al., 2011), and are presumably in synchronous rotation. But does the habitable zone concept hold water for tidally locked planets?

In this paper, we highlight two closely-related feedbacks which could cause climate destabilization on planets with and low-opacity atmospheres and atmospheres that do not have large optical depth. Both feedbacks require surface temperatures near the substellar point to be significantly higher than the planet-average surface temperature.

- The *enhanced substellar weathering instability* (ESWI) flows out of the same strong temperature dependence of silicate weathering that makes it possible for carbonate-silicate feedback to stabilize Earth's climate (Walker et al., 1981). Weathering and

hence CO_2 drawdown rate increases rapidly with increasing temperature. Weathering also increases with rainfall, which increases with temperature (O'Gorman and Schneider, 2008; Pierrehumbert, 2002; Schneider et al., 2010). Therefore, the global CO_2 loss rate depends heavily on the maximum temperature. On a synchronously-rotating planet where ΔT_s is high, most of the weathering occurs near the substellar point. Suppose weathering is initially adjusted to match net supply of greenhouse gases by other processes (e.g., volcanic degassing). Then consider a small increase in atmospheric pressure. Average temperature must increase, unless there is an antigreenhouse effect. Normally, this would lead to an increase in weathering. However, on a planet with a strong day-night temperature contrast, most of the weathering occurs near the substellar point. An increase in atmospheric pressure can decrease temperature around the substellar point, if increased advection of heat away from the hotspot by winds outweighs any increase in greenhouse forcing. Because this substellar area is cooling, and most of the weathering is around the substellar point, the planet-averaged weathering rate declines. Volcanic supply of greenhouse gases now outpaces removal by weathering, and a further increase in pressure occurs. This instability can lead to very strong greenhouse forcing, and may trigger a moist runaway greenhouse (Kasting, 1988). Conversely, a small decrease in pressure from the unstable equilibrium can lead to atmospheric collapse. ESWI requires that weathering is an important sink for the major climate-controlling greenhouse gas, which is also the dominant atmospheric constituent. It also requires that the atmosphere is important in setting the mean surface temperature.

- *Substellar dissolution feedback* (SDF) supposes an increasing gradient in surface temperature on an initially frozen planet, which allows a liquid phase to form (or be uncovered) around the substellar point. Some atmosphere dissolves in the new liquid phase. Positive feedback is possible if the decrease in atmospheric pressure due to dissolution raises the temperature around the substellar point, increasing the fraction of the planet's surface area above the melting point. (We assume for the moment that P exceeds the triple point). In order for the mass of atmosphere sequestered in the pond to increase with decreasing pressure, increasing pond volume must outcompete both Henry's-law decrease in gas dissolved per unit volume, and the decrease in gas solubility with increasing temperature. For example, suppose $c \propto P$, where c is the concentration of gas in the pond and P is the atmospheric pressure, and $V \propto P^{-n}$ with V the ocean volume. Then $n > 1$ is sufficient for positive feedback, and $n > 2$ is sufficient for runaway. So long as the runaway condition is satisfied, the area of liquid stability will continue to expand: a pond becomes an ocean, drawing down the atmosphere. As with the ESWI, the key is that substellar temperature increases as pressure decreases. Runaway SDF implies a climate bistability for a given inventory of volatile substance. One equilibrium has all of the volatile in the atmosphere. The other equilibrium has most of the volatile substance sequestered in a regional ocean and a

little in the atmosphere, with the ocean prevented from completely freezing over by the steep temperature gradient that the thin atmosphere enables. A similar hysteresis was proposed for ancient Titan by Lorenz et al. (1997). Runaway SDF is separate from the feedback between retreating ice cover and increased absorption of sunlight (ice-albedo feedback; Roe and Baker (2010)), although both are likely to operate together.

Both instabilities occur more slowly than thermal equilibration of the atmosphere and surface. This separation of timescales allows us to solve for the fast processes that set the surface temperature (in §6.2), and then separately address each of the two slower processes which may cause atmospheric pressure to change (in §6.3-§6.4).

Day-night color temperature contrast is among the 'easiest' parameters to be measured for a transiting exoplanet (Cowan and Agol, 2011), but there is currently no theory for ΔT_s on planets with observable surfaces. One motivation for this paper is to contribute to this emerging theory. We use a simplified approach which complements more sophisticated exoplanet Global Circulation Models (GCMs) (Joshi et al., 1997; Joshi, 2003; Merlis and Schneider, 2010; Edson et al., 2011; Wordsworth, 2011; Pierrehumbert, 2011). §6.2 sets out the energy balance model that is used for both instabilities, and §6.3 explains the enhanced substellar weathering instability including our choice of weathering parameterization. §6.4 explains the substellar dissolution feedback (considering only the 1:1 spin-orbit resonance). We find that SDF doesn't work in most cases, so readers motivated by short-term detectability can safely omit §6.4 and move to §6.5. §6.5.1 discusses relevant solar system data, including the possibility that Mars underwent a form of ESWI. §6.5.2 discusses applicability to exoplanets, and §6.6 summarizes results.

6.2 Idealized energy balance model

Consider a planet in synchronous rotation on which surface liquid water is stable, with an atmospheric temperature that decreases with height along the dry adiabat. Slow rotation weakens the Coriolis effect, allowing the atmospheric circulation to all but eliminate horizontal gradients in atmospheric temperature at the top of the boundary layer, T_a. This is the weak temperature gradient approximation often made for Earth's tropics (e.g. Merlis and Schneider (2010)). Figure 6.1 shows the setup for our idealized energy balance model.

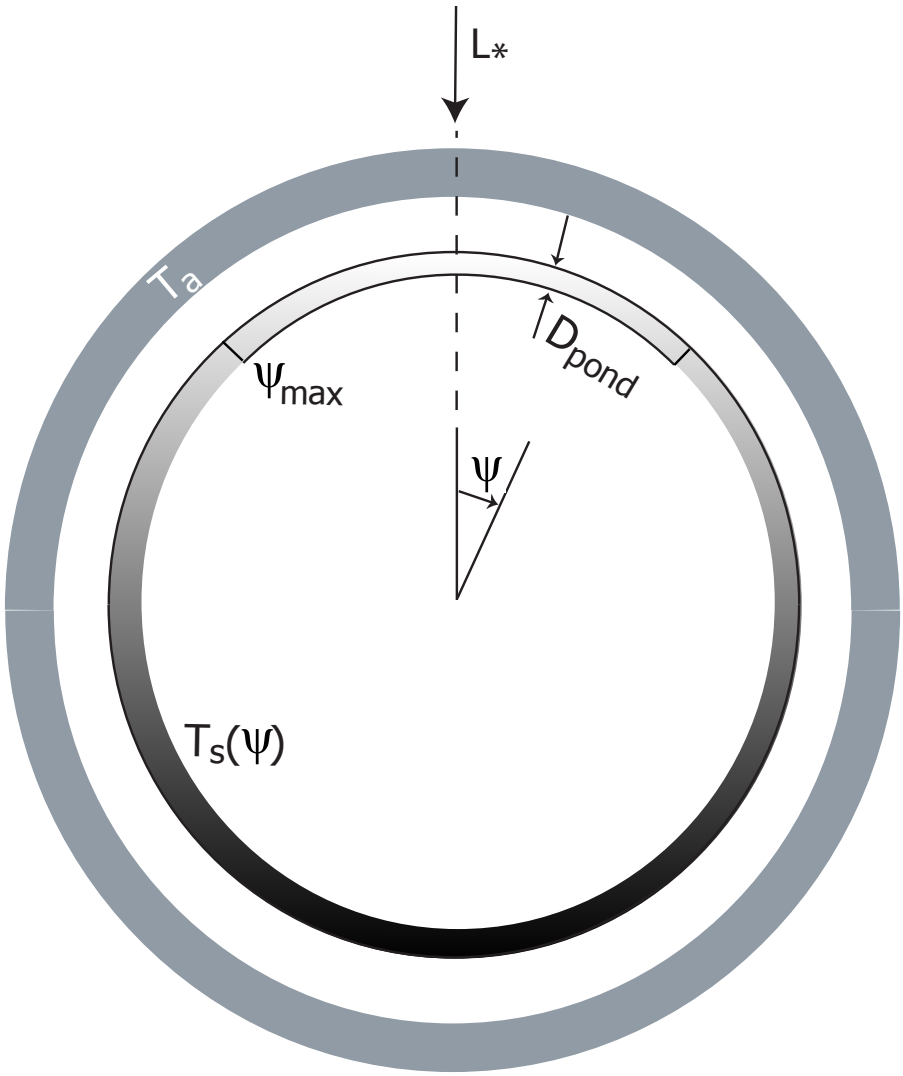

Figure 6.1 Geometry of the idealized energy balance model for an exoplanet in 1:1 spin-orbit resonance. Uneven distribution of starlight (L_*) on the planet leads to a hot (white shading, high T_s) dayside surface and a cool (black shading, low T_s) nightside surface. The atmosphere (uniform gray shading), with horizontally uniform boundary-layer temperature T_a, tends to reduce this temperature gradient (ΔT_s). When $T_s > T_{melt}$, a melt pond can form around the substellar point $\psi = 0$, with angular radius ψ_{max} and depth D_{pond}. Because rotation is slow, meridional winds are as fast as zonal winds, so T_s depends only on the angular distance from the substellar point (ψ).

The surface temperature $T_s(\psi)$ at an angular separation ψ from the substellar point is set by the local surface energy balance:-

$$SW_s(\psi) - LW\uparrow(\psi) + LW\downarrow - \beta(T_s(\psi) - T_a) = 0 \tag{6.1}$$

where $SW_s(\psi)$ is starlight absorbed by the surface, $LW\uparrow(\psi) = \eta\sigma T_s(\psi)^4$ (where σ is the Stefan-Boltzmann constant and $\eta \approx 1.0$ is the emissivity at thermal wavelengths) is the surface thermal radiation, $LW\downarrow$ is backradiation from the atmosphere, β is a turbulent heat transfer coefficient ($\beta = k_{TF}\ \rho$, where ρ is the near-surface atmospheric density divided by Earth's sea-level atmospheric density, and k_{TF} is a turbulent flux proportionality constant), and T_a is the temperature of the atmosphere at the top of the boundary layer[1]. The shortwave flux $SW_s(\psi) = L_*(1-\alpha)\cos(\psi)$ corresponds to stellar flux L_*, attenuated by surface albedo α. There is negligible transport of heat below the surface: we assume seas are not globally interconnected (or are shallow, or are deeply buried, or do not exist) and energy flux from the interior is small.

$LW\downarrow$ ($= \frac{1}{2}\int_0^\pi LW\uparrow(\psi)\sin\psi\,\mathrm{d}\psi - OLR$, ignoring turbulent fluxes) is longwave flux from the atmosphere to the surface. OLR (Outgoing Longwave Radiation, longwave energy exiting the top of the atmosphere) is given by interpolation in a look-up table. To build this look-up table, we slightly modified R.T. Pierrehumbert's scripts at `http://geosci.uchicago.edu/~rtp1/Principles/PlanetaryClimate/`, particularly `PureCO2LR.py`. The look-up table gives $OLR(P_\Lambda, T_s)$ for a pure noncondensing CO_2 atmosphere on the dry adiabat, with the temperature at the bottom of the adiabat equal to the energy-weighted average T_s, and with Earth gravity (9.8 m/s^2). Our noncondensing assumption introduces large errors for $T_s < 175$K, so we assume that the top-of-atmosphere effective emissivity $OLR/LW\uparrow$ at these low temperatures is the same as at $T_s = 175$K.

To investigate atmospheres not made of pure CO_2, we introduce an opacity ratio or relative radiative efficiency Λ, which is the ratio of the radiative efficiency of the atmosphere of interest to that of pure noncondensing CO_2. Λ is a simplification of the complicated behavior of real gas mixtures (Pierrehumbert, 2010). Λ can be greater than 1 if the atmosphere contains radiatively very efficient gases (chloroflourocarbons, CH_4, NH_3, or the "terraforming gases"; Marinova et al. (2005)). We then query the look-up table using $P_\Lambda = \Lambda P$. Smaller values of Λ have a weaker greenhouse effect (increased OLR).

Rayleigh scattering is relatively unimportant for planets orbiting M-dwarfs. Starlight is concentrated at red wavelengths where Rayleigh scattering is ineffective (falling off as λ^{-4}, where λ is wavelength). The optical depth to Rayleigh scattering of 1 bar of Earth air is 0.16 for light from the Sun, but only 0.02 for light from the Super-Earth hosting M3 dwarf Gliese 581 (approximating both stars as blackbodies). In addition, absorption of starlight by the atmosphere is much stronger in the NIR than the visible, and so is more effective at

[1]Equatorial superrotating jets can cause the hottest point on the surface to be downwind from the substellar point (Knutson et al., 2009; Mitchell and Vallis, 2010; Liu and Schneider, 2011)

compensating for Rayleigh scattering as star temperature decreases (Pierrehumbert, 2010). We neglect Rayleigh scattering and absorption of starlight by the atmosphere.

The horizontally uniform atmospheric boundary layer temperature, T_a, is set by the total energy balance of the atmosphere,

$$\frac{1}{2}\int_0^\pi [LW\uparrow(\psi) + \beta(T_s(\psi) - T_a)] \sin\psi \, \mathrm{d}\psi - OLR - LW\downarrow = 0 \tag{6.2}$$

where the integral gives the average flux from the surface. This reduces to

$$T_a = \tfrac{1}{2}\int_0^\pi T_s(\psi) \sin\psi \, \mathrm{d}\psi$$

because of our particular choice of $LW\downarrow$. In effect, we assume that the boundary layer only interacts with the ground through turbulent fluxes.

For a given P_Λ, we iterate to find T_a and $T_s(\psi)$. ψ resolution is 5 degrees. The initial condition has the surface in radiative equilibrium, and the atmosphere in equilibrium with this surface temperature distribution. Convergence tolerance is $\approx 2 \times 10^{-6}$.

Throughout the paper, we assume $k_{TF} = C_p(T_a) C_D U$, where $C_p(T_a)$ is the temperature-dependent specific heat capacity of CO_2 (≈850 J/kg/K at 300K), C_D is a drag coefficient, and U is characteristic near-surface wind speed. $C_D = \frac{k_{VK}^2}{\ln(z_1/z_0)^2}$ where $k_{VK} = 0.4$ is von Karman's constant, $z_1 = 10$m is a reference altitude, and z_0 is the surface roughness length (10^{-4} m, which is bracketed by the measured values for sand, snow, and smooth mud flats; Pielke (2002)). For our reference $U = 10$ m/s, this gives $k_{TF}\,\rho = 12.3$ W/m^2/K. We assume a Prandtl number near unity. §6.5.2 reports sensitivity tests using different values of U.

We accept the following inconsistencies to reduce the complexity of the model:- (1) Radiative disequilibrium drives T_s to a higher value than T_a at the surface, and turbulence can never completely remove this difference. Therefore, setting the temperature at the bottom of the atmosphere to the surface temperature will lead to an overestimate of $LW\downarrow$ at low P. (2) The expression for k_{TF} is appropriate for a neutrally stable atmospheric surface layer, but turbulent mixing is inhibited on the nightside by a thermal inversion (Merlis and Schneider, 2010). This will tend to make the coupling between nightside atmosphere and nightside surface too strong. (3) We assume an all-troposphere atmosphere with horizontally uniform temperature. Merlis and Schneider (2010) find temperatures are nearly horizontally uniform for Earthlike surface pressure and for levels in the atmosphere at pressures less than half the surface pressure. Atmospheric temperature is approximately horizontally uniform when the transit time for a parcel of gas across the nightside, $\tau_{advect} = \frac{a}{U_h}$, is short compared to the nightside radiative timescale, $\tau_{rad} \sim \frac{P}{g}\frac{C_p}{4\epsilon\sigma T^3}$ (Showman and Guillot, 2002). Here, a is planet radius (1 Earth radius), U_h is high-altitude wind speed ($\sim$ 30 m/s: Merlis and Schneider (2010)), ϵ is an greenhouse parameter corresponding to the fraction of the emitted radiation that is not absorbed by the upper atmosphere and escapes to space, and $T = 250$K is the atmospheric temperature, the radiative equilibrium temperature on the darkside being zero. Picking $\epsilon = 0.5$, this gives $\tau_{advect} \sim 2$ days and $\tau_{rad} \sim 50$ days. (4) The treatment of T_a is

crude. (5) We assume the atmosphere is transparent to stellar radiation, which is a crude approximation under M-dwarf (or cloudy) skies. (6) We neglect condensation within the atmosphere.

Representative temperature plots are shown in Figure 6.2, for $\Lambda = 0.1$ and $L_* = 900$ W/m^2.

At low pressures, nightside temperatures are close to absolute zero, and substellar temperature is close to radiative equilibrium. Increasing pressure cools $\psi < 60°$, and warms $\psi > 70°$. This is because the atmosphere is warmer than the surface on the nightside, and cooler than the surface on the dayside. Therefore, the increase in $P(\propto \beta)$ increases the $\beta(T_s - T_a)$ term, which warms the nightside, but cools the dayside. For positive Λ, $LW\downarrow$ will increase with P and warm the entire planet. However, for the relatively small value of Λ shown here, the substellar point still undergoes net cooling with increasing pressure. This cooling with increasing P is what makes the ESWI and SDF possible. When the surface becomes nearly isothermal, as for the "10-bar" curve in Figure 6.2, the entire surface warms with increasing pressure, and the ESWI and SDF cannot occur.

For $\Lambda \geq 0$, $\bar{T}_s$ must increase with P. Even if there is no greenhouse effect, the homogenization of the atmosphere will warm the planet on average because of the nonlinear dependence of T on energy input (Edson et al., 2011). For small optical depth, nightside $T_s \propto \ln(P)$. The fractional area of the planet over which liquid water is stable is 27% at radiative equilibrium, decreasing with pressure and vanishing at ∼0.7 bars. As P increases the greenhouse effect further, liquid stability reappears at ∼2.4 bars, rapidly becoming global.

6.3 Climate destabilization mechanism #1: Enhanced substellar weathering instability (ESWI)

6.3.1 Weathering parameterization

.

The Berner and Kothavala (2001) weathering relation, which is specific to CO_2 weathering of Ca-Mg silicate rocks, states

$$\frac{W_\psi}{W_0} = \left(\frac{P}{P_0}\right)^{0.5} \underbrace{\exp\left[k_{ACT}\ (T_s(\psi) - T_o)\right]}_{\text{direct T dependence}} \underbrace{\left[1 + k_{RUN}\ (T_s(\psi) - T_o)\right]^{0.65}}_{\text{hydrology dependence}} \tag{6.3}$$

where W_ψ is local weathering rate, W_0 is a reference weathering rate, P is atmospheric pressure, P_0 is a reference pressure, $T_o = 273$K is a reference temperature, $k_{ACT} = 0.09$ is an activation energy coefficient, and k_{RUN} is a temperature-runoff coefficient fit to Earth GCMs. Equation 3 is widely used, but uncertain and controversial (§6.5.2). In our model, the strong temperature dependence leads to a strong concentration of weathering near the substellar point. For example, for a 1-bar atmosphere with $\Lambda = 0.1$ (shown in Figure 6.2),

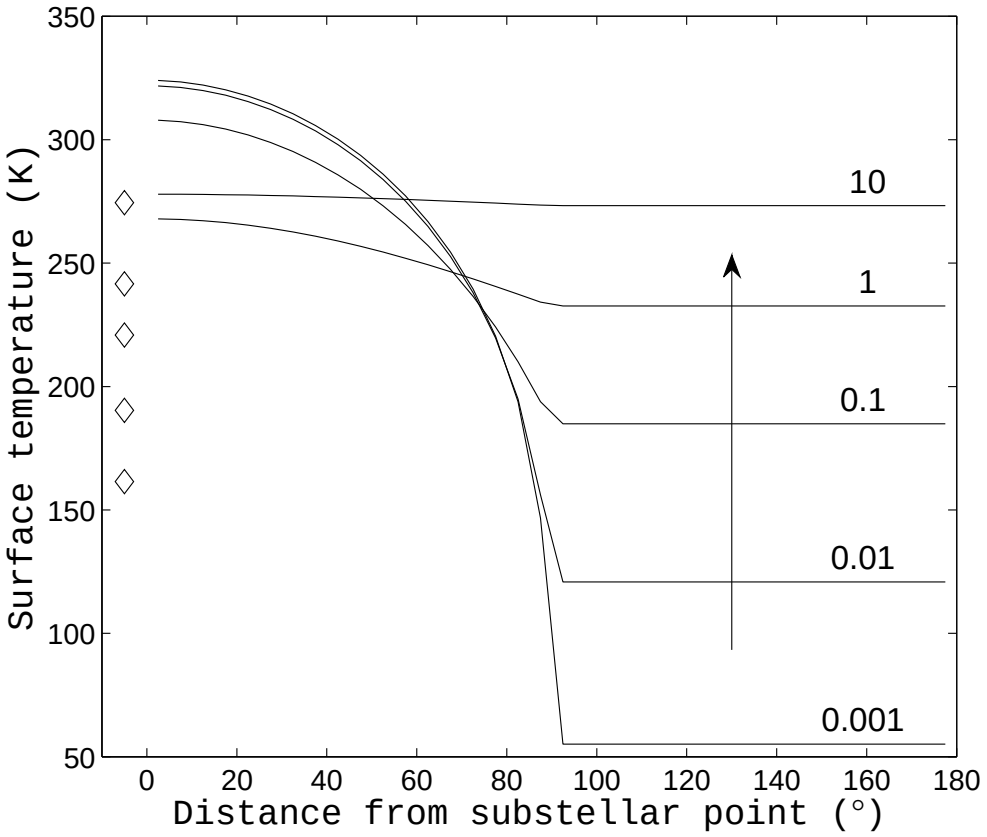

Figure 6.2 Surface temperature as a function of distance from the substellar point in our energy balance model. Diamonds correspond to atmospheric temperature (horizontally uniform). In order of increasing temperature, the pressures corresponding to the diamonds are 10^{-3}, 10^{-2}, 10^{-1}, 1 and 10 bars. Arrow is the direction of increasing pressure. Radiative efficiency $\Lambda = 0.1$, stellar flux $L_* = 900$ W/m^2.

93% of the weathering occurs in 10% of the planet's area. The planet-averaged weathering rate is

$$W_t(P) = \frac{1}{4\pi} \int_0^{\pi} W_\psi A_\psi \, \mathrm{d}\psi \tag{6.4}$$

Climate is in equilibrium ($\frac{\partial P}{\partial t} = 0$) when planet-integrated weathering of greenhouse gases, W_t, is equal to net supply V_n by other processes. The climate equilibrium is stable if $\mathrm{d}W_t/\mathrm{d}P > 0$ – in this case, carbonate-silicate feedback enables long-term climate stability (Walker et al., 1981). Climate destabilization occurs when $\mathrm{d}W_t/\mathrm{d}P < 0$. The weathering feedback that underpins the Circumstellar Habitable Zone concept (Kasting et al., 1993) changes sign, and acts to destabilize these climates.

6.3.2 ESWI results

Figure 6.3 shows weathering rates corresponding to the temperatures in Figure 6.2.

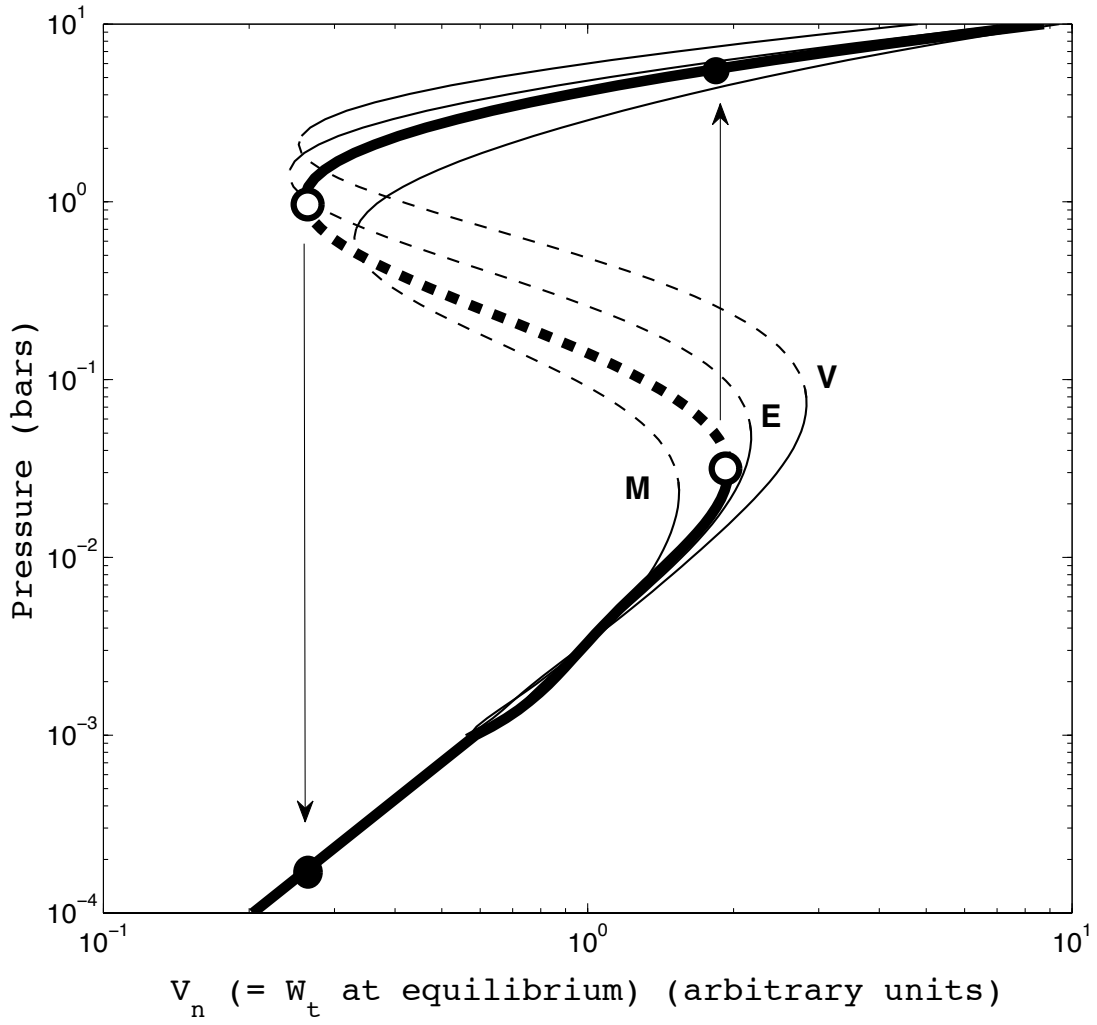

Figure 6.3 Bifurcation diagram to show the enhanced substellar weathering instability for radiative efficiency $\Lambda = 0.1$, stellar flux $L_* = 900$ W/m^2. The thick black line shows the planet-integrated weathering, W_t, corresponding to the temperature maps shown in Figure 6.2. If $V_n = 0$, $W_t \propto -\left(\frac{\partial P}{\partial t}\right)$. $\frac{\partial P}{\partial t} = 0$ at equilibrium, and W_t equals net supply by other processes, V_n. For both the lowest and highest P, $W_t\uparrow$ as $P\uparrow$. Equilibria on these branches are stable. For intermediate pressures, $W_t\downarrow$ as $P\uparrow$. The thick dashed line is this unstable branch. The rapid climate transitions which bound the hysteresis loop are shown by vertical arrows. The corresponding unstable equilibria are shown by open circles, and stable equilibria are shown by closed circles. The thin black lines correspond to Mars, Earth and Venus insolation (in order of increasing normalized weathering rate). The shape of the curve is explained in the text. These curves are an 8th-order polynomial fit to the model output. Note that as $L_*\uparrow$, both inflection points move to higher P.

The lines show equilibria between weathering consumption of greenhouse gases and net supply by other processes (Figure 6.3). The units of weathering are normalized to the weathering rate at $P = 3$ mbar. Along the curves, planet-integrated weathering of greenhouse gases, W_t, is equal to net supply V_n by other processes. These other processes can include volcanic degassing, metamorphic release, biology, sediment dissolution, and loss to space. The shape of this curve is set by competition between three effects:- (1) the greenhouse effect (Λ), (2) advective heat transport (β, k_{TF}) which enlarges and maintains unstable regions, and (3) stellar flux (L_*), which shrinks the unstable region. The curve has two stable branches and an unstable branch. The slope of the low-pressure stable branch is set by the (P/P_o) term in Equation 5 - for small P, $\tau \propto \ln(P)$ and $\beta \propto P$ are small and the atmosphere has little effect on T_s. On the intermediate pressure unstable branch – dashed in Figure 6.2 – the atmosphere is important to energy balance but β outcompetes τ. The homogenizing effect of β cools the substellar region, and planet-integrated weathering decreases with increasing pressure. In the high-pressure stable branch, the planet is close to isothermal. Further increases in β have little effect on ΔT_s, but τ warms the whole planet and now is able to increase W_t. Catastrophic jumps in the pressure caused by small changes in the supply V_n occur at $\sim$0.05 bar (for increasing volcanic activity) and $\sim$1 bars (for decreasing volcanic activity). The jumps correspond to a $>10^2$-fold increase in pressure, or a $>10^3$-fold decrease in pressure, respectively. The existence and location of these bifurcations are sensitive to small changes in the coefficients of Equation 6.3. The timescale for the climate regime jump is set by the rate of weathering and/or rate of volcanism on each specific planet. For example, Earth today supplies $\sim$15 mbar CO_2 in 10^5 yr (atmosphere + ocean: linearizing, $\sim$2 x 10^7 yr to build up 1 bar CO_2), but an Io-like rate of resurfacing (Rathbun et al., 2004) with the same magmatic volatile content would build up 1 bar in $\sim O(10^{4-5})$ yr. A natural weathering-rate experiment occurred on Earth 0.054 Gya, with very rapid release of CO_2 from an unknown source. The warmed climate required $\Delta t \sim O(10^5)$ yr (Murphy et al. (2010), using ^{3}He accumulation dating) to draw down 0.9 mbar of excess CO_2 (Zeebe et al., 2009).

Figure 6.4 shows habitable-zone climate regimes as a function of equilibrium pressure and stellar flux, which can change (Figure 6.4) due to stellar evolution, tidal migration (Jackson et al., 2010), or close encounters with other planets and small bodies (Morbidelli et al., 2007).

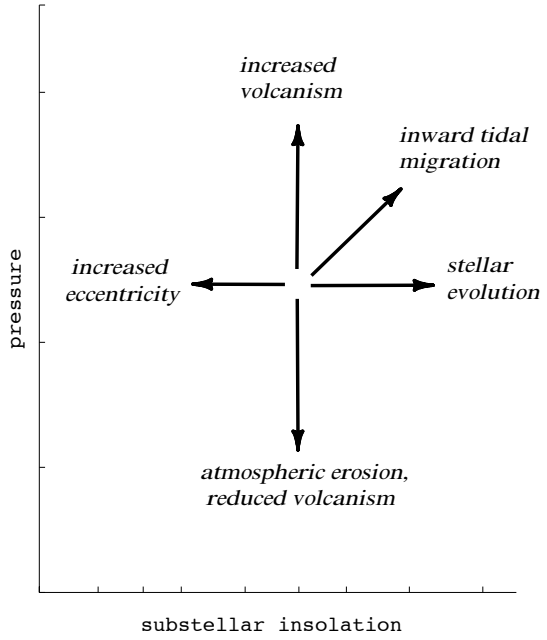
increased volcanism
inward tidal migration
increased eccentricity
stellar evolution
atmospheric erosion, reduced volcanism
pressure
substellar insolation

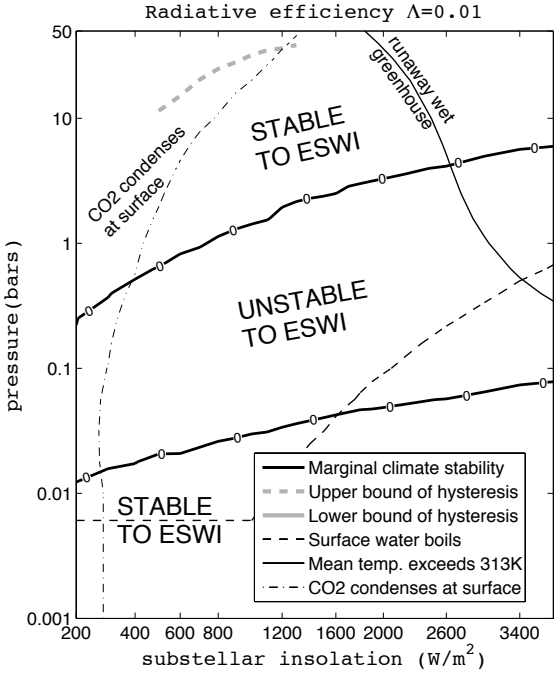
Radiative efficiency Λ=0.01
runaway wet greenhouse
CO2 condenses at surface
STABLE TO ESWI
UNSTABLE TO ESWI
STABLE TO ESWI
Marginal climate stability
Upper bound of hysteresis
Lower bound of hysteresis
Surface water boils
Mean temp. exceeds 313K
CO2 condenses at surface
pressure(bars)
substellar insolation (W/m2)

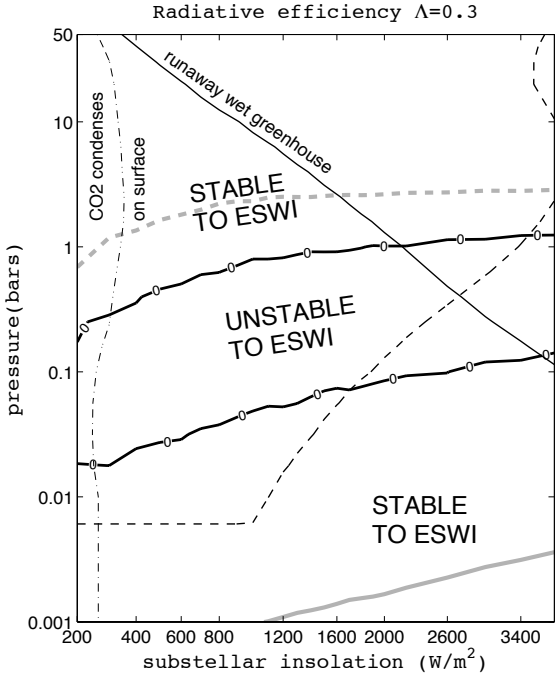
Radiative efficiency Λ=0.3
runaway wet greenhouse
CO2 condenses on surface
STABLE TO ESWI
UNSTABLE TO ESWI
STABLE TO ESWI
pressure(bars)
substellar insolation (W/m2)

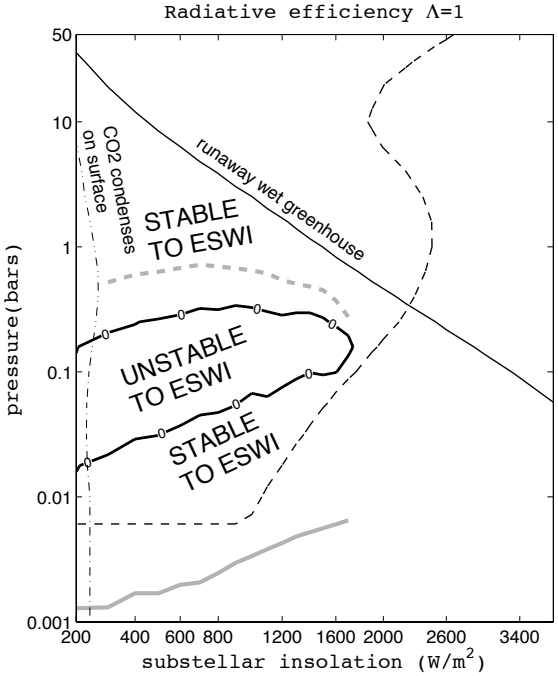
Radiative efficiency Λ=1
runaway wet greenhouse
CO2 condenses on surface
STABLE TO ESWI
UNSTABLE TO ESWI
STABLE TO ESWI
pressure(bars)
substellar insolation (W/m2)

Figure 6.4 Top left: Mechanisms that can cause secular change in the location of the climate equilibrium $W_t = V_n$. Remaining panels: Habitable zone (HZ) stability diagrams for (top right) $\Lambda = 0.01$, (bottom left) $\Lambda = 0.3$, (bottom right) $\Lambda = 1.0$. (Climates with $\Lambda >> 1$ are always stable against the enhanced substellar weathering instability). The climate states at intermediate pressure within the thick black line labeled with zeros are unstable to ESWI $\left(\frac{\partial W_t}{\partial P} < 0\right)$. Climates that approach the unstable zone from below will jump up to the dashed gray line. Climates that approach the unstable zone from above will jump down to the solid gray line. These jumps can be extreme; for example, in (b) the solid gray line is everywhere < 0.001 bars (and so is not visible). See the text for discussion of the speed of jumps. The hysteresis loop does not exist for high L_* and high Λ, and so the thick gray lines vanish towards the right of (d). The thin lines correspond to previously-described challenges to habitable-zone climate stability: moist runaway greenhouse (thin solid line); nightside atmospheric condensation of CO_2 (dash-dotted line); boiling of surface water (thin dashed line).

Climate stability depends strongly on Λ, so we show this (Figure 6.4) for three values of Λ - an almost radiatively inert gas, an intermediate $\Lambda = 0.1$ case, and a strong opacity that only just allows the ESWI ($\Lambda = 1.0$; higher values are stable against ESWI). The thick black line labeled with zeros corresponds to marginally stable climate equilibrium. Increasing L_* widens the range of P that sits within the low-pressure stable branch. That is because higher L_* produces higher absolute temperatures, and higher absolute temperatures favor radiative exchange between atmosphere and surface ($\propto 4(T_s - T_a)^3$ for small $(T_s - T_a)$) versus turbulent exchange ($\propto (T_s - T_a)^1$). Therefore, a given equilibrium value of P on the low pressure branch is more stable at low L_* than high L_* :– for a small increase in P the radiative warming will be less counteracted by the cooling of the substellar point. Increasing L_* pushes the high pressure branch to higher values. Other instabilities that contain the habitable zone are shown by thin lines. The dash-dotted line corresponds to pressures in excess of the nightside CO_2 saturation vapor pressure. CO_2 atmospheres to the left of this line condense on fast, dynamical timescales. Increasing Λ couples the horizontally-isothermal atmosphere more strongly to the nightside surface, and causes the CO_2 collapse threshold to move to the left. The thin solid line corresponds to mean surface temperatures above 40°C, which is the lower edge of the moist runaway greenhouse zone (Kasting, 1988; Pierrehumbert, 1995) - our model does not include fluxes of latent heat or the greenhouse effect of water vapor, so the position of this line is notional. The maximum pressure and minimum pressure of the bifurcation loop (Figure 6.3) are shown by thick gray lines in Figure 6.4. In some cases, the lower end-of-transition pressures are so low that water boils (thin dashed line). This would initiate the boiling of a global ocean. If boiling continued, the eventual fate could be a steam ocean, or restriction of liquid water stability to a thin belt near the terminator. The upper end-of-transition pressures are often >10 bars, with a nearly isothermal T_s. Such planets would have weak and perhaps undetectable phase curves in the absorbing bands

(Selsis et al., 2011).

For the almost radiatively inert gas, geologically stable equilibria usually have P <0.01 bars or P >0.3 bar. Intermediate pressures cannot be stable over geological time. The overall pattern is similar for $\Lambda = 0.3$. Increasing Λ always shrinks the domain of the unstable branch. For much higher Λ the climate is stable everywhere. We show the last gasp of the instability in the bottom right panel of Figure 6.4. Higher radiative efficiency means that for a small change in P, when ΔT_s is significant, radiative heat transfer overcomes advective heat transfer, the substellar patch warms, and overall planet temperature increases.

Figure 6.5 summarizes the effects of ESWI in a stability phase diagram (against axes of gas radiative efficiency and incident stellar radiation).

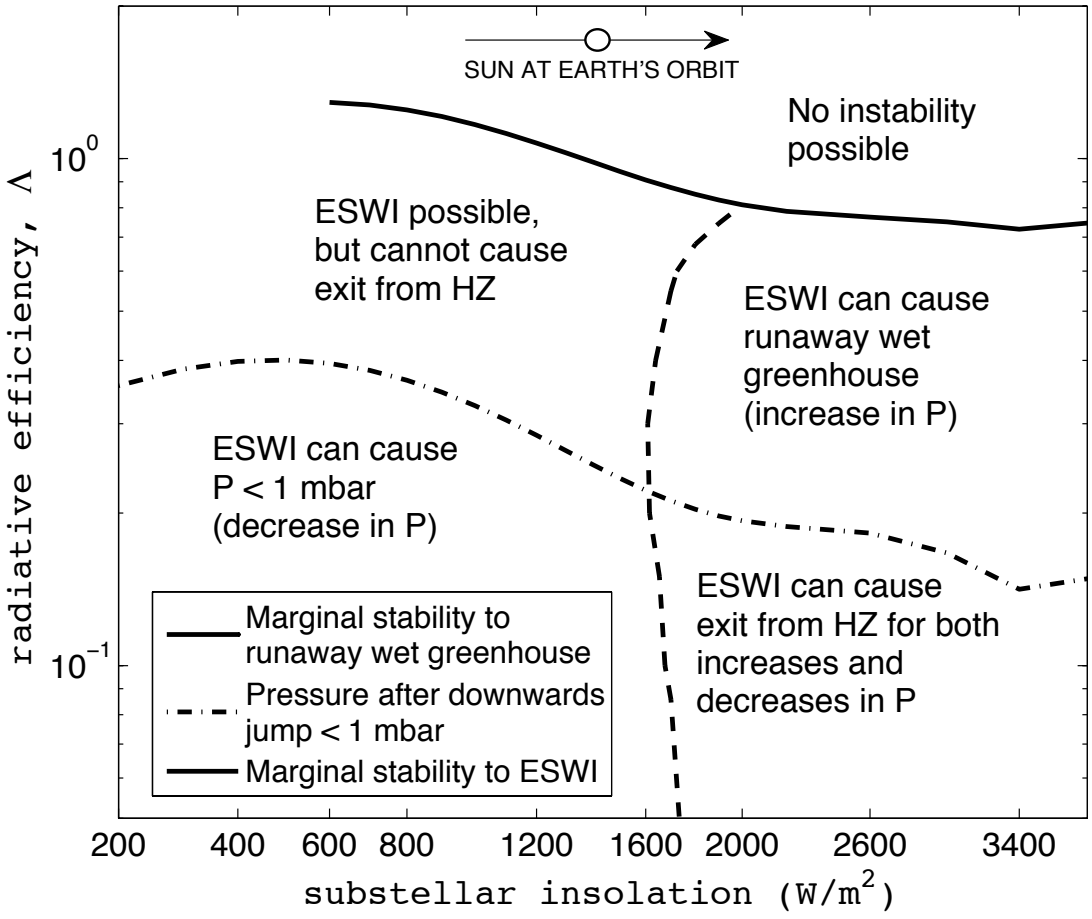

Figure 6.5 Stability phase diagram, showing the effects of the enhanced substellar weathering instability as a function of L_* and Λ. The jump in pressure due to ESWI can cause a runaway wet greenhouse (for a jump upwards in P), or a decrease in P to the triple point of water (for a jump downwards in P). To account for microclimates and solid-state greenhouse effects, we conservatively define "$P <$ triple point" as "$P < 1$ mbar", which is below the boiling curves in Figure 6.4. Some curves have been smoothed with a 5th-order polynomial in order to remove small wiggles due to numerical artifacts. The arrow shows the change in stellar flux at 1AU for a solar-mass star over 8 Gyr of stellar evolution in the model of Bahcall et al. (2001), and the circle marks the current solar flux.

For $\Lambda > \sim 1$, the climate is stable to ESWI. For $\Lambda < \sim 1$, ESWI is possible but the pressure jumps caused by ESWI do not always have a catastrophic effect. Higher L_* warms the climate towards the runaway moist greenhouse threshold, and upward jumps in pressure for $L_* > \sim 2000$ W m^{-2} may initiate the moist runaway greenhouse (points to the right of

the vertical dashed line in Figure 5). Atmospheric collapse to $\sim$ 1 mbar (well below the triple point of water) only occurs below $\Lambda < 0.4$. Increasing L_* increases both the bottom and the top pressure for instability, implying that tidal migration towards the star should be destabilizing for thick atmospheres but stabilizing for thin atmospheres.

6.4 Climate destabilization mechanism #2: Substellar dissolution feedback (SDF)

Water ice and basalt are the most common planetary surface materials in the Solar System, and are expected to be common elsewhere.When these melt (around 273K for ice and 1300K for basalt), atmosphere can dissolve into the melt. Counterintuitively, a decrease in P and in average surface temperature $\bar{T}_s$ can favor melting if ΔT_s is large, as pointed out for Mars by Richardson and Mischna (2005). For a synchronously-rotating planet entirely coated in condensed material (ice, rock, or carbon-rich ceramic), surface liquid will first appear near the substellar point. Atmosphere will dissolve into this warm little pond, approaching Henry's-law equilibrium:

$$P_{pond} = \frac{g}{P_{Earth}} \underbrace{\left(D_{pond} \frac{1}{2} \left(1 - \cos \psi_{max}\right) \right)}_{\text{global-equivalent liquid depth}} \underbrace{\left(P^d \, m \, \rho_l \, k_H(T^o) \exp\left[C \left(\frac{1}{T_{pond}} - \frac{1}{T^o} \right) \right] \right)}_{\text{mass of gas per unit liquid volume}} \quad (6.5)$$

where P_{pond} (in bars) is the equivalent atmospheric pressure of gases dissolved in the ocean, g is surface gravity, P_{Earth} = 1.01 x 10^5 Pa is a normalization constant, D_{pond} is pond depth, ρ_l is liquid density, ψ_{max} is the angular radius of the pond, P is the surface pressure, d is a dissolution exponent ($\sim$0.5 for water in silicate liquids and $\sim$1 for gases in water), m is the molecular mass of the atmosphere, k_H and C are Henry's-law coefficients, T_{pond} is the pond temperature, and T^o is a reference temperature. Here, the first term in brackets is the depth of the pond in global-equivalent meters, and the second term in brackets is the mass of gas per unit volume of pond. We have neglected the distinction between fugacity and partial pressure. The pond is assumed to be well-mixed so that $T_{pond} = \frac{1}{1-\cos\psi_{max}} \int_0^{\psi_{max}} T_{s,\psi} \sin\psi \, \mathrm{d}\psi$. This relation assumes a uniform heat transfer coefficient between the surface and the pond.

Instability occurs when a decrease (increase) in surface pressure results in an uptake (release) of gases from the pond that exceeds that which is consistent with that change in pressure, i.e. $\frac{\partial P_{pond}}{\partial P} < -1$. In this case the feedback has infinite gain (Roe, 2009). Pond growth rate is limited by the balance between insolation and the latent heat of melting ($O(10^3)$ yr for melting of a 1km-thick ice sheet, Earthlike insolation, $\alpha = 0.6$, and 10% of sunlight going to melting), or by thermal diffusion of heat into a stratified pond. For tectonic activity levels that are not too high, the SDF is much faster than the ESWI, which is limited by volcanic degassing rates and tectonic resurfacing rates (0.05 mm/yr on Earth

(Leeder, 1999); 16 mm/yr on Io (Rathbun et al., 2004)). The SDF stops when insolation is insufficient to allow further pond growth. What happens after the SDF has operated will depend on the sign of the carbonate-silicate feedback at the new, modified P. If $\partial W_t/\partial P > 0$, the normal carbonate-silicate feedback will rejuvenate the atmosphere on a volcanic degassing timescale, freezing the ocean. If $\partial W_t/\partial P < 0$, pressure decreases further.

Gases that react chemically with seawater (such as SO_2 and CO_2; Zeebe and Wolf-Gladrow (2001)) can have P_{pond} much greater than that given by Henry's law. For example, total Dissolved Inorganic Carbon (DIC, $\propto P_{pond}$) is buffered against changes in P by carbonate chemistry, and P_{pond} changes much more slowly than Henry's law. $P_{pond} \propto P^{0.1}$ for the modern Earth ocean, as opposed to $P_{pond} \propto P$ for Henry's law (Zeebe and Wolf-Gladrow, 2001; Goodwin et al., 2009). For a decrease in P that increases ψ_{max}, this buffering favors the tendency of increasing pond volume to draw down more atmosphere, against the Henry's Law decrease in atmospheric concentration per unit pond. Carbonate buffering is less important for $P >\sim 1$ bar, because at the correspondingly low pH the DIC partitions almost entirely into CO_2. For CO_2, we use R. Zeebe's scripts (`http://www.soest.hawaii.edu/oceanography/faculty/zeebe_files/CO2_System_in_Seawater/csys.html`) to find the additional DIC held in the ocean as HCO_3^- and CO_3^{2-}. We use fixed alkalinity, 2400 μmol/kg (similar to the present Earth ocean; Zeebe and Wolf-Gladrow (2001)). Figure 6.6 shows the results.

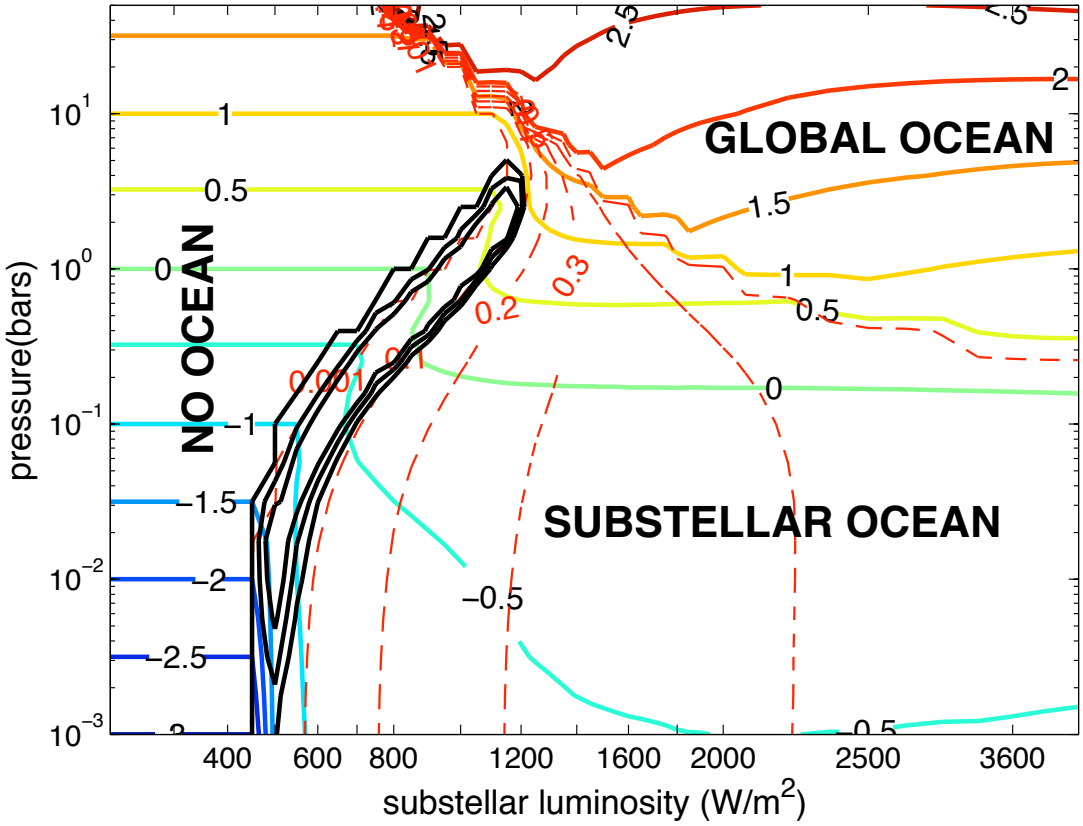

Figure 6.6 Substellar dissolution feedback, for CO_2/seawater equilibria, $\Lambda = 0.03$ (note that $\Lambda = 0.03$ is unrealistically low for all-CO_2 atmospheres), and a 100km-deep ocean. The vertical axis is P. Colored solid lines correspond to log10($P + P_{pond}$), i.e. the sum of the atmospheric and ocean inventory (in bars). Where these are equal to P, there is no ocean. Fractional ocean coverage is shown by the red dashed contours (contour interval is 0.1 in units of planet fractional surface area). Because nightside temperature is constant, fractional ocean coverage jumps from 0.5 (hemispheric ocean) to 1.0 (global ocean). The outermost black line encloses the area where SDF is a positive feedback on small changes in P. Outside this area, $\frac{\partial P_{pond}}{\partial P} \geq 0$ (zero or negative climate feedback). The inner two contours correspond to $\frac{\partial P_{pond}}{\partial P}$ < -0.5 (strong positive feedback) and $\frac{\partial P_{pond}}{\partial P}$ < -1 (innermost contour; runaway). Runaways can only occur for deep oceans and small pond area.

ψ_{max} is set by Equation 6.1 through $T_s(\psi)$. Ocean circulation adds additional heat transport terms to Equation 6.1, which we ignore. We also do not consider buffering by dissolution and precipitation of carbonates or salts (such as sulfates).

As an example of SDF, consider the partitioning of an initial 1-bar total inventory of

CO_2 (blue-green contour labeled '0' in Figure 6.6) with increasing L_*. Initially, the planet's surface is below freezing. As stellar flux is increased to 800 W/m^2, a small sea forms and dissolves some of the CO_2. The system is within the area where SDF is a positive feedback on small changes in P (outermost black contour in Figure 6.6), which accelerates sea growth. A small further increase in L_* leads to runaway SDF (innermost black contour in Figure 6.6), and ocean area quickly grows with from ∼5% to ∼15% of planet surface area with no change in L_*. After this change the atmospheric inventory is reduced to 1/4 bar with the remaining 3/4 bar dissolved in the ocean. Further pond growth requires further increase in L_*. Increasing T_{pond} decreases solubility and shallows the slope of increasing volatile inventory stored in the ocean. By $L_* = 3800$ W/m^2 (the highest considered), the ocean covers almost the entire lightside hemisphere, and stores ∼5/6 of the initial CO_2 inventory. Further small increases in L_* cause a global ocean.

Three main effects control this system:- (1) Cosine fall-off of starlight weakens the ability of decreasing pressure to increase ocean area beyond a relatively small ψ_{max}. Following a line of decreasing pressure, the dashed red lines (fractional ocean area) become more widely spaced with decreasing pressure. Cosine falloff of stellar radiation is responsible. This restricts the scope of the instability, which tends to produce Eyeball states (discussed in Pierrehumbert (2011)). We do not find any cases where the SDF can turn a dry planet into an ocean-covered planet or vice versa. (2) Ocean instability disappears above ∼5 bars, when the surface is nearly isothermal. Because decreases in pressure always decrease $\bar{T}_s$ (except when there is an antigreenhouse), decreases in pressure can only cause oceans to freeze over. Below ∼5 bars, ΔT_s is not negligible. If a decrease in pressure allows the substellar temperature to rise above freezing, an ocean can form. (3) Rectification of starlight by the terminator, and of ocean area by the melting point, divides the phase diagram into 'no ocean', 'substellar ocean' and 'global ocean' zones. On the nightside T_s is constant, so ocean area jumps from 50% to 100%. Notice the change in sign of L_* dependence below and above the dashed red line corresponding to 50% ocean area. In the substellar ocean zone, increasing L_* increases ocean area and the ocean inventory increases. However, in the global ocean zone, increasing L_* cannot increase ocean area. The decrease in gas solubility with increasing temperature dominates, and the ocean inventory decreases.

Figure 6.6 does show unstable regions in parameter space for which substellar dissolution is a positive feedback on changes in P (solid black lines). These always correspond to small oceans (<10% of planet surface area). But the gain of the feedback is small, and runaways cannot occur unless ocean depth >10km. Factor–of–3 decreases (or increases) in atmospheric pressure can occur with no change in the total (atmosphere + ocean) inventory of volatile substance. The SDF is a minor positive feedback (or a negative feedback) for most gases which dissolve simply according to Henry's Law. The buffering effect is not sufficient to allow ocean area to give a strong positive feedback. Finally, $\Lambda = 0.03$ is unrealistically low for all-CO_2 atmospheres. Setting $\Lambda = 1$ would shut down the instability. We conclude that the CO_2 SDF is unlikely to be important for planets in synchronous rotation, and is important in fewer cases than is the ice-albedo feedback (Roe and Baker, 2010; Pierrehumbert, 2010).

6.5 Discussion

6.5.1 Solar system climate stability – is Mars a solar system example of ESWI?

Although ESWI is most relevant for planets in synchronous rotation, it can work for any planet with sufficiently high ΔT_s. Therefore, in order to test ESWI against available data, we compare the requirements for ESWI to Solar System data (Table 1). After correcting for the distorting effects of life, all of the Solar System's non-giant atmospheres are overwhelmingly one gas. Except for Earth, the principal gas is also the main greenhouse gas. Venus' atmospheric composition is not controlled by the abundance of surface liquid (nor in solid-state equilibrium with surface minerals; Hashimoto and Abe (2005); Treiman and Bullock), and Triton's atmosphere is too thin to stabilize liquid nitrogen. Climate regulation on Titan is not well understood. Currently, the greenhouse effect of CH_4 outcompetes the antigreenhouse effect of the organic haze layer (McKay et al., 1991). The production rate of the organic haze layer depends on $[CH_4]$ (McKay et al., 1991; Lorenz et al., 1997). ESWI is not currently possible on Titan because ΔT_s is too small, 2.5-3.5K (Jennings et al., 2009). Therefore, out of 5 nearby worlds with atmospheres and surfaces, only Mars is a candidate for ESWI (§6.5.1). Solar System data suggest that the conditions for the ESWI are quite restrictive, and that most planets will not be susceptible to the ESWI.

Table 6.1 Solar system climates, showing vulnerability to ESWI and SDF.

Planet	Atmospheric Composition	Climate-controlling GHG	Requirements: (1)	(2)	(3)	(4)
Venus	97% CO_2	CO_2	√	√	×	×
Earth	99% N_2 (a)	CO_2	×	√	√	×
Mars	95% CO_2	CO_2	√	√	√/?	√
Titan	98% N_2	N_2 or H_2/CH_4 (b)	(√)	√	√	√
Triton	>99.9% N_2	n.a.	√	×	×	n.a. (c)

Notes. Requirements for the instability include that (1) the principal gas in the atmosphere is the main climate-controlling greenhouse gas. (2) The atmosphere significantly influences surface temperature. (3) Removal of gas by liquid phase, *via* weathering or dissolution, is an important loss mechanism. (4) $\bar{T} < T_{\rm melt} < \max(T_s)$. (a) Earth: ignoring oxygen, which is an artifact of biology. (b) Titan: small fractional or absolute changes in $[N_2]$ have the largest effect on Titan's τ (Lorenz et al. 1999). However, this ignores vapor-pressure and photochemical feedbacks which may put $[H_2]$ in control (McKay et al. 1991). (c) Triton: surface melting is impossible, because N_2's triple point is $10^4\times$ greater than Triton's surface pressure.

Mars may have passed through ESWI in the past. The main climate-controlling greenhouse gas (CO_2) can dissolve in liquid water and be sequestered as carbonate minerals. Mars has low P (95% CO_2). It has widespread deposits of carbonate minerals (Bandfield et al., 2003; Wray et al., 2011b), but little or no surface liquid water. It currently sits at the gas-liquid sublimation boundary (Kahn, 1985), with ΔT_s ∼100K , and GCMs show that $\Delta T_s\downarrow$

as $P\uparrow$ (Richardson and Mischna, 2005). These geologic and climatic observations are all consistent with a past rapid transition via ESWI from an early thicker atmosphere to the current state, as follows. Increasing solar luminosity could have permitted transient liquid water, allowing carbonate formation. The corresponding drawdown in P would increase noontime temperature, allowing a further increase in liquid water availability and the rate of carbonate formation. The runaway would slow as P approached the triple-point buffer: loss of liquid water stability may have throttled weathering and buffered the climate near the triple point (Kahn, 1985; Halevy et al., 2007). However, ice is not ubiquitous on the surface and can migrate away from warm spots, so unusual orbital conditions are neccessary for melting (Chapters 2 and 3). Alongside carbonate formation, atmospheric escape, polar cold trapping and volcanic degassing are the four main processes affecting P on Mars over the last 3 Ga. However, recent volcanism has been sluggish and probably CO_2-poor (Hirschmann and Withers, 2008; Werner, 2009; Stanley et al., 2011), and present-day atmospheric escape appears slow (Barabash et al., 2007). Polar cold traps hold $\sim$1 Mars atmosphere of CO_2 as ice today (Phillips et al., 2011), but this trapping should be reversible at high obliquity. Therefore, it is quite possible that substellar ($\equiv$ noontime) carbonate formation has been the dominant flux affecting the secular evolution of Mars' atmosphere since 3.0 Gya. This hypothesis deserves further investigation.

6.5.2 Application to exoplanets

How general is our feedback?

ESWI requires:

– *Strong temperature dependence of the weathering drawdown of greenhouse gases.* Decreasing k_{ACT} to 0.03 (from the nominal 0.09) eliminates the ESWI except for radiatively inert atmospheric compositions. On the other hand, increasing k_{ACT} to 0.27 causes a large unstable region even for $\Lambda = 1.0$, with at least a 1 dex range of atmospheric pressure unstable to ESWI for all habitable-zone luminosities.

Earth data on the value of k_{ACT} are consistent with $k_{ACT} \sim 0.1$. However, deep-time calibration of weathering-temperature relations such as Equation 6.3 is difficult. There is only one planet (Earth) to use as laboratory, with constantly drifting boundary conditions, and rather few natural experiments. Chemical weathering rates of silicate minerals in the laboratory are definitely temperature-dependent (White and Brantley, 1995), but erosion-rate dependence is also important at the scale of river catchments (West et al., 2005). Confirming temperature dependence on geological scales is difficult, in part because today's weathering rate contains echoes of glacial-interglacial cycles (Vance et al., 2009). Regression of present-day river loads on watershed climatology by West et al. (2005) suggests an e-folding temperature of 8.5(+5.5/-2.9)K. $^{187}Os/^{188}Os$ data suggest continental weathering rates increased 4-8x in $\ll 10^6$ yr during a Jurassic hyperthermal ($\Delta T \leq 10$K) 0.183 Gya (Cohen et al., 2004),

implying an e-folding temperature $<(5-7)$K. Analysis of the apparent time dependence of weathering rate gives support to a hydrological control on weathering rates (Maher, 2010), but on a planetary scale precipitation always increases when T_s increases (O'Gorman and Schneider, 2008), provided that there is surface liquid. That is, $\frac{DW}{Dt} = \frac{\partial W}{\partial T_s} + \frac{\partial W}{\partial R}\frac{\partial R}{\partial T_s}$ with $\frac{\partial R}{\partial T_s} > 0$.

Overall, Equation 3 is consistent with deep-time, present-epoch, and laboratory estimates for Earth. Though Equation 3 is used in this paper as a general rule for Earth-like planets, the weathering-temperature relation is shaped by biological innovations. For example, the symbiosis between vascular plants and root fungi (arbuscular mycorrhizae) acidifies soil, profoundly accelerates weathering, and may be unique to Earth (Taylor et al., 2009). All geologically important surface weathering reactions require a liquid phase (White and Brantley, 1995). We assume weathering reactions do continue below the freezing point (due to microclimates, or monolayers of water). However, the results shown in Figure 6.4 and 6.5 did not change qualitatively when we set $W = 0$ for $T < T_{melt}$.

Strong temperature dependence could break down in several ways. For example, erosion is needed to expose fresh mineral surfaces for weathering. On a tectonically quiescent planet (and for tectonically quiescent regions of an active planet) weathering may be limited by supply of fresh surfaces, with weathering going to completion on all exposed silicate minerals. On tectonically very active planets with little or no land, hydrothermal alteration and rapid seafloor spreading maintain low greenhouse gas levels with little or no temperature dependence (Sleep and Zahnle, 2001). A planet with weathering rates that are limited by the availability of liquid water (like Mars) can have effectively temperature-dependent weathering, but only if the atmospheric pressure is well above that fluid's triple point.

– *Large* ΔT_s. The high-ΔT_s requirement cannot be met if the atmosphere is thick. A deep global ocean circulation behaves like a thick atmosphere - Earth abyssal temperatures vary <2K from tropics to poles (Schlitzer, 2000). Therefore, the climate destabilization mechanism cannot operate on a planet with a deep global ocean circulation - at least some land is necessary. Evaporation will dry out land at the substellar point if $\bar{T}_s$ is high, so weathering activity may be concentrated at cooler ψ in this case. ΔT_s varies little, or even increases, with rotation frequency (Merlis and Schneider, 2010; Edson et al., 2011). Therefore, ESWI could work for rapidly-rotating planets such as Mars (§6.5.1). However, the isothermal approximation does not apply when the Coriolis force prevents fast equator-to-pole winds. For rapid rotators, T_s is a function of latitude and longitude, and our idealized energy balance model is not appropriate.

– *Small* Λ. Strong greenhouse gases have high Λ, which suppresses ESWI. On the other hand, Λ can be negative if there is an antigreenhouse effect ($\Lambda < 0$). M-dwarfs later than M4, with fully convective interiors, seem to remain active with high UV fluxes for much longer than do Sunlike stars. High UV fluxes broadly favor CH_4 accumulation (Segura et al., 2005) and perhaps antigreenhouse haze effects. When $\Lambda < 0$, ESWI will apply for all P and L_*.

– *Surface-atmosphere coupling.* This consists of radiative and turbulent coupling. Turbulent coupling requires a nonzero near-surface wind speed, and that the global near-surface atmosphere is not stably stratified. A sensitivity test with a 10–fold reduction in U showed that the pressure range unstable to ESWI moves to $\sim 10\times$ higher pressure. The range of Λ subject to ESWI was significantly reduced. We assume U is not a function of P, but simulations show that U increases as P decreases (Melinda A. Kahre, via email). This would strengthen the instability.
SDF has very similar requirements to ESWI, but the constraint on rotation rate is stricter. Large-amplitude libration or nonsynchronous rotation would prevent the development of a deep pond around the substellar point. (A low-latitude liquid belt can be imagined, but the idealized EBM of §6.2 is not appropriate to that case). Kepler data show that only a small proportion of close-in small-radius exoplanets in multi-planet systems are in mean-motion resonance (Lissauer et al., 2011), but that most are close to resonance and could maintain nonzero eccentricity. This would allow for significant nonsynchronous rotation if the planet's spin rate adjusts to keep the substellar point aligned with the star during periapse passage (pseudo-synchronous rotation). In addition, SDF requires very soluble gases: by contrast, the N_2 content of even a 100km deep ocean at 298K is only $\sim$0.2 bar per bar of atmospheric N_2. In this paper we assume that volatiles are excluded from the ice when the ice freezes. If clathrate phases form, they could absorb volatiles and make the SDF irreversible.

Climate evolution into the unstable region

Planets could undergo ESWI early in their history if they form in the unstable region. In addition, many common geodynamic and astronomical processes can shift the equilibrium between W_t and V_n (Figure 6.4a), causing a secular drift of the equilibrium across the phase space $\{L_*, \Lambda, V_t\}$ (Figures 6.3 and 6.5). This drift can take a planet from a stable equilibrium to an unstable equilibrium via a saddle-node bifurcation.

• *Dynamics and stellar evolution:* Theory predicts that the secular increase in solar flux should have gradually shifted the position of Earth's climate equilibrium. This is consistent with the sedimentary record of the last 2.5 x 10^9 yr (Grotzinger and Kasting, 1993; Grotzinger and James, 2000; Ridgwell and Zeebe, 2005; Kah and Riding, 2007). For Kepler field (Sunlike, rapidly evolving) stars, this could also occur and potentially cause the ESWI for planets with initially thick atmospheres (Figure 6.4). For M stars, main-sequence insolation changes little over the lifetime of the Universe.

• *Atmospheric evolution:* Λ can change as atmospheric composition evolves. For example, the rise in atmospheric oxygen following the emergence of oxygenic photosynthesizers probably oxidized atmospheric CH_4 and may have caused a catastrophic decline in Λ (Kopp et al., 2005; Domagal-Goldman et al., 2008). Even gases with negligible opacity, such as N_2, alter Λ through pressure broadening (Li et al., 2009). Carbonate-silicate weathering equilibrium is impossible for planets where atmospheric erosion exceeds geological degassing. For these

planets, V_n is negative. Strong stellar winds and high XUV flux are observed for many M stars. Removal of atmosphere by strong stellar winds or, for smaller planets, high XUV flux (Tian, 2009) could trigger an instability for a planet orbiting an M-star, by reducing P (Figure 4a).

• *Tectonics and volcanism:* Volcanic activity decays with radioactivity (Chapter 5; also Sleep (2000, 2007); Stevenson (2003)), so in the absence of tidal heating the equilibrium pressure will gradually fall (on a stable branch where W_t increases with P) (Figure 6.4). Superimposed on this decline are pulses in volcanic activity due to mantle plumes, and perhaps planetwide volcanic overturns as seem to have occurred on Venus. This will cause spikes in equilibrium pressure. The rate of resurfacing is very sensitive to mantle composition, tidal heating, and tectonic style (Chapter 5; see also Valencia and O'Connell (2009); Korenaga (2010); Běhounková et al. (2010, 2011); van Summeren et al. (2011)). Shutdown of volcanism (such that $V_n \leq 0$) extinguishes the possibility of a stable climate equilibrium; P will fall monotonically. ESWI can accelerate this decay, and Mars may be an example of this (§6.5.1). Mountain range uplift exposes fresh rock and may provide a $O(10^7)$ yr increase in weathering rate that cools the planet (as arguably and controversially may have occurred for Tibet, Earth: Garzione (2008)). This may trigger ESWI by lowering pressure. More speculatively, drift of continents can cause very large atmospheric pressure fluctuations if greenhouse-gas drawdown occurs mainly on land and is strongly focussed in a high-weathering patch near $\psi = 0$. A continent drifting over the patch will increase planet-averaged weatherability, and pressure will go down.

6.6 Context and conclusions

Nearby M-dwarfs are targeted by several planet searches:- MEarth (Charbonneau et al., 2009); the VLT+UVES M-dwarf planet search (Zechmeister et al., 2009); the VLT+CRIRES M-dwarf planet search (Bean et al., 2010b); HARPS (Forveille et al., 2011); M2K (Apps et al., 2010); and proposed space missions TESS (Deming et al., 2009); ELEKTRA; PLATO; and ExoplanetSat (Smith et al., 2010). These searches are driven in part by the hope that planets orbiting M-dwarves can maintain surface liquid water and be habitable. Maintaining surface liquid water over geological time involves equilibrium between greenhouse-gas supply and removal. Balance is thought to be maintained on habitable planets through temperature-dependent weathering reactions. Climate stability can be undermined by several previously-studied climate instabilities. These include atmospheric collapses (Haberle et al., 1994; Read and Lewis, 2004), photochemical collapses (Zahnle et al., 2008; Lorenz et al., 1997), greenhouse runaways (Kasting, 1988; Lorenz et al., 1999; Sugiyama et al., 2005), ice-albedo feedback (Roe and Baker, 2010), and ocean thermohaline circulation bistability (Stommel, 1961; Epica Community Members et al., 2006). Climate stability can also be undermined if the sign of the dependence of mean surface weathering rate on mean surface temperature is reversed. This paper identifies two new climate instabilities that involve such a reversal,

and are particularly relevant for planets orbiting M-dwarves.

Competition between radiative and advective heat transfer timescales sets surface temperature on synchronously-rotating planets with an atmosphere. The atmosphere moves the surface temperature towards the planetary average, through radiative and turbulent heat exchange, on timescale t_{dyn}. The dayside insolation gradient acts to reestablish gradients in surface temperature, on timescale t_{rad}. We refer to planets with $t_{dyn} < t_{rad}$ as dynamically equilibrated, because surface temperature is set by atmospheric dynamics. Venus and Titan are nearby examples. We refer to planets where $t_{dyn} \geq t_{rad}$ as radiatively equilibrated. Mars is a nearby example.

Steeper horizontal temperature gradients promote atmospheric depletion if they stabilize surface liquid films, ponds or oceans in which the atmosphere can dissolve. Once dissolved, the atmospheric gases may be sequestered in the crust by weathering. Weathering rates are much faster when solvents are present and temperatures are high. Weathering and mineral formation can be mediated by thin films of water, and are largely irreversible on habitable-zone planets with stagnant lid geodynamics (karst and oceanic dissolution layers are minor exceptions). Lithospheric recycling may cause metamorphic decomposition of weathering products, returning greenhouse gases to the atmosphere on tectonic timescales. In the absence of weathering, growth of an ocean can reduce atmospheric pressure through dissolution. For example, the fundamental greenhouse gas on Earth is CO_2. The partitioning of CO_2 between the atmosphere, ocean (solution) and crust (weathering products) is in the ratio $1{:}50{:}10^5$ for Earth. Dissolution is fully reversible. Positive feedback occurs if reduced atmospheric pressure further steepens the temperature gradient. Rising maximum temperature resulting from atmosphere drawdown allow further expansion of liquid stability, leading to more drawdown. The zone where liquid is stable spreads over the substellar hemisphere. A halt to the atmospheric collapse occurs when pressure approaches the boiling curve, or when the liquid phase is stable over most of the dayside, or when thermal decomposition by crustal recycling returns weathering products to the atmosphere as fast as they are produced.

Our idealized-model results motivate study of the instabilities with GCMs.

We conclude from this study that:-

1. Enhanced substellar weathering instability (ESWI) may destabilize climate on some habitable-zone planets. ESWI requires large ΔT_s, which is most likely on planets in synchronous rotation. ESWI does not require strict 1:1 synchronous rotation.

2. Substellar dissolution feedback (SDF) is less likely to destabilize climate. It is only possible for restrictive conditions: small oceans, highly soluble gases, and relatively thin, radiatively weak atmospheres. Furthermore, small amounts of nonsynchronous rotation can eliminate SDF.

3. The proposed instabilities only work when most of the greenhouse forcing is associated with a weak greenhouse gas that also forms the majority of the atmosphere (it does

not work for Earth). There are no exact solar system analogs to ESWI, although Mars comes close. Therefore, it would be incorrect to use these tentative results to argue against prioritizing M-dwarfs for transiting rocky planet searches.

4. If the ESWI is widespread, we would expect to see a bimodal distribution of day-night temperature contrasts and thermal emission from habitable-zone rocky planets in synchronous rotation. Rocky planets with surface pressures in the unstable region would be rare, so emission temperatures would be either close to isothermal, or close to radiative equilibrium.

Chapter 7

Synthesis and future observations.

7.1 Mars

7.1.1 Synthesis: Formation of sedimentary rocks by snowmelt-limited induration of atmospherically-transported sediment

This section puts Chapter 4 results in context. Chapter 4 argues for snowmelt-limited sedimentary rock formation on Early Mars, as opposed to sediment-supply limited formation or ice-limited induration. Here I relate this to active processes, geologically younger processes and alternative limiting factors.

Transport rates for atmospherically-transported sediment on Mars are comparable to past accumulation rates of sedimentary rocks, so sedimentary rock formation on Mars was probably limited by the ability to pin down (indurate) sediment rather than sediment availability. Mars dust storms change the albedo of large patches of the surface on interannual and decadal timescales (Geissler, 2005). Mars dust diameter is 2μm (Wolff and Clancy, 2003), and the albedo changes require deposition of at least a monolayer of dust. Viking lander observations imply a present day gross deposition rate of dust of a few μm/yr (Arvidson et al., 1979). Rover tracks are initially visible from orbit but are erased during seasonal dust storms in $\sim$ 1 Mars year (Geissler et al., 2010). These accumulation rates are not much less (given the difference in age) than the accumulation rate inferred for ancient quasi-periodically layered sedimentary rocks: 20-50 μm/yr at the best-measured site (Lewis et al., 2008), assuming that the quasi-periodic bedding is laid down by astronomical forcing, and the main source of error is whether eccentricity, obliquity, or precession are the main control on deposition. However, "cleaning events," strong winds that remove accumulated dust which blocks light from reaching the rovers' solar cells, prove that deposited dust does not always stay there. The inferred dust deposition rate cannot, therefore, be a net deposition rate: the flux of dust tends to reverse over years to decades (Geissler, 2005). With spectacular exceptions (Bourke et al., 2008; Chojnacki et al., 2011; Hansen et al., 2011; Silvestro

et al., 2010), aeolian bedforms migrate at cm/yr or less in the current climate. However, cross-cutting relationships between aeolian bedforms and young impact craters at the Opportunity site imply that the most recent bedform migration was between ∼50 Kya and ∼200 Kya (Golombek et al., 2010), and the crater age of most aeolian bedforms on Mars is comparably small. Present-day inactivity can be reconciled with overall youthfulness if the ∼6 mbar CO_2 reservoir within the South Polar Layered Deposits is partly released at higher obliquity, as seems necessary to explain high-elevation (P <6mbar) gullies (Head et al., 2008; Phillips et al., 2011). Aeolian transport on Mars is very sensitive to small increases in surface stress (Newman et al., 2005). Therefore, past gross dust deposition rates were probably > a few μm/yr. Global reservoirs of present-day sediment are large: the dust cover at high elevations on Tharsis is >6m thick (Bridges et al., 2010), and tens of meters thick in E Arabia Terra (Mangold et al., 2009). We estimate 5-23 m global equivalent of sediment has cycled through the diurnal skin depth during the Amazonian. [Edwin S. Kite and Itay Halevy, "Martian climate under a brightening Sun", unpublished manuscript]. Sedimentary rock formation is probably not limited by sediment availability. The difficulty is instead to pin the sediment in place for > 3.3 Gyr.

Ice can pin down atmospherically-transported sediment as long as orbital conditions permit ice stability, but sublimes in a short fraction of Mars history when orbital conditions are unfavorable for ice (Hudson et al., 2007; Hudson and Aharonson, 2008). Mars currently has $\sim 3 \times 10^6$ km^3 of water ice near the poles. Much (perhaps all) migrates to the equator at high obliquity (Forget et al., 2006). The North Polar Layered Deposits are up to 2500m thick and may have formed in the last 5 Myr, implying a annual accumulation rate of 500 μm/yr (Phillips et al., 2008). They contain up to 5 percent ice, and dust–rich layers are shown by radar (Grima et al., 2009). North polar linear dunes show strong evidence for induration by ice (Schatz et al., 2006). Southern hemisphere sand dunes develop aprons and become increasingly dissected approaching the pole because of ground ice pinning (Fenton and Hayward, 2010). Theory predicts that ice cannot endure at low latitudes (Mellon and Jakosky, 1995). Moats marking the past location of glaciers equatorward of 30° support this theory (Hauber et al., 2008). The low (<30°) latitudes are also where all almost all the sedimentary rocks are found (Chapter 4), so ice pinning cannot be the solution for sedimentary rock formation.

Cementation by aqueous minerals can lithify atmospherically-transported sediment indefinitely. Spirit found shallow subsurface layers (crusts and clods) of sulfate at the Troy site that apparently formed by downward transport of soluble elements (Arvidson et al., 2010). Crusts in the soil were also found by Opportunity. The young crater retention age of Troy suggests that these are $< 10^7$ Ma old [Raymond E. Arvidson, via email]. One Earth year of monitoring of nearby sulfate-rich crusts exhumed by rover trenching showed no evidence that the mineralogy of these crusts was altered by exchange of vapor with today's dry equatorial atmosphere (Rice et al., 2011). Because exhumation of the crusts placed them out of equilibrium, the timescale for destruction (and formation?) of crusts is much longer than one Earth year. Sulfate crust formation is not understood. However, the crusts are not load

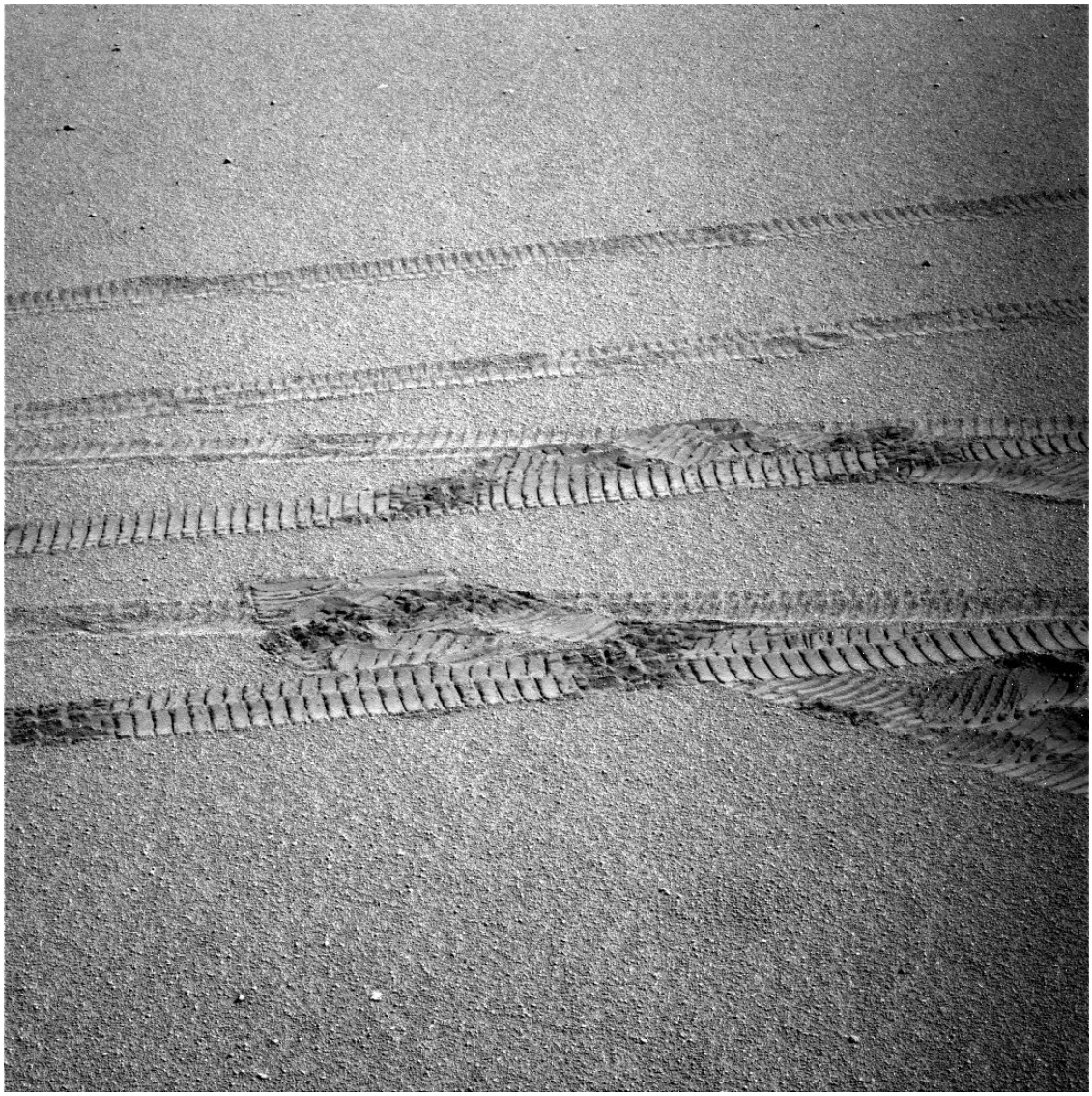

Figure 7.1 Rapid erasure of Mars rover tracks shows high rate of present-day aeolian transport Mars Exploration Rover Pancam image 1P275290377EFF90SPP2352R1C1 (436nm-centered filter). The image was taken on Opportunity's ascent out of Victoria Crater in September 2008 (Mars Year 29, $Ls = 131$, aphelion season). The uppermost, crisp-appearing tracks date from the descent 1.01 Earth years prior (Mars Year 28, $L_s = 311$). The older, faded tracks are 1.93 years old (Mars Year 28 $Ls \sim 113$). They predate the Mars Year 28 dust storm season ($L_s \approx 180$–330.) *NASA/JPL/Cornell.*

bearing (Spirit broke through one, fatally) and have lower strength than the much older cliff-forming sedimentary rocks. Opportunity found that the cliff-forming sedimentary rocks at Meridiani Planum are aqueously cemented (McLennan and Grotzinger, 2008). Multiple lines of evidence indicate that weathering was water limited and at low water-rock ratio (Berger et al., 2009). Valles Marineris interior layered deposits also show sulfate, with resistant hematite grains apparently forming lag deposits downslope, suggesting that sedimentary rocks in Valles are also aqueously cemented (Bibring et al., 2007). Snowmelt is an obvious candidate water source for water-limited, low water-rock ratio cementation (Chapter 4).

Melting on flat surfaces requires orbital conditions and atmospheric pressure different from the present day. Evaporitic cooling prevents melting in the current climate. Exceptions require low albedo, steep slopes, or both (Morgan et al., 2010). For flat-lying surfaces and the albedo of Mars' dust continents (0.28, Mellon et al. (2000)), we find that the distribution of sedimentary rocks on Mars best correlates with a background climate ($O(10^2)$ mbar CO_2) that was usually globally dry and only allowed melting during unusual orbital conditions. Significant overland flow would occur for an even narrower range of orbital parameters (we do not model percolation of meltwater and runoff generation). The best-fit model produces many years of marginal snowmelt for every year of significant surface runoff: this accounts for the evidence for relatively gentle reworking of the aeolian material rocks by rivers: there are few unconformities. Gale's mound shows only a few fluvial canyons and depositional fans, but many aeolian yardangs (Anderson and Bell, 2010).

High obliquity and moderately higher atmospheric pressure are necessary for melting on flat surfaces, but also greatly increase atmospheric ability to transport sediment. Global average surface wind stress increases as $P^{(2/3)}$, where P is atmospheric pressure [based on simulation output provided by Melinda A. Kahre, via email], and aeolian sediment transport increases with surface wind stress (Newman et al., 2005). The extremely strong present-day dependence of dust transport on P is shown by the numerous dust-devil streaks on the floor of low-elevation craters. Because of resupply of atmospherically-transported sediment during dry intervals, fluvial erosion fed by snowmelt during unusual orbital optima would have been transport limited. Ultimately, the supply of fine-grained material to the Mars system is limited by comminution of impact ejecta and volcanic ash (Goetz et al., 2010).

7.1.2 Future observations and tests

This section describes future work to extend and test the ideas in Chapters 2–4.

Discriminating top-down versus bottom-up water sources for sedimentary rock formation:

Chapter 4 identifies and trials a snowmelt framework for mapping between paleoclimate and past melt rates. This framework can be tested, and if successful, used to reconstruct (wet-pass filtered) climate over the Hesperian and Amazonian. This requires a shift from global

models to climate reconstruction using a sequence of well-dated watershed-scale natural laboratories. Similarly, archaeologists shift from survey to excavation phase once key sites have been identified. Inverted rivers and meander belts in the Gale-Aeolis-Zephyria region (Burr et al., 2009, 2010) allow an immediate test of the snowmelt hypothesis. These rivers are up to 10^3 km long – the longest on Mars – and have been tentatively correlated with the lower Gale mound. River long profiles run both up and downhill, suggesting that thick ice bodies were present at or near the surface when the rivers formed. If other indicators support the presence of thick ice bodies when the rivers formed, this would be a key constraint requiring long-term mean surface temperature <273K when the rivers formed, ruling out global groundwater upwelling as a source for the river discharge, disfavoring rainfall and supporting snowmelt.

Preliminary discharge estimates from hydraulic geometry have already been made for 15 watersheds by Irwin et al. (2005b). Ideal sites for relating a paleodischarge rate to a snowmelt generation rate are well-dated, have 1m-per-pixel DTMs that resolve channel depth, have a well-constrained paleo-watershed, involve multiple adjacent watersheds (for reproducibility) and have lower-resolution DTMs for watershed context. Currently understudied sites with well-preserved channels and watersheds include Southwest Melas Chasma (Metz et al., 2009a), Lyot and the Acheron supraglacial channels. The Dorsa Argentea Formation and Gale-Aeolis-Zephyria do not have well-defined paleo-watersheds, but are uniquely well-preserved and so are important enough to try anyway. For eskers, basal melting water source is a plausible alternative water source to surficial melt. Key uncertainties in this work are relating hydraulic geometry to discharge (Montgomery and Gran, 2001; Finnegan et al., 2005), and partitioning of snowmelt between refreezing and runoff (Dunne et al., 1976; Marsh and Woo, 1984). The aim is to provide lower limits on differences from the present day.

Data from the Antarctic Dry Valleys could be used to benchmark the snowmelt model. 2m-resolution DTMs are available, along with discharge estimates from the McMurdo Long-Term Ecological Research (LTER) study (McKnight, 2011). Chemical weathering rates in the endorheic zone have been measured and are remarkably high given the brief wet season (Nezat et al., 2001).

The locations of interannually-persistent snow track orbital forcing (Chapter 3), but ice area lags orbital forcing. Rapid changes in insolation at a site can cause ice melting. I hypothesize that melting of out-of-orbital-equilibrium ice led to relatively young ($\sim$3.0 Ga, (Grant and Wilson, 2011)) alluvial fans on Mars (and perhaps the delta at Eberswalde, Malin and Edgett (2003)). On a smaller scale, melting of out-of-orbital-equilibrium ice may have formed the gullies in the last few Ma (Head et al., 2008). The largest alluvial fans are clustered at low elevations in the 20-25S latitude band (Kraal et al., 2008a), suggesting an insolation control. An ice melting model requires an ensemble of orbital forcing data that accurately characterizes the pdf in the rate-of-change of insolation over many Gya. These exist (Laskar et al., 2004), but are not publicly available.

Exploiting Gale: inverting 3D stratigraphy for the rules of mound growth and destruction:

The growth and destruction of intra-canyon mounds and intra-crater mounds (like the one in Gale targeted by Mars Science Laboratory) is the central problem in Mars sedimentary geology. The present-day deflation surface is clearly shaped by the wind, but the processes which grew the mound (and eroded earlier versions of it) are unknown.

Most of Earth's land area is shaped by hillslope processes and fluvial transport. Geomorphic transport laws have been developed for these processes (Dietrich, 2003). As a first step for doing the same for Mars, we seek to use the 3D stratigraphy of Mars mounds to constrain kinematic (not necessarily physically based) growth and destruction rules. The goal is a predictive model for layer orientation and mound cross-sectional profile, similar to those used by the petroleum industry to model accumulation and erosion of deltas.

A reasonable starting point is to assume (1) that the growth process is a function of elevation only, and (2) that material is removed by katabatic winds. The first idealization is acceptable because we do not know the dominant processes in accumulating and cementing the material that forms the Mars mounds, and elevation dependence constrains process. For example, evaporites form preferentially in local lows, fallout of ash transported through the stratosphere is independent of elevation, and ice tends to accumulate on regional high ground if the atmospheric density is high. Yardangs, dunes and wind streaks show that aeolian erosion of Mars mounds is ongoing, and most of the ancient stratigraphic section examined by the Opportunity rover was transported by the wind (Hayes et al., 2011). Unconformities are rarely seen in exposures of Mars mound layers. This suggests that fluvial erosion was not the dominant process during mound construction, because fluvial erosion is by definition channelized and so produces small–scale angular unconformities that are relatively easy to detect.

Upcoming observations by MSL can test this model by providing sedimentary evidence for transport processes at Gale. For example, the orientation of aeolian cross-bedding relative to layer orientations would provide evidence for whether or not ancient winds blowed downslope (or if layer orientations have been modified by tectonics).

Impact induced "fluvial" geomorphology:

There are three types of "fluvial" geomorphology that are concentrated in Noachian Mars. Two could be the result of local impacts into ice-rich crust :-

- Equatorward of 38°-40°, **shallow crater floors and muted rims** are only found for ancient craters. Younger craters are deeper, and there is a bimodal distribution of crater depth/diameter ratio (Forsberg-Taylor et al., 2004). Shallow crater floors appear in simulations of impacts into layered ice-rock targets, due to resurge of the weak ice layers during transient-cavity collapse (Senft and Stewart, 2008). Almost all crater floors poleward of 38°-40° on Mars today are shallow (Robbins, 2011). This is

consistent with ground ice persisting at high latitudes but not at low latitudes (so that resurge of weak ice layers occurs at high latitudes but not low latitudes in the present epoch). It is also consistent with high-latitude glacial erosion/infilling.

- **Valleyed crater rims** could form in the hours to millennia after impact from plume rainout, ejecta dewatering, or impact-induced precipitation.
- **Dendritic valley networks** sometimes extend over thousands of km, forming inlet and exit breaches in large craters. Large liquid water volumes and regional extent cannot plausibly result from local impacts. Snowmelt, rainfall, or transient global greenhouses events (following major impacts) are alternatives.

The standard explanation for valleyed crater rims and shallow crater floors is fluvial infilling during a globally warm and wet early period on Mars (Craddock and Maxwell, 1990, 1993; Craddock et al., 1997; Craddock and Howard, 2002; Irwin et al., 2005a; Howard, 2007). How can the weak-early-crust hypothesis be tested against the fluvial infill hypothesis?

There are two attractive routes into the topic:
(1) *Using Mojave Crater as an young analog of impact-induced fluvial geomorphology on Early Mars.* The goal here is to determine the processes responsible for Mojave's alluvial fans (ejecta dewatering, impact plume rainout, or sustained impact-induced precipitation), their relative timing, the sediment, water and energy budgets of fluvial processes triggered by the Mojave impact, and the fraction of Mojave impact energy that contributed to fluvial transport. In ongoing work, we are using CTH hydrocode to set the initial conditions for MRAMS simulations of impact–induced precipitation. The output can then be compared to geologic observations.
(2a) *Comparing patterns in the ensemble of Mars crater radial profiles to predictions from fluvial infilling.* Icy moons have shallow-floored craters (Senft and Stewart, 2011) because water ice has a low yield strength. The trend seen on Early Mars craters is "icelike." To satisfy mass balance, fluvial infilling requires crater diameters to expand to supply material for floor infilling. This prediction can be tested where crater rims intersect. Impact simulations and fluvial-infill simulations predict different trends in radial profile with diameter, which can be tested against Mars Orbiter Laser Altimeter (MOLA) data.
(2b) *Comparing morphometric trends in HRSC DTMs of crater rims to predictions from simulations of impact induced precipitation.* Shocked-rock temperature increases more rapidly with impactor diameter than does crater diameter, so there is a threshold crater size for snow melting at the rim. Fluvial incision many millennia after impact does not have this threshold, so the presence or absence of a strong dependence of rim fluvial erosion on crater diameter is a good test for impact-induced fluvial geomorphology.

If Noachian craters are shallow because the crust was icy, then this ice must have been lost in order to produce the modern, "lunar" craters. Therefore, a requirement of the weak-early-crust hypothesis is a mechanism for rapid escape to space of a crustal water reservoir around the late Noachian/early Hesperian. Rapid desiccation of the crust is observed in models

(Grimm and Painter, 2009). The Mars Atmosphere Volatile Evolution Mission (MAVEN) will measure present day water loss rates, helping to determine whether rapid early water loss is possible.

Impact-induced geomorphology is important independent of the Early Mars climate problem: impacts, together with the rapid early differentiation that is enabled by impact energy, are the fundamental processes in planetary science. Dwarf planet Ceres will be orbited by the Dawn spacecraft in 2015, and may have a mixed ice-rock crust (McCord et al., 2011). If Ceres does have a mixed ice-rock crust, then the weak-early-crust hypothesis predicts that it should have shallow-floored craters.

Summary: Early Mars

The research agenda described above could test the following scenario:

> At the beginning of the stratigraphically coherent Martian geological record, the planet has an ice-rich crust and atmospheric pressure 0.1-1 bars. Most years, temperatures are below freezing year round. Impacts strike ice-rich crust and produce transient runoff. The area around the transient cavity contains warm ice and hot rock, and this combination produces lahars which infill the crater floor and reduce the topography of the crater rims. In addition to these local effects, the higher atmospheric pressure pressure-broadens the H_2O lines and prolongs rare impact greenhouse events triggered by large impacts. Regionally-integrated valley networks are carved by snowmelt and perhaps limited rainfall. High ground is favored for snow, so most valleys form on high ground. Water is lost through hydrogen escape, and the planet is acidified and desiccated (Hurowitz et al., 2010). Fractional surface area with thick ice declines, so fewer impacts involve enough water to produce geomorphically effective runoff. Impact-produced vapor becomes the exception. Carbon escape is slower. Subsequently, unusual orbital conditions allow continued melting, but only at low elevations and low latitudes, or on steep slopes. Aqueous weathering and carbonate formation reduces pCO_2. Minimalist explanations for Mars' observed valley networks and aqueous minerals are suggested by the record of aqueous alteration (Ehlmann et al., 2011), which is mainly a record of subsurface clay formation. There is little room in this scenario for feedback-stabilized, clement climates.
>
> Wet events on Mars involved rare perturbations - impacts, eruptions, or unusual orbital conditions. The decline in wet activity recorded by Mars stratigraphy results from secular atmospheric escape of water and carbon. This reduced the ability of the rare perturbations to produce wet events.

This scenario makes no claims about whether Mars could have once hosted life. Snowmelt-limited formation of sedimentary rocks under unusual orbital conditions is not favorable for life or for the preservation of organic carbon. The cumulative duration of wet intervals

may have been <1% of the Late Noachian/Hesperian (Lewis et al., 2010), and the surface would have been triply sterilized (by low temperatures, high ultraviolet fluxes, and high energy particles) between rare wet intervals. However, environments earlier than the oldest stratigraphy that can be reconstructed from orbit ("pre-Noachian") are not part of the scenario. Fragments of more ancient aqueous environments are preserved in megabreccia and in the Nili Fossae, and could be inspected by future missions.

Disfavoring organic carbon preservation in the stratigraphically coherent record of sedimentary rocks does seriously reduce the expected information content of Mars for astrobiology. A negative result from a returned sample of megabreccia contains little information – there could be biological evidence in the next breccia block. It would be very hard to generalize without stratigraphic context, because water moves slowly through rocks. Because a negative result from a Mars astrobiology mission to the pre-Noachian would be uninformative, any such mission would be a gamble on a positive result. This should be contrasted with Europa, where a syringefull of ocean water would all but resolve the life question for the whole moon. A negative result from Europa would be very constraining on the probability $P(o|h)$, where o is an origin of life and h is a habitable environment

7.2 Exoplanets

Characterizing true Earth analogs (habitable zone rocky planets orbiting G-type stars) is a technological jump away. Even the James Webb Space Telescope (JWST) is only marginally capable of characterizing the atmospheres of habitable-zone planets (Postman et al., 2010). Near-term efforts focus on close-in planets (Gaidos et al., 2007). Cost overruns have delayed the launch of the capable JWST to 2018, or later. The pathway to finding more rocky planets runs through small "spotter" telescopes such as TESS (Deming et al., 2009). Other telescopes are only marginally able to characterize rocky exoplanets (unless they have thick low-molecular-weight atmospheres, which makes them less interesting to geologists). Seven years wait for a capable telescope is plenty of time for reflection. Theoretical studies could focus on the effect of gross climate parameters (such as temperature, pressure) on planetary surface properties (such as wind speed). This could have broader impacts on our understanding of the fundamentals of Earth's general circulation.

Very hot rocky planets are an attractive short-term target. They are known to be common, to frequently transit, and to have much higher signal:noise on secondary eclipse than true Earths (Gaidos et al., 2007). At least two, Kepler-10b and CoRoT-7b, are close enough to their star to develop magma ponds centered on the substellar point. Ground-clearing work has been done on the composition and radiative-equilibrium radius of these magma ponds (Léger et al., 2011; Castan and Menou, 2011; Rouan et al., 2011), but no work has been done on substellar magma pond dynamics. Horizontal convection (Hughes and Griffiths, 2008) must drive flow away from the substellar point, with downwelling at the pond edges. Peridotite viscosity is 10^{-1} Pa s at 1850K (Dingwell et al., 2004), so viscous forces

are negligible compared to rotational and inertial forces above the liquidus. The Rossby and Ekman numbers of a substellar magma vortex are comparable to Earth's oceans. To be detectable, the magmatic circulation must affect the surface temperature distribution across the planet's surface. An attractive target for future work is to determine how fast the magma must circulate to be detectable. A self-consistent model of the magma flow is a longer-term goal.

7.3 Climate stability science and technology

Although we have not even finished checking the Solar System for non-Earth life, there is already have enough information to make "life is extremely rare" our null hypothesis. The anthropic principle deletes the Copernican assumption. Earth-radius planets are common but galaxy-modifying civilizations do not exist: there must be a great filter (Bostrom, 2008), and the origin of life is a good candidate location for this filter. Chondritic meteorites sample asteroid parent bodies. Large asteroids conduct natural experiments in the origin-of-life: early hydrothermal systems with 1% organic matter, abundant chemical energy, and millions of years of water flow. But chondritic meteorites lack life, so either the origin of life is not easy even given the right conditions, or it requires a habitable surface interface. Mars' surface shows little evidence for prolonged habitable conditions (Ehlmann et al., 2011). Fifty years of failure to make life *de novo* (Conway Morris, 2003) also suggests life is rare: while the timescales and volumes in life-creation experiments are smaller than in Nature, the temperatures and concentrations of prebiotic molecules have been optimized for life. The early emergence of life on Earth is not strong evidence that the origin of life is easy (Spiegel and Turner, 2011). There is no reason to believe that simple life is widespread in the universe. Carter's anthropic argument suggests complex life will be extraordinarily more rare than simple life (Carter, 1983). It would not be a good null hypothesis to assume that life exists anywhere in the Universe beyond Earth. The longer that searches continue to return negative results, the more probable it is that Earth life has already survived the great filter, and that it is up to us to extend life beyond Earth.

Ongoing exploration could upend this null hypothesis. For example, we currently have no samples from ice-covered oceans (Hand et al., 2009). Three outcomes are possible from our exploration of the Solar System and nearby stars: -

– **Sterile**: All nearby planets require large adjustments to establish Earth-derived life.
If so, the problem of extending life beyond Earth could be safely delegated to our grandchildren.
– **Fallow**: All or nearly all habitable planets lack any sign of life.
In some cases, a small adjustment to the environment, on the planetary scale, would allow Earth-derived life to take root there. Mars is a nearby example of a fallow planet.
– **Fertile**: All habitable planets show signs of life. This would motivate development of

interstellar propulsion (Marcy, 2011).

Mars is the obvious first planet to modify in order to allow life to establish itself ("terraform"). We do not understand Mars well enough to know exactly what would be needed to establish life there. No technical showstoppers are known (Gerstell et al., 2001; Marinova et al., 2005; Osterloo et al., 2008, 2010; Phillips et al., 2011), and an improved understanding of the changes needed to establish life on Mars is a corollary of ongoing exploration (Phillips et al., 2011). Objections to terraforming include supposed great expense, unproven feasibility, a perceived need to prove that Mars does not have life before introducing Earth–derived life ("planetary protection"), and misplaced priorities / opportunity costs. Infrastructure commitments made over the last ten years make clear that anthropogenic climate change in our lifetime will not be mitigated by emissions reductions (McKinsey, 2009; Pielke, 2011; Gardiner, 2011; PriceWaterhouseCoopers, 2011), unless unexpected technological or political change occurs. If anthropogenic climate change turns out to be a serious problem, the alternative to emissions reductions is some mix of adaptation, reparations, and geoengineering (Crutzen, 2006; Salter et al., 2008; Caldeira and Wood, 2008; MacMynowski, 2009; Ban-Weiss and Caldeira, 2010). Geoengineering, if used successfully, would remove most of the concerns about terraforming Mars.

Bibliography

D. S. Abbot and E. R. Switzer. The Steppenwolf: A Proposal for a Habitable Planet in Interstellar Space. *Astrophysical Journal Letters*, 735, 2011. doi: 10.1088/2041-8205/735/2/L27.

J. C. Afonso, G. Ranalli, and M. Fernàndez. Density structure and buoyancy of the oceanic lithosphere revisited. *Geophysical Research Letters*, 341:L10302, 2007. doi: 10.1029/2007GL029515.

C. B. Agee. Crystal-liquid density inversions in terrestrial and lunar magmas. *Physics of the Earth and Planetary Interiors*, 107:63–74, 1998. doi: 10.1016/S0031-9201(97)00124-6.

C. B. Agnor and D. N. C. Lin. On the Migration of Jupiter and Saturn: Constraints from Linear Models of Secular Resonant Coupling with the Terrestrial Planets. *ArXiv e-prints*, 2011.

O. Aharonson, M. T. Zuber, D. H. Rothman, N. Schorghofer, and K. X. Whipple. Drainage basins and channel incision on Mars. *Proceedings of the National Academy of Science*, 99:1780–1783, 2002. doi: 10.1073/pnas.261704198.

R. Amundson, S. Ewing, W. Dietrich, B. Sutter, J. Owen, O. Chadwick, K. Nishiizumi, M. Walvoord, and C. McKay. On the in situ aqueous alteration of soils on Mars. *Geochimica et Cosmochimica Acta*, 72: 3845–3864, 2008. doi: 10.1016/j.gca.2008.04.038.

E. Anders and N. Grevesse. Abundances of the elements - Meteoritic and solar. *Geochimica et Cosmochimica Acta*, 53:197–214, 1989. doi: 10.1016/0016-7037(89)90286-X.

R. B. Anderson and J. F. Bell, III. Geologic mapping and characterization of Gale Crater and implications for its potential as a Mars Science Laboratory landing site. *International Journal of Mars Science and Exploration*, 5:76–128, 2010. doi: 10.1555/mars.2010.0004.

J. C. Andrews-Hanna and K. W. Lewis. Early Mars hydrology: 2. Hydrological evolution in the Noachian and Hesperian epochs. *Journal of Geophysical Research (Planets)*, 116:E02007, 2011. doi: 10.1029/2010JE003709.

J. C. Andrews-Hanna and R. J. Phillips. Hydrological modeling of outflow channels and chaos regions on Mars. *Journal of Geophysical Research (Planets)*, 112:E08001, 2007. doi: 10.1029/2006JE002881.

J. C. Andrews-Hanna, R. J. Phillips, and M. T. Zuber. Meridiani Planum and the global hydrology of Mars. *Nature*, 446:163–166, March 2007. doi: 10.1038/nature05594.

K. Apps, K. I. Clubb, D. A. Fischer, E. Gaidos, A. Howard, J. A. Johnson, G. W. Marcy, H. Isaacson, M. J. Giguere, J. A. Valenti, V. Rodriguez, C. Chubak, and S. Lepine. M2K: I. A Jupiter-Mass Planet Orbiting the M3V Star HIP 79431. *Publications of the Astronomical Society of the Pacific*, 122:156–161, 2010. doi: 10.1086/651058.

R. E. Arvidson, E. Guinness, and S. Lee. Differential aeolian redistribution rates on Mars. *Nature*, 278: 533–535, 1979. doi: 10.1038/278533a0.

R. E. Arvidson, J. F. Bell, P. Bellutta, N. A. Cabrol, J. G. Catalano, J. Cohen, L. S. Crumpler, D. J. Des Marais, T. A. Estlin, W. H. Farrand, R. Gellert, J. A. Grant, R. N. Greenberger, E. A. Guinness, K. E. Herkenhoff, J. A. Herman, K. D. Iagnemma, J. R. Johnson, G. Klingelhöfer, R. Li, K. A. Lichtenberg, S. A. Maxwell, D. W. Ming, R. V. Morris, M. S. Rice, S. W. Ruff, A. Shaw, K. L. Siebach, P. A. de Souza, A. W. Stroupe, S. W. Squyres, R. J. Sullivan, K. P. Talley, J. A. Townsend, A. Wang, J. R. Wright, and A. S. Yen. Spirit Mars Rover Mission: Overview and selected results from the northern Home Plate Winter Haven to the side of Scamander crater. *Journal of Geophysical Research (Planets)*, 115:E00F03, 2010. doi: 10.1029/2010JE003633.

J. N. Bahcall, M. H. Pinsonneault, and S. Basu. Solar Models: Current Epoch and Time Dependences, Neutrinos, and Helioseismological Properties. *Astrophysical Journal*, 555:990–1012, 2001. doi: 10.1086/321493.

V. R. Baker. Water and the Martian landscape. *Nature*, 412:228–236, 2001.

V. R. Baker, R. G. Strom, V. C. Gulick, J. S. Kargel, and G. Komatsu. Ancient oceans, ice sheets and the hydrological cycle on Mars. *Nature*, 352:589–594, 1991. doi: 10.1038/352589a0.

G.A. Ban-Weiss and K. Caldeira. Geoengineering as an optimization problem. *Environmental Research Letters*, 5(3), 2010. ISSN 1748-9326. doi: 10.1088/1748-9326/5/3/034009.

J. L. Bandfield, T. D. Glotch, and P. R. Christensen. Spectroscopic Identification of Carbonate Minerals in the Martian Dust. *Science*, 301:1084–1087, 2003. doi: 10.1126/science.1088054.

J. L. Bandfield, A. Deanne Rogers, and C. S. Edwards. The role of aqueous alteration in the formation of martian soils. *Icarus*, 211:157–171, 2011. doi: 10.1016/j.icarus.2010.08.028.

S. Barabash, A. Fedorov, R. Lundin, and J.-A. Sauvaud. Martian Atmospheric Erosion Rates. *Science*, 315: 501–, 2007. doi: 10.1126/science.1134358.

A. S. Bargery and L. Wilson. Dynamics of the ascent and eruption of water containing dissolved CO_2 on Mars. *Journal of Geophysical Research (Planets)*, 115:E05008, 2010. doi: 10.1029/2009JE003403.

C. J. Barnhart and F. Nimmo. Role of impact excavation in distributing clays over Noachian surfaces. *Journal of Geophysical Research (Planets)*, 116:E01009, January 2011.

C. J. Barnhart, A. D. Howard, and J. M. Moore. Long-term precipitation and late-stage valley network formation: Landform simulations of Parana Basin, Mars. *Journal of Geophysical Research (Planets)*, 114: E01003, 2009. doi: 10.1029/2008JE003122.

N. M. Batalha, W. J. Borucki, S. T. Bryson, L. A. Buchhave, D. A. Caldwell, J. Christensen-Dalsgaard, D. Ciardi, E. W. Dunham, F. Fressin, T. N. Gautier, III, R. L. Gilliland, M. R. Haas, S. B. Howell, J. M. Jenkins, H. Kjeldsen, D. G. Koch, D. W. Latham, J. J. Lissauer, G. W. Marcy, J. F. Rowe, D. D. Sasselov, S. Seager, J. H. Steffen, G. Torres, G. S. Basri, T. M. Brown, D. Charbonneau, J. Christiansen, B. Clarke, W. D. Cochran, A. Dupree, D. C. Fabrycky, D. Fischer, E. B. Ford, J. Fortney, F. R. Girouard, M. J. Holman, J. Johnson, H. Isaacson, T. C. Klaus, P. Machalek, A. V. Moorehead, R. C. Morehead, D. Ragozzine, P. Tenenbaum, J. Twicken, S. Quinn, J. VanCleve, L. M. Walkowicz, W. F. Welsh, E. Devore, and A. Gould. Kepler's First Rocky Planet: Kepler-10b. *Astrophysical Journal*, 729:27, 2011.

J. L. Bean, E. Miller-Ricci Kempton, and D. Homeier. A ground-based transmission spectrum of the super-Earth exoplanet GJ 1214b. *Nature*, 468:669–672, 2010a. doi: 10.1038/Nature09596.

J. L. Bean, A. Seifahrt, H. Hartman, H. Nilsson, G. Wiedemann, A. Reiners, S. Dreizler, and T. J. Henry. The CRIRES Search for Planets Around the Lowest-mass Stars. I. High-precision Near-infrared Radial Velocities with an Ammonia Gas Cell. *Astrophysical Journal*, 713:410–422, 2010b. doi: 10.1088/0004-637X/713/1/410.

J. Bell, III. *The Martian Surface - Composition, Mineralogy, and Physical Properties*, volume 9 of *Cambridge Planetary Science Series*. Cambridge University Press, 2008.

G. Berger, M. J. Toplis, E. Treguier, C. D'Uston, and P. Pinet. Evidence in favor of small amounts of ephemeral and transient water during alteration at Meridiani Planum, Mars. *American Mineralogist*, 94: 1279–1282, 2009.

RA Berner and Z Kothavala. GEOCARB III: A revised model of atmospheric CO_2 over phanerozoic time. *American Journal of Science*, 301(2):182–204, 2001.

M. G. Best and E. H. Christiansen. *Igneous Petrology (Oxford: Wiley-Blackwell)*. 2001.

J.-P. Bibring, R. E. Arvidson, A. Gendrin, B. Gondet, Y. Langevin, S. Le Mouelic, N. Mangold, R. V. Morris, J. F. Mustard, F. Poulet, C. Quantin, and C. Sotin. Coupled Ferric Oxides and Sulfates on the Martian Surface. *Science*, 317:1206–, 2007. doi: 10.1126/science.1144174.

J.P. Bibring, Y. Langevin, J. F. Mustard, F. Poulet, R. Arvidson, A. Gendrin, B. Gondet, N. Mangold, P. Pinet, and F. Forget. Global Mineralogical and Aqueous Mars History Derived from OMEGA/Mars Express Data. *Science*, 312:400–404, 2006. doi: 10.1126/science.1122659.

M. J. Bickle. Metamorphic decarbonation, silicate weathering and the long-term carbon cycle. *Terra Nova*, 8:270, 1996.

J. L. Bishop, M. Parente, C. M. Weitz, E. Z. Noe Dobrea, L. H. Roach, S. L. Murchie, P. C. McGuire, N. K. McKeown, C. M. Rossi, A. J. Brown, W. M. Calvin, R. Milliken, and J. F. Mustard. Mineralogy of Juventae Chasma: Sulfates in the light-toned mounds, mafic minerals in the bedrock, and hydrated silica and hydroxylated ferric sulfate on the plateau. *Journal of Geophysical Research (Planets)*, 114:E00D09, 2009. doi: 10.1029/2009JE003352.

L. Borg and M. J. Drake. A review of meteorite evidence for the timing of magmatism and of surface or near-surface liquid water on Mars. *Journal of Geophysical Research (Planets)*, 110:E12S03, 2005. doi: 10.1029/2005JE002402.

N. Bostrom. Where are they? Why I hope the search for extraterrestrial life turns up nothing. *MIT Technology Review*, 111(3):72–77, 2008. ISSN 1099-274X.

N. Bostrom. *Anthropic Bias*. Routledge, 2010.

M. C. Bourke, K. S. Edgett, and B. A. Cantor. Recent aeolian dune change on Mars. *Geomorphology*, 94: 247–255, 2008. doi: 10.1016/j.geomorph.2007.05.012.

J. E. Box and K. Ski. Remote sounding of Greenland supraglacial melt lakes: implications for subglacial hydraulics. *Journal of Glaciology*, 53:257–265, 2007. doi: 10.3189/172756507782202883.

J. M. Boyce and H. Garbeil. Geometric relationships of pristine Martian complex impact craters, and their implications to Mars geologic history. *Geophysical Research Letters*, 341:L16201, 2007. doi: 10.1029/2007GL029731.

W. V. Boynton, W. C. Feldman, S. W. Squyres, T. H. Prettyman, J. Brückner, L. G. Evans, R. C. Reedy, R. Starr, J. R. Arnold, D. M. Drake, P. A. J. Englert, A. E. Metzger, I. Mitrofanov, J. I. Trombka, C. d'Uston, H. Wänke, O. Gasnault, D. K. Hamara, D. M. Janes, R. L. Marcialis, S. Maurice, I. Mikheeva, G. J. Taylor, R. Tokar, and C. Shinohara. Distribution of Hydrogen in the Near Surface of Mars: Evidence for Subsurface Ice Deposits. *Science*, 297:81–85, 2002. doi: 10.1126/science.1073722.

D. A. Brain and B. M. Jakosky. Atmospheric loss since the onset of the Martian geologic record: Combined role of impact erosion and sputtering. *Journal of Geophysical Research*, 1032:22689–22694, 1998. doi: 10.1029/98JE02074.

R. Brasser and K. J. Walsh. Stability analysis of the martian obliquity during the Noachian era. *Icarus*, 213:423–427, 2011. doi: 10.1016/j.icarus.2011.02.024.

N. T. Bridges, M. E. Banks, R. A. Beyer, F. C. Chuang, E. Z. Noe Dobrea, K. E. Herkenhoff, L. P. Keszthelyi, K. E. Fishbaugh, A. S. McEwen, T. I. Michaels, B. J. Thomson, and J. J. Wray. Aeolian bedforms, yardangs, and indurated surfaces in the Tharsis Montes as seen by the HiRISE Camera: Evidence for dust aggregates. *Icarus*, 205:165–182, 2010. doi: 10.1016/j.icarus.2009.05.017.

B. W. Brock, I. C. Willis, and M. J. Sharp. Measurement and parameterization of aerodynamic roughness length variations at Haut Glacier d'Arolla, Switzerland. *Journal of Glaciology*, 52:281–297, 2006. doi: 10.3189/172756506781828746.

K. Bucher and M. Frey. *Petrogenesis of Metamorphic Rocks, 7th ed.* Berlin: Springer, 2002.

E. M. Burbidge, G. R. Burbidge, W. A. Fowler, and F. Hoyle. Synthesis of the Elements in Stars. *Reviews of Modern Physics*, 29:547–650, 1957. doi: 10.1103/RevModPhys.29.547.

D. M. Burr, M.-T. Enga, R. M. E. Williams, J. R. Zimbelman, A. D. Howard, and T. A. Brennand. Pervasive aqueous paleoflow features in the Aeolis/Zephyria Plana region, Mars. *Icarus*, 200:52–76, 2009. doi: 10.1016/j.icarus.2008.10.014.

D. M. Burr, R. M. E. Williams, K. D. Wendell, M. Chojnacki, and J. P. Emery. Inverted fluvial features in the Aeolis/Zephyria Plana region, Mars: Formation mechanism and initial paleodischarge estimates. *Journal of Geophysical Research (Planets)*, 115:E07011, 2010. doi: 10.1029/2009JE003496.

N.J. Butterfield. Macroevolution and macroecology through deep time. *Palaeontology*, 50(Part 1):41–55, 2007.

M. Běhounková, G. Tobie, G. Choblet, and O. Čadek. Coupling mantle convection and tidal dissipation: Applications to Enceladus and Earth-like planets. *Journal of Geophysical Research (Planets)*, 115:E09011, 2010. doi: 10.1029/2009JE003564.

M. Běhounková, G. Tobie, G. Choblet, and O. Čadek. Tidally Induced Thermal Runaways on Extrasolar Earths: Impact on Habitability. *Astrophysical Journal*, 728:89, 2011. doi: 10.1088/0004-637X/728/2/89.

K. Caldeira and L. Wood. Global and Arctic climate engineering: numerical model studies. *Royal Society of London Philosophical Transactions Series A*, 366:4039–4056, 2008. doi: 10.1098/rsta.2008.0132.

I. H. Campbell and S. R. Taylor. No water, no granites – no oceans, no continents. *Geophysical Research Letters*, 10:1061–1064, 1983. doi: 10.1029/GL010i011p01061.

R. L. Carlson and C. N. Herrick. Densities and porosities in the oceanic crust and their variations with depth and age. *Journal of Geophysical Research*, 95:9153–9170, 1990. doi: 10.1029/JB095iB06p09153.

M. H. Carr. The Martain drainage system and the origin of valley networks and fretted channels. *Journal of Geophysical Research*, 100:7479–7507, 1995. doi: 10.1029/95JE00260.

M. H. Carr and J. W. Head. Basal melting of snow on early Mars: A possible origin of some valley networks. *Geophysical Research Letters*, 30:2245, 2003a. doi: 10.1029/2003GL018575.

M. H. Carr and J. W. Head. Oceans on Mars: An assessment of the observational evidence and possible fate. *Journal of Geophysical Research (Planets)*, 108:5042, 2003b. doi: 10.1029/2002JE001963.

M. H. Carr and J. W. Head. Geologic history of Mars. *Earth and Planetary Science Letters*, 294:185–203, 2010. doi: 10.1016/j.epsl.2009.06.042.

M. H. Carr and M. C. Malin. Meter-Scale Characteristics of Martian Channels and Valleys. *Icarus*, 146: 366–386, 2000. doi: 10.1006/icar.2000.6428.

SB Carroll. Chance and necessity: the evolution of morphological complexity and diversity. *Nature*, 409 (6823):1102–1109, 2001.

B. Carter. The anthropic principle and its implications for biological evolution. *Philosophical Transactions of the Royal Society of London A*, 310:347–363, 1983.

W. S. Cassata, D. L. Shuster, P. R. Renne, and B. P. Weiss. Evidence for shock heating and constraints on Martian surface temperatures revealed by $^{40}Ar/^{39}Ar$ thermochronometry of Martian meteorites. *Geochimica et Cosmochimica Acta*, 74:6900–6920, 2010.

T. Castan and K. Menou. Atmospheres of Hot Super-Earths. *ArXiv e-prints*, 2011.

D. C. Catling, S. E. Wood, C. Leovy, D. R. Montgomery, H. M. Greenberg, C. R. Glein, and J. M. Moore. Light-toned layered deposits in Juventae Chasma, Mars. *Icarus*, 181:26–51, 2006. doi: 10.1016/j.icarus.2005.10.020.

G. Cescutti. An inhomogeneous model for the Galactic halo: a possible explanation for the spread observed in s- and r-process elements. *Astronomy and Astrophysics*, 481:691–699, 2008. doi: 10.1051/0004-6361:20078571.

M. G. Chapman, G. Neukum, A. Dumke, G. Michael, S. van Gasselt, T. Kneissl, W. Zuschneid, E. Hauber, V. Ansan, N. Mangold, and P. Masson. Noachian-Hesperian geologic history of the Echus Chasma and Kasei Valles system on Mars: New data and interpretations. *Earth and Planetary Science Letters*, 294: 256–271, 2010a. doi: 10.1016/j.epsl.2009.11.032.

M. G. Chapman, G. Neukum, A. Dumke, G. Michael, S. van Gasselt, T. Kneissl, W. Zuschneid, E. Hauber, and N. Mangold. Amazonian geologic history of the Echus Chasma and Kasei Valles system on Mars: New data and interpretations. *Earth and Planetary Science Letters*, 294:238–255, 2010b. doi: 10.1016/j.epsl.2009.11.034.

D. Charbonneau, Z.K. Berta, J. Irwin, C.J. Burke, P. Nutzman, L.A. Buchhave, C. Lovis, X. Bonfils, D.W. Latham, S. Udry, R.A. Murray-Clay, M.J. Holman, E.E. Falco, J.N. Winn, D. Queloz, F. Pepe, M. Mayor, X. Delfosse, and T. Forveille. A super-Earth transiting a nearby low-mass star. *Nature*, 462(7275):891–894, 2009. ISSN 0028-0836. doi: 10.1038/Nature08679.

Z. Chen, J. Zhang, Y. Chen, W. Cui, and B. Zhang. The Yields of r-Process Elements and Chemical Evolution of the Galaxy. *Astrophysical Journal Supplement Series*, 306:33–39, 2006. doi: 10.1007/s10509-006-9229-2.

J. D. Chittenden, V. Chevrier, L. A. Roe, K. Bryson, R. Pilgrim, and D. W. G. Sears. Experimental study of the effect of wind on the stability of water ice on Mars. *Icarus*, 196:477–487, 2008. doi: 10.1016/j.icarus.2008.01.016.

M. Chojnacki, D. M. Burr, J. E. Moersch, and T. I. Michaels. Orbital observations of contemporary dune activity in Endeavor crater, Meridiani Planum, Mars. *Journal of Geophysical Research (Planets)*, 116: E00F19, 2011. doi: 10.1029/2010JE003675.

P. R. Christensen. Formation of recent martian gullies through melting of extensive water-rich snow deposits. *Nature*, 422:45–48, 2003.

R. T. Clancy, M. J. Wolff, B. A. Cantor, M. C. Malin, and T. I. Michaels. Valles Marineris cloud trails. *Journal of Geophysical Research (Planets)*, 114:E11002, 2009. doi: 10.1029/2008JE003323.

M Cloos. Lithospheric Buoyancy and Collisional Orogenesis. *Geological Society of America Bulletin*, 105(6): 715–737, 1993.

G. D. Clow. Generation of liquid water on Mars through the melting of a dusty snowpack. *Icarus*, 72:95–127, 1987. doi: 10.1016/0019-1035(87)90123-0.

G. D. Clow. Minimum Discharge Rates Required for Sustained Water Flow on the Martian Surface. In *Lunar and Planetary Institute Science Conference Abstracts*, volume 25 of *Lunar and Planetary Institute Science Conference Abstracts*, page 275, 1994.

G. D. Clow and R. M. Haberle. Free Convection in the Martian Atmosphere. In *Lunar and Planetary Institute Science Conference Abstracts*, volume 21 of *Lunar and Planetary Institute Science Conference Abstracts*, page 210, 1990.

A. S. Cohen, A. L. Coe, S. M. Harding, and L. Schwark. Osmium isotope evidence for the regulation of atmospheric CO_2 by continental weathering. *Geology*, 32:157, 2004. doi: 10.1130/G20158.1.

A. Colaprete and O. B. Toon. Carbon dioxide clouds in an early dense Martian atmosphere. *Journal of Geophysical Research (Planets)*, 108:5025, 2003. doi: 10.1029/2002JE001967.

A. Colaprete, O. B. Toon, and J. A. Magalhães. Cloud formation under Mars Pathfinder conditions. *Journal of Geophysical Research*, 104:9043–9054, 1999. doi: 10.1029/1998JE900018.

S. C. Colbeck. An Analysis of Water Flow in Dry Snow. *Water Resources Research*, 12:523–527, 1976. doi: 10.1029/WR012i003p00523.

N. M. Coleman and V. R. Baker. Evidence that a Paleolake Overflowed the Rim of Juventae Chasma, Mars. In *Lunar and Planetary Institute Science Conference Abstracts*, volume 38 of *Lunar and Planetary Institute Science Conference Abstracts*, page 1046, 2007.

K. C. Condie and K. Benn. Archean geodynamics: Similar to or different from modern geodynamics? In Benn, K., et al., editor, *Archean Geodynamics and Environments*, page 47. 2006.

K.C. Condie and V. Pease. *When Did Tectonics Begin on Planet Earth?* Special paper 440; Boulder, CO: Geol. Soc. Am., 2008.

S. J. Conway, M. P. Lamb, M. R. Balme, M. C. Towner, and J. B. Murray. Enhanced runout and erosion by overland flow at low pressure and sub-freezing conditions: Experiments and application to Mars. *Icarus*, 211:443–457, 2011. doi: 10.1016/j.icarus.2010.08.026.

S. Conway Morris. *Life's Solution.* Cambridge University Press, 2003.

N. B. Cowan and E. Agol. The Statistics of Albedo and Heat Recirculation on Hot Exoplanets. *Astrophysical Journal*, 729:54, 2011. doi: 10.1088/0004-637X/729/1/54.

R. A. Craddock and A. D. Howard. The case for rainfall on a warm, wet early Mars. *Journal of Geophysical Research (Planets)*, 107:5111, 2002. doi: 10.1029/2001JE001505.

R. A. Craddock and T. A. Maxwell. Resurfacing of the Martian highlands in the Amenthes and Tyrrhena region. *Journal of Geophysical Research*, 951:14265–14278, 1990.

R. A. Craddock and T. A. Maxwell. Geomorphic evolution of the Martian highlands through ancient fluvial processes. *Journal of Geophysical Research*, 98:3453–3468, 1993. doi: 10.1029/92JE02508.

R. A. Craddock, T. A. Maxwell, and A. D. Howard. Crater morphometry and modification in the Sinus Sabaeus and Margaritifer Sinus regions of Mars. *Journal of Geophysical Research*, 1021:13321–13340, 1997. doi: 10.1029/97JE01084.

L. S. Crumpler, R. E. Arvidson, S. W. Squyres, T. McCoy, A. Yingst, S. Ruff, W. Farrand, Y. McSween, M. Powell, D. W. Ming, R. V. Morris, J. F. Bell, III, J. Grant, R. Greeley, D. DesMarais, M. Schmidt, N. A. Cabrol, A. Haldemann, K. W. Lewis, A. E. Wang, C. Schröder, D. Blaney, B. Cohen, A. Yen, J. Farmer, R. Gellert, E. A. Guinness, K. E. Herkenhoff, J. R. Johnson, G. Klingelhöfer, A. McEwen, J. W. Rice, Jr., M. Rice, P. deSouza, and J. Hurowitz. Field reconnaissance geologic mapping of the Columbia Hills, Mars, based on Mars Exploration Rover Spirit and MRO HiRISE observations. *Journal of Geophysical Research (Planets)*, 116:E00F24, 2011. doi: 10.1029/2010JE003749.

P. J. Crutzen. Albedo enhancement by stratospheric sulfur injections: A contribution to resolve a policy dilemma? *Climatic Change*, 77(3-4):211–219, 2006. ISSN 0165-0009. doi: 10.1007/s10584-006-9101-y.

K. Cuffey and W. S. B. Paterson. *The Physics of Glaciers, 4th edition: Academic Press.* 2010.

J. A. Cutts and K. R. Blasius. Origin of Martian outflow channels - The eolian hypothesis. *Journal of Geophysical Research*, 86:5075–5102, 1981. doi: 10.1029/JB086iB06p05075.

N. Dauphas and A. Pourmand. Hf-W-Th evidence for rapid growth of Mars and its status as a planetary embryo. *Nature*, 473(7348):489–U227, 2011. doi: 10.1038/Nature10077.

G. F. Davies. On the emergence of plate tectonics. *Geology*, 20:963, 1992. doi: 10.1130/0091-7613(1992)020<0963:OTEOPT>2.3.CO;2.

G. F. Davies. Controls on density stratification in the early mantle. *Geochemistry, Geophysics, Geosystems*, 80:Q04006, 2007. doi: 10.1029/2006GC001414.

V. Debaille, A. D. Brandon, Q. Z. Yin, and B. Jacobsen. Coupled ^{142}Nd-^{143}Nd evidence for a protracted magma ocean in Mars. *Nature*, 450:525–528, 2007. doi: 10.1038/Nature06317.

E. Dehouck, N. Mangold, S. Le Mouélic, V. Ansan, and F. Poulet. Ismenius Cavus, Mars: A deep paleolake with phyllosilicate deposits. *Planetary and Space Science*, 58:941–946, 2010. doi: 10.1016/j.pss.2010.02.005.

D. Deming, S. Seager, J. Winn, E. Miller-Ricci, M. Clampin, D. Lindler, T. Greene, D. Charbonneau, G. Laughlin, G. Ricker, D. Latham, and K. Ennico. Discovery and Characterization of Transiting Super Earths Using an All-Sky Transit Survey and Follow-up by the James Webb Space Telescope. *Publications of the Astronomical Society of the Pacific*, 121:952–967, 2009. doi: 10.1086/605913.

W. E. Dietrich. Geomorphic Transport Laws for Predicting Landscape Form and Dynamics. In Wilcock, P. R. and Iverson, R. M., editor, *Prediction in Geomorphology*, volume 135 of *AGU Geophysical Monographs*. 2003.

DB Dingwell, P Courtial, D Giordano, and ARL Nichols. Viscosity of peridotite liquid. *Earth and Planetary Science Letters*, 226(1-2):127–138, 2004. ISSN 0012-821X. doi: 10.1016/j.epsl.2004.07.017.

S. D. Domagal-Goldman, J. F. Kasting, D. T. Johnston, and J. Farquhar. Organic haze, glaciations and multiple sulfur isotopes in the Mid-Archean Era. *Earth and Planetary Science Letters*, 269:29–40, 2008. doi: 10.1016/j.epsl.2008.01.040.

Peter T. Doran, W. Berry Lyons, and Diane M. McKnight. *Life in Antarctic deserts and other cold dry environments: astrobiological analogs*. Cambridge University Press, 2010.

S. Douté, B. Schmitt, Y. Langevin, J.-P. Bibring, F. Altieri, G. Bellucci, B. Gondet, F. Poulet, and MEX OMEGA team. South Pole of Mars: Nature and composition of the icy terrains from Mars Express OMEGA observations. *Planetary and Space Science*, 55:113–133, 2007. doi: 10.1016/j.pss.2006.05.035.

C. M. Dundas and S. Byrne. Modeling sublimation of ice exposed by new impacts in the Martian mid-latitudes. *Icarus*, 206:716–728, 2010. doi: 10.1016/j.icarus.2009.09.007.

T. Dunne, AG Price, and SC Colbeck. Generation of Runoff from Subarctic Snowpacks. *Water Resources Research*, 12(4):677–685, 1976.

K. S. Edgett. The sedimentary rocks of Sinus Meridiani: Five key observations from data acquired by the Mars Global Surveyor and Mars Odyssey orbiters. *International Journal of Mars Science and Exploration*, 1:5–58, 2005. doi: 10.1555/mars.2005.0002.

K. S. Edgett and M. C. Malin. MRO Context Camera (CTX) Investigation Primary Mission Results. *AGU Fall Meeting Abstracts*, page D4, December 2008.

J. M. Edmond and Y. Huh. Non-steady state carbonate recycling and implications for the evolution of atmospheric pCO_2. *Earth and Planetary Science Letters*, 216:125–139, 2003. doi: 10.1016/S0012-821X(03)00510-7.

A. Edson, S. Lee, P. Bannon, J. F. Kasting, and D. Pollard. Atmospheric circulations of terrestrial planets orbiting low-mass stars. *Icarus*, 212:1–13, 2011. doi: 10.1016/j.icarus.2010.11.023.

B. L. Ehlmann, J. F. Mustard, G. A. Swayze, R. N. Clark, J. L. Bishop, F. Poulet, D. J. Des Marais, L. H. Roach, R. E. Milliken, J. J. Wray, O. Barnouin-Jha, and S. L. Murchie. Identification of hydrated silicate minerals on Mars using MRO-CRISM: Geologic context near Nili Fossae and implications for aqueous alteration. *Journal of Geophysical Research (Planets)*, 114:E00D08, 2009. doi: 10.1029/2009JE003339.

B. L. Ehlmann, J. F. Mustard, and S. L. Murchie. Geologic setting of serpentine deposits on Mars. *Geophysical Research Letters*, 370:L06201, 2010. doi: 10.1029/2010GL042596.

B. L. Ehlmann, J.F. Mustard, S. L. Murchie, J.-P. Bibring, A. Meunier, A.A. Fraeman, and Y. Langevin. Subsurface water and clay mineral formation during the early history of Mars. *unpublished manuscript*, 2011.

V.L. Eichenlaub. *Weather and climate of the Great Lakes region.* University of Notre Dame Press, 1979.

L. T. Elkins-Tanton and S. Seager. Ranges of Atmospheric Mass and Composition of Super-Earth Exoplanets. *Astrophysical Journal*, 685:1237–1246, 2008a. doi: 10.1086/591433.

L. T. Elkins-Tanton and S. Seager. Coreless Terrestrial Exoplanets. *Astrophysical Journal*, 688:628–635, 2008b. doi: 10.1086/592316.

L. T. Elkins-Tanton, S. E. Smrekar, P. C. Hess, and E. M. Parmentier. Volcanism and volatile recycling on a one-plate planet: Applications to Venus. *Journal of Geophysical Research (Planets)*, 112:E04S06, 2007. doi: 10.1029/2006JE002793.

M.E. Elwood Madden, A.S. Madden, and J.D Rimstidt. How long was Meridiani Planum wet? Applying a jarosite stopwatch to constrain the duration of diagenesis. *Geology*, page 635, 2009.

K.E. Emanuel. *Atmospheric Convection.* Oxford University Press, 1994.

Epica Community Members, C. Barbante, J.-M. Barnola, S. Becagli, J. Beer, M. Bigler, C. Boutron, T. Blunier, E. Castellano, O. Cattani, J. Chappellaz, D. Dahl-Jensen, M. Debret, B. Delmonte, D. Dick, S. Falourd, S. Faria, U. Federer, H. Fischer, J. Freitag, A. Frenzel, D. Fritzsche, F. Fundel, P. Gabrielli, V. Gaspari, R. Gersonde, W. Graf, D. Grigoriev, I. Hamann, M. Hansson, G. Hoffmann, M. A. Hutterli, P. Huybrechts, E. Isaksson, S. Johnsen, J. Jouzel, M. Kaczmarska, T. Karlin, P. Kaufmann, S. Kipfstuhl, M. Kohno, F. Lambert, A. Lambrecht, A. Lambrecht, A. Landais, G. Lawer, M. Leuenberger, G. Littot, L. Loulergue, D. Lüthi, V. Maggi, F. Marino, V. Masson-Delmotte, H. Meyer, H. Miller, R. Mulvaney, B. Narcisi, J. Oerlemans, H. Oerter, F. Parrenin, J.-R. Petit, G. Raisbeck, D. Raynaud, R. Röthlisberger, U. Ruth, O. Rybak, M. Severi, J. Schmitt, J. Schwander, U. Siegenthaler, M.-L. Siggaard-Andersen, R. Spahni, J. P. Steffensen, B. Stenni, T. F. Stocker, J.-L. Tison, R. Traversi, R. Udisti, F. Valero-Delgado, M. R. van den Broeke, R. S. W. van de Wal, D. Wagenbach, A. Wegner, K. Weiler, F. Wilhelms, J.-G. Winther, and E. Wolff. One-to-one coupling of glacial climate variability in Greenland and Antarctica. *Nature*, 444:195–198, 2006. doi: 10.1038/Nature05301.

ExoPlanetTaskForce. Worlds beyond: A strategy for the detection and characterization of exoplanets. Technical report, Exoplanet Task Force, 2008.

A. G. Fairén. A cold and wet Mars. *Icarus*, 208:165–175, 2010. doi: 10.1016/j.icarus.2010.01.006.

A. G. Fairén, V. Chevrier, O. Abramov, G. A. Marzo, P. Gavin, A. F. Davila, L. L. Tornabene, J. L. Bishop, T. L. Roush, C. Gross, T. Kneissl, E. R. Uceda, J. M. Dohm, D. Schulze-Makuch, J. A. P. Rodriguez, R. Amils, and C. P. McKay. From the Cover: Noachian and more recent phyllosilicates in

impact craters on Mars. *Proceedings of the National Academy of Science*, 1071:12095–12100, 2010. doi: 10.1073/pnas.1002889107.

C. I. Fassett and J. W. Head. The timing of martian valley network activity: Constraints from buffered crater counting. *Icarus*, 195:61–89, 2008a. doi: 10.1016/j.icarus.2007.12.009.

C. I. Fassett and J. W. Head. Valley network-fed, open-basin lakes on Mars: Distribution and implications for Noachian surface and subsurface hydrology. *Icarus*, 198:37–56, 2008b. doi: 10.1016/j.icarus.2008.06.016.

C. I. Fassett and J. W. Head. Sequence and timing of conditions on early Mars. *Icarus*, 211:1204–1214, 2011. doi: 10.1016/j.icarus.2010.11.014.

C. I. Fassett, J. L. Dickson, J. W. Head, J. S. Levy, and D. R. Marchant. Supraglacial and proglacial valleys on Amazonian Mars. *Icarus*, 208:86–100, 2010. doi: 10.1016/j.icarus.2010.02.021.

J. L. Fastook, J. W. Head, D. R. Marchant, and F. Forget. Tropical mountain glaciers on Mars: Altitude-dependence of ice accumulation, accumulation conditions, formation times, glacier dynamics, and implications for planetary spin-axis/orbital history. *Icarus*, 198:305–317, 2008. doi: 10.1016/j.icarus.2008.08.008.

L. K. Fenton and R. K. Hayward. Southern high latitude dune fields on Mars: Morphology, aeolian inactivity, and climate change. *Geomorphology*, 121:98–121, 2010. doi: 10.1016/j.geomorph.2009.11.006.

S. Ferraz-Mello, M. Tadeu Dos Santos, C. Beaugé, T. A. Michtchenko, and A. Rodríguez. On the mass determination of super-Earths orbiting active stars: the CoRoT-7 system. *Astronomy & Astrophysics*, 531:A161+, 2011. doi: 10.1051/0004-6361/201016059.

N. J. Finnegan, G. Roe, D. R. Montgomery, and B. Hallet. Controls on the channel width of rivers: Implications for modeling fluvial incision of bedrock. *Geology*, 33:229, 2005. doi: 10.1130/G21171.1.

F. Forget and R. T. Pierrehumbert. Warming Early Mars with Carbon Dioxide Clouds That Scatter Infrared Radiation. *Science*, 278:1273, 1997. doi: 10.1126/science.278.5341.1273.

F. Forget, R. M. Haberle, F. Montmessin, B. Levrard, and J. W. Head. Formation of Glaciers on Mars by Atmospheric Precipitation at High Obliquity. *Science*, 311:368–371, 2006. doi: 10.1126/science.1120335.

F. Forget, F. Costard, and P. Lognonné. *Planet Mars: Story of Another World*. Springer-Praxis, 2008.

N. K. Forsberg-Taylor, A. D. Howard, and R. A. Craddock. Crater degradation in the Martian highlands: Morphometric analysis of the Sinus Sabaeus region and simulation modeling suggest fluvial processes. *Journal of Geophysical Research (Planets)*, 109:E05002, 2004. doi: 10.1029/2004JE002242.

T. Forveille, X. Bonfils, G. Lo Curto, X. Delfosse, S. Udry, F. Bouchy, C. Lovis, M. Mayor, C. Moutou, D. Naef, F. Pepe, C. Perrier, D. Queloz, and N. Santos. The HARPS search for southern extra-solar planets. XXVI. Two giant planets around M0 dwarfs. *Astronomy and Astrophysics*, 526:A141+, 2011. doi: 10.1051/0004-6361/201016034.

A. C. Fowler. On the thermal state of the earth's mantle. *Journal of Geophysics Zeitschrift Geophysik*, 53: 42–51, 1983.

A. A. Fraeman, J. F. Mustard, B. L. Ehlmann, L. H. Roach, R. E. Milliken, and S. L. Murchie. Evaluating Models of Crustal Cooling Using CRISM Observations of Impact Craters in Terra Tyrrhena and Noachis Terra. In *Lunar and Planetary Institute Science Conference Abstracts*, volume 40 of *Lunar and Planetary Institute Science Conference Abstracts*, page 2320, 2009.

A. Frebel. Metal-poor Stars. In A. Frebel, J. R. Maund, J. Shen, & M. H. Siegel, editor, *New Horizons in Astronomy*, volume 393 of *Astronomical Society of the Pacific Conference Series*, page 63, 2008.

E. Gaidos and G. Marion. Geological and geochemical legacy of a cold early Mars. *Journal of Geophysical Research (Planets)*, 108:5055, 2003. doi: 10.1029/2002JE002000.

E. Gaidos, N. Haghighipour, E. Agol, D. Latham, S. Raymond, and J. Rayner. New Worlds on the Horizon: Earth-Sized Planets Close to Other Stars. *Science*, 318:210–, 2007. doi: 10.1126/science.1144358.

E. Gaidos, D. A. Fischer, A. W. Mann, and S. Lepine. On the Nature of Small Planets around the Coolest Kepler Stars. *ArXiv e-prints*, 2011.

E. J. Gaidos. Note: A cosmochemical determinism in the formation of Earth-like planets. *Icarus*, 145: 637–640, 2000. doi: 10.1006/icar.2000.6407.

E. J. Gaidos, M. Güdel, and G. A. Blake. The faint young Sun paradox: An observational test of an alternative solar model. *Geophysical Research Letters*, 27:501–504, 2000. doi: 10.1029/1999GL010740.

A. L. Ganesan, L. T. Elkins-Tanton, and S. Seager. Temperature Distributions on Tidally-Locked Hot Exoplanets. In *Lunar and Planetary Institute Science Conference Abstracts*, volume 39 of *Lunar and Planetary Institute Science Conference Abstracts*, page 1368, 2008.

Stephen M. Gardiner. *A Perfect Moral Storm. The Ethical Tragedy of Climate Change*. Oxford University Press, 2011.

A. S. Gardner and M. J. Sharp. A review of snow and ice albedo and the development of a new physically based broadband albedo parameterization. *Journal of Geophysical Research (Earth Surface)*, 115:F01009, 2010. doi: 10.1029/2009JF001444.

E. J. Garnero and A. K. McNamara. Structure and Dynamics of Earth's Lower Mantle. *Science*, 320:626–, 2008. doi: 10.1126/science.1148028.

J. R. Garratt. *The atmospheric boundary layer*. Cambridge University Press, 1992.

C.N. Garzione. Research Focus: Surface uplift of Tibet and Cenozoic global cooling. *Geology*, 36(12): 1003–1004, 2008. doi: 10.1130/focus122008.1.

P. E. Geissler. Three decades of Martian surface changes. *Journal of Geophysical Research (Planets)*, 110: E02001, 2005. doi: 10.1029/2004JE002345.

P. E. Geissler, R. Sullivan, M. Golombek, J. R. Johnson, K. Herkenhoff, N. Bridges, A. Vaughan, J. Maki, T. Parker, and J. Bell. Gone with the wind: Eolian erasure of the Mars Rover tracks. *Journal of Geophysical Research (Planets)*, 115:E00F11, 2010. doi: 10.1029/2010JE003674.

M. F. Gerstell, J. S. Francisco, Y. L. Yung, C. Boxe, and E. T. Aaltonee. Special Feature: Keeping Mars warm with new super greenhouse gases. *Proceedings of the National Academy of Science*, 98:2154–2157, 2001. doi: 10.1073/pnas.051511598.

M. S. Ghiorso, M. M. Hirschmann, P. W. Reiners, and V. C. Kress. The pMELTS: A revision of MELTS for improved calculation of phase relations and major element partitioning related to partial melting of the mantle to 3 GPa. *Geochemistry, Geophysics, Geosystems*, page 1030, 2002. doi: 10.1029/2001GC000217.

M. S. Ghiorso, M. M. Hirschmann, and T. L. Grove. xMELTS: A thermodynamic model for the estimation of magmatic phase relations over the pressure range 0-30 GPa and at temperatures up to 2500 C. *AGU Fall Meeting Abstracts*, page C608, 2007.

MS Ghiorso. An equation of state for silicate melts. I. Formulation of a general model. *American Journal of Science*, 304(8-9):637–678, 2004. doi: 10.2475/ajs.304.8-9.637.

W. Goetz, P. Bertelsen, C. S. Binau, H. P. Gunnlaugsson, S. F. Hviid, K. M. Kinch, D. E. Madsen, M. B. Madsen, M. Olsen, R. Gellert, G. Klingelhöfer, D. W. Ming, R. V. Morris, R. Rieder, D. S. Rodionov, P. A. de Souza, C. Schröder, S. W. Squyres, T. Wdowiak, and A. Yen. Indication of drier periods on Mars from the chemistry and mineralogy of atmospheric dust. *Nature*, 436:62–65, 2005. doi: 10.1038/Nature03807.

W. Goetz, W. T. Pike, S. F. Hviid, M. B. Madsen, R. V. Morris, M. H. Hecht, U. Staufer, K. Leer, H. Sykulska, E. Hemmig, J. Marshall, J. M. Morookian, D. Parrat, S. Vijendran, B. J. Bos, M. R. El Maarry, H. U. Keller, R. Kramm, W. J. Markiewicz, L. Drube, D. Blaney, R. E. Arvidson, J. F. Bell, R. Reynolds, P. H. Smith, P. Woida, R. Woida, and R. Tanner. Microscopy analysis of soils at the Phoenix landing site, Mars: Classification of soil particles and description of their optical and magnetic properties. *Journal of Geophysical Research (Planets)*, 115:E00E22, 2010. doi: 10.1029/2009JE003437.

C. Goldblatt and K. J. Zahnle. Faint young Sun paradox remains. *Nature*, 474, June 2011. doi: 10.1038/nature09961.

M. Golombek and R. J. Phillips. Mars Tectonics. In Watters, T. R. and Schultz, R. A., editor, *Planetary Tectonics*, volume 11 of *Cambridge Planetary Science Series*, pages 183–232. Cambridge University Press, 2009.

M. Golombek, K. Robinson, A. McEwen, N. Bridges, B. Ivanov, L. Tornabene, and R. Sullivan. Constraints on ripple migration at Meridiani Planum from Opportunity and HiRISE observations of fresh craters. *Journal of Geophysical Research (Planets)*, 115:E00F08, 2010. doi: 10.1029/2010JE003628.

M. P. Golombek, J. A. Grant, L. S. Crumpler, R. Greeley, R. E. Arvidson, J. F. Bell, C. M. Weitz, R. Sullivan, P. R. Christensen, L. A. Soderblom, and S. W. Squyres. Erosion rates at the Mars Exploration Rover landing sites and long-term climate change on Mars. *Journal of Geophysical Research (Planets)*, 111: E12S10, 2006. doi: 10.1029/2006JE002754.

R. Gomes, H. F. Levison, K. Tsiganis, and A. Morbidelli. Origin of the cataclysmic Late Heavy Bombardment period of the terrestrial planets. *Nature*, 435:466–469, May 2005. doi: 10.1038/nature03676.

P. Goodwin, R. G. Williams, A. Ridgwell, and M. J. Follows. Climate sensitivity to the carbon cycle modulated by past and future changes in ocean chemistry. *Nature Geoscience*, 2:145–150, 2009. doi: 10.1038/ngeo416.

P. Gorenstein and P. Bjorkholm. Detection of Radon Emanation from the Crater Aristarchus by the Apollo 15 Alpha Particle Spectrometer. *Science*, 179:792–794, 1973. doi: 10.1126/science.179.4075.792.

J. A. Grant and S. A. Wilson. Late alluvial fan formation in southern Margaritifer Terra, Mars. *Geophysical Research Letters*, 380:L08201, 2011. doi: 10.1029/2011GL046844.

J. A. Grant, S. A. Wilson, E. Noe Dobrea, R. L. Fergason, J. L. Griffes, J. M. Moore, and A. D. Howard. HiRISE views enigmatic deposits in the Sirenum Fossae region of Mars. *Icarus*, 205:53–63, January 2010. doi: 10.1016/j.icarus.2009.04.009.

O. Grasset and E. M. Parmentier. Thermal convection in a volumetrically heated, infinite Prandtl number fluid with strongly temperature-dependent viscosity: Implications for planetary evolution. *Journal of Geophysical Research*, 1031:18171–18181, 1998. doi: 10.1029/98JB01492.

R. Greeley and J. D. Iversen. *Wind as a geological process on Earth, Mars, Venus and Titan.*, volume 4 of *Cambridge Planetary Science Series (Old)*. Cambridge University Press, 1985.

J. P. Greenwood, S. Itoh, N. Sakamoto, E. P. Vicenzi, and H. Yurimoto. Hydrogen isotope evidence for loss of water from Mars through time. *Geophysical Research Letters*, 350:L05203, 2008. doi: 10.1029/2007GL032721.

C. Grima, W. Kofman, J. Mouginot, R. J. Phillips, A. Hérique, D. Biccari, R. Seu, and M. Cutigni. North polar deposits of Mars: Extreme purity of the water ice. *Geophysical Research Letters*, 360:L03203, 2009. doi: 10.1029/2008GL036326.

R. E. Grimm and S. L. Painter. On the secular evolution of groundwater on Mars. *Geophysical Research Letters*, 362:L24803, 2009. doi: 10.1029/2009GL041018.

M. Grott, A. Morschhauser, D. Breuer, and E. Hauber. Volcanic outgassing of CO_2 and H_2O on Mars. *Earth and Planetary Science Letters*, 308:391–400, 2011. doi: 10.1016/j.epsl.2011.06.014.

J. Grotzinger, J. Bell, III, K. Herkenhoff, J. Johnson, A. Knoll, E. McCartney, S. McLennan, J. Metz, J. Moore, S. Squyres, R. Sullivan, O. Ahronson, R. Arvidson, B. Joliff, M. Golombek, K. Lewis, T. Parker, and J. Soderblom. Sedimentary textures formed by aqueous processes, Erebus crater, Meridiani Planum, Mars. *Geology*, 34:1085, 2006. doi: 10.1130/G22985A.1.

J. P. Grotzinger and N. P. James. Precambrian carbonates; evolution of understanding. In J. P. Grotzinger and N. P. James, editors, *Carbonate Sedimentation and Diagenesis in the Evolving Precambrian World*, pages 3–20. SEPM, The Society for Sedimentary Geology, 2000.

J. P. Grotzinger and J. F. Kasting. New Constraints on Precambrian Ocean Composition. *Journal of Geology*, 101:235–243, 1993. doi: 10.1086/648218.

V. C. Gulick and V. R. Baker. Fluvial valleys and Martian palaeoclimates. *Nature*, 341:514–516, 1989. doi: 10.1038/341514a0.

J. A. Guzik and K. Mussack. Exploring Mass Loss, Low-Z Accretion, and Convective Overshoot in Solar Models to Mitigate the Solar Abundance Problem. *Astrophysical Journal*, 713:1108–1119, 2010. doi: 10.1088/0004-637X/713/2/1108.

R. M. Haberle. Early Mars Climate Models. *Journal of Geophysical Research*, 1032:28467–28480, 1998. doi: 10.1029/98JE01396.

R. M. Haberle, J. B. Pollack, J. R. Barnes, R. W. Zurek, C. B. Leovy, J. R. Murphy, H. Lee, and J. Schaeffer. Mars atmospheric dynamics as simulated by the NASA Ames General Circulation Model. I - The zonal-mean circulation. *Journal of Geophysical Research*, 98:3093–3123, 1993. doi: 10.1029/92JE02946.

R. M. Haberle, D. Tyler, C. P. McKay, and W. L. Davis. A model for the evolution of CO_2 on Mars. *Icarus*, 109:102–120, 1994. doi: 10.1006/icar.1994.1079.

R. M. Haberle, J. R. Murphy, and J. Schaeffer. Orbital change experiments with a Mars general circulation model. *Icarus*, 161:66–89, 2003. doi: 10.1016/S0019-1035(02)00017-9.

I. Halevy, M. T. Zuber, and D. P. Schrag. A Sulfur Dioxide Climate Feedback on Early Mars. *Science*, 318: 1903, 2007. doi: 10.1126/science.1147039.

I. Halevy, R. T. Pierrehumbert, and D. P. Schrag. Radiative transfer in CO_2-rich paleoatmospheres. *Journal of Geophysical Research (Atmospheres)*, 114:D18112, 2009. doi: 10.1029/2009JD011915.

K. P. Hand, C. F. Chyba, J. C. Priscu, R. W. Carlson, and K. H. Nealson. Astrobiology and the Potential for Life on Europa. In Pappalardo, R. T., McKinnon, W. B., & Khurana, K. K., editor, *Europa*, page 589. University of Arizona Press, Tucson, 2009.

C. J. Hansen, M. Bourke, N. T. Bridges, S. Byrne, C. Colon, S. Diniega, C. Dundas, K. Herkenhoff, A. McEwen, M. Mellon, G. Portyankina, and N. Thomas. Seasonal Erosion and Restoration of Mars' Northern Polar Dunes. *Science*, 331:575, 2011. doi: 10.1126/science.1197636.

B Hardy. I.T.S.-90 formulations for vapor pressure, frostpoint temperature, dewpoint temperature, and enhancement factors in the range -100C to +100C. Technical report, Natl. Phys. Lab., Teddington, U. K., 1998.

K. P. Harrison and M. G. Chapman. Evidence for ponding and catastrophic floods in central Valles Marineris, Mars. *Icarus*, 198:351–364, 2008. doi: 10.1016/j.icarus.2008.08.003.

K. P. Harrison and R. E. Grimm. Multiple flooding events in Martian outflow channels. *Journal of Geophysical Research (Planets)*, 113:E02002, 2008. doi: 10.1029/2007JE002951.

T. N. Harrison, M. C. Malin, K. S. Edgett, D. E. Shean, M. R. Kennedy, L. J. Lipkaman, B. A. Cantor, and L. V. Posiolova. Impact-induced overland fluid flow and channelized erosion at Lyot Crater, Mars. *Geophysical Research Letters*, 372:L21201, 2010. doi: 10.1029/2010GL045074.

W. K. Hartmann. Martian cratering 8: Isochron refinement and the chronology of Mars. *Icarus*, 174:294–320, 2005. doi: 10.1016/j.icarus.2004.11.023.

G. L. Hashimoto and Y. Abe. Climate control on Venus: Comparison of the carbonate and pyrite models. *Planetary and Space Science*, 53:839–848, 2005. doi: 10.1016/j.pss.2005.01.005.

E. Hauber, S. van Gasselt, M. G. Chapman, and G. Neukum. Geomorphic evidence for former lobate debris aprons at low latitudes on Mars: Indicators of the Martian paleoclimate. *Journal of Geophysical Research (Planets)*, 113:E02007, 2008. doi: 10.1029/2007JE002897.

E. M. Hausrath, A. K. Navarre-Sitchler, P. B. Sak, C. I. Steefel, and S. L. Brantley. Basalt weathering rates on Earth and the duration of liquid water on the plains of Gusev Crater, Mars. *Geology*, 36:67–70, 2008.

A. G. Hayes, J. P. Grotzinger, L. A. Edgar, S. W. Squyres, W. A. Watters, and J. Sohl-Dickstein. Reconstruction of eolian bed forms and paleocurrents from cross-bedded strata at Victoria Crater, Meridiani Planum, Mars. *Journal of Geophysical Research (Planets)*, 116:E00F21, 2011.

J. W. Head, D. R. Marchant, and M. A. Kreslavsky. From the Cover: Formation of gullies on Mars: Link to recent climate history and insolation microenvironments implicate surface water flow origin. *Proceedings of the National Academy of Science*, 1051:13258–13263, 2008. doi: 10.1073/pnas.0803760105.

J. W. Head, III and M. Kreslavsky. Medusae Fossae Formation: Ice-rich Airborne Dust Deposited During Periods of High Obliquity? In S. Mackwell & E. Stansbery, editor, *Lunar and Planetary Institute Science Conference Abstracts*, volume 35 of *Lunar and Planetary Institute Science Conference Abstracts*, page 1635, 2004.

M. H. Hecht. Metastability of Liquid Water on Mars. *Icarus*, 156:373–386, 2002. doi: 10.1006/icar.2001.6794.

CH Hendy. Late Quaternary lakes in the McMurdo Sound region of Antarctica. *Geografiska Annaler Series A – Physical Gegraphy*, 82A(2-3):411–432, 2000.

K. E. Herkenhoff, M. P. Golombek, E. A. Guinness, J. B. Johnson, A. Kusack, L. Richter, R. J. Sullivan, and S. Gorevan. In situ observations of the physical properties of the Martian surface. In Bell, J., III, editor, *The Martian Surface - Composition, Mineralogy, and Physical Properties*, page 451. 2008a.

K. E. Herkenhoff, J. Grotzinger, A. H. Knoll, S. M. McLennan, C. Weitz, A. Yingst, R. Anderson, B. A. Archinal, R. E. Arvidson, J. M. Barrett, K. J. Becker, J. F. Bell, C. Budney, M. G. Chapman, D. Cook, B. Ehlmann, B. Franklin, L. R. Gaddis, D. M. Galuszka, P. A. Garcia, P. Geissler, T. M. Hare, E. Howington-Kraus, J. R. Johnson, L. Keszthelyi, R. L. Kirk, P. Lanagan, E. M. Lee, C. Leff, J. N. Maki, K. F. Mullins, T. J. Parker, B. L. Redding, M. R. Rosiek, M. H. Sims, L. A. Soderblom, N. Spanovich, R. Springer, S. W. Squyres, D. Stolper, R. M. Sucharski, T. Sucharski, R. Sullivan, and J. M. Torson. Surface processes recorded by rocks and soils on Meridiani Planum, Mars: Microscopic Imager observations during Opportunity's first three extended missions. *Journal of Geophysical Research (Planets)*, 113: E12S32, November 2008b. doi: 10.1029/2008JE003100.

C. Herzberg, K. Condie, and J. Korenaga. Thermal history of the Earth and its petrological expression. *Earth and Planetary Science Letters*, 292:79–88, 2010. doi: 10.1016/j.epsl.2010.01.022.

M. M. Hirschmann and A. C. Withers. Ventilation of CO_2 from a reduced mantle and consequences for the early Martian greenhouse. *Earth and Planetary Science Letters*, 270:147–155, 2008. doi: 10.1016/j.epsl.2008.03.034.

N. Hoffman. White Mars: A New Model for Mars' Surface and Atmosphere Based on CO_2. *Icarus*, 146: 326–342, 2000. doi: 10.1006/icar.2000.6398.

M. R. T. Hoke and B. M. Hynek. Roaming zones of precipitation on ancient Mars as recorded in valley networks. *Journal of Geophysical Research (Planets)*, 114:E08002, 2009. doi: 10.1029/2008JE003247.

A. D. Howard. Simulating the development of Martian highland landscapes through the interaction of impact cratering, fluvial erosion, and variable hydrologic forcing. *Geomorphology*, 91:332–363, 2007. doi: 10.1016/j.geomorph.2007.04.017.

A. D. Howard. How to make a meandering river. *Proceedings of the National Academy of Science*, 1061: 17245–17246, 2009. doi: 10.1073/pnas.0910005106.

A. D. Howard and J. M. Moore. Late Hesperian to early Amazonian midlatitude Martian valleys: Evidence from Newton and Gorgonum basins. *Journal of Geophysical Research (Planets)*, 116:E05003, 2011. doi: 10.1029/2010JE003782.

A. D. Howard, J. M. Moore, and R. P. Irwin. An intense terminal epoch of widespread fluvial activity on early Mars: 1. Valley network incision and associated deposits. *Journal of Geophysical Research (Planets)*, 110:E12S14, 2005. doi: 10.1029/2005JE002459.

A. D. Howard, J. M. Moore, R. P. Irwin, and W. E. Dietrich. Boulder Transport Across the Eberswalde Delta. In *Lunar and Planetary Institute Science Conference Abstracts*, volume 38 of *Lunar and Planetary Institute Science Conference Abstracts*, page 1168, 2007.

A. W. Howard, G. W. Marcy, J. A. Johnson, D. A. Fischer, J. T. Wright, H. Isaacson, J. A. Valenti, J. Anderson, D. N. C. Lin, and S. Ida. The Occurrence and Mass Distribution of Close-in Super-Earths, Neptunes, and Jupiters. *Science*, 330:653–, October 2010. doi: 10.1126/science.1194854.

A. W. Howard, G. W. Marcy, S. T. Bryson, J. M. Jenkins, J. F. Rowe, N. M. Batalha, W. J. Borucki, D. G. Koch, E. W. Dunham, T. N. Gautier, III, J. Van Cleve, W. D. Cochran, D. W. Latham, J. J. Lissauer, G. Torres, T. M. Brown, R. L. Gilliland, L. A. Buchhave, D. A. Caldwell, J. Christensen-Dalsgaard, D. Ciardi, F. Fressin, M. R. Haas, S. B. Howell, H. Kjeldsen, S. Seager, L. Rogers, D. D. Sasselov, J. H. Steffen, G. S. Basri, D. Charbonneau, J. Christiansen, B. Clarke, A. Dupree, D. C. Fabrycky, D. A. Fischer, E. B. Ford, J. J. Fortney, J. Tarter, F. R. Girouard, M. J. Holman, J. A. Johnson, T. C. Klaus, P. Machalek, A. V. Moorhead, R. C. Morehead, D. Ragozzine, P. Tenenbaum, J. D. Twicken, S. N. Quinn, H. Isaacson, A. Shporer, P. W. Lucas, L. M. Walkowicz, W. F. Welsh, A. Boss, E. Devore, A. Gould, J. C. Smith, R. L. Morris, A. Prsa, and T. D. Morton. Planet Occurrence within 0.25 AU of Solar-type Stars from Kepler. *ArXiv e-prints*, 2011.

T. L. Hudson and O. Aharonson. Diffusion barriers at Mars surface conditions: Salt crusts, particle size mixtures, and dust. *Journal of Geophysical Research (Planets)*, 113:E09008, 2008. doi: 10.1029/2007JE003026.

T. L. Hudson, O. Aharonson, N. Schorghofer, C. B. Farmer, M. H. Hecht, and N. T. Bridges. Water vapor diffusion in Mars subsurface environments. *Journal of Geophysical Research (Planets)*, 112:E05016, 2007. doi: 10.1029/2006JE002815.

T. L. Hudson, O. Aharonson, and N. Schorghofer. Laboratory experiments and models of diffusive emplacement of ground ice on Mars. *Journal of Geophysical Research (Planets)*, 114:E01002, 2009. doi: 10.1029/2008JE003149.

G. O. Hughes and R. W. Griffiths. Horizontal Convection. *Annual Review of Fluid Mechanics*, 40:185–208, 2008. doi: 10.1146/annurev.fluid.40.111406.102148.

H. F. Hunt. The Functions of the Martian Canals. *Nature*, 82:69, 1909. doi: 10.1038/082069d0.

J. A. Hurowitz and S. M. McLennan. A ∼3.5 Ga record of water-limited, acidic weathering conditions on Mars. *Earth and Planetary Science Letters*, 260:432–443, 2007. doi: 10.1016/j.epsl.2007.05.043.

J. A. Hurowitz, W. W. Fischer, N. J. Tosca, and R. E. Milliken. Origin of acidic surface waters and the evolution of atmospheric chemistry on early Mars. *Nature Geoscience*, 3:323–326, 2010. doi: 10.1038/ngeo831.

P. Huybers and O. Aharonson. Orbital tuning, eccentricity, and the frequency modulation of climatic precession. *Paleoceanography*, 25(26):PA4228, 2010. doi: 10.1029/2010PA001952.

B. M. Hynek and R. J. Phillips. New data reveal mature, integrated drainage systems on Mars indicative of past precipitation. *Geology*, 31:757, 2003. doi: 10.1130/G19607.1.

B. M. Hynek, R. J. Phillips, and R. E. Arvidson. Explosive volcanism in the Tharsis region: Global evidence in the Martian geologic record. *Journal of Geophysical Research (Planets)*, 108:5111, September 2003. doi: 10.1029/2003JE002062.

B. M. Hynek, M. Beach, and M. R. T. Hoke. Updated global map of Martian valley networks and implications for climate and hydrologic processes. *Journal of Geophysical Research (Planets)*, 115:E09008, 2010. doi: 10.1029/2009JE003548.

S. Ida and D. N. C. Lin. Toward a Deterministic Model of Planetary Formation. I. A Desert in the Mass and Semimajor Axis Distributions of Extrasolar Planets. *Astrophysical Journal*, 604:388–413, 2004. doi: 10.1086/381724.

M. Ikoma, H. Emori, and K. Nakazawa. Formation of Giant Planets in Dense Nebulae: Critical Core Mass Revisited. *Astropysical Journal*, 553:999–1005, 2001. doi: 10.1086/320954.

A. P. Ingersoll. Mars: Occurrence of Liquid Water. *Science*, 168:972–973, 1970. doi: 10.1126/science.168.3934.972.

L. T. Iraci, B. D. Phebus, B. M. Stone, and A. Colaprete. Water ice cloud formation on Mars is more difficult than presumed: Laboratory studies of ice nucleation on surrogate materials. *Icarus*, 210:985–991, 2010. doi: 10.1016/j.icarus.2010.07.020.

R. P. Irwin, A. D. Howard, R. A. Craddock, and J. M. Moore. An intense terminal epoch of widespread fluvial activity on early Mars: 2. Increased runoff and paleolake development. *Journal of Geophysical Research (Planets)*, 110:E12S15, 2005a. doi: 10.1029/2005JE002460.

R. P. Irwin, III, R. A. Craddock, and A. D. Howard. Interior channels in Martian valley networks: Discharge and runoff production. *Geology*, 33:489, 2005b. doi: 10.1130/G21333.1.

B. Jackson, R. Greenberg, and R. Barnes. Tidal Evolution of Close-in Extrasolar Planets. *Astrophysical Journal*, 678:1396–1406, 2008. doi: 10.1086/529187.

B. Jackson, N. Miller, R. Barnes, S. N. Raymond, J. J. Fortney, and R. Greenberg. The roles of tidal evolution and evaporative mass loss in the origin of CoRoT-7 b. *Monthly Notices of the Royal Astronomical Society*, 407:910–922, 2010. doi: 10.1111/j.1365-2966.2010.17012.x.

B. M. Jakosky. Mars volatile evolution - Evidence from stable isotopes. *Icarus*, 94:14–31, 1991. doi: 10.1016/0019-1035(91)90138-J.

B. M. Jakosky and M. H. Carr. Possible precipitation of ice at low latitudes of Mars during periods of high obliquity. *Nature*, 315:559–561, 1985. doi: 10.1038/315559a0.

B. M. Jakosky, B. G. Henderson, and M. T. Mellon. Chaotic obliquity and the nature of the Martian climate. *Journal of Geophysical Research*, 100:1579–1584, 1995. doi: 10.1029/94JE02801.

D. E. Jennings, F. M. Flasar, V. G. Kunde, R. E. Samuelson, J. C. Pearl, C. A. Nixon, R. C. Carlson, A. A. Mamoutkine, J. C. Brasunas, E. Guandique, R. K. Achterberg, G. L. Bjoraker, P. N. Romani, M. E. Segura, S. A. Albright, M. H. Elliott, J. S. Tingley, S. Calcutt, A. Coustenis, and R. Courtin. Titan's Surface Brightness Temperatures. *Astrophysical Journal Letters*, 691:L103–L105, 2009. doi: 10.1088/0004-637X/691/2/L103.

S. S. Johnson, M. A. Mischna, T. L. Grove, and M. T. Zuber. Sulfur-induced greenhouse warming on early Mars. *Journal of Geophysical Research (Planets)*, 113:E08005, 2008. doi: 10.1029/2007JE002962.

A. P. Jones, A. S. McEwen, L. L. Tornabene, V. R. Baker, H. J. Melosh, and D. C. Berman. A geomorphic analysis of Hale crater, Mars: The effects of impact into ice-rich crust. *Icarus*, 211:259–272, 2011. doi: 10.1016/j.icarus.2010.10.014.

M. Joshi. Climate Model Studies of Synchronously Rotating Planets. *Astrobiology*, 3:415–427, 2003. doi: 10.1089/153110703769016488.

M. M. Joshi, R. M. Haberle, and R. T. Reynolds. Simulations of the Atmospheres of Synchronously Rotating Terrestrial Planets Orbiting M Dwarfs: Conditions for Atmospheric Collapse and the Implications for Habitability. *Icarus*, 129:450–465, 1997. doi: 10.1006/icar.1997.5793.

T. Juteau and R. Maury. *The Oceanic Crust, from Accretion to Mantle Recycling.* Springer-Praxis, 1999.

S. J. Kadish, J. W. Head, and N. G. Barlow. Pedestal crater heights on Mars: A proxy for the thicknesses of past, ice-rich, Amazonian deposits. *Icarus*, 210:92–101, 2010. doi: 10.1016/j.icarus.2010.06.021.

L. C. Kah and R. Riding. Mesoproterozoic carbon dioxide levels inferred from calcified cyanobacteria. *Geology*, 35:799, 2007. doi: 10.11302FG23680A.1.

R. Kahn. The evolution of CO_2 on Mars. *Icarus*, 62:175–190, 1985. doi: 10.1016/0019-1035(85)90116-2.

M. A. Kahre and R. M. Haberle. Mars CO_2 cycle: Effects of airborne dust and polar cap ice emissivity. *Icarus*, 207:648–653, 2010. doi: 10.1016/j.icarus.2009.12.016.

M. A. Kahre, J. R. Murphy, and R. M. Haberle. Modeling the Martian dust cycle and surface dust reservoirs with the NASA Ames general circulation model. *Journal of Geophysical Research (Planets)*, 111:E06008, 2006. doi: 10.1029/2005JE002588.

S. Karato. *Deformation of Earth Materials: An Introduction to the Rheology of Solid Earth.* Cambridge University Press, 2008.

J. F. Kasting. Runaway and moist greenhouse atmospheres and the evolution of earth and Venus. *Icarus*, 74:472–494, 1988. doi: 10.1016/0019-1035(88)90116-9.

J. F. Kasting. CO_2 condensation and the climate of early Mars. *Icarus*, 94:1–13, 1991. doi: 10.1016/0019-1035(91)90137-I.

J. F. Kasting, D. P. Whitmire, and R. T. Reynolds. Habitable Zones around Main Sequence Stars. *Icarus*, 101:108–128, 1993. doi: 10.1006/icar.1993.1010.

R. F. Katz, M. Spiegelman, and C. H. Langmuir. A new parameterization of hydrous mantle melting. *Geochemistry, Geophysics, Geosystems*, 4:1073, 2003.

A. Kereszturi, M. Vincendon, and F. Schmidt. Water ice in the dark dune spots of Richardson crater on Mars. *Planetary and Space Science*, 59:26–42, 2011. doi: 10.1016/j.pss.2010.10.015.

M. L. Khodachenko, I. Ribas, H. Lammer, J.-M. Grießmeier, M. Leitner, F. Selsis, C. Eiroa, A. Hanslmeier, H. K. Biernat, C. J. Farrugia, and H. O. Rucker. Coronal Mass Ejection (CME) Activity of Low Mass M Stars as An Important Factor for The Habitability of Terrestrial Exoplanets. I. CME Impact on Expected Magnetospheres of Earth-Like Exoplanets in Close-In Habitable Zones. *Astrobiology*, 7:167–184, 2007. doi: 10.1089/ast.2006.0127.

H. H. Kieffer, T. Z. Martin, S. C. Chase, Jr., E. D. Miner, and F. D. Palluconi. Martian north pole summer temperatures - Dirty water ice. *Science*, 194:1341–1344, 1976. doi: 10.1126/science.194.4271.1341.

E. S. Kite, I. Matsuyama, M. Manga, J. T. Perron, and J. X. Mitrovica. True Polar Wander driven by late-stage volcanism and the distribution of paleopolar deposits on Mars. *Earth and Planetary Science Letters*, 280:254–267, April 2009. doi: 10.1016/j.epsl.2009.01.040.

E.S. Kite. Net assessment of the impact hypothesis for fluvial activity at Eberswalde and tests with MSL. 5th Mars Science Laboratory Landing Site Selection Workshop, 2011.

E.S. Kite, T.I. Michaels, S.C.R. Rafkin, W.E. Dietrich, and M. Manga. Localized precipitation and channel formation on Mars: Under what conditions can one landing site be a proxy for global environments? 4th Mars Science Laboratory Landing Site Selection Workshop, 2010.

E.S. Kite, M. Manga, I. Halevy, and M.A. Kahre. Gale as a preferred site for snowmelt-limited induration of atmospherically transported sediment. 5th Mars Science Laboratory Landing Site Selection Workshop, 2011.

M. G. Kleinhans. Flow discharge and sediment transport models for estimating a minimum timescale of hydrological activity and channel and delta formation on Mars. *Journal of Geophysical Research (Planets)*, 110:E12003, 2005. doi: 10.1029/2005JE002521.

M. G. Kleinhans, H. E. van de Kasteele, and E. Hauber. Palaeoflow reconstruction from fan delta morphology on Mars. *Earth and Planetary Science Letters*, 294:378–392, 2010. doi: 10.1016/j.epsl.2009.11.025.

A. H. Knoll. The multiple origins of complex multicellularity. *Annual Review of Earth and Planetary Sciences*, 39:217–239, 2011. doi: 10.1146/annurev.earth.031208.100209.

A. H. Knoll, B. L. Jolliff, W. H. Farrand, J. F. Bell, III, B. C. Clark, R. Gellert, M. P. Golombek, J. P. Grotzinger, K. E. Herkenhoff, J. R. Johnson, S. M. McLennan, R. Morris, S. W. Squyres, R. Sullivan, N. J. Tosca, A. Yen, and Z. Learner. Veneers, rinds, and fracture fills: Relatively late alteration of sedimentary rocks at Meridiani Planum, Mars. *Journal of Geophysical Research (Planets)*, 113:E06S16, 2008. doi: 10.1029/2007JE002949.

H. A. Knutson, D. Charbonneau, L. E. Allen, J. J. Fortney, E. Agol, N. B. Cowan, A. P. Showman, C. S. Cooper, and S. T. Megeath. A map of the day-night contrast of the extrasolar planet HD 189733b. *Nature*, 447:183–186, 2007. doi: 10.1038/Nature05782.

H. A. Knutson, D. Charbonneau, N. B. Cowan, J. J. Fortney, A. P. Showman, E. Agol, G. W. Henry, M. E. Everett, and L. E. Allen. Multiwavelength Constraints on the Day-Night Circulation Patterns of HD 189733b. *Astrophysical Journal*, 690:822–836, 2009. doi: 10.1088/0004-637X/690/1/822.

G. Komatsu, G. di Achille, C. Popa, S. di Lorenzo, A. P. Rossi, and J. A. P. Rodriguez. Paleolakes, paleofloods, and depressions in Aurorae and Ophir Plana, Mars: Connectivity of surface and subsurface hydrological systems. *Icarus*, 201:474–491, 2009. doi: 10.1016/j.icarus.2009.01.010.

R. E. Kopp, J. L. Kirschvink, I. A. Hilburn, and C. Z. Nash. The Paleoproterozoic snowball Earth: A climate disaster triggered by the evolution of oxygenic photosynthesis. *Proceedings of the National Academy of Science*, 1021:11131–11136, 2005. doi: 10.1073/pnas.0504878102.

J. Korenaga. Urey ratio and the structure and evolution of Earth's mantle. *Reviews of Geophysics*, 46: RG2007, 2008. doi: 10.1029/2007RG000241.

J. Korenaga. On the Likelihood of Plate Tectonics on Super-Earths: Does Size Matter? *Astrophysical Journal Letters*, 725:L43–L46, 2010. doi: 10.1088/2041-8205/725/1/L43.

E. R. Kraal, E. Asphaug, J. M. Moore, A. Howard, and A. Bredt. Catalogue of large alluvial fans in martian impact craters. *Icarus*, 194:101–110, 2008a. doi: 10.1016/j.icarus.2007.09.028.

E. R. Kraal, M. van Dijk, G. Postma, and M. G. Kleinhans. Martian stepped-delta formation by rapid water release. *Nature*, 451:973–976, 2008b. doi: 10.1038/Nature06615.

M. A. Kreslavsky and J. W. Head. North-south topographic slope asymmetry on Mars: Evidence for insolation-related erosion at high obliquity. *Geophysical Research Letters*, 30(15):1815, 2003. doi: 10.1029/2003GL017795.

M. J. Kuchner and S. Seager. Extrasolar Carbon Planets. *ArXiv Astrophysics e-prints*, 2005.

K. F. Kuiper, A. Deino, F. J. Hilgen, W. Krijgsman, P. R. Renne, and J. R. Wijbrans. Synchronizing Rock Clocks of Earth History. *Science*, 320:500–, 2008. doi: 10.1126/science.1154339.

M.P. Lamb, J. Grotzinger, J.B. Southard, and N. Tosca. Were ripples on Mars formed by flowing brines? In Grotzinger, J. P. and Milliken, R., editor, *Sedimentary Geology on Mars*. SEPM, The Society for Sedimentary Geology, 2011.

Y. Langevin, F. Poulet, J.-P. Bibring, and B. Gondet. Sulfates in the North Polar Region of Mars Detected by OMEGA/Mars Express. *Science*, 307:1584–1586, 2005. doi: 10.1126/science.1109091.

C. H. Langmuir, E. M. Klein, and T. Plank. Petrological systematics of mid-ocean ridge basalts: constraints on melt generation beneath ocean ridges. In Phipps–Morgan, J. et al., editor, *Mantle flow and melt generation at mid-ocean ridges*, volume 71 of *Amer. Geophys. Union,Geophysical Monograph*, pages 183–280. 1992.

T. J. Lapen, M. Righter, A. D. Brandon, V. Debaille, B. L. Beard, J. T. Shafer, and A. H. Peslier. A Younger age for ALH84001 and its geochemical link to shergottite sources in Mars. *Science*, 328:347, 2010. doi: 10.1126/science.1185395.

J. Laskar. Chaotic diffusion in the Solar System. *Icarus*, 196:1–15, 2008. doi: 10.1016/j.icarus.2008.02.017.

J. Laskar and P. Robutel. The chaotic obliquity of the planets. *Nature*, 361:608–612, 1993. doi: 10.1038/361608a0.

J. Laskar, A. C. M. Correia, M. Gastineau, F. Joutel, B. Levrard, and P. Robutel. Long term evolution and chaotic diffusion of the insolation quantities of Mars. *Icarus*, 170:343–364, 2004. doi: 10.1016/j.icarus.2004.04.005.

L. Le Deit, O. Bourgeois, D. Mège, E. Hauber, S. Le Mouélic, M. Massé, R. Jaumann, and J.-P. Bibring. Morphology, stratigraphy, and mineralogical composition of a layered formation covering the plateaus around Valles Marineris, Mars: Implications for its geological history. *Icarus*, 208:684–703, 2010. doi: 10.1016/j.icarus.2010.03.012.

C.-T. A. Lee, D. M. Morton, M. G. Little, R. Kistler, U. N. Horodyskyj, W. P. Leeman, and A. Agranier. Regulating continent growth and composition by chemical weathering. *Proceedings of the National Academy of Science*, 105:4981–4986, 2008. doi: 10.1073/pnas.0711143105.

M.R. Leeder. *Sedimentary basins: from turbulence to tectonics (1st edition)*. Blackwell Scientific, 1999.

A. Léger, D. Rouan, J. Schneider, P. Barge, M. Fridlund, B. Samuel, M. Ollivier, E. Guenther, M. Deleuil, H. J. Deeg, M. Auvergne, R. Alonso, S. Aigrain, A. Alapini, J. M. Almenara, A. Baglin, M. Barbieri, H. Bruntt, P. Bordé, F. Bouchy, J. Cabrera, C. Catala, L. Carone, S. Carpano, S. Csizmadia, R. Dvorak, A. Erikson, S. Ferraz-Mello, B. Foing, F. Fressin, D. Gandolfi, M. Gillon, P. Gondoin, O. Grasset,

T. Guillot, A. Hatzes, G. Hébrard, L. Jorda, H. Lammer, A. Llebaria, B. Loeillet, M. Mayor, T. Mazeh, C. Moutou, M. Pätzold, F. Pont, D. Queloz, H. Rauer, S. Renner, R. Samadi, A. Shporer, C. Sotin, B. Tingley, G. Wuchterl, M. Adda, P. Agogu, T. Appourchaux, H. Ballans, P. Baron, T. Beaufort, R. Bellenger, R. Berlin, P. Bernardi, D. Blouin, F. Baudin, P. Bodin, L. Boisnard, L. Boit, F. Bonneau, S. Borzeix, R. Briet, J.-T. Buey, B. Butler, D. Cailleau, R. Cautain, P.-Y. Chabaud, S. Chaintreuil, F. Chiavassa, V. Costes, V. Cuna Parrho, F. de Oliveira Fialho, M. Decaudin, J.-M. Defise, S. Djalal, G. Epstein, G.-E. Exil, C. Fauré, T. Fenouillet, A. Gaboriaud, A. Gallic, P. Gamet, P. Gavalda, E. Grolleau, R. Gruneisen, L. Gueguen, V. Guis, V. Guivarc'h, P. Guterman, D. Hallouard, J. Hasiba, F. Heuripeau, G. Huntzinger, H. Hustaix, C. Imad, C. Imbert, B. Johlander, M. Jouret, P. Journoud, F. Karioty, L. Kerjean, V. Lafaille, L. Lafond, T. Lam-Trong, P. Landiech, V. Lapeyrere, T. Larqué, P. Laudet, N. Lautier, H. Lecann, L. Lefevre, B. Leruyet, P. Levacher, A. Magnan, E. Mazy, F. Mertens, J.-M. Mesnager, J.-C. Meunier, J.-P. Michel, W. Monjoin, D. Naudet, K. Nguyen-Kim, J.-L. Orcesi, H. Ottacher, R. Perez, G. Peter, P. Plasson, J.-Y. Plesseria, B. Pontet, A. Pradines, C. Quentin, J.-L. Reynaud, G. Rolland, F. Rollenhagen, R. Romagnan, N. Russ, R. Schmidt, N. Schwartz, I. Sebbag, G. Sedes, H. Smit, M. B. Steller, W. Sunter, C. Surace, M. Tello, D. Tiphène, P. Toulouse, B. Ulmer, O. Vandermarcq, E. Vergnault, A. Vuillemin, and P. Zanatta. Transiting exoplanets from the CoRoT space mission. VIII. CoRoT-7b: the first super-Earth with measured radius. *Astronomy and Astrophysics*, 506:287–302, 2009. doi: 10.1051/0004-6361/200911933.

A. Léger, O. Grasset, B. Fegley, F. Codron, A. F. Albarede, P. Barge, R. Barnes, P. Cance, S. Carpy, F. Catalano, C. Cavarroc, O. Demangeon, S. Ferraz-Mello, P. Gabor, J.-M. Grießmeier, J. Leibacher, G. Libourel, A.-S. Maurin, S. N. Raymond, D. Rouan, B. Samuel, L. Schaefer, J. Schneider, P. A. Schuller, F. Selsis, and C. Sotin. The extreme physical properties of the CoRoT-7b super-Earth. *Icarus*, 213:1–11, 2011. doi: 10.1016/j.icarus.2011.02.004.

A. Lenardic, L.-N. Moresi, A. M. Jellinek, and M. Manga. Continental insulation, mantle cooling, and the surface area of oceans and continents [rapid communication]. *Earth and Planetary Science Letters*, 234: 317–333, 2005. doi: 10.1016/j.epsl.2005.01.038.

A. Lenardic, A. M. Jellinek, and L.-N. Moresi. A climate induced transition in the tectonic style of a terrestrial planet. *Earth and Planetary Science Letters*, 271:34–42, 2008. doi: 10.1016/j.epsl.2008.03.031.

D. W. Leverington. A volcanic origin for the outflow channels of Mars: Key evidence and major implications. *Geomorphology*, 132:51–75, 2011.

J.S. Levy and J.W. Head. Evidence for remnants of ancient ice-rich deposits: Mangala Valles outflow channel, Mars. *Terra Nova*, 17(6):503–509, 2005.

K. W. Lewis, O. Aharonson, J. P. Grotzinger, R. L. Kirk, A. S. McEwen, and T.-A. Suer. Quasi-Periodic Bedding in the Sedimentary Rock Record of Mars. *Science*, 322:1532–, 2008. doi: 10.1126/science.1161870.

K. W. Lewis, O. Aharonson, J. P. Grotzinger, A. S. McEwen, and R. L. Kirk. Global significance of cyclic sedimentary deposits on Mars. In *Lunar and Planetary Institute Science Conference Abstracts*, volume 41 of *Lunar and Planetary Institute Science Conference Abstracts*, page 2648, 2010.

S. R. Lewis, M. Collins, P. L. Read, F. Forget, F. Hourdin, R. Fournier, C. Hourdin, O. Talagrand, and J.-P. Huot. A climate database for Mars. *Journal of Geophysical Research*, 1042:24177–24194, 1999. doi: 10.1029/1999JE001024.

King-Fai Li, Kaveh Pahlevan, Joseph L. Kirschvink, and Yuk L. Yung. Atmospheric pressure as a natural climate regulator for a terrestrial planet with a biosphere. *Proceedings of the National Academy of Sciences*, 106(24):9576–9579, 2009. ISSN 0027-8424. doi: 10.1073/pnas.0809436106.

R. J. Lillis, H. V. Frey, and M. Manga. Rapid decrease in Martian crustal magnetization in the Noachian era: Implications for the dynamo and climate of early Mars. *Geophysical Research Letters*, 351:L14203, 2008. doi: 10.1029/2008GL034338.

J. J. Lissauer, D. Ragozzine, D. C. Fabrycky, J. H. Steffen, E. B. Ford, J. M. Jenkins, A. Shporer, M. J. Holman, J. F. Rowe, E. V. Quintana, N. M. Batalha, W. J. Borucki, S. T. Bryson, D. A. Caldwell, J. A. Carter, D. Ciardi, E. W. Dunham, J. J. Fortney, T. N. Gautier, III, S. Howell, D. G. Koch, D. W. Latham, G. W. Marcy, R. C. Morehead, and D. Sasselov. Architecture and Dynamics of Kepler's Candidate Multiple Transiting Planet Systems. *ArXiv e-prints*, 2011.

J. Liu and T. Schneider. Convective generation of equatorial superrotation in planetary atmospheres. *Journal of Atmospheric Sciences*, 38:in press, 2011.

J. Liu, M. I. Richardson, and R. J. Wilson. An assessment of the global, seasonal, and interannual spacecraft record of Martian climate in the thermal infrared. *Journal of Geophysical Research (Planets)*, 108:5089, 2003. doi: 10.1029/2002JE001921.

R. M. C. Lopes and J. R. Spencer. *Io After Galileo: A New View of Jupiter's Volcanic Moon*. Springer Praxis Books / Geophysical Sciences, 2007.

R. D. Lorenz, C. P. McKay, and J. I. Lunine. Photochemically-induced collapse of Titan's atmosphere. *Science*, 275:642–644, 1997. doi: 10.1126/science.275.5300.642.

R. D. Lorenz, C. P. McKay, and J. I. Lunine. Analytic investigation of climate stability on Titan: sensitivity to volatile inventory. *Planetary and Space Science*, 47:1503–1515, 1999. doi: 10.1016/S0032-0633(99)00038-0.

R. D. Lorenz, E. R. Kraal, E. E. Eddlemon, J. Cheney, and R. Greeley. Sea-surface wave growth under extraterrestrial atmospheres: Preliminary wind tunnel experiments with application to Mars and Titan. *Icarus*, 175:556–560, 2005. doi: 10.1016/j.icarus.2004.11.019.

P. Lowell. The New Canals of Mars. *Nature*, 82:489–491, 1910. doi: 10.1038/082489d0.

S. J. Loyd, T. W. Becker, C. P. Conrad, C. Lithgow-Bertelloni, and F. A. Corsetti. Time variability in Cenozoic reconstructions of mantle heat flow: Plate tectonic cycles and implications for Earth's thermal evolution. *Proceedings of the National Academy of Science*, 1041:14266–14271, 2007. doi: 10.1073/pnas.0706667104.

M. Lüthje, L. T. Pedersen, N. Reeh, and W. Greuell. Modelling the evolution of supraglacial lakes on the West Greenland ice-sheet margin. *Journal of Glaciology*, 52:608–618, 2006. doi: 10.3189/172756506781828386.

T. Lyubetskaya and J. Korenaga. Chemical composition of Earth's primitive mantle and its variance: 2. Implications for global geodynamics. *Journal of Geophysical Research (Solid Earth)*, 112:B03212, 2007. doi: 10.1029/2005JB004224.

D.G. MacMynowski. Can we control El Nino? *Environmental Research Letters*, 4(4), 2009. ISSN 1748-9326. doi: 10.1088/1748-9326/4/4/045111.

J.-B. Madeleine, F. Forget, J. W. Head, B. Levrard, F. Montmessin, and E. Millour. Amazonian northern mid-latitude glaciation on Mars: A proposed climate scenario. *Icarus*, 203:390–405, 2009. doi: 10.1016/j.icarus.2009.04.037.

K. Maher. The dependence of chemical weathering rates on fluid residence time. *Earth and Planetary Science Letters*, 294:101–110, 2010. doi: 10.1016/j.epsl.2010.03.010.

M. C. Malin and K. S. Edgett. Oceans or seas in the Martian northern lowlands: High resolution imaging tests of proposed coastlines. *Geophysical Research Letters*, 26:3049–3052, 1999. doi: 10.1029/1999GL002342.

M. C. Malin and K. S. Edgett. Sedimentary Rocks of Early Mars. *Science*, 290:1927–1937, 2000. doi: 10.1126/science.290.5498.1927.

M. C. Malin and K. S. Edgett. Evidence for Persistent Flow and Aqueous Sedimentation on Early Mars. *Science*, 302:1931–1934, 2003. doi: 10.1126/science.1090544.

M. C. Malin, K. S. Edgett, L. V. Posiolova, S. M. McColley, and E. Z. N. Dobrea. Present-Day Impact Cratering Rate and Contemporary Gully Activity on Mars. *Science*, 314:1573–, 2006. doi: 10.1126/science.1135156.

M. C. Malin, K. S. Edgett, B. A. Cantor, M. A. Caplinger, G. E. Danielson, E. H. Jensen, M. A. Ravine, J. L. Sandoval, and K. D. Supulver. An overview of the 1985-2006 Mars Orbiter Camera science investigation. *International Journal of Mars Science and Exploration*, 5:1–60, 2010. doi: 10.1555/mars.2010.0001.

N. Mangold. Post-Early Mars Fluvial Landforms on Mid-Latitude Impact Ejecta. In *Lunar and Planetary Institute Science Conference Abstracts*, volume 42 of *Lunar and Planetary Institute Science Conference Abstracts*, page 1378, 2011.

N. Mangold and V. Ansan. Detailed study of an hydrological system of valleys, a delta and lakes in the Southwest Thaumasia region, Mars. *Icarus*, 180:75–87, 2006. doi: 10.1016/j.icarus.2005.08.017.

N. Mangold, C. Quantin, V. Ansan, C. Delacourt, and P. Allemand. Evidence for Precipitation on Mars from Dendritic Valleys in the Valles Marineris Area. *Science*, 305:78–81, 2004. doi: 10.1126/science.1097549.

N. Mangold, V. Ansan, P. Masson, C. Quantin, and G. Neukum. Geomorphic study of fluvial landforms on the northern Valles Marineris plateau, Mars. *Journal of Geophysical Research (Planets)*, 113:E08009, 2008. doi: 10.1029/2007JE002985.

N. Mangold, L. Roach, R. Milliken, S. Le Mouélic, V. Ansan, J. P. Bibring, P. Masson, J. F. Mustard, S. Murchie, and G. Neukum. A Late Amazonian alteration layer related to local volcanism on Mars. *Icarus*, 207:265–276, 2010. doi: 10.1016/j.icarus.2009.10.015.

N. Mangold, V. Ansan, P. Masson, and C. Vincendon. Estimate of aeolian dust thickness in Arabia Terra, Mars: Implications of a thick mantle (¿ 20 m) for hydrogen detection. *Geomorphologie - Relief Processus Environnement*, (1):23–31, 2009. ISSN 1266-5304.

G.W. Marcy. Stars and planets within our reach. In *The Next 40 Years of Exoplanets*, 2011.

M. M. Marinova, C. P. McKay, and H. Hashimoto. Radiative-convective model of warming Mars with artificial greenhouse gases. *Journal of Geophysical Research (Planets)*, 110:E03002, 2005. doi: 10.1029/2004JE002306.

P. Markowski and Y. Richardson. *Mesoscale Meteorology in Midlatitudes*. Wiley, 2010.

P. Marsh and M.K. Woo. Wetting front advance and freezing of meltwater within a snow cover. 1. Observations in the Canadian Arctic. *Water Resources Research*, 20(12):1853–1864, 1984.

B. Marty and K. Marti. Signatures of early differentiation of Mars. *Earth and Planetary Science Letters*, 196:251–263, 2002. doi: 10.1016/S0012-821X(01)00612-4.

G. A. Marzo, A. F. Davila, L. L. Tornabene, J. M. Dohm, A. G. Fairén, C. Gross, T. Kneissl, J. L. Bishop, T. L. Roush, and C. P. McKay. Evidence for Hesperian impact-induced hydrothermalism on Mars. *Icarus*, 208:667–683, 2010. doi: 10.1016/j.icarus.2010.03.013.

M. Massé, O. Bourgeois, S. Le Mouélic, C. Verpoorter, L. Le Deit, and J. P. Bibring. Martian polar and circum-polar sulfate-bearing deposits: Sublimation tills derived from the North Polar Cap. *Icarus*, 209: 434–451, 2010. doi: 10.1016/j.icarus.2010.04.017.

I. Matsuyama and M. Manga. Mars without the equilibrium rotational figure, Tharsis, and the remnant rotational figure,. *J. Geophys. Res.*, 115:E1020, 2010. doi: doi:10.1029/2010JE003686.

T. B. McCord, J. Castillo-Rogez, and A. Rivkin. Ceres: Its Origin, Evolution and Structure and Dawn's Potential Contribution. *Space Science Reviews*, page 92, 2011. doi: 10.1007/s11214-010-9729-9.

A. S. McEwen, C. J. Hansen, W. A. Delamere, E. M. Eliason, K. E. Herkenhoff, L. Keszthelyi, V. C. Gulick, R. L. Kirk, M. T. Mellon, J. A. Grant, N. Thomas, C. M. Weitz, S. W. Squyres, N. T. Bridges, S. L. Murchie, F. Seelos, K. Seelos, C. H. Okubo, M. P. Milazzo, L. L. Tornabene, W. L. Jaeger, S. Byrne, P. S. Russell, J. L. Griffes, S. Martínez-Alonso, A. Davatzes, F. C. Chuang, B. J. Thomson, K. E. Fishbaugh, C. M. Dundas, K. J. Kolb, M. E. Banks, and J. J. Wray. A Closer Look at Water-Related Geologic Activity on Mars. *Science*, 317:1706–, 2007. doi: 10.1126/science.1143987.

A. S. McEwen, L. Ojha, C. M. Dundas, S. S. Mattson, S. Byrne, J. J. Wray, S. C. Cull, S. L. Murchie, N. Thomas, and V. C. Gulick. Seasonal Flows on Warm Martian Slopes. *Science*, 333:740–, 2011. doi: 10.1126/science.1204816.

T. R. McGetchin, M. Settle, and J. W. Head. Radial thickness variation in impact crater ejecta: Implications for lunar basin deposits. *Earth and Planetary Science Letters*, 20:226–236, 1973. doi: 10.1016/0012-821X(73)90162-3.

C. P. McKay, R. A. Wharton, Jr., S. W. Squyres, and G. D. Clow. Thickness of ice on perennially frozen lakes. *Nature*, 313:561, February 1985. doi: 10.1038/313561a0.

C. P. McKay, J. B. Pollack, and R. Courtin. The greenhouse and antigreenhouse effects on Titan. *Science*, 253:1118–1121, 1991. doi: 10.1126/science.253.5024.1118.

D. McKenzie. The generation and compaction of partially molten rock. *Journal of Petrology*, 5:713–765, 1984.

D. McKenzie and M. J. Bickle. The volume and composition of melt generated by extension of the lithosphere. *Journal of Petrology*, 29:625–679, 1988.

D. McKenzie and F. Nimmo. The generation of martian floods by the melting of ground ice above dykes. *Nature*, 397:231–233, 1999. doi: 10.1038/16649.

D. McKenzie, J. Jackson, and K. Priestley. Thermal structure of oceanic and continental lithosphere [rapid communication]. *Earth and Planetary Science Letters*, 233:337–349, 2005. doi: 10.1016/j.epsl.2005.02.005.

McKinsey. Pathways to a low-carbon economy: version 2 of the greenhouse gas abatement cost curve. Technical report, McKinsey, 2009.

D. McKnight. Onyx River at Vanda gauge measurements. National Science Foundation McMurdo Dry Valleys Long Term Ecological Research Signature Datasets knb-lter-mcm.9022.4, 2011.

S. M. McLennan and J. P. Grotzinger. The sedimentary rock cycle of Mars. In Bell, J., III, editor, *The Martian Surface - Composition, Mineralogy, and Physical Properties*, volume 9 of *Cambridge Planetary Science Series*, page 541. Cambridge University Press, 2008.

S. M. McLennan, J. F. Bell, W. M. Calvin, P. R. Christensen, B. C. Clark, P. A. de Souza, J. Farmer, W. H. Farrand, D. A. Fike, R. Gellert, A. Ghosh, T. D. Glotch, J. P. Grotzinger, B. Hahn, K. E. Herkenhoff, J. A. Hurowitz, J. R. Johnson, S. S. Johnson, B. Jolliff, G. Klingelhöfer, A. H. Knoll, Z. Learner, M. C. Malin, H. Y. McSween, J. Pocock, S. W. Ruff, L. A. Soderblom, S. W. Squyres, N. J. Tosca, W. A. Watters, M. B. Wyatt, and A. Yen. Provenance and diagenesis of the evaporite-bearing Burns formation, Meridiani Planum, Mars. *Earth and Planetary Science Letters*, 240:95–121, 2005. doi: 10.1016/j.epsl.2005.09.041.

M. T. Mellon and B. M. Jakosky. The distribution and behavior of Martian ground ice during past and present epochs. *Journal of Geophysical Research*, 1001:11781–11799, 1995. doi: 10.1029/95JE01027.

M. T. Mellon, B. M. Jakosky, H. H. Kieffer, and P. R. Christensen. High-Resolution Thermal Inertia Mapping from the Mars Global Surveyor Thermal Emission Spectrometer. *Icarus*, 148:437–455, 2000. doi: 10.1006/icar.2000.6503.

M. T. Mellon, M. C. Malin, R. E. Arvidson, M. L. Searls, H. G. Sizemore, T. L. Heet, M. T. Lemmon, H. U. Keller, and J. Marshall. The periglacial landscape at the Phoenix landing site. *Journal of Geophysical Research (Planets)*, 114:E00E06, 2009. doi: 10.1029/2009JE003418.

MEPAG. Mars scientific goals, objectives, investigations, and priorities, version 17. Technical report, Mars Exploration Program Analysis Group (MEPAG), 2010. URL `http://mepag.jpl.nasa.gov/reports/MEPAG_Goals_Document_2010_v17.pdf`.

T. M. Merlis and T. Schneider. Atmospheric dynamics of Earth-like tidally locked aquaplanets. *Journal of Advances in Modeling Earth Systems*, 2:13, 2010. doi: 10.3894/JAMES.2010.2.13.

J. M. Metz, J. P. Grotzinger, D. Mohrig, R. Milliken, B. Prather, C. Pirmez, A. S. McEwen, and C. M. Weitz. Sublacustrine depositional fans in southwest Melas Chasma. *Journal of Geophysical Research (Planets)*, 114:E10002, 2009a. doi: 10.1029/2009JE003365.

J. M. Metz, J. P. Grotzinger, D. M. Rubin, K. W. Lewis, S. W. Squyres, and J. F. Bell. Sulfate-Rich Eolian and Wet Interdune Deposits, Erebus Crater, Meridiani Planum, Mars. *Journal of Sedimentary Research*, 79:247–264, 2009b. doi: 10.2110/jsr.2009.033.

T. I. Michaels and S. C. R. Rafkin. Meteorological predictions for candidate 2007 Phoenix Mars Lander sites using the Mars Regional Atmospheric Modeling System (MRAMS). *Journal of Geophysical Research (Planets)*, 113:E00A07, 2008. doi: 10.1029/2007JE003013.

T. I. Michaels, A. Colaprete, and S. C. R. Rafkin. Significant vertical water transport by mountain-induced circulations on Mars. *Geophysical Research Letters*, 331:L16201, 2006. doi: 10.1029/2006GL026562.

R. E. Milliken, G. A. Swayze, R. E. Arvidson, J. L. Bishop, R. N. Clark, B. L. Ehlmann, R. O. Green, J. P. Grotzinger, R. V. Morris, S. L. Murchie, J. F. Mustard, and C. Weitz. Opaline silica in young deposits on Mars. *Geology*, 36:847–850, 2008.

R. E. Milliken, J. P. Grotzinger, and B. J. Thomson. Paleoclimate of Mars as captured by the stratigraphic record in Gale Crater. *Geophysical Research Letters*, 370:L04201, 2010. doi: 10.1029/2009GL041870.

E. Millour, F. Forget, and S. R. Lewis. European Mars Climate Database v4.3 Detailed Design Document. Technical report, Lab. de Météorol. Dyn., Paris. (Available at http://www-mars.lmd.jussieu.fr/), 2008.

D. W. Ming, R. V. Morris, and B. C. Clark. Aqueous alteration on Mars. In Bell, J., III, editor, *The Martian Surface - Composition, Mineralogy, and Physical Properties*, volume 9 of *Cambridge Planetary Science Series*, page 519. Cambridge University Press, 2008.

D. A. Minton and R. Malhotra. Assessing the Massive Young Sun Hypothesis to Solve the Warm Young Earth Puzzle. *Astrophysical Journal*, 660:1700–1706, 2007. doi: 10.1086/514331.

M. A. Mischna and M. I. Richardson. A reanalysis of water abundances in the Martian atmosphere at high obliquity. *Geophysical Research Letters*, 320:L03201, 2005. doi: 10.1029/2004GL021865.

M. A. Mischna, M. I. Richardson, R. J. Wilson, and D. J. McCleese. On the orbital forcing of Martian water and CO_2 cycles: A general circulation model study with simplified volatile schemes. *Journal of Geophysical Research (Planets)*, 108:5062, 2003. doi: 10.1029/2003JE002051.

J. L. Mitchell and G. K. Vallis. The transition to superrotation in terrestrial atmospheres. *Journal of Geophysical Research (Planets)*, 115:E12008, 2010. doi: 10.1029/2010JE003587.

D. T. F. Möhlmann, M. Niemand, V. Formisano, H. Savijärvi, and P. Wolkenberg. Fog phenomena on Mars. *Planetary and Space Science*, 57:1987–1992, 2009. doi: 10.1016/j.pss.2009.08.003.

D. R. Montgomery and K. B. Gran. Downstream variations in the width of bedrock channels. *Water Resources Research*, 37:1841–1846, 2001. doi: 10.1029/2000WR900393.

J. M. Moore and A. D. Howard. Large alluvial fans on Mars. *Journal of Geophysical Research (Planets)*, 110:E04005, 2005. doi: 10.1029/2004JE002352.

W. B. Moore. Note: The Thermal State of Io. *Icarus*, 154:548–550, 2001. doi: 10.1006/icar.2001.6739.

W. B. Moore. Tidal heating and convection in Io. *Journal of Geophysical Research (Planets)*, 108:5096, 2003. doi: 10.1029/2002JE001943.

A. Morbidelli, K. Tsiganis, A. Crida, H. F. Levison, and R. Gomes. Dynamics of the Giant Planets of the Solar System in the Gaseous Protoplanetary Disk and Their Relationship to the Current Orbital Architecture. *Astronomical Journal*, 134:1790–1798, 2007. doi: 10.1086/521705.

G. A. Morgan, J. W. Head, F. Forget, J.-B. Madeleine, and A. Spiga. Gully formation on Mars: Two recent phases of formation suggested by links between morphology, slope orientation and insolation history. *Icarus*, 208:658–666, 2010. doi: 10.1016/j.icarus.2010.02.019.

J. Mouginot, A. Pommerol, W. Kofman, P. Beck, B. Schmitt, A. Herique, C. Grima, A. Safaeinili, and J. J. Plaut. The 3-5 MHz global reflectivity map of Mars by MARSIS/Mars Express: Implications for the current inventory of subsurface H_2O. *Icarus*, 210:612–625, 2010. doi: 10.1016/j.icarus.2010.07.003.

S. Murchie, L. Roach, F. Seelos, R. Milliken, J. Mustard, R. Arvidson, S. Wiseman, K. Lichtenberg, J. Andrews-Hanna, J. Bishop, J.-P. Bibring, M. Parente, and R. Morris. Evidence for the origin of layered deposits in Candor Chasma, Mars, from mineral composition and hydrologic modeling. *Journal of Geophysical Research (Planets)*, 114:E00D05, 2009a. doi: 10.1029/2009JE003343.

S. L. Murchie, J. F. Mustard, B. L. Ehlmann, R. E. Milliken, J. L. Bishop, N. K. McKeown, E. Z. Noe Dobrea, F. P. Seelos, D. L. Buczkowski, S. M. Wiseman, R. E. Arvidson, J. J. Wray, G. Swayze, R. N. Clark, D. J. Des Marais, A. S. McEwen, and J.-P. Bibring. A synthesis of Martian aqueous mineralogy after 1 Mars year of observations from the Mars Reconnaissance Orbiter. *Journal of Geophysical Research (Planets)*, 114:E00D06, 2009b. doi: 10.1029/2009JE003342.

B. H. Murphy, K. A. Farley, and J. C. Zachos. An extraterrestrial ^{3}He-based timescale for the Paleocene-Eocene thermal maximum (PETM) from Walvis Ridge, IODP Site 1266. *Geochimica et Cosmochimca Acta*, 74:5098–5108, 2010. doi: 10.1016/j.gca.2010.03.039.

C. D. Murray and S. F. Dermott. *Solar System Dynamics*. Cambridge University Press, 1999.

J. F. Mustard, B. L. Ehlmann, S. L. Murchie, F. Poulet, N. Mangold, J. W. Head, J.-P. Bibring, and L. H. Roach. Composition, Morphology, and Stratigraphy of Noachian Crust around the Isidis basin. *Journal of Geophysical Research (Planets)*, 114:E00D12, 2009. doi: 10.1029/2009JE003349.

National Research Council. Vision and voyages for planetary science in the decade 2013-2022. Technical report, Space Studies Board, 2011.

G. Neukum, A. T. Basilevsky, T. Kneissl, M. G. Chapman, S. van Gasselt, G. Michael, R. Jaumann, H. Hoffmann, and J. K. Lanz. The geologic evolution of Mars: Episodicity of resurfacing events and ages from cratering analysis of image data and correlation with radiometric ages of Martian meteorites. *Earth and Planetary Science Letters*, 294:204–222, 2010. doi: 10.1016/j.epsl.2009.09.006.

S. Newcomb. The optical and psychological principles involved in the interpretation of the so-called canals of Mars. *Astrophysical Journal*, 26:1, 1907. doi: 10.1086/141466.

C. E. Newman, S. R. Lewis, and P. L. Read. The atmospheric circulation and dust activity in different orbital epochs on Mars. *Icarus*, 174:135–160, 2005. doi: 10.1016/j.icarus.2004.10.023.

H. E. Newsom. Composition of the Solar System, Planets, Meteorites, and Major Terrestrial Reservoirs. In T. J. Ahrens, editor, *Global Earth Physics: A Handbook of Physical Constants*, page 159, 1995.

CA Nezat, WB Lyons, and KA Welch. Chemical weathering in streams of a polar desert, Taylor Valley, Antarctica. *Geological Society of American Bulletin*, 113(11):1401–1408, NOV 2001.

P. B. Niles and J. Michalski. Meridiani Planum sediments on Mars formed through weathering in massive ice deposits. *Nature Geoscience*, 2:215–220, 2009. doi: 10.1038/ngeo438.

F. Nimmo. Energetics of the core (chapter 8.02). In Gerald Schubert, editor, *Treatise on Geophysics*, pages 8.31 – 8.65. Elsevier, Amsterdam, 1 edition, 2007.

F. Nimmo and K. Tanaka. Early Crustal Evolution of Mars. *Annual Review of Earth and Planetary Sciences*, 33:133–161, 2005. doi: 10.1146/annurev.earth.33.092203.122637.

P. A. O'Gorman and T. Schneider. The Hydrological Cycle over a Wide Range of Climates Simulated with an Idealized GCM. *Journal of Climate*, 21:3815, 2008. doi: 10.1175/2007JCLI2065.1.

E. Ohtani and M. Maeda. Density of basaltic melt at high pressure and stability of the melt at the base of the lower mantle. *Earth and Planetary Science Letters*, 193:69–75, 2001. doi: 10.1016/S0012-821X(01)00505-2.

C. H. Okubo. Strength and deformability of light-toned layered deposits observed by MER Opportunity: Eagle to Erebus craters, Mars. *Geophysical Research Letters*, 34:L20205, October 2007. doi: 10.1029/2007GL031327.

A.A. Olsen and J.D. Rimstidt. Using a mineral lifetime diagram to evaluate the persistence of olivine on Mars. *American Mineralogist*, 92(4):598–602, 2007. doi: 10.2138/am.2007.2462.

C. O'Neill and A. Lenardic. Geological consequences of super-sized Earths. *Geophysical Research Letters*, 341:L19204, 2007. doi: 10.1029/2007GL030598.

C. Oppenheimer. Volcanic Degassing. *Treatise on Geochemistry*, 3:123–166, 2003. doi: 10.1016/B0-08-043751-6/03020-6.

M. M. Osterloo, V. E. Hamilton, J. L. Bandfield, T. D. Glotch, A. M. Baldridge, P. R. Christensen, L. L. Tornabene, and F. S. Anderson. Chloride-Bearing Materials in the Southern Highlands of Mars. *Science*, 319:1651, 2008. doi: 10.1126/science.1150690.

M. M. Osterloo, F. S. Anderson, V. E. Hamilton, and B. M. Hynek. Geologic context of proposed chloride-bearing materials on Mars. *Journal of Geophysical Research (Planets)*, 115:E10012, 2010. doi: 10.1029/2010JE003613.

P. Papale. Modeling of the solubility of a one-component H_2O or CO_2 fluid in silicate liquids. *Contributions to Mineralogy and Petrology*, 126:237–251, 1997. doi: 10.1007/s004100050247.

P. Papale. Modeling of the solubility of a two-component H_2O+CO_2 fluid in silicate liquids. *American Mineralogist*, 84(4):477–492, 1999. ISSN 0003-004X.

A. M. Papuc and G. F. Davies. The internal activity and thermal evolution of Earth-like planets. *Icarus*, 195:447–458, 2008. doi: 10.1016/j.icarus.2007.12.016.

T. J. Parker, D. S. Gorsline, R. S. Saunders, D. C. Pieri, and D. M. Schneeberger. Coastal geomorphology of the Martian northern plains. *Journal of Geophysical Research*, 981:11061, 1993. doi: 10.1029/93JE00618.

E. M. Parmentier and M. T. Zuber. Early evolution of Mars with mantle compositional stratification or hydrothermal crustal cooling. *Journal of Geophysical Research (Planets)*, 112:E02007, 2007. doi: 10.1029/2005JE002626.

J. T. Perron, M. P. Lamb, C. D. Koven, I. Y. Fung, E. Yager, and M. Ádámkovics. Valley formation and methane precipitation rates on Titan. *Journal of Geophysical Research (Planets)*, 111:E11001, 2006. doi: 10.1029/2005JE002602.

R. J. Phillips, M. T. Zuber, S. E. Smrekar, M. T. Mellon, J. W. Head, K. L. Tanaka, N. E. Putzig, S. M. Milkovich, B. A. Campbell, J. J. Plaut, A. Safaeinili, R. Seu, D. Biccari, L. M. Carter, G. Picardi, R. Orosei, P. S. Mohit, E. Heggy, R. W. Zurek, A. F. Egan, E. Giacomoni, F. Russo, M. Cutigni, E. Pettinelli, J. W. Holt, C. J. Leuschen, and L. Marinangeli. Mars North Polar Deposits: Stratigraphy, Age, and Geodynamical Response. *Science*, 320:1182–, 2008. doi: 10.1126/science.1157546.

R. J. Phillips, B. J. Davis, K. L. Tanaka, S. Byrne, M. T. Mellon, N. E. Putzig, R. M. Haberle, M. A. Kahre, B. A. Campbell, L. M. Carter, I. B. Smith, J. W. Holt, S. E. Smrekar, D. C. Nunes, J. J. Plaut, A. F. Egan, T. N. Titus, and R. Seu. Massive CO_2 Ice Deposits Sequestered in the South Polar Layered Deposits of Mars. *Science*, 332:838–, 2011. doi: 10.1126/science.1203091.

R. Pielke, Jr. *The Climate Fix*. Basic Books, 2011.

R. A. Pielke and Y. Mahrer. Verification Analysis of the University of Virginia Three-Dimensional Mesoscale Model Prediction over South Florida for 1 July 1973. *Monthly Weather Review*, 106:1568, 1978. doi: 10.1175/1520-0493(1978)106<1568:VAOTUO>2.0.CO;2.

R.A. Pielke. *Mesoscale Meteorological Modeling, 2nd edition*. Academic Press, 2002.

R. Pierrehumbert. *Principles of Planetary Climate*. Cambridge University Press, 2010.

R. Pierrehumbert and E. Gaidos. Hydrogen Greenhouse Planets Beyond the Habitable Zone. *Astrophysical Journal Letters*, 734:L13+, 2011. doi: 10.1088/2041-8205/734/1/L13.

R. T. Pierrehumbert. Thermostats, Radiator Fins, and the Local Runaway Greenhouse. *Journal of Atmospheric Sciences*, 52:1784–1806, 1995. doi: 10.1175/1520-0469(1995)052<1784:TRFATL>2.0.CO;2.

R. T. Pierrehumbert. The hydrologic cycle in deep-time climate problems. *Nature*, 419:191–198, 2002.

R. T. Pierrehumbert. A Palette of Climates for Gliese 581g. *Astrophysical Journal Letters*, 726:L8+, 2011. doi: 10.1088/2041-8205/726/1/L8.

J. J. Plaut, G. Picardi, A. Safaeinili, A. B. Ivanov, S. M. Milkovich, A. Cicchetti, W. Kofman, J. Mouginot, W. M. Farrell, R. J. Phillips, S. M. Clifford, A. Frigeri, R. Orosei, C. Federico, I. P. Williams, D. A. Gurnett, E. Nielsen, T. Hagfors, E. Heggy, E. R. Stofan, D. Plettemeier, T. R. Watters, C. J. Leuschen, and P. Edenhofer. Subsurface Radar Sounding of the South Polar Layered Deposits of Mars. *Science*, 316:92–, April 2007. doi: 10.1126/science.1139672.

C. S. Plesko, E. Asphaug, R. P. Weaver, K. H. Wohletz, and D. G. Korycansky. Initial Conditions of an Impact-generated Greenhouse Event from Hydrocode Models of Large Impacts on Noachian Mars. In *Lunar and Planetary Institute Science Conference Abstracts*, volume 40 of *Lunar and Planetary Inst. Technical Report*, page 2167, 2009.

J. B. Pollack, J. F. Kasting, S. M. Richardson, and K. Poliakoff. The case for a wet, warm climate on early Mars. *Icarus*, 71:203–224, 1987. doi: 10.1016/0019-1035(87)90147-3.

F. Pont and L. Eyer. Isochrone ages for field dwarfs: method and application to the age-metallicity relation. *Monthly Notices of the Royal Astronomical Society*, 351:487–504, 2004. doi: 10.1111/j.1365-2966.2004.07780.x.

F. Postberg, S. Kempf, J. Schmidt, N. Brilliantov, A. Beinsen, B. Abel, U. Buck, and R. Srama. Sodium salts in E-ring ice grains from an ocean below the surface of Enceladus. *Nature*, 459:1098–1101, June 2009. doi: 10.1038/nature08046.

M. Postman, W. A. Traub, J. Krist, K. Stapelfeldt, R. Brown, W. Oegerle, A. Lo, M. Clampin, R. Soummer, J. Wiseman, and M. Mountain. Advanced Technology Large-Aperture Space Telescope (ATLAST): Characterizing Habitable Worlds. In V. Coudé Du Foresto, D. M. Gelino, & I. Ribas, editor, *Pathways Towards Habitable Planets*, volume 430 of *Astronomical Society of the Pacific Conference Series*, page 361, 2010.

PriceWaterhouseCoopers. Counting the cost of carbon: low carbon economy index 2011. Technical report, PriceWaterhouseCoopers, 2011.

N. E. Putzig and M. T. Mellon. Apparent thermal inertia and the surface heterogeneity of Mars. *Icarus*, 191:68–94, 2007. doi: 10.1016/j.icarus.2007.05.013.

C. Quantin, P. Allemand, N. Mangold, G. Dromart, and C. Delacourt. Fluvial and lacustrine activity on layered deposits in Melas Chasma, Valles Marineris, Mars. *Journal of Geophysical Research (Planets)*, 110:E12S19, 2005. doi: 10.1029/2005JE002440.

S. C. R. Rafkin and T. I. Michaels. Meteorological predictions for 2003 Mars Exploration Rover high-priority landing sites. *Journal of Geophysical Research (Planets)*, 108:8091, 2003. doi: 10.1029/2002JE002027.

S. C. R. Rafkin, R. M. Haberle, and T. I. Michaels. The Mars Regional Atmospheric Modeling System: Model Description and Selected Simulations. *Icarus*, 151:228–256, 2001. doi: 10.1006/icar.2001.6605.

J. A. Rathbun, J. R. Spencer, L. K. Tamppari, T. Z. Martin, L. Barnard, and L. D. Travis. Mapping of Io's thermal radiation by the Galileo PhotoPolarimeter-Radiometer (PPR) instrument. *Icarus*, 169:127–139, 2004. doi: 10.1016/j.icarus.2003.12.021.

S. N. Raymond, T. Quinn, and J. I. Lunine. Making other earths: dynamical simulations of terrestrial planet formation and water delivery. *Icarus*, 168:1–17, 2004. doi: 10.1016/j.icarus.2003.11.019.

S. N. Raymond, T. Quinn, and J. I. Lunine. High-resolution simulations of the final assembly of Earth-like planets I. Terrestrial accretion and dynamics. *Icarus*, 183:265–282, 2006. doi: 10.1016/j.icarus.2006.03.011.

P. R. Read and S. R. Lewis. *The Martian climate revisited: atmosphere and environment of a desert planet*. Springer-Praxis, 2004.

M. S. Rice and J. F. Bell. Geologic Mapping of the Proposed Mars Science Laboratory (MSL) Landing Ellipse in Eberswalde Crater. In *Lunar and Planetary Institute Science Conference Abstracts*, volume 41 of *Lunar and Planetary Institute Science Conference Abstracts*, page 2524, 2010.

M. S. Rice, J. F. Bell, E. A. Cloutis, J. J. Wray, K. E. Herkenhoff, R. Sullivan, J. R. Johnson, and R. B. Anderson. Temporal observations of bright soil exposures at Gusev crater, Mars. *Journal of Geophysical Research (Planets)*, 116:E00F14, 2011. doi: 10.1029/2010JE003683.

M. I. Richardson and M. A. Mischna. Long-term evolution of transient liquid water on Mars. *Journal of Geophysical Research (Planets)*, 110:E03003, 2005. doi: 10.1029/2004JE002367.

M. I. Richardson and A. Soto. Controls on precipitation and aridity for ancient Mars. In *Second Workshop on Mars Valley Networks*, Smithson. Inst., Moab, Utah., 2008a.

M. I. Richardson and A. Soto. Water at the surface of ancient Mars. In *Second Workshop on Mars Valley Networks*, Smithson. Inst., Moab, Utah., 2008b.

A. Ridgwell and R. E. Zeebe. The role of the global carbonate cycle in the regulation and evolution of the Earth system [rapid communication]. *Earth and Planetary Science Letters*, 234:299–315, 2005. doi: 10.1016/j.epsl.2005.03.006.

A. E. Ringwood. Phase transformations and their bearing on the constitution and dynamics of the mantle. *Geochimica et Cosmochimica Acta*, 55:2083–2110, 1991. doi: 10.1016/0016-7037(91)90090-R.

E. J. Rivera, J. J. Lissauer, R. P. Butler, G. W. Marcy, S. S. Vogt, D. A. Fischer, T. M. Brown, G. Laughlin, and G. W. Henry. A 7.5 Earth Mass Planet Orbiting the Nearby Star, GJ 876. *Astrophysical Journal*, 634:625–640, 2005. doi: 10.1086/491669.

L. H. Roach, J. F. Mustard, G. Swayze, R. E. Milliken, J. L. Bishop, S. L. Murchie, and K. Lichtenberg. Hydrated mineral stratigraphy of Ius Chasma, Valles Marineris. *Icarus*, 206:253–268, 2010. doi: 10.1016/j.icarus.2009.09.003.

S.R. Robbins. *Planetary Surface Properties, Cratering Physics, and the Volcanic History of Mars from a New Global Martian Crater Database*. PhD thesis, University of Colorado, Boulder, 2011.

G. Roe. Feedbacks, Timescales, and Seeing Red. *Annual Review of Earth and Planetary Sciences*, 37:93–115, 2009. doi: 10.1146/annurev.earth.061008.134734.

G. H. Roe and M. B. Baker. Notes on a Catastrophe: A Feedback Analysis of Snowball Earth. *Journal of Climate*, 23:4694–4703, 2010. doi: 10.1175/2010JCLI3545.1.

R.R. Rogers and M.K. Yau. *A short course in cloud physics*. Wiley-Oxford, 1989.

M.T. et al. Rosing. The rise of continents - An essay on the geologic consequences of photosynthesis. *Palaeogeogr. Palaeoclimatol. Palaeoecol.*, 232:99, 2006.

D. Rouan, H. J. Deeg, O. Demangeon, B. Samuel, C. Cavarroc, B. Fegley, and A. Léger. The Orbital Phases and Secondary Transits of Kepler-10b. A Physical Interpretation Based on the Lava-ocean Planet Model. *Astrophysical Journal Letters*, 741:L30, 2011. doi: 10.1088/2041-8205/741/2/L30.

S. Salter, G. Sortino, and J. Latham. Sea-going hardware for the cloud albedo method of reversing global warming. *Philosophical Transactions of the Royal Society A*, 366(1882):3989–4006, 2008. ISSN 1364-503X. doi: 10.1098/rsta.2008.0136.

D. L. Santiago, A. Colaprete, R. M. Haberle, L. C. Sloan, and E. Asphaug. Outflow Channels Influencing Martian Climate: Global Circulation Model Simulations with Emplaced Water. In S. Mackwell & E. Stansbery, editor, *36th Annual Lunar and Planetary Science Conference*, volume 36 of *Lunar and Planetary Institute Science Conference Abstracts*, page 1787, 2005.

D. L. Santiago, A. Colaprete, R. M. Haberle, L. C. Sloan, and E. Asphaug. Clouds, Cap, and Consequences: Outflow Events and Mars Hesperian Climate. In S. Mackwell & E. Stansbery, editor, *37th Annual Lunar and Planetary Science Conference*, volume 37 of *Lunar and Planetary Institute Science Conference Abstracts*, page 1484, 2006.

G. G. Schaber, R. G. Strom, H. J. Moore, L. A. Soderblom, R. L. Kirk, D. J. Chadwick, D. D. Dawson, L. R. Gaddis, J. M. Boyce, and J. Russell. Geology and distribution of impact craters on Venus - What are they telling us? *Journal of Geophysical Research*, 971:13257, 1992.

V. Schatz, H. Tsoar, K. S. Edgett, E. J. R. Parteli, and H. J. Herrmann. Evidence for indurated sand dunes in the Martian north polar region. *Journal of Geophysical Research (Planets)*, 111:E04006, 2006. doi: 10.1029/2005JE002514.

R. Schlitzer. Electronic atlas of WOCE hydrographic and tracer data now available. *EoS Transactions*, 81: 45–45, 2000. doi: 10.1029/00EO00028.

T. Schneider, P. A. O'Gorman, and X. J. Levine. Water vapor and the dynamics of climate changes. *Reviews of Geophysics*, 48:RG3001, 2010. doi: 10.1029/2009RG000302.

N. Schorghofer. Fast numerical method for growth and retreat of subsurface ice on Mars. *Icarus*, 208: 598–607, 2010. doi: 10.1016/j.icarus.2010.03.022.

N. Schorghofer and O. Aharonson. Stability and exchange of subsurface ice on Mars. *Journal of Geophysical Research (Planets)*, 110:E05003, 2005. doi: 10.1029/2004JE002350.

G. Schubert, D. L. Turcotte, and P. Olson. *Mantle Convection in the Earth and Planets*. Cambridge University Press, 2001.

S. Schumacher and D. Breuer. An alternative mechanism for recent volcanism on Mars. *Geophysical Research Letters*, 341:L14202, 2007. doi: 10.1029/2007GL030083.

S. Seager, M. Kuchner, C. A. Hier-Majumder, and B. Militzer. Mass-Radius Relationships for Solid Exoplanets. *Astrophysical Journal*, 669:1279–1297, 2007. doi: 10.1086/521346.

A. Segura, J. F. Kasting, V. Meadows, M. Cohen, J. Scalo, D. Crisp, R. A. H. Butler, and G. Tinetti. BiosigNatures from Earth-Like Planets Around M Dwarfs. *Astrobiology*, 5:706–725, 2005. doi: 10.1089/ast.2005.5.706.

T. L. Segura and A. Colaprete. Global Modeling of Impact-induced Greenhouse Warming on Early Mars. In *Lunar and Planetary Institute Science Conference Abstracts*, volume 40 of *Lunar and Planetary Institute Science Conference Abstracts*, page 1056, 2009.

T. L. Segura, O. B. Toon, A. Colaprete, and K. Zahnle. Environmental Effects of Large Impacts on Mars. *Science*, 298:1977–1980, 2002. doi: 10.1126/science.1073586.

T. L. Segura, O. B. Toon, and A. Colaprete. Modeling the environmental effects of moderate-sized impacts on Mars. *Journal of Geophysical Research (Planets)*, 113:E11007, 2008. doi: 10.1029/2008JE003147.

F. Selsis, R. D. Wordsworth, and F. Forget. Thermal phase curves of nontransiting terrestrial exoplanets. I. Characterizing atmospheres. *Astronomy and Astrophysics*, 532:A1+, 2011. doi: 10.1051/0004-6361/201116654.

M. M. Selvans, J. J. Plaut, O. Aharonson, and A. Safaeinili. Internal structure of Planum Boreum, from Mars advanced radar for subsurface and ionospheric sounding data. *Journal of Geophysical Research (Planets)*, 115:E09003, September 2010. doi: 10.1029/2009JE003537.

L. E. Senft and S. T. Stewart. Impact crater formation in icy layered terrains on Mars. *Meteoritics and Planetary Science*, 43:1993–2013, 2008. doi: 10.1111/j.1945-5100.2008.tb00657.x.

L. E. Senft and S. T. Stewart. Modeling the morphological diversity of impact craters on icy satellites. *Icarus*, 214:67–81, 2011. doi: 10.1016/j.icarus.2011.04.015.

A. M. Serenelli. New results on standard solar models. *Astrophysics and Space Science*, 328:13–21, 2010. doi: 10.1007/s10509-009-0174-8.

J Shaw and TR Healy. Morphology of the Onyx River system, McMurdo sound region, Antarctica. *New Zealand Journal of Geology and Geophysics*, 23(2):223–238, 1980.

D. E. Shean. Candidate ice-rich material within equatorial craters on Mars. *Geophysical Research Letters*, 372:L24202, 2010. doi: 10.1029/2010GL045181.

D. E. Shean, J. W. Head, J. L. Fastook, and D. R. Marchant. Recent glaciation at high elevations on Arsia Mons, Mars: Implications for the formation and evolution of large tropical mountain glaciers. *Journal of Geophysical Research (Planets)*, 112:E03004, 2007. doi: 10.1029/2006JE002761.

A. P. Showman and T. Guillot. Atmospheric circulation and tides of "51 Pegasus b-like" planets. *Astronomy and Astrophysics*, 385:166–180, 2002. doi: 10.1051/0004-6361:20020101.

D. L. Shuster and B. P. Weiss. Martian Surface Paleotemperatures from Thermochronology of Meteorites. *Science*, 309:594–597, 2005. doi: 10.1126/science.1113077.

S. Silvestro, L. K. Fenton, D. A. Vaz, N. T. Bridges, and G. G. Ori. Ripple migration and dune activity on Mars: Evidence for dynamic wind processes. *Geophysical Research Letters*, 372:L20203, 2010. doi: 10.1029/2010GL044743.

J. A. Skinner and K. L. Tanaka. Evidence for and implications of sedimentary diapirism and mud volcanism in the southern Utopia highland lowland boundary plain, Mars. *Icarus*, 186:41–59, 2007. doi: 10.1016/j.icarus.2006.08.013.

N. H. Sleep. Evolution of the mode of convection within terrestrial planets. *Journal of Geophysical Research*, 105:17563–17578, 2000. doi: 10.1029/2000JE001240.

N. H. Sleep and K. Zahnle. Carbon dioxide cycling and implications for climate on ancient Earth. *Journal of Geophysical Research*, 106:1373–1400, 2001. doi: 10.1029/2000JE001247.

N. H. Sleep and M. D. Zoback. Did Earthquakes Keep the Early Crust Habitable? *Astrobiology*, 7:1023–1032, 2007. doi: 10.1089/ast.2006.0091.

N.H. Sleep. Plate Tectonics through Time (Chapter 9.06). In Gerald Schubert, editor, *Treatise on Geophysics*, pages 145 – 169. Elsevier, Amsterdam, 2007. ISBN 978-0-444-52748-6. doi: 10.1016/B978-044452748-6.00143-7.

N.H. Sleep and D. Bird. Niches of the pre-photosynthetic biosphere and geologic preservation of Earth's earliest ecology. *Geobiology*, 5(2):101–117, 2007. ISSN 1472-4677. doi: 10.1111/j.1472-4669.2007.00105.x.

M. D. Smith. The annual cycle of water vapor on Mars as observed by the Thermal Emission Spectrometer. *Journal of Geophysical Research (Planets)*, 107:5115, 2002. doi: 10.1029/2001JE001522.

M. D. Smith. Interannual variability in TES atmospheric observations of Mars during 1999-2003. *Icarus*, 167:148–165, 2004. doi: 10.1016/j.icarus.2003.09.010.

M. R. Smith, A. R. Gillespie, and D. R. Montgomery. Effect of obliteration on crater-count chronologies for Martian surfaces. *Geophysical Research Letters*, 351:L10202, 2008. doi: 10.1029/2008GL033538.

M. W. Smith, S. Seager, C. M. Pong, J. S. Villaseñor, G. R. Ricker, D. W. Miller, M. E. Knapp, G. T. Farmer, and R. Jensen-Clem. ExoplanetSat: detecting transiting exoplanets using a low-cost CubeSat platform. In *Society of Photo-Optical Instrumentation Engineers (SPIE) Conference Series*, volume 7731 of *Society of Photo-Optical Instrumentation Engineers (SPIE) Conference Series*, 2010. doi: 10.1117/12.856559.

P. M. Smith and P. D. Asimow. Adiabat_1ph: A new public front-end to the MELTS, pMELTS, and pHMELTS models. *Geochemistry, Geophysics, Geosystems*, 60:Q02004, 2005.

R. J. Soare, D. M. Green, and W. H. Pollard. The habitability of Europa: A cautionary note. *EOS Transactions*, 83:231–, 2002. doi: 10.1029/2002EO000161.

S. C. Solomon, O. Aharonson, J. M. Aurnou, W. B. Banerdt, M. H. Carr, A. J. Dombard, H. V. Frey, M. P. Golombek, S. A. Hauck, J. W. Head, B. M. Jakosky, C. L. Johnson, P. J. McGovern, G. A. Neumann, R. J. Phillips, D. E. Smith, and M. T. Zuber. New Perspectives on Ancient Mars. *Science*, 307:1214–1220, 2005. doi: 10.1126/science.1101812.

S. M. Som, D. R. Montgomery, and H. M. Greenberg. Scaling relations for large Martian valleys. *Journal of Geophysical Research (Planets)*, 114:E02005, 2009. doi: 10.1029/2008JE003132.

A. Soto, M. I. Richardson, and C. E. Newman. Global Constraints on Rainfall on Ancient Mars: Oceans, Lakes, and Valley Networks. In *Lunar and Planetary Institute Science Conference Abstracts*, volume 41 of *Lunar and Planetary Institute Science Conference Abstracts*, page 2397, 2010.

A. Soto, M. A. Mischna, and M. I. Richardson. Ancient Mars and Atmospheric Collapse. In F. Forget & E. Millour, editor, *Mars Atmosphere: Modelling and observation*, pages 449–452, 2011.

J. Southworth. Homogeneous studies of transiting extrasolar planets - I. Light-curve analyses. *Monthly Notices of the Royal Astronomical Society*, 386:1644–1666, May 2008. doi: 10.1111/j.1365-2966.2008.13145.x.

D. S. Spiegel and E. L. Turner. Life might be rare despite its early emergence on Earth: a Bayesian analysis of the probability of abiogenesis. *ArXiv e-prints*, 2011.

A. Spiga and F. Forget. A new model to simulate the Martian mesoscale and microscale atmospheric circulation: Validation and first results. *Journal of Geophysical Research (Planets)*, 114:E02009, 2009. doi: 10.1029/2008JE003242.

S. W. Squyres and J. F. Kasting. Early Mars: How Warm and How Wet? *Science*, 265:744–749, 1994. doi: 10.1126/science.265.5173.744.

S. W. Squyres, R. E. Arvidson, J. F. Bell, J. Brückner, N. A. Cabrol, W. Calvin, M. H. Carr, P. R. Christensen, B. C. Clark, L. Crumpler, D. J. Des Marais, C. d'Uston, T. Economou, J. Farmer, W. Farrand, W. Folkner, M. Golombek, S. Gorevan, J. A. Grant, R. Greeley, J. Grotzinger, L. Haskin, K. E. Herkenhoff, S. Hviid, J. Johnson, G. Klingelhöfer, A. H. Knoll, G. Landis, M. Lemmon, R. Li, M. B. Madsen, M. C. Malin, S. M. McLennan, H. Y. McSween, D. W. Ming, J. Moersch, R. V. Morris, T. Parker, J. W. Rice, L. Richter, R. Rieder, M. Sims, M. Smith, P. Smith, L. A. Soderblom, R. Sullivan, H. Wänke, T. Wdowiak, M. Wolff, and A. Yen. The Opportunity Rover's Athena Science Investigation at Meridiani Planum, Mars. *Science*, 306:1698–1703, December 2004. doi: 10.1126/science.1106171.

S. W. Squyres, O. Aharonson, B. C. Clark, B. A. Cohen, L. Crumpler, P. A. de Souza, W. H. Farrand, R. Gellert, J. Grant, J. P. Grotzinger, A. F. C. Haldemann, J. R. Johnson, G. Klingelhöfer, K. W. Lewis, R. Li, T. McCoy, A. S. McEwen, H. Y. McSween, D. W. Ming, J. M. Moore, R. V. Morris, T. J. Parker, J. W. Rice, S. Ruff, M. Schmidt, C. Schröder, L. A. Soderblom, and A. Yen. Pyroclastic Activity at Home Plate in Gusev Crater, Mars. *Science*, 316:738–, May 2007. doi: 10.1126/science.1139045.

S. W. Squyres, A. H. Knoll, R. E. Arvidson, J. W. Ashley, J. F. Bell, W. M. Calvin, P. R. Christensen, B. C. Clark, B. A. Cohen, P. A. de Souza, L. Edgar, W. H. Farrand, I. Fleischer, R. Gellert, M. P. Golombek, J. Grant, J. Grotzinger, A. Hayes, K. E. Herkenhoff, J. R. Johnson, B. Jolliff, G. Klingelhöfer, A. Knudson, R. Li, T. J. McCoy, S. M. McLennan, D. W. Ming, D. W. Mittlefehldt, R. V. Morris, J. W. Rice, C. Schröder, R. J. Sullivan, A. Yen, and R. A. Yingst. Exploration of Victoria Crater by the Mars Rover Opportunity. *Science*, 324:1058–, May 2009. doi: 10.1126/science.1170355.

B.D. Stanley, M.M. Hirschmann, and A.C. Withers. CO_2 solubility in Martian basalts and Martian atmospheric evolution. *Geochimica et Cosmochimica Acta*, 75(20):5987 – 6003, 2011. ISSN 0016-7037. doi: 10.1016/j.gca.2011.07.027.

D. Stevenson. Les styles de convection du manteau et leur influence sur l'évolution des planètes. *Comptes Rendus Geoscience*, 335:99–111, 2003. doi: 10.1016/S1631-0713(03)00009-9.

D. J. Stevenson. Planetary Diversity. *Physics Today*, 57(4):040000–48, 2004. doi: 10.1063/1.1752421.

H. Stommel. Thermohaline convection with two stable regimes of flow. *Tellus*, 13:224, 1961.

M. Sugiyama, P.H. Stone, and K.A. Emanuel. The role of relative humidity in radiative-convective equilibrium. *Journal of the Atmospheric Sciences*, 62(6):2001–2011, 2005. ISSN 0022-4928. doi: 10.1175/JAS3434.1.

R. Sullivan, R. Greeley, M. Kraft, G. Wilson, M. Golombek, K. Herkenhoff, J. Murphy, and P. Smith. Results of the Imager for Mars Pathfinder windsock experiment. *Journal of Geophysical Research*, 105: 24547–24562, 2000. doi: 10.1029/1999JE001234.

J. C. Tarter, P. R. Backus, R. L. Mancinelli, J. M. Aurnou, D. E. Backman, G. S. Basri, A. P. Boss, A. Clarke, D. Deming, L. R. Doyle, E. D. Feigelson, F. Freund, D. H. Grinspoon, R. M. Haberle, S. A. Hauck, II, M. J. Heath, T. J. Henry, J. L. Hollingsworth, M. M. Joshi, S. Kilston, M. C. Liu, E. Meikle, I. N. Reid, L. J. Rothschild, J. Scalo, A. Segura, C. M. Tang, J. M. Tiedje, M. C. Turnbull, L. M. Walkowicz, A. L. Weber, and R. E. Young. A Reappraisal of The Habitability of Planets around M Dwarf Stars. *Astrobiology*, 7:30–65, 2007. doi: 10.1089/ast.2006.0124.

L. L. Taylor, J. R. Leake, J. Quirk, K. Hardy, S. A. Banwart, and D. J. Beerling. Biological weathering and the long-term carbon cycle: integrating mycorrhizal evolution and function into the current paradigm. *Geobiology*, 7(2):171–191, 2009. ISSN 1472-4677. doi: 10.1111/j.1472-4669.2009.00194.x.

S. R. Taylor and S. McLennan. *Planetary Crusts: Their Composition, Origin and Evolution*, volume 10 of *Cambridge Planetary Science Series*. Cambridge University Press, 2009.

B.J. Thomson, N.T. Bridges, R. Milliken, A. Baldridge, S.J. Hook, J.K. Crowley, G.M. Marion, C.R. de Souza Filho, A.J. Brown, and C.M. Weitz. Constraints on the origin and evolution of the layered mound in Gale Crater, Mars using Mars Reconnaissance Orbiter data. *Icarus*, 214(2):413 – 432, 2011. doi: 10.1016/j.icarus.2011.05.002.

F. Tian. Thermal Escape from Super Earth Atmospheres in the Habitable Zones of M Stars. *Astrophysical Journal*, 703:905–909, 2009. doi: 10.1088/0004-637X/703/1/905.

F. Tian, M. W. Claire, J. D. Haqq-Misra, M. Smith, D. C. Crisp, D. Catling, K. Zahnle, and J. F. Kasting. Photochemical and climate consequences of sulfur outgassing on early Mars. *Earth and Planetary Science Letters*, 295:412–418, 2010. doi: 10.1016/j.epsl.2010.04.016.

T. N. Titus, H. H. Kieffer, and P. R. Christensen. Exposed Water Ice Discovered near the South Pole of Mars. *Science*, 299:1048–1051, 2003. doi: 10.1126/science.1080497.

O. B. Toon, R. P. Turco, D. Westphal, R. Malone, and M. S. Liu. A multidimensional model for aerosols - Description of computational analogs. *Journal of Atmospheric Sciences*, 45:2123–2143, 1988. doi: 10.1175/1520-0469(1988)045<2123:AMMFAD>2.0.CO;2.

O. B. Toon, C. P. McKay, T. P. Ackerman, and K. Santhanam. Rapid calculation of radiative heating rates and photodissociation rates in inhomogeneous multiple scattering atmospheres. *Journal of Geophysical Research*, 941:16287–16301, 1989. doi: 10.1029/JD094iD13p16287.

O. B. Toon, T. Segura, and K. Zahnle. The Formation of Martian River Valleys by Impacts. *Annual Review of Earth and Planetary Sciences*, 38:303–322, 2010. doi: 10.1146/annurev-earth-040809-152354.

O.B. Toon, J.B. Pollack, W. Ward, J.A. Burns, and K. Bilski. The astronomical theory of climatic change on mars. *Icarus*, 44(3):552 – 607, 1980. ISSN 0019-1035. doi: 10.1016/0019-1035(80)90130-X.

N. J. Tosca and A. H. Knoll. Juvenile chemical sediments and the long term persistence of water at the surface of Mars. *Earth and Planetary Science Letters*, 286:379–386, 2009. doi: 10.1016/j.epsl.2009.07.004.

J. Touma and J. Wisdom. The chaotic obliquity of Mars. *Science*, 259:1294–1297, 1993. doi: 10.1126/science.259.5099.1294.

D. C. Tozer. Factors determining the temperature evolution of thermally convecting earth models. *Physics of the Earth and Planetary Interiors*, 2:393–398, 1969. doi: 10.1016/0031-9201(69)90036-3.

A.H. Treiman and M.A. Bullock. Mineral reaction buffering of venus' atmosphere: A thermochemical constraint and implications for venus-like planets. *Icarus*. doi: 10.1016/j.icarus.2011.08.019. URL `http://www.sciencedirect.com/science/article/pii/S0019103511003368`.

D. J. Tritton. *Physical fluid dynamics (2nd revised and enlarged edition)*. Oxford University Press, 1988.

S. Turck-Chièze, L. Piau, and S. Couvidat. The Solar Energetic Balance Revisited by Young Solar Analogs, Helioseismology, and Neutrinos. *Astrophysical Journal Letters*, 731:L29+, 2011. doi: 10.1088/2041-8205/731/2/L29.

D. L. Turcotte and G. Schubert. *Geodynamics*. Cambridge University Press, 2002.

K. Umemoto, R. M. Wentzcovitch, and P. B. Allen. Dissociation of $MgSiO_3$ in the Cores of Gas Giants and Terrestrial Exoplanets. *Science*, 311:983–986, 2006. doi: 10.1126/science.1120865.

D. Valencia and R. J. O'Connell. Convection scaling and subduction on Earth and super-Earths. *Earth and Planetary Science Letters*, 286:492–502, 2009. doi: 10.1016/j.epsl.2009.07.015.

D. Valencia, R. J. O'Connell, and D. Sasselov. Internal structure of massive terrestrial planets. *Icarus*, 181: 545–554, 2006. doi: 10.1016/j.icarus.2005.11.021.

D. Valencia, R. J. O'Connell, and D. D. Sasselov. Inevitability of Plate Tectonics on Super-Earths. *Astrophysical Journal Letters*, 670:L45–L48, 2007. doi: 10.1086/524012.

A. R. van Eaton, M. Herzog, C. J. Wilson, and J. McGregor. Microphysical Controls on Ascent of Water-Rich Ash Clouds from Supereruptions. *AGU Fall Meeting Abstracts*, pages C2375+, 2010.

J. van Summeren, C. P. Conrad, and E. Gaidos. Mantle Convection, Plate Tectonics, and Volcanism on Hot Exo-Earths. *Astrophysical Journal Letters*, 736:L15+, 2011. doi: 10.1088/2041-8205/736/1/L15.

D. Vance, D. A. H. Teagle, and G. L. Foster. Variable Quaternary chemical weathering fluxes and imbalances in marine geochemical budgets. *Nature*, 458:493–496, 2009. doi: 10.1038/Nature07828.

J. Vaucher, D. Baratoux, N. Mangold, P. Pinet, K. Kurita, and M. Grégoire. The volcanic history of central Elysium Planitia: Implications for martian magmatism. *Icarus*, 204:418–442, 2009. doi: 10.1016/j.icarus.2009.06.032.

G. J. Vermeij. Historical contingency and the purported uniqueness of evolutionary innovations. *Proceedings of the National Academy of Science*, 103:1804–1809, 2006. doi: 10.1073/pnas.0508724103.

M. Vincendon, F. Forget, and J. Mustard. Water ice at low to midlatitudes on Mars. *Journal of Geophysical Research (Planets)*, 115:E10001, 2010. doi: 10.1029/2010JE003584.

N. J. Vlaar, P. E. van Keken, and A. P. van den Berg. Cooling of the Earth in the Archaean: Consequences of pressure-release melting in a hotter mantle. *Earth and Planetary Science Letters*, 121:1–18, 1994. doi: 10.1016/0012-821X(94)90028-0.

J. C. G. Walker, P. B. Hays, and J. F. Kasting. A negative feedback mechanism for the long-term stabilization of the earth's surface temperature. *Journal of Geophysical Research*, 86:9776–9782, 1981. doi: 10.1029/JC086iC10p09776.

J. M. Wallace and P. V. Hobbs. *Atmosphere science - an introductory survey (2nd edition)*, volume 92 of *International Geophysics Series*. Academic Press., 2006.

D. Waltham. Anthropic selection and the habitability of planets orbiting M and K dwarfs. *Icarus*, 215: 518–521, October 2011. doi: 10.1016/j.icarus.2011.07.023.

C.-Y. Wang, M. Manga, and A. Wong. Floods on Mars released from groundwater by impact. *Icarus*, 175: 551–555, 2005. doi: 10.1016/j.icarus.2004.12.003.

P. Ward. *The Medea Hypothesis*. Princeton University Press, 2009.

N. Warner, S. Gupta, S.-Y. Lin, J.-R. Kim, J.-P. Muller, and J. Morley. Late Noachian to Hesperian climate change on Mars: Evidence of episodic warming from transient crater lakes near Ares Vallis. *Journal of Geophysical Research (Planets)*, 115:E06013, 2010. doi: 10.1029/2009JE003522.

J.K. Warren. *Evaporites: sediments, resources and hydrocarbons*. Springer, 2006.

S. G. Warren. Review. Impurities in snow: effects on albedo and snowmelt. *Annals of Glaciology*, 5:177–179, 1984.

S. G. Warren and W. J. Wiscombe. A Model for the Spectral Albedo of Snow. II: Snow Containing Atmospheric Aerosols. *Journal of Atmospheric Sciences*, 37:2734–2745, 1980. doi: 10.1175/1520-0469(1980)037<2734:AMFTSA>2.0.CO;2.

A.J. Watson. Implications of an anthropic model of evolution for emergence of complex life and intelligence. *Astrobiology*, 8:175–185, 2008.

T. R. Watters, B. Campbell, L. Carter, C. J. Leuschen, J. J. Plaut, G. Picardi, R. Orosei, A. Safaeinili, S. M. Clifford, W. M. Farrell, A. B. Ivanov, R. J. Phillips, and E. R. Stofan. Radar Sounding of the Medusae Fossae Formation Mars: Equatorial Ice or Dry, Low-Density Deposits? *Science*, 318:1125, 2007. doi: 10.1126/science.1148112.

C. M. Weitz, R. E. Milliken, J. A. Grant, A. S. McEwen, R. M. E. Williams, and J. L. Bishop. Light-toned strata and inverted channels adjacent to Juventae and Ganges chasmata, Mars. *Geophysical Research Letters*, 351:L19202, 2008. doi: 10.1029/2008GL035317.

C. M. Weitz, R. E. Milliken, J. A. Grant, A. S. McEwen, R. M. E. Williams, J. L. Bishop, and B. J. Thomson. Mars Reconnaissance Orbiter observations of light-toned layered deposits and associated fluvial landforms on the plateaus adjacent to Valles Marineris. *Icarus*, 205:73–102, 2010. doi: 10.1016/j.icarus.2009.04.017.

M. J. Wenzel, M. Manga, and A. M. Jellinek. Tharsis as a consequence of Mars' dichotomy and layered mantle. *Geophysical Research Letters*, 310:L04702, 2004. doi: 10.1029/2003GL019306.

S. C. Werner. The global Martian volcanic evolutionary history. *Icarus*, 201:44–68, 2009. doi: 10.1016/j.icarus.2008.12.019.

A. J. West, A. Galy, and M. Bickle. Tectonic and climatic controls on silicate weathering [rapid communication]. *Earth and Planetary Science Letters*, 235:211–228, 2005. doi: 10.1016/j.epsl.2005.03.020.

A. F. White and S. L. Brantley. *Chemical Weathering Rates of Silicate Minerals*. Mineralogical Society of America, 1995.

R.S. White, T.A. Minshull, M.J. Bickle, and C.J. Robinson. Melt generation at very slow-spreading oceanic ridges: Constraints from geochemical and geophysical data. *Journal of Petrology*, 42(6):1171–1196, 2001. ISSN 0022-3530. doi: 10.1093/petrology/42.6.1171.

J. A. Whiteway, L. Komguem, C. Dickinson, C. Cook, M. Illnicki, J. Seabrook, V. Popovici, T. J. Duck, R. Davy, P. A. Taylor, J. Pathak, D. Fisher, A. I. Carswell, M. Daly, V. Hipkin, A. P. Zent, M. H. Hecht, S. E. Wood, L. K. Tamppari, N. Renno, J. E. Moores, M. T. Lemmon, F. Daerden, and P. H. Smith. Mars Water-Ice Clouds and Precipitation. *Science*, 325:68, July 2009. doi: 10.1126/science.1172344.

K. E. Williams, O. B. Toon, J. L. Heldmann, and M. T. Mellon. Ancient melting of mid-latitude snowpacks on Mars as a water source for gullies. *Icarus*, 200:418–425, 2009. doi: 10.1016/j.icarus.2008.12.013.

R. M. Williams, R. J. Phillips, and M. C. Malin. Flow rates and duration within Kasei Valles, Mars: Implications for the formation of a martian ocean. *Geophysical Research Letters*, 27:1073, 2000. doi: 10.1029/1999GL010957.

R. M. E. Williams. Global Spatial Distribution of Raised Curvilinear Features on Mars. In *Lunar and Planetary Institute Science Conference Abstracts*, volume 38 of *Lunar and Planetary Institute Science Conference Abstracts*, page 1821, 2007.

R. M. E. Williams and M. C. Malin. Sub-kilometer fans in Mojave Crater, Mars. *Icarus*, 198:365–383, 2008. doi: 10.1016/j.icarus.2008.07.013.

R. M. E. Williams, M. C. Malin, and K. S. Edgett. Remnants of the Courses of Fine-Scale, Precipitation-Fed Runoff Streams Preserved in the Martian Rock Record. In S. Mackwell & E. Stansbery, editor, *36th Annual Lunar and Planetary Science Conference*, volume 36 of *Lunar and Planetary Institute Science Conference Abstracts*, page 1173, 2005.

R. M. E. Williams, T. C. Chidsey, and D.E. Eby. Exhumed paleochanncels in central Utah - Analogs for raised curvilinear features on Mars? In Willis, G. C. and Hylland, M. D. and Clark, D.L. and Chidsey, T.C., editor, *Central Utah – diverse geology of a dynamic landscape*, volume 36 of *Utah Geological Association Publication*, pages 220–235. 2007.

R. M. E. Williams, A. Deanne Rogers, M. Chojnacki, J. Boyce, K. D. Seelos, C. Hardgrove, and F. Chuang. Evidence for episodic alluvial fan formation in far western Terra Tyrrhena, Mars. *Icarus*, 211:222–237, 2011. doi: 10.1016/j.icarus.2010.10.001.

L. Wilson. Evidence for episodicity in the magma supply to the large Tharsis volcanoes. *Journal of Geophysical Research*, 106:1423–1434, 2001. doi: 10.1029/2000JE001280.

J. N. Winn, J. M. Matthews, R. I. Dawson, D. Fabrycky, M. J. Holman, T. Kallinger, R. Kuschnig, D. Sasselov, D. Dragomir, D. B. Guenther, A. F. J. Moffat, J. F. Rowe, S. Rucinski, and W. W. Weiss. A Super-Earth Transiting a Naked-eye Star. *Astrophysical Journal Letters*, 737:L18+, 2011. doi: 10.1088/2041-8205/737/1/L18.

M. J. Wolff and R. T. Clancy. Constraints on the size of Martian aerosols from Thermal Emission Spectrometer observations. *Journal of Geophysical Research (Planets)*, 108:5097, 2003. doi: 10.1029/2003JE002057.

R. Wordsworth. Exploring the climate of Early Mars through GCM modeling. In *Exoclimes: Exploring the diversity of planetary atmospheres*, University of Exeter/European Space Agency, page 12, 2010.

R. Wordsworth. Transient conditions for biogenesis on low-mass exoplanets with escaping hydrogen atmospheres. *ArXiv e-prints*, 2011.

R. Wordsworth, F. Forget, and V. Eymet. Infrared collision-induced and far-line absorption in dense CO_2 atmospheres. *Icarus*, 210:992–997, 2010. doi: 10.1016/j.icarus.2010.06.010.

R. K. Workman and S. R. Hart. Major and trace element composition of the depleted MORB mantle (DMM). *Earth and Planetary Science Letters*, 231:53–72, 2005. doi: 10.1016/j.epsl.2004.12.005.

J. J. Wray, E. Z. Noe Dobrea, R. E. Arvidson, S. M. Wiseman, S. W. Squyres, A. S. McEwen, J. F. Mustard, and S. L. Murchie. Phyllosilicates and sulfates at Endeavour Crater, Meridiani Planum, Mars. *Geophysical Research Letters*, 362:L21201, 2009. doi: 10.1029/2009GL040734.

J. J. Wray, R. E. Milliken, C. M. Dundas, G. A. Swayze, J. C. Andrews-Hanna, A. M. Baldridge, M. Chojnacki, J. L. Bishop, B. L. Ehlmann, S. L. Murchie, R. N. Clark, F. P. Seelos, L. L. Tornabene, and S. W. Squyres. Columbus crater and other possible groundwater-fed paleolakes of Terra Sirenum, Mars. *Journal of Geophysical Research (Planets)*, 116:E01001, 2011a. doi: 10.1029/2010JE003694.

J. J. Wray, S. L. Murchie, B. L. Ehlmann, R. E. Milliken, K. D. Seelos, E. Z. Noe Dobrea, J. F. Mustard, and S. W. Squyres. Evidence for Regional Deeply Buried Carbonate-Bearing Rocks on Mars. In *Lunar and Planetary Institute Science Conference Abstracts*, volume 42 of *Lunar and Planetary Institute Science Conference Abstracts*, page 2635, 2011b.

K. J. Zabrusky and J. C. Andrews-Hanna. Reconstructing the Original Volume and Extent of the Sedimentary Deposits of Meridiani Planum and Arabia Terra. In *Lunar and Planetary Institute Science Conference Abstracts*, volume 41 of *Lunar and Planetary Institute Science Conference Abstracts*, page 2529, March 2010.

K. J. Zabrusky, J. C. Andrews-Hanna, and S. M. Wiseman. The Distribution and Depositional History of Sedimentary Deposits in Arabia Terra. In *Lunar and Planetary Institute Science Conference Abstracts*, volume 42 of *Lunar and Planetary Institute Science Conference Abstracts*, page 2558, March 2011.

K. Zahnle, R. M. Haberle, D. C. Catling, and J. F. Kasting. Photochemical instability of the ancient Martian atmosphere. *Journal of Geophysical Research (Planets)*, 113:E11004, 2008. doi: 10.1029/2008JE003160.

N. L. Zakamska, M. Pan, and E. B. Ford. Observational biases in determining extrasolar planet eccentricities in single-planet systems. *Monthly Notices of the Royal Astronomical Society*, 410:1895–1910, 2011. doi: 10.1111/j.1365-2966.2010.17570.x.

M. Zechmeister, M. Kürster, and M. Endl. The M dwarf planet search programme at the ESO VLT + UVES. A search for terrestrial planets in the habitable zone of M dwarfs. *Astronomy and Astrophysics*, 505:859–871, 2009. doi: 10.1051/0004-6361/200912479.

R. E. Zeebe and K. Caldeira. Close mass balance of long-term carbon fluxes from ice-core CO_2 and ocean chemistry records. *Nature Geoscience*, 1:312–315, 2008. doi: 10.1038/ngeo185.

R. E. Zeebe, J. C. Zachos, and G. R. Dickens. Carbon dioxide forcing alone insufficient to explain Palaeocene-Eocene Thermal Maximum warming. *Nature Geoscience*, 2:576–580, 2009. doi: 10.1038/ngeo578.

R.E. Zeebe and D.A. Wolf-Gladrow. *CO_2 in seawater: equilibrium, kinetics, isotopes*. Elsevier, 2001.

X. Zeng, M. Zhao, and R. E. Dickinson. Intercomparison of Bulk Aerodynamic Algorithms for the Computation of Sea Surface Fluxes Using TOGA COARE and TAO Data. *Journal of Climate*, 11:2628–2644, 1998. doi: 10.1175/1520-0442(1998)011<2628:IOBAAF>2.0.CO;2.

C. Zmasek and A. Godzik. Strong functional patterns in the evolution of eukaryotic genomes revealed by the reconstruction of ancestral protein domain repertoires. *Genome Biology*, 12(1), 2011. ISSN 1474-7596. doi: 10.1186/gb-2011-12-1-r4.